

**KAOLINITE COLLOID TRANSPORT IN POROUS MEDIA AND
ITS IMPLICATIONS ON CONTAMINANT TRANSPORT**

A Thesis
Presented to
The Academic Faculty

by

Jong Muk Won

In Partial Fulfillment
of the Requirements for the Degree
Doctor of Philosophy in the School of Civil Engineering

Georgia Institute of Technology

December 2017

Copyright © 2017 by Jong Muk Won

KAOLINITE COLLOID TRANSPORT IN POROUS MEDIA AND ITS IMPLICATIONS ON CONTAMINANT TRANSPORT

Approved by:

Dr. Susan E. Burns, Advisor
School of Civil and Environmental
Engineering
Georgia Institute of Technology

Dr. Chloé Arson
School of Civil and Environmental
Engineering
Georgia Institute of Technology

Dr. Sheng Dai
School of Civil and Environmental
Engineering
Georgia Institute of Technology

Dr. J. David Frost
School of Civil and Environmental
Engineering
Georgia Institute of Technology

Dr. Christian Huber
School of Earth and Atmospheric
Sciences
Georgia Institute of Technology

Date Approved: Sep 7, 2017

To my wife, sons, parents and sisters

ACKNOWLEDGEMENTS

I firstly would like to thank my advisor, Dr. Susan E. Burns, for her guidance, insightful advice, encouragement, and all support throughout my Ph.D. study. It was my honor to have a chance to be one of her graduate students. I learned a lot from her professionally and personally: how to perform research from start to the end and how to manage the research group.

I want to acknowledge my thesis committee members, Dr. David Frost, Dr. Chloé Arson, Dr. Sheng Dai, and Dr. Christian Huber, for their insightful comments and suggestions. Their invaluable comments truly contributed to this thesis to be organized correctly.

I also would like to thank the past and current members of Geoenvironmental Laboratory for their help and support: Dr. Hyunwook Choo, Dr. Nortey Yeboah, Dr. Christopher Gray, Dr. Aditya Bhatt, Nicole Caruso, Randy Pettyjohn, Zhi Ge, Akin Akinsola, Xenia Wirth, Junghwoon Lee, and Hejintao Huang. I owe my sincere gratitude to my friends in geosociety and CEE at Georgia Tech, especially to Dr. Junbong Jang, Dr. Sihyun Kim, Dr. Yongha Kim, Junghee Park, Jongchan Kim, Sungho Ahn, Minjae Kim, Hyunwoong Cho, Daejin Kim, Jiwoong Park, Gun Kim, Jiuk Shin, Koochul Ji, Boyoung Jung, Seth Mallett, Madhi Roozbahani and Longde Jin.

Last but not the least, I want to thank my wife, Sojin Park, and my parents for their selfless and priceless support during my Ph.D. study.

TABLE OF CONTENTS

ACKNOWLEDGEMENTS	iv
SUMMARY	ix
LIST OF TABLES	xi
LIST OF FIGURES.....	xii
CHAPTER 1 INTRODUCTION.....	1
1.1 Research motivation.....	1
1.2 Thesis organization	3
CHAPTER 2 LITERATURE REVIEW.....	7
2.1 Colloid transport in porous media.....	7
2.2 Colloid associated contaminant transport in porous media.....	13
CHAPTER 3 INFLUENCE OF IONIC STRENGTH ON CLAY PARTICLE RETENTION AND HYDRAULIC CONDUCTIVITY OF A SAND MEDIUM.....	17
3.1 Introduction	17
3.2 Mathematical model.....	21
3.2.1 Colloidal transport in saturated porous media	21
3.2.2 Blocking phenomenon for ψ_{att}	24
3.2.3 Saturated hydraulic conductivity (K_s) reduction with deposited clay colloids 25	25
3.2.4 Nonlinear least-square curve fit.....	27
3.2.5 Single-collector efficiency of kaolinite.....	27
3.3 Experimental program.....	28
3.3.1 Materials	28
3.3.2 Experimental setup and procedure.....	30
3.4 Results and discussion.....	32
3.4.1 Hydrometer test of kaolinite and calculated single-collector efficiency	32
3.4.2 Retention profiles of clay particles	36
3.4.3 Optimization of first order attachment coefficients (k_{att} , k_{det} and k_{str})	42
3.4.4 K_s reduction curve according to the depth.....	44
3.5 Summary	48

CHAPTER 4	IMPACT OF SOLUTION CHEMISTRY ON THE DEPOSITION AND BREAKTHROUGH BEHAVIORS OF KAOLINITE IN A SILICA SAND	50
4.1	Introduction	50
4.2	Experimental program.....	50
4.2.1	Materials	50
4.2.2	Experimental methods	50
4.3	Results and discussion.....	53
4.3.1	Low flow rate.....	53
4.3.2	High flow rate	60
4.4	Summary	67
CHAPTER 5	A STOCHASTIC APPROACH OF CLAY COLLOID TRANSPORT IN A SAND MEDIUM	70
5.1	Introduction	70
5.2	Mathematical models	74
5.2.1	Colloids transport in saturated porous media.....	74
5.2.2	DLVO and k_{att} calculation	75
5.2.3	Sampling procedure from GSD of sand and clay	77
5.2.4	Numerical procedure.....	80
5.3	Results and discussion.....	83
5.3.1	Simulated RP with experimental result.....	83
5.3.2	Uncertainty of RP using Metropolis-Hastings algorithm	86
5.3.3	Sensitivity analysis.....	91
5.4	Summary	96
CHAPTER 6	ESTIMATION OF MACROSCALE PARAMETERS FOR COLLOID TRANSPORT IN POROUS MEDIA USING PORE NETWORK MODELING	97
6.1	Introduction	97
6.2	Model formulation.....	99
6.2.1	Network construction.....	99
6.2.2	Calculation of fluid flow	100
6.2.3	Sampling of colloids	102
6.2.4	Colloids transport/retention in the network	103
6.2.5	Continuum equation of colloids transport.....	107

6.2.6	The size of the network and calibration of hydraulic conductivity (k).....	108
6.3	Results and discussion.....	111
6.3.1	Effect of parameter θ_0 and particle size distribution of clay colloid (μ_c and σ_c)	112
6.3.2	Size distributions of colloids in retention profiles and breakthrough curves	120
6.3.3	Optimized first-order coefficients in the continuum equation.....	124
6.4	Summary	126
CHAPTER 7 THE ROLE OF IMMOBILE KAOLINITE COLLOIDS IN THE METAL TRANSPORT: A LABORATORY STUDY.....		
7.1	Introduction	128
7.2	Theoretical framework.....	131
7.2.1	Colloid associated contaminant transport in porous media	131
7.2.2	Determination of dispersion coefficient.....	133
7.2.3	Optimization analysis for first-order coefficients.....	135
7.3	Experimental investigation.....	136
7.3.1	Materials	136
7.3.2	Sample preparation and soil-column experiment	138
7.3.3	Equilibrium and kinetic adsorption test	141
7.4	Test results and discussion	142
7.4.1	Adsorption equilibrium and kinetic adsorption test.....	142
7.4.2	Soil-column experiment.....	144
7.4.3	Optimization analysis.....	157
7.5	Summary	161
CHAPTER 8 AN EXPERIMENTAL STUDY OF COTRANSPORT OF HEAVY METALS WITH KAOLINITE COLLOIDS		
8.1	Introduction	163
8.2	Materials and methods	166
8.2.1	Materials	166
8.2.2	Column experiments and experimental conditions.....	167
8.2.3	Batch adsorption equilibrium and kinetic test for single and multi-metal	169
8.3	Mathematical model.....	169
8.3.1	Kaolinite colloid transport	169

8.3.2	Cotransport of kaolinite colloid and heavy metal	170
8.3.3	Optimization analysis.....	171
8.3.4	Bed efficiency and metal saturation.....	176
8.4	Results and discussion.....	177
8.4.1	Results of batch kinetic and equilibrium tests	177
8.4.2	Cotransport of heavy metals in silica sand	180
8.4.3	Cotransport of heavy metals under presence of kaolinite colloids (multi-metal system).....	182
8.4.4	Cotransport of heavy metals under presence of kaolinite colloids (multi-metal system).....	190
8.5	Summary	193
CHAPTER 9 CONCLUSION AND FUTURE WORK.....		195
REFERENCES.....		201
VITA		217

SUMMARY

Organic and inorganic colloidal particles are ubiquitous in the geologic subsurface environment and they transport readily through porous media due to their relatively small size when compared to pore spaces. While an extensive body of research exists that quantifies colloid and colloid-associated contaminant transport in porous media, few studies have investigated the physical impact of clay colloid retention and transport on the hydraulic properties of the formation, and its subsequent impact on contaminant transport. Specifically, changes in the geochemistry and groundwater flowrate within the formation can result in aggregation or dispersion of colloids. Depending on the prevailing attachment mechanisms, colloids can clog the porous media, and can either facilitate or retard contaminant transport. The work performed in this study used DLVO theory to quantify colloidal clay attachment and transport mechanisms within sand column experiments, and its subsequent impact on hydraulic conductivity and contaminant transport through the soil media. Column tests were performed to measure the reduction of hydraulic conductivity due to physical clogging by colloids, as a function of flowrate and solution chemistry. In addition, stochastic and pore network modeling were applied to predict clay colloidal transport in order to account for the polydispersed characteristics of both the sand medium and the colloidal clay particles. Finally, column tests and batch adsorption tests were performed to quantify clay colloid associated heavy metal transport (facilitated or retarded) to determine the impact of the presence of clay colloids on single-ion and multi-ion metal transport. All soil-column experiments performed in this work were quantified by evaluating optimized first-order rate coefficients associated with clay-sand interaction, clay-metal interaction, and sand-metal interaction, which provided quantitative

representation of the experimentally obtained retention profiles and breakthrough curves. The major findings of this research are as follows: i) solution chemistry played an important role in hydraulic conductivity and contaminant transport, particularly at low flow rates, ii) the reduction of hydraulic conductivity was not only a function of retained clay colloids but also depended on the dominant retention mechanism (attachment and/or straining), iii) polydispersed characteristics of clay colloids and uncertainty in the size of clay clusters should be considered in predicting clay colloid transport, and iv) retention of clay colloids retarded heavy metal transport while the transport of clay colloids facilitated heavy metal transport.

LIST OF TABLES

Table 3-1. Measured Soil Properties.....	29
Table 3-2. Testing Conditions.....	32
Table 3-3. Evaluated First-Order Coefficient (k_{att} , k_{det} and k_{str}) as a Result of the Optimization Analyses in the Least Square Sense in Two Scenarios.....	43
Table 3-4. Optimized k_{att} and k_{str} with Fixed k_{det} in the Least Squares Analysis	44
Table 3-5. The Experimental and Theoretical K_{rel} after 10 PV	46
Table 4-1. Recovered Fraction of Attached Kaolinite in a Sand Medium (M_s), Observed Kaolinite at Effluent during 20 PVs Injection (M_e), Detached Kaolinite during 10 PVs of DI Water Injection (M_d), and Kaolinite Mass Balance (MB)	64
Table 6-1. Optimized k_{att} in All Conditions (Equation (6-15))	125
Table 7-1. Summary of Kaolinite and Sand Properties	136
Table 7-2. Experimental Conditions for Lead Sorption Column Tests	141
Table 7-3. Equilibrium and Kinetic Parameters Measured for Tested Soils	142
Table 7-4. Transport Parameters used in Optimization Analysis	160
Table 7-5. Results of Optimization Analysis in Two Scenarios for Each Condition	161
Table 8-1. Optimized Coefficients Associated with Metal Adsorption/Desorption to the Mobile Kaolinite Colloids (Equation (8-6)) Based on Batch Kinetic Test (ionic strength = 0.003 M, $C_f = 16.7$ g / L).....	174
Table 8-2. Optimized Rates (k_{att} , k_{det} and k_{str} in Equation (3-5)) Associated with the Transport of Kaolinite Colloids from the Experimental Retention Profiles after 10 Pore Volumes of Injection (ionic strength = 0.003 M).....	175
Table 8-3. Optimized Langmuir Parameters for Three Metals in the Absence of Kaolinite Colloids. Data from Experimental Breakthrough Curves of Competitive Heavy Metal Transport and Dispersion Coefficients (D and D_c) of Metal and Kaolinite Colloids (ionic strength = 0.003 M).....	176
Table 8-4. β and ϕ of Experimental Breakthrough Curve and Optimized k_{aic} , k_{dic} , and ω in Multi-metal System.....	188
Table 8-5. β and ϕ of Experimental Breakthrough Curve and Optimized k_{aic} , k_{dic} and ω in Single-metal System	192

LIST OF FIGURES

Figure 2.1. Example of DLVO calculation in two different scales when $r_c = 1 \mu\text{m}$, $r_s = 360 \mu\text{m}$ and $IC = 0.01 \text{ M}$ of 1:2 electrolytes (e.g. CaCl_2), where $r_c =$ radius of colloid (L), $r_s =$ radius of sand (L), $IC =$ ionic concentration, $G =$ total interaction energy (J), $G_{VDW} =$ van der Waals interaction energy (J), $G_{DL} =$ double layer interaction energy (J), and $G_{\text{min}} =$ secondary minimum energy (J).....	9
Figure 2.2. Conceptual drawing of surface cake, straining, attachment and detachment (Boulding and Ginn 2003).	11
Figure 3.1. Experimental setup for flow conditions with pumped colloidal suspensions.	31
Figure 3.2. Hydrometer test result of the kaolinite at different ionic concentration: d_{50} of deionized with no dispersant $\approx 18 \mu\text{m}$, d_{50} of $0.001 \text{ M CaCl}_2 \approx 18 \mu\text{m}$, d_{50} of $0.01 \text{ M CaCl}_2 \approx 12 \mu\text{m}$, d_{50} of $0.1 \text{ M CaCl}_2 \approx 7.4 \mu\text{m}$, d_{50} of $0.1 \text{ M NaCl} \approx 12 \mu\text{m}$, and d_{50} of deionized with dispersant (following the test procedure of ASTM D422, Sodium hexametaphosphate ($(\text{NaPO}_3)_6$) used as a dispersant) $\approx 0.45 \mu\text{m}$	34
Figure 3.3. Single-collector efficiency (η_0) of the kaolinite particles calculated by Equation (3-1). Open circles represent the η_0 with gravity term ($\eta_0 = \eta_D + \eta_I + \eta_G$), open squares represent the η_0 without gravity term ($\eta_0 = \eta_D + \eta_I$) according to the diameter of the kaolinite (d_c). Also, the range of the d_c (d_{50} of the kaolinite according to the solution chemistry obtained by the hydrometer test in Figure 3.2) and shift of the gravity line in case of $\rho_c = 1 \text{ g / cm}^3$ are illustrated.	35
Figure 3.4. Experimental (open markers) and curve fitted clay RP (dotted, dashed, and dot-dashed lines) with depth according to the type of sand.....	37
Figure 3.5. Experimental (open markers) and curve fitted clay RP (solid and dotted lines) with depth according to the type of sand and the concentration of clay suspension: The biggest value for number of particles at the same depth represent the experiments A3 and G3 whereas the smallest number of particles represent the experiments A1 and G1. From the left hand side, LS fit curves represent A1, A2 and A3 for solid lines and G1, G2 and G3 for dotted lines.	40
Figure 3.6. Experimental (open markers) and curve fitted clay RP (solid and dotted lines) with depth according to the solution chemistry at the relatively low concentration (1 g / L) of clay suspension.	41
Figure 3.7. Experimental (open markers) and curve fitted clay RP (solid and dotted lines) with depth according to the solution chemistry at the relatively high concentration (5 g / L) of clay suspension.	42
Figure 3.8. The reduction of K_{rel} with PV for the experiment A1	45
Figure 4.1. Schematic of experimental setup.....	53

Figure 4.2. Breakthrough curves of kaolinite under low flow rate: (a) pH ~ 6 under different IS and (b) pH ~ 3 and 9 with IS = 0.001 and 0.1 M. C/C_0 on y axis represents the normalized concentration of kaolinite colloids at effluent.	55
Figure 4.3. Normalized pressure difference (dP / dP_0) during the injection under low flow rate: (a) as function of ionic strength at pH ~ 6, (b) as function of pH at IS ~ 0.001 M and (c) as function of pH at IS ~ 0.1 M.....	56
Figure 4.4. Kaolinite deposition profile after the injection under low flow rate: (a) as function of ionic strength at pH ~ 6, (b) as function of pH at IS ~ 0.001 M and (c) as function of pH at IS ~ 0.1 M.	57
Figure 4.5. Breakthrough curves of kaolinite under high flow rate: (a) pH ~ 6 under different IS and (b) pH ~ 3 and 9 with IS = 0.001 and 0.1 M (c) pH ~ 9 and IS = 0.001 M in a larger C/C_0 scale.....	61
Figure 4.6. Normalized pressure difference (dP / dP_0) during the injection under high flow rate: (a) as function of ionic strength at pH ~ 6 (b) as function of pH at IS ~ 0.001 M and (c) as function of pH at IS ~ 0.1 M.....	62
Figure 4.7. Kaolinite deposition profile after the injection under high flow rate: (a) as a function of ionic strength at pH ~ 6 (b) as a function of pH at IS ~ 0.001 M and (c) as a function of pH at IS ~ 0.1 M.	63
Figure 5.1. Sampling under $N = 50$ using the Metropolis-Hastings algorithm and the LHCS method at the target lognormal CDF from the clay colloids grain size distribution, where μ and σ are mean and standard deviation of lognormally fitted target CDF, r_{c50} is the median value of sampled r_c , and R^2 is the coefficient of determination between the CDF and the experimental grain size distribution. The experimental grain size distribution was obtained by hydrometer test using Georgia kaolinite with ionic strength = 3×10^{-3} M (CaCl_2). Unexpectedly high r_{c50} was observed in this sampling for Metropolis-Hastings algorithm due to the relatively small N , while r_{c50} evaluated by LHCS method was almost identical to the r_{c50} in the lognormal CDF and well distributed to the target CDF, even under small N	79
Figure 5.2. Example calculation of k_{att} and k_{str} as a function of r_c and r_s when $N_{rc} = N_{rs} = 1000$. Both k_{att} and k_{str} nonlinearly increase as r_c / r_s ratio decreases. The target lognormal PDFs used in the calculation were $\mu_s = 5.17$, $\sigma_s = 0.34$, $\mu_c = -0.93$, and $\sigma_c = 1.52$ (μ and σ indicate mean and standard deviation of normal PDF corresponding to the target lognormal PDF, subscript s = sand, c = clay), $r_{c50} \approx 0.47 \mu\text{m}$, and $r_{s50} \approx 181.27 \mu\text{m}$. The Metropolis-Hastings algorithm was used for sampling here.	83
Figure 5.3. Experimental GSDs and corresponding target CDFs.....	85
Figure 5.4. Observed and simulated RPs until 10 PV for dispersed kaolinite colloids and kaolinite cluster. Note that observed RP for the dispersed system is not available, Metropolis-Hastings algorithm used here with $N_{rc} = 10^4$ and $N_{rs} = 1$, and $r_{s50} = 360 \mu\text{m}$, $U = 7.3 \times 10^{-2} \text{ cm / s}$, $n_0 = 0.365$	86

Figure 5.5. The histogram of r_{c50} in 100 sets of random sampling using the Metropolis-Hastings algorithm when $N_{rc} = 100$. The median value of r_{c50} ($\text{Med}[r_{c50}]$) is almost equal to the median value of the target CDF ($\approx 0.4 \mu\text{m}$, Figure 5.3), which indicates that the combination of 100 set of sampling is well distributed to the target CDF without biased toward the one direction.	87
Figure 5.6. Maximum, minimum, and mean of simulated retention profile along with the box plot and retention profile from deterministic r_c and r_s (i.e. $N_{rc} = N_{rs} = 1$) with respect to 100 sets of sampled r_c (Figure 5.5). The edges of the boxes correspond to 25% and 75% coverage, and the central line in the boxes represents the median value of retained colloids in each discretized spatial point. The whisker line of each box plot indicates 99 % coverage for a distribution in each depth.	89
Figure 5.7. Variation of k_{att} (Equation (5-4)), k_{str} (Equation (3-7)), α (Equation (5-5)) and η_0 according to r_c . All other parameters (e.g. r_s , v_s , A_{swc}) in the calculation remain constant except the parameters change as a function of r_c (e.g. D_∞ , G_{DL} , G_{VDW} , where D_∞ (L^2T^{-1}) is the bulk diffusion coefficient).	90
Figure 5.8. Simulated retention profiles according to the different σ_c (or C_u) under constant μ_c and μ_s (i.e. r_{c50} and r_{s50}). LHCS method was used here with $N_{rc} = 1000$ and $N_{rs} = 1$ (again, $r_s = 360 \mu\text{m}$).	93
Figure 5.9. Simulated breakthrough curves according to the different σ_c (or C_u) under constant μ_c and μ_s	93
Figure 5.10. Normalized S_{sum} according to r_{c50} / r_{s50} ratios under three different simulated conditions.	94
Figure 6.1. Flow chart describing key features of the model.	106
Figure 6.2. The effect of numbers of pores in x, y, and z axes (N_x , N_y , and N_z) on the hydraulic conductivity (k) of the network. Note that $N_x = N_y$ in this calculation.	109
Figure 6.3. An example visualization of the regular cubic pore network used in this simulation. Colloid suspension was injected at the top of the network and part of throats were eliminated randomly until $CN \sim 5.4$. The color of pores indicates pressure values at pores from high (colored in red) to low (colored in blue).	110
Figure 6.4. Calibration of the hydraulic conductivity of the network (k_{pnm}) to experimentally measured hydraulic conductivity (k_{exp}).	111
Figure 6.5. (a) Retention profiles after the injection, (b) breakthrough curves, and (c) the reduction of hydraulic conductivity during the injection under varied θ_0 at $\mu_c = 2.2$ and $\sigma_c = 0.01$. $S+nC/\rho_b$ presented in (a) represents retained colloids in the solid phase (S) and aqueous phase (nC/ρ_b).	114
Figure 6.6. (a) Bed efficiency of colloids (β , Equation (7-13)), and (b) the final value of hydraulic conductivity after 10 PV of injection as a function of θ_0	116

Figure 6.7. (a) Retention profiles after the injection, (b) breakthrough curves, and (c) the reduction of hydraulic conductivity during the injection under varied σ_c at $\mu_c = 1.8$ and $\theta_0 = 4$.	118
Figure 6.8. (a) Retention profiles after the injection, (b) breakthrough curves, and (c) the reduction of hydraulic conductivity during the injection at $\mu_c = 2.2, 1.8$ and 1.3 ($\theta_0 = 8$ and $\sigma_c = 0.3$).	120
Figure 6.9. Size distributions of retained colloids under varied θ_0 at $\mu_c = 1.8$ and $\sigma_c = 0.3$.	122
Figure 6.10. Size distributions of colloids in effluent under varied θ_0 at $\mu_c = 1.8$ and $\sigma_c = 0.3$.	123
Figure 6.11. Optimized k_{att} under varied θ_0 at $\mu_c = 2.2, 1.8, 1.3$ and $\sigma_c = 0.01, 0.3$.	126
Figure 7.1. The retention profile of kaolinite colloids after injecting the kaolinite suspension into the ASTM-graded sand in deionized water: the diameter and the height of the column were 7.62 cm (3 inches) and 30.48 cm (12 inches), respectively, water flux was 0.0365 cm/s, and the sand was initially packed to $D_r = 70\%$ (D_r is relative density, $D_r = (e_{max} - e) / (e_{max} - e_{min})$).	138
Figure 7.2. Turbidity and electrical conductivity measured during injection of first 15 PVs. Kaolinite concentration = 3%, and background solution was deionized water.	140
Figure 7.3. The result of the Pb(II) equilibrium adsorption test for the kaolinite and the sand.	143
Figure 7.4. The result of the Pb(II) kinetic adsorption test for the kaolinite and the sand: the $C(t)$ represents the Pb(II) concentration of supernatant at time t .	143
Figure 7.5. Pb(II) breakthrough curves under two KC and two C_i with deionized water.	145
Figure 7.6. Pb(II) breakthrough curves under two flow rates and three KC: $Q = 6$ and $20 \text{ cm}^3 / \text{min}$ are corresponding to low and high v_s for each KC in Table 7-1, elapsed time for $Q = 6$ and $20 \text{ cm}^3 / \text{min}$ were roughly 9.5 hrs and 2.8 hrs, and $C_i \approx 5 \text{ mg/L}$ and deionized water was used for all cases.	146
Figure 7.7. Calculated β and Pb(II) saturation of the bed from Equation (7-13) and (7-14), respectively according to kaolinite concentration and flow rate.	148
Figure 7.8. Pb(II) breakthrough curves according to pH at three different values of kaolinite concentration: $Q = 20 \text{ cm}^3 / \text{min}$, $C_i \approx 5 \text{ mg/L}$ and $IS \approx 0$ for all experiments.	150
Figure 7.9. Zeta potential of kaolinite as a function of pH: Samples were prepared by mixing 500 mg/L of the kaolinite in deionized water for 30 min, and controlling pH with HNO_3 and NaOH .	153

Figure 7.10. Calculated β and Pb(II) saturation of the bed from Equation (7-13) and (7-14) respectively according to kaolinite concentration and pH: Pb(II) saturation = 2.2 at kaolinite concentration = 1% and pH = 9 (data not shown).	154
Figure 7.11. Pb(II) breakthrough curves according to four different level of IS: $Q = 20 \text{ cm}^3 / \text{min}$, $C_i \approx 5 \text{ mg/L}$, $\text{pH} \approx 5.6$ and $\text{KC} = 3 \%$ for all experiments.	156
Figure 7.12. Calculated β and Pb(II) saturation of the bed from Equation (7-13) and (7-14) respectively according to IS.....	157
Figure 7.13. k_a / k_d ratio based on the optimization analysis according to KC: (a) flow rate and IS, (b) pH.....	159
Figure 8.1. Batch equilibrium test results of kaolinite colloids in (a) multi-metal system and (b) single-metal system.	178
Figure 8.2. Batch kinetic test results of kaolinite colloids ($C_i = 5 \text{ mg L}^{-1}$) in (a) multi-metal system and (b) single-metal system. Data fitted to Equation (8-6) and the corresponding k_{amc} and k_{dmc} values are presented in Table 8-1. Data for 240 and 1440 min are not presented here.	179
Figure 8.3. Observed and simulated breakthrough curves of three metals under the absence of kaolinite colloids: (a) $q = 2.22 \text{ cm/min}$; (b) $q = 0.74 \text{ cm/min}$	181
Figure 8.4. Observed and simulated breakthrough curve of heavy metals and kaolinite in the multi-metal system under the difference kaolinite concentration under high flow rate.	185
Figure 8.5. Observed and simulated breakthrough curve of heavy metals in the multi-metal system under the difference kaolinite concentration with low flow rate. No kaolinite was observed ($C_c / C_{c0} < 0.01$ for 10 pore volumes).....	187
Figure 8.6. Observed and simulated retention profiles of kaolinite colloids under (a) high flow rate and (b) low flow rate in three different inlet concentrations. Optimized coefficients associated with retention profiles are presented in Table 8-2.	189
Figure 8.7. Observed and simulated breakthrough curve of heavy metal ions in the single-metal system under two different flow rates.....	191

CHAPTER 1 INTRODUCTION

1.1 Research motivation

Organic and inorganic colloidal particles present in the subsurface environment can transport through porous media due to their relatively small size when compared to the pore size of the porous media (McCarthy and Zachara 1989). A colloid is typically defined as a particle that has a grain size less than 10 μm . Colloid transport is important because these particles can facilitate transport of organic or inorganic contaminants through favorable attachment of the contaminants onto colloidal particles. This results in transport of the colloid/contaminant that can be faster or slower than the flow of fluid, which poses challenges in transport modeling. Additionally, in some cases, the colloid itself is considered a contaminant (Mills et al. 1991) and under relatively high concentrations of suspended colloids, physical clogging of the pore space of the porous media can decrease the hydraulic conductivity and downgrade the performance of subsurface infrastructure, such as artificial recharge systems (Bouwer 1996), infiltration structures (Siriwardene et al. 2007), and oil well recovery systems (Valdes and Santamarina 2006).

For contaminant transport in saturated porous media, the two-phase model has traditionally been used to model the process of transport by including partitioning of the contaminant between the immobile solid phase and the mobile aqueous phase (van Genuchten and Wierenga 1976). However, it is now commonly believed that the three-phase model is more appropriate to account for contaminant transport under the presence of mobile or immobile colloids (Corapcioglu and Jiang 1993; Šimůnek et al. 2006; Um and Papelis 2002). If contaminants are favorably attached to the colloidal particle, and most of

the colloids are attached to the bulk soil solid (such as sand), contaminants are more likely to be retarded and transport more slowly than the pore fluid. In contrast, if the colloids are strongly associated with the contaminants and are not attached to the soil solids, but are highly mobile, the transport of contaminants may be faster than the pore fluid. The former case is known as “colloid retarded contaminant transport” while the latter is known as “colloid-facilitated contaminant transport”, and together they are generally referred to as “colloid associated contaminant transport” (Sen and Khilar (2006)). The application of a three-phase model is mathematically more complex than the two-phase model in terms of quantitative characterization of colloid associated contaminant transport.

Natural colloids occur in a variety of shapes, sizes, and material types but clay colloids are one of the most prevalent types encountered in the subsurface environment. Investigating clay mineral colloidal transport in porous media is inherently distinct from the transport of semi-monosized colloids, such as pathogenic bacteria, due to their high variability of size, and the tendency of aggregation and/or flocculation and clustering (Berka and Rice 2005; Heidmann et al. 2005; Zbik et al. 2008). Aggregation of clay colloids can occur in four primary types of formation (edge-to-face, edge-to-edge, face-to-face association, and combined face-to-face and edge-to-face association), which is driven primarily by the solution chemistry of the pore fluid (Palomino and Santamarina 2005). In addition, regardless of aggregation behavior, the aggregates can generally be described with a coefficient of uniformity (C_u) approximately equal to 10 (Mitchell and Soga 2005). Consequently, these two factors must be taken into account in clay colloidal transport because the behavior is impacted by the size of transporting unit. In terms of contaminant transport, predicting the retention profile or breakthrough curve of clay colloids is crucial,

particularly for the contaminants that have a high tendency to adsorb on to clay colloids (e.g., radionuclides and metals) (Chen et al. 2005; Ho and Miller, N. H 1986; Tang and Weisbrod 2009; Um and Papelis 2002; Vilks and Baik 2001; Yin et al. 2010; Zhuang et al. 2003). Due to the high specific surface and cation exchange capacity of clay colloids, transport of these contaminants is controlled by the mobility of clay colloids.

While an extensive amount of research and modeling have been performed for quantifying colloid and colloid-associated contaminant transport in porous media, fewer studies have been implemented for clay colloid retention/transport despite its importance in the performance of infrastructure, which can be degraded by the reduction of hydraulic conductivity and contaminant transport caused by favorable adsorption of contaminants to clay colloids. Therefore, additional research is needed to investigate transport in systems of colloidal clay particles.

1.2 Thesis organization

The work performed in this study focused on an experimental investigation of clay colloid retention/transport and heavy metal transport in the presence of immobile/mobile clay colloids. Laboratory soil-column experiments were performed and the optimized first-order coefficients were evaluated for the observed retention profiles or breakthrough curves. Analysis was performed by numerically solving governing equations in three experimental conditions (colloid-sand system, contaminant-immobile colloid-sand system, and contaminant-mobile-immobile-sand system). In addition, clay colloid retention/transport in a sand medium was modeled using a stochastic approach and a pore network in order to account for the polydispersed characteristics of clay colloids and a sand medium.

The work performed in this investigation is divided into the following Chapters:

The work performed in Chapter 2 provides a review of colloid and colloid-associated contaminant transport in porous media, including the fundamental mechanisms involved in those two phenomena.

The work performed in Chapter 3 details experimental work to quantify clay colloid retention as a function of ionic strength and the size of the filter media. The reduction of saturated hydraulic conductivity due to colloid retention was also investigated analytically and experimentally. Retention mechanisms of clay colloids were explored by optimized first-order coefficients associated with straining, attachment, and detachment of clay colloids.

The work performed in Chapter 4 explores the coupled effects of pH and ionic strength on transport/retention of clay colloids in a sand medium. Derjaguin, Landau, Verwey, and Overbeek (DLVO) theory was used to explain the shapes of observed retention profiles, and the recovered fraction in breakthrough curves were evaluated to quantitatively determine transport/retention of clay colloids.

The work performed in Chapter 5 presents the results of a stochastic model for clay colloid transport in a sand medium. Sampled sizes of clay colloids and sand grains at given grain size distributions were applied in a numerical scheme to account for the stochastic nature of continuum colloid transport models. DLVO theory and colloid filtration theory were used to evaluate an attachment coefficient as a function of the size of clay colloid and sand, in order to investigate the uncertainty of the retention profile and breakthrough curves of clay colloids.

The work performed in Chapter 6 presents the development of a pore network model for colloid transport in a sand medium, and colloid retention/transport and the reduction of hydraulic conductivity, which provided pore-scale evaluation of colloid transport. This chapter also assesses the impacts of particle size distribution of colloids (mean and standard deviation of given lognormal distribution) and size distributions of colloids in retention profiles and breakthrough curves after ten pore volumes of flow. Also, the role of immobile/mobile clay colloids in heavy metal transport in porous media was investigated by performing a series of soil-column experiments and by evaluating optimized first-order coefficients associated with immobile colloids-metal reaction and mobile colloids-metal reaction.

The work performed in Chapter 7 quantifies Pb(II) transport in a sand medium under the presence of immobile clay colloids. The variables included pH, ionic strength, and kaolinite content in a sand medium, and the breakthrough curves measured during injection of Pb(II) solution for 100 pore volumes of flow are presented. Bed efficiency and Pb(II) saturation were measured, which allowed quantitative presentation of the amount of adsorbed Pb(II) by the bed during the injection of 100 pore volumes, based on batch-adsorption test results between Pb(II) and kaolinite.

The work performed in Chapter 8 investigates heavy metal transport in porous media in the presence of mobile clay colloids. Cu(II), Zn(II), and Pb(II) were used as heavy metals, and the breakthrough curves of these three metals and clay colloids were presented. Retention profiles and breakthrough curves of clay colloids and optimized coefficients

associated with the reaction between mobile colloids and metals provided a fundamental insight for co-transport of heavy metals and clay colloids.

Overall, the work performed in this dissertation used experimental, analytical, and numerical methods to study the transport characteristics of colloidal particles moving through a sand filter media, with the following variables:

- under conditions of variable ionic strength and pH, which impacted the aggregation and flocculation behavior of the clay colloid, and impacted attachment/straining of colloidal particles
- under variable filter media particle size (and pore size)
- under conditions of decreasing hydraulic conductivity due to colloidal retention
- under conditions of varying grain size (clay and sand), modeled with a stochastic approach
- under pore network scale conditions, modeled by numerically for retention and breakthrough of colloidal particles
- under heavy metal ion transport conditions, with immobile colloids, mobile colloids, and competitive sorption

CHAPTER 2 LITERATURE REVIEW

2.1 Colloid transport in porous media

Three main mechanisms are involved in retention of colloids in saturated porous media: attachment, detachment, and straining. Attachment of colloids primarily takes place due to the net attractive interaction energy between colloids and the soil substrate (assumed to be silica sand in this investigation). The interaction energy is obtained by summing van der Waals interaction energy and the double layer interaction energy, based on the theory originally proposed by Derjaguin, Landau, Verwey, and Overbeek (DLVO theory) (Derjaguin and Landau 1941; Verwey and Overbeek 1948). If the size of the sand grain is much bigger than that of colloid, total interaction (G) between colloid and sand by DLVO theory can be expressed as (Israelachvili 2011):

$$G = G_{DL} + G_{VDW} = (r_c Z \exp(-\kappa H)) + (-A_{swc} r_c / 6H) \quad (2-1)$$

where G_{DL} (ML^2T^{-2}) and G_{VDW} (ML^2T^{-2}) are the interaction energy attribute to double layer repulsion and van der Waals attraction, respectively, r_c is the radius of colloid (L), Z (ML^2T^{-3}) is the interaction constant as a function of surface potential of sand and clay colloid, κ (L^{-1}) is a reverse of Debye length as a function of ionic concentration and valence, H (L) is the separation distance, and A_{swc} (ML^2T^{-2}) is the Hamaker constant in sand-water-colloid system, calculated using the refractive index and dielectric constant of those three materials. The electrostatic double layer interaction energy between colloids and silica sand grains typically results in repulsion (positive energy) due to the characteristic negative surface charge of both the colloid and sand (i.e., unfavorable condition). In contrast, van der Waals interaction energy results in attraction (negative energy), mainly caused by the

positive Hamaker constant in colloid-water-sand systems (Bradford et al. 2011). The net interaction energy profile is characterized by primary and secondary minimums due to the energy barrier from high van der Waals attraction at the surface of the sand and slightly higher van der Waals attraction compared to the double layer repulsion at some separation distance from the surface (Figure 2.1). Under prevailing unfavorable conditions, the attachment of colloids primarily takes place at the secondary minimum due to the relatively large energy barrier which is difficult to overcome by colloids, making it difficult to reach the primary minimum (Hahn et al. 2004; Litton and Olson 1996). In addition, the magnitude of the energy barrier increases as ionic strength decreases, due to the formation of a larger double layer in both colloidal and sand particles (Santamarina et al. 2001; Tufenkji and Elimelech 2005). To account for this behavior in the colloidal mass balance equation, the first order attachment coefficient (k_{att}) is frequently expressed as a function of attachment efficiency (α) by colloid filtration theory (Rajagopalan and Tien 1976; Tufenkji and Elimelech 2004; Yao et al. 1971), and α is written as a function of the secondary minimum energy with the assumption that the velocity distribution of colloids follows the Maxwell distribution in the secondary minimum (Bradford et al. 2011; Dong et al. 2002; Shen et al. 2007).

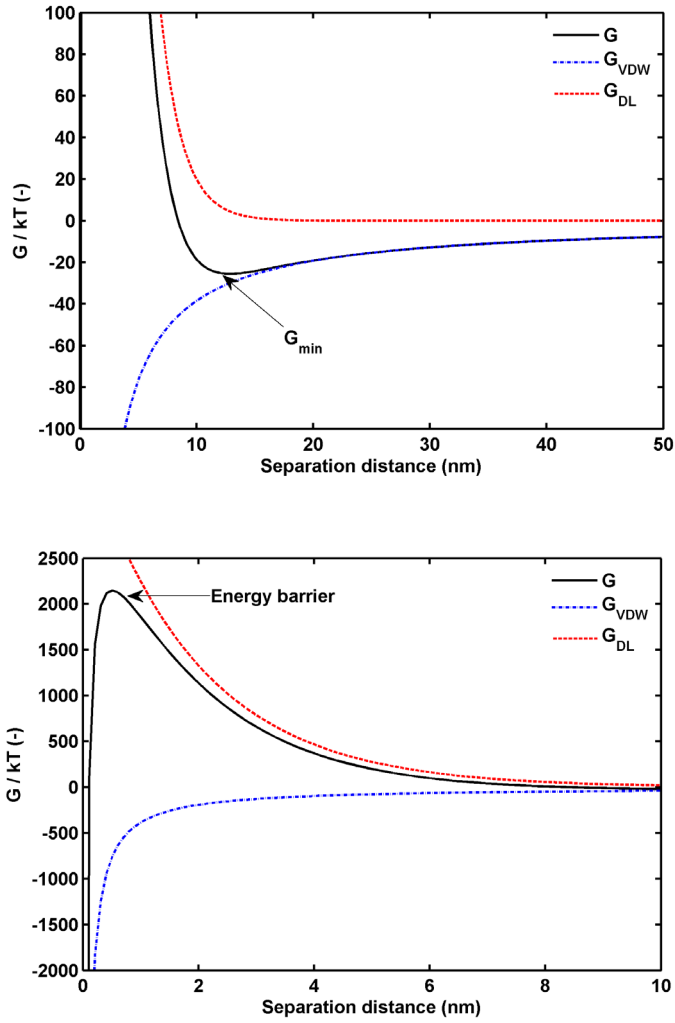


Figure 2.1. Example of DLVO calculation in two different scales when $r_c = 1 \mu\text{m}$, $r_s = 360 \mu\text{m}$ and $IC = 0.01 \text{ M}$ of 1:2 electrolytes (e.g. CaCl_2), where r_c = radius of colloid (L), r_s = radius of sand (L), IC = ionic concentration, G = total interaction energy (J), G_{VDW} = van der Waals interaction energy (J), G_{DL} = double layer interaction energy (J), and G_{min} = secondary minimum energy (J).

After attachment of colloids to the sand grain, detachment of colloids can also occur. The detachment process is mainly caused by a change in solution chemistry or hydrodynamic shear (Bergendahl and Grasso 1999, 2000b). A change of solution chemistry

also changes the surface charge of both the colloid and sand particle and colloids may be detached from the sand when pH increases and ionic concentration decreases, even under favorable attachment condition (i.e., no energy barrier present) (Shen et al. 2012a). Under such conditions in the solution chemistry, the repulsive interaction energy becomes dominant and finally leads to a decrease in both the primary and secondary minimum (Amirtharajah and Raveendran 1993; Bergendahl and Grasso 2003; Nocito-Gobel and Tobiason 1996). In addition, an extensive amount of recent work revealed that surface roughness of a sand grain also plays an important role for colloidal detachment (Kraft et al. 2012; Shen et al. 2012b; Torkzaban and Bradford 2016). According to Torkzaban and Bradford (2016), both the primary minimum and the difference between the energy barrier and secondary minimum decrease with increasing surface roughness, which implies that detachment of colloids is more likely to occur with significant surface roughness. In contrast, rolling of colloids induced by hydrodynamic force has been considered as the main mechanism of colloid detachment (Bergendahl and Grasso 1998; Bradford et al. 2013; Tsai et al. 1991). Therefore, detachment of colloids occurs when the resistance torque based on DLVO calculation is smaller than the hydrodynamic torque from the lift and drag forces applied to the attached colloids. Overall, the mechanism of detachment can be explained by coupling the effects of thermodynamic and hydrodynamic actions applied to the attached colloids.

The straining mechanism of removal is defined as colloid immobilization due to the relatively narrow pore size of the sand medium (Auset and Keller 2006; Bradford et al. 2003; Torkzaban et al. 2008; Xu et al. 2006). This mechanism relies on physical removal rather than physicochemical removal through attachment or detachment processes. In

straining, the size ratio between the colloid and sand particles (r_c / r_s ratio) is the most important factor. It is commonly accepted that the larger grain size of sand leads to a larger pore size (Arya et al. 1999a; Reddi et al. 2005). Previous literature reported that straining becomes more substantial than attachment and detachment when r_c / r_s ratio is larger than 0.0017 ~ 0.005 (Bradford et al. 2002, 2006; Johnson et al. 2007). In addition, recent studies demonstrated that the strained colloids are irreversibly attached, even under changes in solution chemistry, and independent of the degree of saturation (Sang et al. 2013). Straining is dominant under relatively low ionic strength, small Young's modulus of the colloid, and high surface roughness (Bradford et al. 2013). If the sizes of all colloids introduced in a sand medium are larger than all ranges of pore sizes, a surface cake may form, which decreases hydraulic conductivity significantly (Bradford et al. 2002) (Figure 2.2).

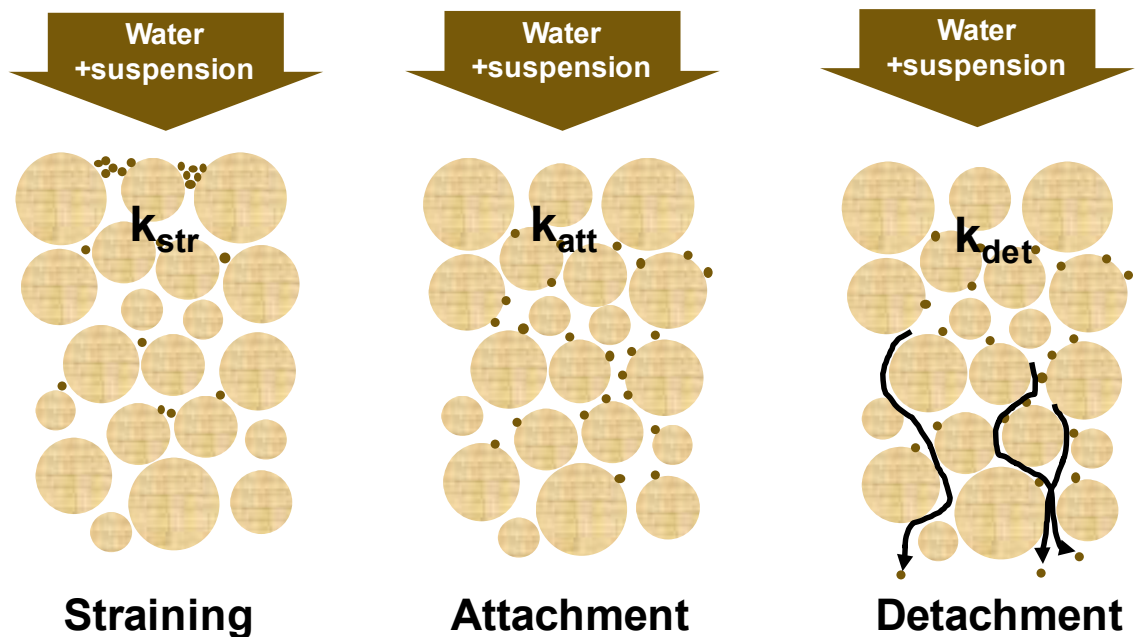


Figure 2.2. Conceptual drawing of surface cake, straining, attachment and detachment (after Boulding and Ginn 2003).

A number of mathematical models have been proposed to account for colloidal transport in porous media from a theoretical standpoint. One model, colloid filtration theory (CFT) (Yao et al. 1971), was developed to consider the deposition behavior of colloids on a single grain collector based on the Happel sphere-in-cell model (Happel 1958). The collision efficiency of colloids with the soil-water interface in CFT is described as a combination of diffusion, interception, and gravitational sedimentation (Rajagopalan and Tien 1976; Tufenkji and Elimelech 2004). However, CFT is not able to capture the impact of the pore structure and the shape of grain, which are also important for the deposition (or retention) of colloids, particularly for straining (Bradford et al. 2006). In addition, while CFT can provide the microscale insight for mechanisms involved in colloidal attachment, it is still difficult to apply CFT to the macroscale or continuous domain. Several models have built on CFT, with additions such as first-order attachment and detachment coefficients to the conventional advection-dispersion equation, describing attachment and detachment in first order kinetics of colloids in the aqueous phase and solid phase respectively (Corapcioglu and Choi 1996; Harvey and Garabedian 1991; Ryan and Gschwend 1994), two-site kinetics approach, modeling the mass balance of colloids with the amount of attached colloids that can be reversibly and irreversibly attached (Compère et al. 2001; Hendry et al. 1997; Yan 1996), a dual-porosity model to account for effective porosity where fluid is accessible and able to flow (Corapcioglu and Wang 1999), a dual permeability approach to consider the velocity profile of fluid flow in the cross section of the pore structure (Bradford et al. 2011). Additionally, some stochastic models have been proposed due to the inherent chemical heterogeneity of colloids (Tufenkji et al. 2003), the

uncertainty of attachment coefficient (Bradford and Toride 2007), and the spatial heterogeneity of hydraulic conductivity (Bekhit and Hassan 2005).

2.2 Colloid associated contaminant transport in porous media

Many laboratory and field studies have been performed to investigate contaminant transport in porous media in the presence of colloids. Recent research shows that only a relatively small concentration of colloids (~few mg / L) should be considered to properly predict the transport of a contaminant that is favorably attached to colloidal particles. For example, previous experimental studies reported that the transport of radionuclides (e.g. ^{137}Cs and ^{239}Pu) was enhanced or facilitated by the mobile clay or oxide colloidal particles (Kretzschmar et al. 1999; Torok et al. 1990). In addition, Penrose et al. (1990) observed plutonium travels 1200 times faster than predicted in an alluvial deposit, and Puls and Powell (1992) showed approximately 20 times faster transport of the arsenic ion (As^{2+}) compared to transport in the absence of colloids. Therefore, prediction the contaminant transport without taking colloids into account can significantly underestimate the travel velocity and distance of a contaminant (Denaix et al. 2001; Grolimund et al. 1996; Jensen et al. 1999).

It is well documented that heavy metal species (e.g., Cu, Pb, and Zn) show a pronounced tendency to adsorb onto clay colloids (Abollino et al. 2003; Bhattacharyya and Gupta 2008; Covelo et al. 2007; Li and Li 2000; Tang et al. 2009; Veli and Alyüz 2007), and that heavy metals species preferably attach to clay minerals under relatively high pH, primarily due to the deprotonation of hydroxide functional groups on the clay surface (Abollino et al. 2003; Benjamin and Leckie 1981; Farrah and Pickering 1979; Harter 1983).

Furthermore, less ions are adsorbed, especially under relatively low pH, when ionic strength is relatively high (~ 0.1 M) (Kraepiel et al. 1999). This can be attributed to the effects of deprotonation and the increased zeta potential of clay (i.e., decrease in available adsorption sites for metal species) (Vane and Zang 1997; Yukselen-Aksoy and Kaya 2011). This adsorption behavior of metal species to clay mineral implies that the solution chemistry significantly affects both the behavior of clay colloidal transport and the adsorption of the metal species. For example, based on the DLVO theory, clay colloids are preferably attached on the sand grain under high ionic strength due to the shrinkage of the double layer in both clay and sand (i.e., decrease in double layer repulsion), which indicates the transport of metal species might be retarded, rather than facilitated, when only including the transport of clay colloids. However, an increase in ionic strength decreases the available adsorption sites for metal species on the clay colloid, and the metal species may be more favorably dissolved in the aqueous phase and transported with the flow. Therefore, these coupled effects must be considered simultaneously to appropriately account for colloid associated metal transport in porous media.

An experimental study (Um and Papelis (2002)) demonstrated that the transport of lead (Pb(II)) is facilitated under higher colloidal concentration when compared to identical solution chemistry. They also reported that Pb(II) breakthrough was observed under relatively high ionic strength in spite of a large quantity of colloids that were retained in zeolitized tuffs. Corapcioglu and Jiang (1993) proposed a mathematical model for colloid-facilitated contaminant transport based on first-order kinetics to reflect mass transfer mechanisms in the three-phase system. The breakthrough curves obtained by the numerical implementation also revealed that contaminants transported faster in a higher concentration

of colloidal suspension. In contrast, the experimental study presented in Sen et al. (2002) showed that the transport of nickel (Ni^{2+}) was either facilitated or retarded according to the r_c / r_s ratio. Note this result was not consistent with the results presented in other studies, which demonstrated that the presence of colloids facilitated the transport of contaminants (Kaplan et al. 1993; McCarthy and Zachara 1989; Roy and Dzombak 1997, 1998; Ryan and Elimelech 1996; van de Weerd et al. 1998). It can be deduced that the contaminant transport may be retarded if the r_c / r_s ratio is relatively high, which leads to retention of clay colloids and delay of the transport of contaminants that are favorably adsorbed to the colloids. In contrast, recent studies have demonstrated that freeze-thaw cycling in unsaturated porous media led to colloid mobilization in preferential flow paths and facilitated contaminant transport (Mohanty et al. 2015).

Because long-term transport is difficult to study experimentally, mathematical models have been proposed to properly understand colloid-associated contaminant transport over extended time scales. Modeling this process can be divided into three main categories: colloid transport, the interaction between colloid and contaminant, and contaminant transport (Flury and Qiu 2008). For colloid transport in variably saturated porous media, the air-water interface provides additional attachment sites for colloid immobilization, in addition to the sites at the solid surface (attachment) or pore throat (straining), and decreases the amount of retained colloids (Lenhart and Saiers 2002; Sirivithayapakorn and Keller 2003; Wan and Wilson 1994). Furthermore, the air-water-solid interface can provide additional sites for colloid immobilization (Chen and Flury 2005; Zevi et al. 2005). These two mechanisms are closely related to the capillary force acting on the solid, and any factor that can affect the capillarity may also lead to colloid

remobilization (when capillarity decreases) or further immobilization (when capillarity increases). An additional immobilization mechanism for colloids in unsaturated porous media is at the thin water film under a relatively low degree of saturation, referred to as film straining (Saiers and Lenhart 2003; Šimůnek et al. 2006; Wan and Tokunaga 1997). These three sites (air-water interface, air-water-solid interface, and thin water film) are the main additional causes for colloidal immobilization in unsaturated porous media.

For colloidal transport, four types of interaction between colloids and contaminant can be considered: contaminant transport as a result of advection-dispersion transport of mobile colloids, adsorption and desorption of contaminants associated with mobile colloids, adsorption and desorption of contaminants associated with attached immobile colloids, and adsorption and desorption of contaminants related to immobile colloids at the air-water interface (Flury and Qiu 2008). Each of the involved mechanisms in colloid-contaminant interaction is usually represented by a first order coefficient in the models proposed in previous research (Corapcioglu and Choi 1996; Flury and Qiu 2008; Šimůnek et al. 2006). In addition, the interaction between the contaminant and solid has been frequently described by selecting a two-site sorption model, which was initially proposed by van Genuchten and Wagenet (1989). In the model, the total amount of sorbed contaminant is divided into instantaneous and kinetic sorption, where equilibrium sorption is typically expressed by well-known models such as the Langmuir or Freundlich isotherm.

CHAPTER 3 INFLUENCE OF IONIC STRENGTH ON CLAY PARTICLE RETENTION AND HYDRAULIC CONDUCTIVITY OF A SAND MEDIUM

3.1 Introduction

Filtration of solids, or solids-liquid separation, is a critical component in the design and operation of all infrastructure that collects, transmits, and infiltrates water. Proper design of soil filters is critical to both short- and long-term performance by preventing erosion of the base soil, and by providing filtration for water and wastewater (Hajra et al. 2002). However, because filters can clog due to physical, chemical, and/or biological processes, it is often difficult to estimate the rate of infiltration as a function of time (Rice and Rice 1974), which causes difficulty in the design of infiltration structures (e.g., infiltration basins, detention ponds, and infiltration trenches) (Scholes et al. 2008). An infiltration rate that is too large is unconservative and can result in under sizing of the infiltration structures, resulting in discharge of untreated runoff to receiving streams. This is exacerbated as particle retention increases and the filter clogs, which can cause a significant decrease in the lifespan of the structure if proper maintenance is not performed (Akan 2002). Consequently, in order to select a reasonable design infiltration rate, it is critically important to have a fundamental understanding of the sources and impacts of clogging through the retention of particles and formation of the filter cake.

Sources of clogging in filters are varied, but suspended solids are generally considered the primary factor that induces clogging (Crites 1985; Reddi et al. 2005; Siriwardene et al. 2007). The deposition of solids within a filter is a physicochemical process, which depends on the characteristics of the filter pore fluid. In order to reduce the solids load on the filter, total suspended solid (TSS) is often sedimented through gravity

separation before filtration; however, in many cases, small-size fractions or some low-density large particles will not be removed through sedimentation (Urbonas and Stahre 1993). These colloidal-size particles can be retained on a soil filter and downgrade the performance. The retention of colloidal particles (or colloids) can be theoretically explained by three main mechanisms: straining, attachment, and detachment.

Straining is the physical trapping of colloids in the pore throats of filter sands, which occurs primarily at the surface of filters (Auset and Keller 2006; Bradford et al. 2005; Torkzaban et al. 2008; Xu et al. 2006). This mechanism relies on the physical removal, which means the size ratio between the colloidal particle and the filter particles are the most important factor that control the straining of colloids. Due to geometrical straining, the removed colloids are more irreversibly bound than the physicochemically attached colloids and are not typically detached by the alteration of the geochemical conditions in the pore fluid.

In addition to colloid straining, attachment of colloids to filter grains can occur due to the net attractive interaction energy in colloid-water-sand systems, which can be calculated using the the Darjaguin-Landau-Verwey-Overbeek (DLVO) theory to account for van der Waals attraction and double-layer repulsion. Previous studies demonstrated that the colloids primarily attach to the separation distance corresponding to the secondary minimum, due to the difficulty of colloids overcoming the primary energy barrier (Hahn et al. 2004; Litton and Olson 1996).

Lastly, detachment of colloids may occur due to the alternation of geochemical and hydrodynamic conditions (Bergendahl and Grasso 1999, 2000a). For example, a decrease

in ionic strength leads a decrease in the secondary minimum energy, which corresponds to larger double layer repulsion. In addition, detachment may take place under identical solution chemistry when the flow path changes as a result of increased retention of colloids, which can cause larger fluid drag force on previously attached colloids.

In unsaturated conditions such as infiltration trenches, water infiltrates a particulate media due to a combination of both hydraulic gradient and soil suction. This infiltration rate will converge to saturated hydraulic conductivity (K_s), as shown in Philip's two-term infiltration model (Philip 1957). Even though the initial moisture content in the soil medium is critical for estimation of the initial infiltration rate, K_s of the soil medium is significant for long-term infiltration rate once a soil has reached saturation. Reddi et al. (2005) showed a reduction in saturated hydraulic conductivity of filter sand due to the physical clogging caused by the kaolinite colloids; however, it did not account for straining of clay colloids, which can significantly reduce the saturated hydraulic conductivity due to the formation of a surface filter layer. Bradford et al. (2003) demonstrated that colloids retained in the sand filter were due to straining at a relatively large ratio between colloid diameter (d_c) and median grain size of filter sand (d_s) (i.e., d_c / d_s). Additionally, it is significant that the concentration of retained colloids due to straining can increase rapidly, even at low influent volumes of flow (less than 10 pore volumes (PV)), which can directly impact conductivity within the filter medium (Bradford et al. 2003). In contrast, when colloidal particles are present in an aqueous system, their presence can increase the transport velocity of contaminants (e.g., heavy metals) that are favorably adsorbed onto the mobile clay colloids (Bailey et al. 1999; Ouyang et al. 1996). Consequently, understanding the transport of clay colloids in porous media, and soil filters, is important for both the

prediction of the reduction of saturated hydraulic conductivity, as well as contaminant transport in porous media. While a significant body of literature is available on the filtration behavior of various colloids in water treatment filters (attachment, detachment, and straining), relatively little data are available for the clay colloids filtration.

The saturated hydraulic conductivity of filters and infiltration devices is a function of the retention profile (RP), which will vary as a function of the dominant removal mechanism (straining and attachment). Thus, the aggregation behavior of clay particles is important to changes in the saturated hydraulic conductivity because the size of the clay clusters, as opposed to the single clay particle dimension, will be the critical factor in the deposition and formation of the RP. The size of clay clusters formed during deposition is a function of solution chemistry, including ionic strength (Palomino and Santamarina (2005)), which results in a size ratio between the filtered particles and the filter medium that is a function of solution chemistry. Despite the importance of ionic strength on clay colloid retention, no literature has been investigated the clay colloids RPs under various ionic strength. To provides fundamental understanding and the dominant removal mechanism of clay colloid retention in a sand medium beyond the reduction of K_s , this work quantified the resulting RPs as a function of clay suspension concentration and ionic strength. In addition, this work quantified the reduction in K_s at three depth intervals of a sand column for investigating the effect of straining on total reduction of K_s . The clay RPs were also used to evaluate three first-order reaction coefficients to quantitatively account for the contribution of attachment, detachment, and straining mechanisms to retention by fitting experimental data to the numerical formulation of the colloids mass-balance equation.

3.2 Mathematical model

3.2.1 Colloidal transport in saturated porous media

Colloid transport in saturated porous media can be described using a semiempirical approach based on numerical solution of the convection-diffusion equation to predict single-collector efficiency (i.e., attachment efficiency) (first proposed by Rajagopalan and Tien (1976) and recently modified by Tufenkji and Elimelech (2004)) for application at the particulate scale. In this approach, the single-collector efficiency (η_0) is the sum of the attachment efficiencies due to diffusion (η_D), interception (η_I), and gravity (η_G). Each of three efficiencies consist of a power function of related normalized parameters, with the constants of the power function determined by multiple linear regression analysis of the results of numerical analysis. The single-collector efficiency, η_0 , is expressed as:

$$\begin{aligned} \eta_0 &= \eta_D + \eta_I + \eta_G \\ &= 2.4 A_s^{1/3} N_R^{-0.081} N_{Pe}^{-0.715} N_{vDW}^{0.052} + 0.55 A_s N_R^{1.675} N_A^{0.125} + 0.22 N_R^{-0.24} N_G^{1.11} N_{vDW}^{0.053} \end{aligned} \quad (3-1)$$

There are five normalized parameters in Equation (3-1): Aspect ratio (N_R), Peclet number (N_{Pe}), van der Waals number (N_{vDW}), attraction number, (N_A) and gravity number (N_G), which are defined as follows.

$$N_R = \frac{d_c}{d_s}, \quad N_{Pe} = \frac{U d_s}{D_\infty}, \quad N_{vDW} = \frac{A}{kT}, \quad N_A = \frac{A}{12\pi\mu a_c^2 U}, \quad N_G = \frac{2 a_c^2 (\rho_c - \rho_f) g}{9 \mu U}$$

where d_c (m) is the colloid diameter (corresponding to median diameter of clay in this study), d_s (m) is the collector diameter (corresponding to median diameter of sand in this study), U (m / s) is the fluid approach velocity (i.e., Darcy's velocity), D_∞ (m^2 / s) is the bulk diffusion coefficient in an infinite medium, A (J) is the Hamaker constant, k (J / K) is the Boltzmann constant, T (K) is fluid absolute temperature, a_c (m) is radius of clay colloid,

ρ_c (kg / m^3) is density of clay colloid, ρ_f (kg / m^3) is the fluid density, μ ($kg / m \cdot s$) is the absolute fluid viscosity, g (m / s^2) is the gravitational acceleration, and A_S is a porosity-dependent parameter of the Happel sphere-in-cell model (Happel 1958) written as:

$$A_S = \frac{2(1-\gamma^5)}{2-3\gamma+3\gamma^5-2\gamma^6} \quad (3-2)$$

$$\gamma = (1-n)^{1/3} \quad (3-3)$$

where n is porosity, defined as pore volume (V_V) divided by total volume (V_T): (V_V / V_T). Selecting the term empirical attachment efficiency (α), the actual single collector attachment efficiency (η) is:

$$\eta = \alpha \cdot \eta_0 \quad (3-4)$$

At the global scale, colloid transport has been typically described by adding first-order coefficients to the conventional advection-dispersion equation. The mass balance equation for colloids can be expressed as (Bradford et al. 2003):

$$\frac{\partial(nC)}{\partial t} = -\nabla \cdot J_T - nk_{att}\psi_{att}C + \rho_b k_{det}S_{att} - nk_{str}\psi_{str}C \quad (3-5)$$

where C is the colloid concentration in aqueous phase (g / cm^3), t is time (s), J_T is the total colloid flux (sum of advective, dispersive fluxes), ρ_b is the bulk density of sand (g / cm^3), k_{att} ($1/ s$), k_{det} ($1/ s$) and k_{str} ($1/ s$) are the first-order colloid coefficient account for attachment, detachment and straining, respectively, S_{att} ($g \text{ colloid} / g \text{ sand}$) is the solid-phase concentration of attached colloids, and ψ_{att} and ψ_{str} are dimensionless function for colloid attachment and straining, respectively.

As mentioned in the introduction, straining is the process of physically trapping colloids in pore throats, with the larger particles preferentially trapped at the surface of the filter medium, while smaller colloids are transported and trapped in deeper positions. Consequently, ψ_{str} can be expressed as a power law function of depth (Bradford et al. 2002, 2003; Šimůnek et al. 2006):

$$\psi_{str} = \left(\frac{d_s + z}{d_s}\right)^{-\beta} \quad (3-6)$$

where β (dimensionless) is a fitting parameter that determines the spatial distribution of colloids, and z (m) is distance from the inlet. Bradford et al. (2003) proposed β value as 0.43 considering the shape similarity of retained colloid concentration with depth due to the straining (ψ_{str} exponentially decreases with depth). Additionally, they fitted k_{str} under the fixed value of $\beta = 0.43$ and derived power function correlation between k_{str} and d_c / d_s empirically.

$$k_{str} = 4.495 \left(\frac{d_c}{d_s}\right)^{1.42} \quad (3-7)$$

Equation (3-7) well described the relationship between k_{str} and the aspect ratio (d_c / d_s). Using Equation (3-7), k_{str} can be calculated directly from d_c and d_s instead of evaluating by fitting into the experimental result, which reduces the computational work to fitting of k_{att} and k_{det} .

In addition to straining and attachment, there is one more possible mechanism in colloid-sand interaction known as size exclusion (Ryan and Elimelech 1996; Sirivithayapakorn and Keller 2003). Size exclusion is defined as the exclusion of colloids near the surface of sand grains due to repulsive electrostatic forces that are attributed to the

negative surface charge of both the colloid and sand grain. Therefore, the colloid cannot access the total volume of water in the sand and is only movable in some portion of the water content, which is known as the colloid accessible water content. If the effect of size exclusion is significant in a filter, the colloid accessible water content is much smaller than volumetric water content, and colloids will transport faster than the pore-water velocity; however, the effect of size exclusion was neglected in this study by assuming that colloid pore-water velocity was equal to average pore-water velocity because relatively high influent colloid flux was applied at the inlet of sand medium in the experimental study. Consequently, fluid drag force applied to colloids was much larger than the force induced by size exclusion (see details, Bradford et al. (2003)).

3.2.2 *Blocking phenomenon for ψ_{att}*

Blocking phenomenon that prevent the attachment of clay colloids was considered in this work by assuming decreased ψ_{att} as the colloids attached on the sand grain surface. In other words, the initial value of ψ_{att} before colloid attachment was the largest ($\psi_{att} = 1$) in each condition due to the maximum accessible area of the sand grain. By adopting blocking phenomenon, ψ_{att} can be expressed based on Langmuirian dynamics according to (Adamczyk et al. 1994; Šimůnek et al. 2006):

$$\psi_{att} = 1 - \frac{S_{att}}{S_{max}} \quad (3-8)$$

where S_{max} (*g of clay / g of sand*) is the maximum mass of colloids that can be attached to the sand surface. Assuming clay colloids and sand particles are spherical (radius of clay colloids is assumed Stokes' equivalent radius of clustered clay colloids, and, assuming that

the clustered clay structure was not broken by fluid drag force), S_{max} may be derived approximately using geometry of spherical sand and clay cluster.

$$\begin{aligned}
 S_{max} &= \left(\frac{r_b^3}{r_c^3} \right) \cdot \left(\frac{1}{1+e_b} \right) \cdot \left(\frac{N_c^2 - 8N_c}{4} \right) \cdot \left(\frac{(4/3)r_c^3 \pi G_s^c \rho_w}{(4/3)r_s^3 \pi G_s^s \rho_w} \right) \\
 &= \left(\frac{r_b^3 G_s^c}{r_s^3 G_s^s} \right) \cdot \left(\frac{1}{1+e_b} \right) \cdot \left(\frac{N_c^2 - 8N_c}{4} \right)
 \end{aligned} \tag{3-9}$$

where r_b (cm) is the radius of clay cluster, e_b is the void ratio of clay cluster (assumed 0.5 in this study for kaolinite cluster (Olsen 1960)), r_c (cm) is the radius of clay colloid, r_s (cm) is the radius of sand grain, G_s^s and G_s^c are the specific gravity of sand and clay respectively, ρ_w (g / cm³) is the density of water, and N_c is the maximum number of clay clusters that can be fitted on the sand surface area in a two dimensional domain, calculated simply by sine law:

$$2r_b \sin\left(\frac{\pi(N_c - 2)}{2N_c}\right) = (r_s + r_b) \cdot \sin\left(\frac{2\pi}{N_c}\right) \tag{3-10}$$

The second term $((N_c^2 - 8N_c) / 4)$ in Equation (3-9) represents the maximum number of clay clusters that can be attached on the sand surface, taking the three dimensional domain into consideration. The other terms are used to convert from the number of clay clusters divided by the single grain of sand into the unit of S_{max} .

3.2.3 Saturated hydraulic conductivity (K_s) reduction with deposited clay colloids

When clay colloids are deposited on a sand medium, the resistance for fluid flow increases and the porosity of the sand medium decreases. Under the constant flow-rate condition tested in this work, the pressure difference (ΔP) increased as clay colloids were deposited in the pore space, because a higher pressure gradient was required to maintain

the same volume of flow. Assuming that the shape of pore was cylindrical, the amount of increased pressure ($\Delta P(R_i, r_j)$) at i^{th} single cylindrical pore with radius R_i due to the j^{th} single spherical particle (clay colloid in this study) with radius r_j may be expressed as (Happel and Brenner 1983):

$$\Delta P(R_i, r_j) = \frac{12\mu r_j}{R_i^2} \left(1 - \frac{b_j^2}{R_i^2}\right) \left(U(R_i) \left(1 - \frac{b_j^2}{R_i^2}\right) - U_p \right) K(R_i, r_j) \quad (3-11)$$

where $U(R_i)$ (m/s) is centerline velocity of the pore tube which can be taken as $2v_w$ when assume velocity profile along the tube is parabolic, U_p (m/s) is the particle velocity, b_j (m) is the distance between center of the particle and cylindrical pore axis corresponding to the particle with radius r_j (m), and $K(R_i, r_i)$ is pore wall correction factor written as:

$$K(R_i, r_j) = \frac{1 - (2/3)(r_j / R_i)^2 - 0.202(r_j / R_i)^5}{1 - 2.105(r_j / R_i) + 2.086(r_j / R_i)^3 - 1.707(r_j / R_i)^5 + 0.726(r_j / R_i)^6} \quad (3-12)$$

If the particle with radius r_j is attached on the pore wall of R_i , U_p becomes 0 and $b_j = R_i - r_j$, Eq (3-11) becomes:

$$\Delta P(R_i, r_j) = \frac{12\mu r_j U(R_i)}{R_i^2} \left(1 - \left(1 - \frac{r_j}{R_i}\right)^2\right)^2 K(R_i, r_j) \quad (3-13)$$

The hydraulic gradient ($i(R_i, r_j)$) induced by the change of pressure difference ($\Delta P(R_i, r_j)$) may be expressed as (Reddi et al. 2005):

$$\Delta i(R_i, r_j) = \frac{\Delta P(R_i, r_j)}{\gamma_w \alpha^*} \quad (3-14)$$

where γ_w (N/m^3) is the unit weight of water, and α^* (m) is the characteristic pore length for the validity of assumption of the straight cylindrical pore. By knowing the number of

attached particles on the pore wall at time t , relative saturated hydraulic conductivity at time t ($K_{rel}(t)$) under the constant-flow-rate condition from Darcy's equation is:

$$K_{rel}(t) = \frac{K_s(t)}{K_{s0}} = \frac{i_0}{i(t)} = \frac{i_0}{i_0 + \sum \Delta i(R_i, r_j)_t} \quad (3-15)$$

where K_{s0} (m / s) and $K_s(t)$ (m / s) are the initial saturated hydraulic conductivity at i_0 and the saturated hydraulic conductivity at $i(t)$, respectively, and i is the initial hydraulic gradient.

3.2.4 *Nonlinear least-square curve fit*

To solve Equation (3-5) numerically, backward Euler was used for time evolution with centered in space for both advection dispersion terms in Equation (3-5). Dirichlet type and no flux boundary conditions were utilized at the boundary of inlet and outlet respectively. Equation (3-5) was nonlinear because C and S (S = colloids in solid phase, S = sum of S_{att} and S_{str} where S_{str} is the amount of strained colloids) were dependent in each time step. Therefore, Picard iteration was used following the procedure proposed by Celia et al. (1990), until the difference of C in iteration reached $10^{-8} \times C_i$, where C_i (g / cm^3) was the influent concentration. Using the numerical scheme introduced earlier, optimized k_{att} , k_{det} and k_{str} in each experimental RP were obtained based on trust region reflective least squares algorithm.

3.2.5 *Single-collector efficiency of kaolinite*

The impact of pore fluid chemistry is critically important in the transport behavior of colloidal particles such as kaolinite that exhibit pH dependent behavior. It is well known that the kaolinite will coagulate or disperse as a function of solution chemistry (pH and

ionic concentration), and at low values of pH, kaolinite particles will flocculate to form clusters with edge-to-face association. The formation of particle clusters results from Coulombic attraction between negatively charged clay faces and positively charged clay edges (Santamarina et al. 2001). Consequently, the diameter of the clay clusters becomes the effective particle size in the colloid transport model, as opposed to the diameter of a single clay particle. Use of the diameter of the clay cluster, as opposed to clay particle, as model input results in completely different model values for single-collector efficiency (η_0 , Equation (3-1)), first order coefficients for attraction, detachment, and straining (k_{att} , k_{det} and k_{str} , Equation (3-5)), and for the maximum quantity of attachable clay colloids (S_{max} , Equation (3-8)). Consequently, the work in this study investigated the impact of size of clay clusters in the colloid transport model for evaluating single-collector efficiency.

3.3 Experimental program

3.3.1 Materials

Three standard sands (ASTM 20/30, GS22 20/30 and ASTM graded) were selected as the sand filter mediums and Georgia kaolinite was selected as the representative colloidal particles. ASTM 20/30 sand was used as the reference material, and GS22 20/30 sand and ASTM graded sand were selected to study the impact of angularity and median grain size of the sand medium. All particles smaller than No. 170 sieve ($88 \mu m$) in the sands were removed by mechanical sieving before the initiation of clogging with kaolinite colloids. All sands were thoroughly washed with deionized water to remove excess salts (Branstead E-pure), and oven dried before use. The limiting void ratios (e_{max} and e_{min}) of each sand were measured according to ASTM D4253 and ASTM D4254 and the roundness of the sand grains was evaluated using the method proposed by Wadell (1932). The

electrical conductivity of the supernatant of suspensions made with sand/deionized water and kaolinite/deionized water were measured to verify the removal of salts from the soils. Ten grams of particles were mixed with 200 ml of deionized water using a magnetic stirrer and electrical conductivity was measured after one hour of mixing. All supernatant electrical conductivities measured less than $6 \mu S/cm$, which is on the order of the electrical conductivity of deionized water ($\approx 1 \mu S/cm$) and measurably less than tap water ($\approx 90 \mu S/cm$). The specific gravity of the soils was determined according to ASTM D854, and the median grain sizes (d_{50}) of the sand (d_s) and clay (d_c) were determined according to ASTM D422. The liquid limit of the kaolinite was determined by the fall cone test (British Standard 1377), and the gravimetric specific surface was estimated by the methylene blue test (Santamarina et al. 2002) (Table 3-1). Calcium chloride (Sigma Aldrich) was used to control the ionic strength of the pore fluid solution. Hydrometer tests were performed to measure the size of clay clusters as a function of ionic strength of the pore fluid, according to ASTM D422.

Table 3-1. Measured Soil Properties

Properties	ASTM 20/30	GS22 20/30	ASTM graded	Georgia kaolinite
G_s	2.65	2.65	2.65	2.52
e_{max}	0.742	0.973	0.762	-
e_{min}	0.502	0.685	0.514	-
R	0.90	0.23	0.80	-
$d_{50} (cm)$	0.072	0.072	0.036	4.5×10^{-5}
$S_s (m^2 / g)$	-	-	-	52
$LL (\%)$	-	-	-	72

Note: G_s = specific gravity; e = void ratio = volume of void / volume of solid; e_{max} = maximum void ratio; e_{min} = minimum void ratio; R = roundness; d_{50} (= d_s for sand and d_c for clay) = median grain size; S_s = specific surface.

3.3.2 *Experimental setup and procedure*

A flow cell (7.62 cm in diameter, 30.48 cm in height) was designed to measure pressure change as a function of clogging throughout the duration of the test, with four absolute pressure transducers installed along the sidewall of the cell. Samples were prepared using wet pluviation (to ensure saturation) and symmetric vibration to achieve the chosen target relative density ($D_r = 70\%$ for all tests). At the initiation of colloidal clogging, kaolinite colloidal suspensions, prepared in either deionized water or a calcium chloride background solution, were permeated using a syringe pump in series with a peristaltic pump with continuous stirring. In order to minimize the pulsation effect of the peristaltic pump, less than 10 % of flow rate was injected by the syringe pump for the kaolinite suspension, and the background solution without kaolinite colloids (> 90 % of the total flow rate) was injected by the syringe pump. Magnetic stirrer was used to prevent settling of kaolinite colloids during the injection and pH was remained 5.6 in all experiments.

No. 200 plastic mesh (75 μm) was installed at the bottom of the cell to retain the sand filter media. After 10 PV of flow through the column with the suspended colloids, the concentration of kaolinite (sum of kaolinite colloids suspended in aqueous phase and retained, attached kaolinite colloids at the sand particle surface) was measured by carefully sectioning the column in 2.5 cm increments. The sections were washed over a 200 sieve, oven dried, and the mass of kaolinite colloids was measured. Only the mass of retained colloids was measured; that is, the breakthrough curve was not monitored in this study. All tests were performed at a constant flow rate as presented in Table 3-2 as a volumetric water flux.

Pressure was measured at the top of the soil, at a depth of 7.6 *cm* from the surface, depth of 15.2 *cm* from the surface, and at the bottom of the soil column (Figure 3.1). The initial saturated hydraulic conductivity (K_s) of sand was measured using a constant head test prior to flow of the colloidal kaolinite suspension through the cell. The initial hydraulic conductivity was used to normalize the reduction in K_s as kaolinite colloid retention increased and clogged the pores. After permeation of the sand with suspended colloidal particles was initiated, the value of K_s as a function of pore volumes of flow (PV) was evaluated using Darcy's equation, with the hydraulic gradient determined through the pressure drop recorded across the transducers (Figure 3.1 and Table 3-2).

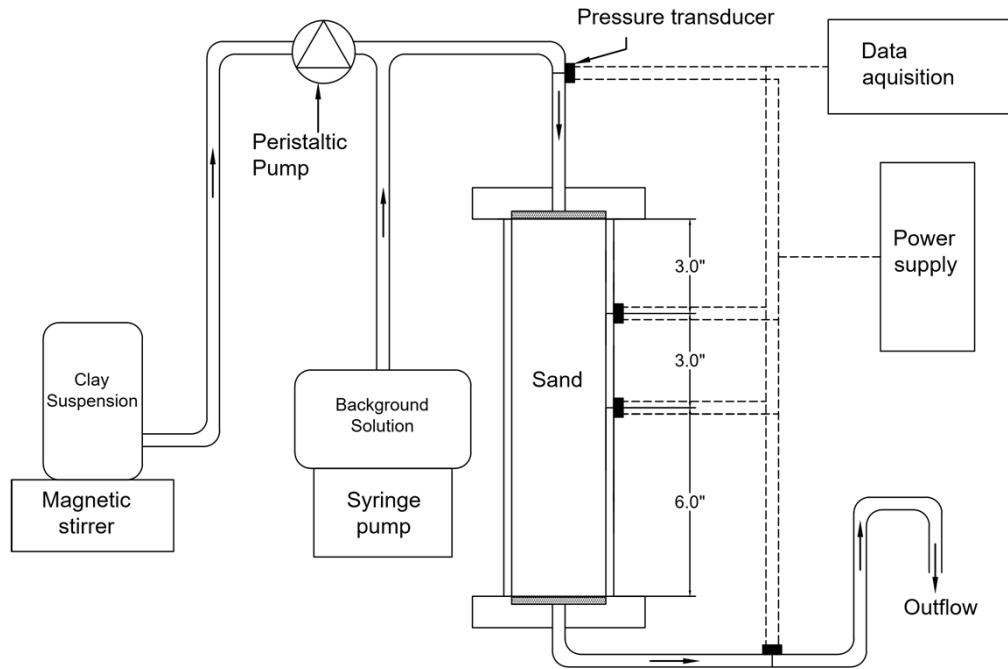


Figure 3.1. Experimental setup for flow conditions with pumped colloidal suspensions.

Table 3-2. Testing Conditions

Exp. name	Influent concentration, $C_i \times 10^9 (N/cm^3)$	Sand type	Volumetric water flux, $q (cm/s)$	Solution chemistry
A1, A2, A3	8.33, 16.7, 41.7	ASTM 20/30	0.073	Deionized water
G1, G2, G3	8.33, 16.7, 41.7	GS22 20/30	0.073	Deionized water
B1	8.33	ASTM graded	0.0365	Deionized water
A4, A5, A6	8.33	ASTM 20/30	0.073	0.001, 0.01, 0.1 <i>M of CaCl₂</i>
A7, A8, A9	41.7	ASTM 20/30	0.073	0.001, 0.01, 0.1 <i>M of CaCl₂</i>
A10	41.7	ASTM 20/30	0.073	0.1 <i>M NaCl</i>

Note: N denotes number of kaolinite particle calculated assuming d_{50} and G_S (Table 3-1). 8.33×10^9 , 1.67×10^{10} , and $4.17 \times 10^{10} N/cm^3$ corresponding with 1, 2, and 5 g / L, respectively. 0.073 and 0.0365 cm / s of volumetric water flux corresponding with 200 and 100 ml / min, respectively. Due to the lower initial K_s of ASTM graded, experiment B1 adjusted flow half time lower than others, not to exceed the maximum flow capacity considering critical hydraulic gradient.

3.4 Results and discussion

3.4.1 Hydrometer test of kaolinite and calculated single-collector efficiency

Tests that were performed according to the standard (i.e., with dispersant added to minimize aggregation of particles) measured significantly lower particle sizes, when compared to tests that were performed in deionized water or salt solutions (concentrations ranging from 0.001 to 0.1 M CaCl₂ or NaCl) (Figure 3.2). The hydrometer test measures changes in fluid density as a function of time, and determines particle size, which is a strong function of solution chemistry, as a function of settling velocity. Comparison of the test results that were obtained with no dispersant to the results performed with sodium hexametaphosphate dispersant (test duration > one week) demonstrated that significant

clustering occurred in the kaolinite in the presence of deionized water (test duration < one hour)). In the absence of dispersant in CaCl₂ solution, the measured equivalent particle sizes of the clusters were approximately one order of magnitude larger than those in the dispersed state. At low ionic strengths (0.001 M CaCl₂), the kaolinite formed clusters similar to those formed in deionized water, and smaller, more dense clusters formed as the ionic strength was increased (Figure 3.2). At higher ionic strength, the thickness of the diffuse double layer decreased, and the probability of face-to-face association of kaolinite particles increased due to van der Waals attraction (Santamarina et al. 2001). The evaluated d_{50} values of kaolinite cluster, which were roughly 18 μm in deionized water and 0.001 M CaCl₂, 12 μm in 0.01 M CaCl₂ and 0.1 M NaCl, and 7.4 μm in 0.1 M CaCl₂, were used in Equations (3-7) and (3-9) for evaluating k_{str} and S_{max} respectively. The d_{50} values of kaolinite cluster were also used as the input to the analytical model (Equation (3-15), followed by taking r_j in Equations (3-11), (3-12), (3-13), and (3-14) as measured cluster size) to determine the reduction in saturated hydraulic conductivity as a function of the pore volume of flow. In addition, the single-collector efficiency (η_0 , Equation (3-1)) can be obtained as a function of particle diameter (cluster diameter) of the kaolinite (Figure 3.3). Given the relevant test conditions, d_s in Equation (3-1) was assumed equal to d_{50} of ASTM 20/30 sand (0.072 cm, Table 3-1), and the Hamaker constant taken as 1×10^{-21} J for kaolinite-water-kaolinite interaction (Visser 1972).

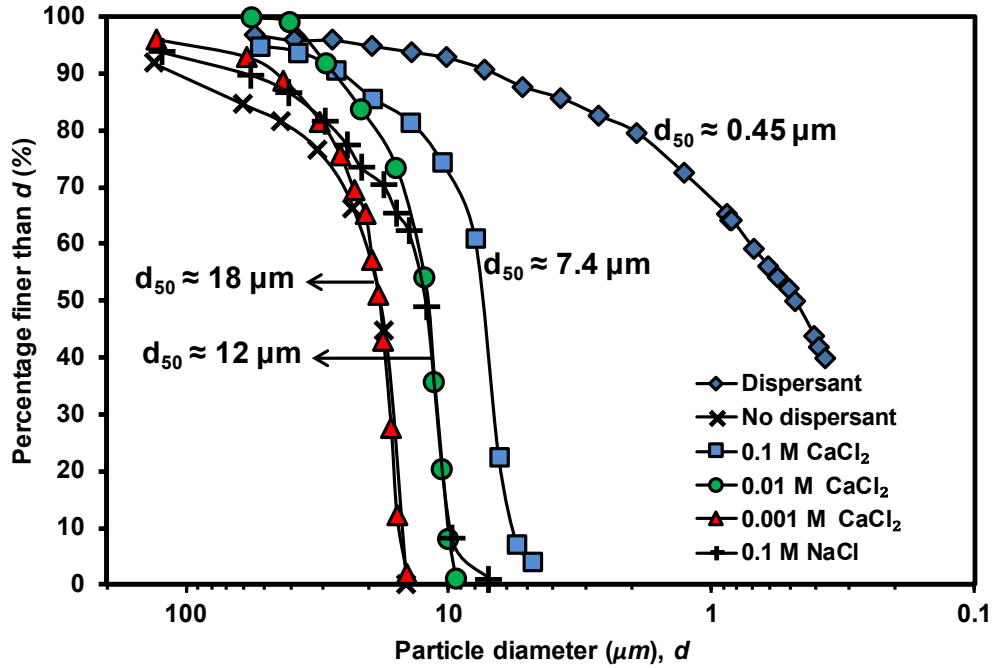


Figure 3.2. Hydrometer test result of the kaolinite at different ionic concentration: d_{50} of deionized with no dispersant $\approx 18 \mu\text{m}$, d_{50} of $0.001 \text{ M CaCl}_2 \approx 18 \mu\text{m}$, d_{50} of $0.01 \text{ M CaCl}_2 \approx 12 \mu\text{m}$, d_{50} of $0.1 \text{ M CaCl}_2 \approx 7.4 \mu\text{m}$, d_{50} of $0.1 \text{ M NaCl} \approx 12 \mu\text{m}$, and d_{50} of deionized with dispersant (following the test procedure of ASTM D422, Sodium hexametaphosphate $((\text{NaPO}_3)_6)$ used as a dispersant) $\approx 0.45 \mu\text{m}$.

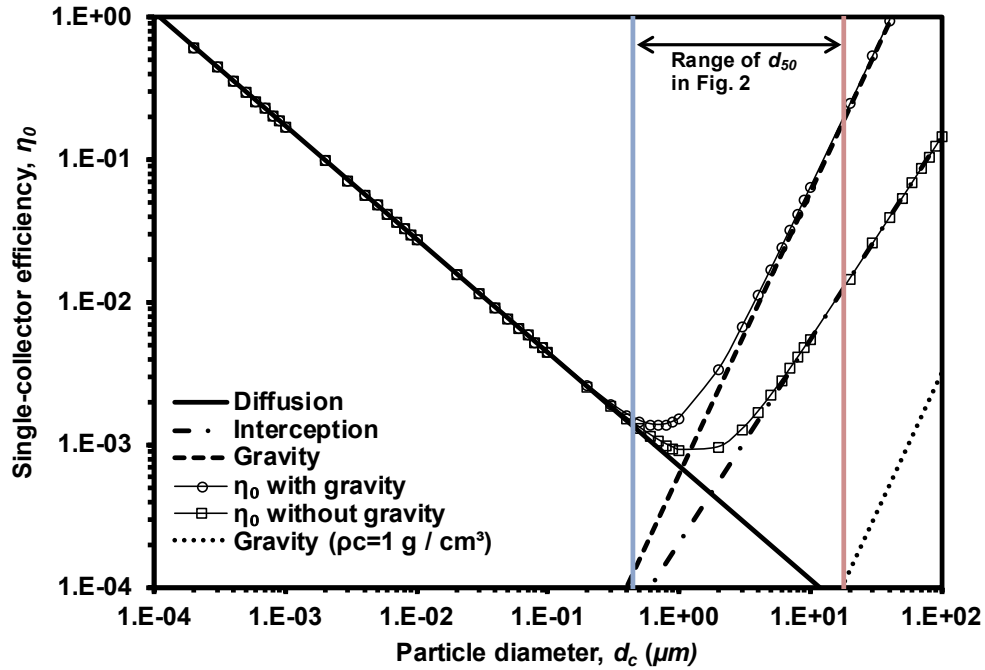


Figure 3.3. Single-collector efficiency (η_0) of the kaolinite particles calculated by Equation (3-1). Open circles represent the η_0 with gravity term ($\eta_0 = \eta_D + \eta_I + \eta_G$), open squares represent the η_0 without gravity term ($\eta_0 = \eta_D + \eta_I$) according to the diameter of the kaolinite (d_c). Also, the range of the d_c (d_{50} of the kaolinite according to the solution chemistry obtained by the hydrometer test in Figure 3.2) and shift of the gravity line in case of $\rho_c = 1 \text{ g / cm}^3$ are illustrated.

Particles can be removed from suspension through transport due to diffusion, interception, or gravitational settling, and the dominant mechanism of removal for single-collector efficiency varies as a function of the d_{50} of the particles or particle cluster. For the smallest particles' sizes ($d_c < 0.45 \mu\text{m}$, perfectly dispersed in suspension), the diffusion term (η_0 in Equation (3-1)) is the most critical mechanism in removal efficiency (η_0) with or without the gravity term (η_G in Equation (3-1)). This implies that when kaolinite is perfectly dispersed, diffusion is dominant for the collision of kaolinite particle to the sand grain (Figure 3.3). In the cases of horizontal flow, gravity may be considered for calculating

η_0 , and the value of collector efficiency for diffusion follows the η_G line when d_c for particles' sizes greater than approximately $1 \mu m$. This scenario is applicable when the density of the particle is much larger than the density of the fluid phase. For particles with particle density similar to that of water, such as latex colloids or biocolloids, the value of η_0 would follow the η_I line (interception), assuming the same flow rate and collector diameter (Figure 3.3, η_G line cannot overcome η_I line). In this study, the kaolinite suspension flowed vertically, with a settling velocity that was much lower than the fluid velocity, so the value of η_0 was assumed equal to: $\eta_0 = \eta_D + \eta_I$ (excluding η_G term). For solution chemistry that resulted in a kaolinite cluster diameter $d_{50} > 7.4 \mu m$, the η_0 would primarily be dominated by the interception mechanism, which is mainly a function of the size ratio between the kaolinite and sand particles (N_R in Equation (3-1)). The diameter at the transition point, the η_D line to the η_I line is approximately $2 \mu m$ without gravity (Figure 3.3) but will vary with gradient, sand particle size, porosity, and flow velocity.

3.4.2 Retention profiles of clay particles

The mass of kaolinite retained in the pore space of sand after 10 PV of flow demonstrated notable differences as a function of sand characteristics (clay concentration = $1 \text{ g} / \text{L}$) (Figure 3.4). The data are shown with a best-fit curve, which was determined by nonlinear least square curve fit for the three coefficients k_{att} , k_{det} , and k_{str} . Depths were normalized and the number of particles retained were calculated based on d_{50} of one kaolinite particle (= $0.45 \mu m$) and reported per unit pore volume.

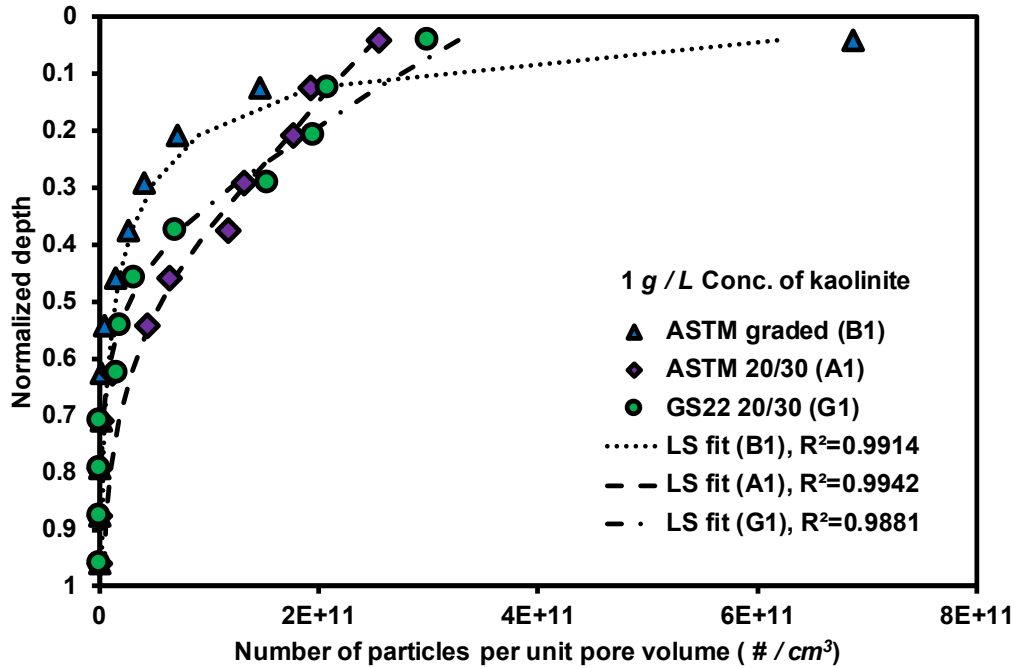


Figure 3.4. Experimental (open markers) and curve fitted clay RP (dotted, dashed, and dot-dashed lines) with depth according to the type of sand.

As anticipated, clay particles were retained at a higher mass at the surface of the ASTM graded sand medium with a smaller d_{50} when compared to the two other test sands (Figure 3.4). The graded sand had a small d_{50} , with a relatively low d_s / d_c ratio = 20 (evaluated based on d_{50} of sand grain and d_{50} of clay cluster) and retained a thin clay layer at the inflow (i.e., severe straining). In contrast, the clay RP was significantly different when the differences in sand and colloidal particle sizes diverged to $d_s / d_c = 40$ (ASTM 20/30 and GS22 filter sands). Comparing the results from the 20/30 sands to the relatively smaller graded sand demonstrated surface retention roughly two thirds lower than the retention for the graded sand. However, while straining occurred in all cases, the penetration depth of the clay was deeper for the sands with larger grain size, which demonstrated the primary attachment mechanism was dominated by van der Waals

attraction or electrostatic force between the clay and sand particles, and virtually no clay particle breakthrough was observed in any experiment (Figure 3.4).

The RP for clay was analyzed as a function of the inflow concentration of the clay colloids and the physical angularity of the sand (Figure 3.5). Retention was again significant within the top layer of the sand column (2.54 cm) because most of the straining at high clay concentration occurred at the surface; however, deeper penetration was observed at high clay concentration, attachment was the dominant mechanism for the retained clay particles. Accordingly, as the number of particles in the influent increased, the shape of the clay RP changed significantly. At low concentrations of clay in the influent, particles were primarily retained within the top 10% of the sand surface, with much smaller deposition as a function of depth. This concentration dependent RPs indicates that blocking attachment (Equation (3-8)) was valid for the sand-clay interaction as opposed to ripening, which is more suitable to describe bacteria growth in porous media (Deshpande and Shonnard 1999). For cases where ripening is the controlling mechanism of attachment, the clay RP would be inverse to that shown in Figure 3.5 (high-concentration clay particles attached in higher mass on sand at the higher position than the lower position). For high-concentration experiments, clay breakthrough was observed after two pore volumes (by measuring turbidity), while no breakthrough was observed at ten pore volumes in the lower-concentration experiments, indicating that the number of retained clay particles was not proportional to the concentration of the influent clay suspension. The dominant mechanism of attachment may transition between blocking and ripening as a function of flow conditions (i.e., flow rate or pressure head). For example, in the case of relatively low flow rate with constant head, ripening tends to dominate as clay particles attach to

previously deposited clay particles because the clay-clay interaction force is stronger than the fluid drag force.

Examination of the clay RPs for angular sand (experiments G1, G2, and G3) demonstrated that in all cases, the angular sand retained more particles in the surficial layers than the rounded sand, and the RPs for all three experiments were similar on a pore volume basis, regardless of the influent concentration of the clay suspension (Figure 3.5). However, because the angular sand (GS22 20/30) had a measurably higher porosity ($n = 0.435$ for GS22 20/30, $n = 0.364$ for ASTM 20/30) when compared to the rounded sand (ASTM 20/30) at a relative density of 70%, it is more appropriate to determine attached clay particle mass with respect to the density of sand (assuming G_s is identical in both cases). Comparison on a mass-to-mass basis demonstrated that the angular sand retained 30 – 50% more clay particles throughout all depths of the column, which likely results from the higher specific surface and higher tortuosity of flow path in the angular sand. Regardless, the impact of the angularity of the sand was of secondary importance to the impact of the grain size of the sand (Figure 3.4) in terms of particle retention because straining was highly sensitive to the colloid-to-sand diameter ratio (d_c / d_s). Note that the RPs in Figure 3.4 and Figure 3.5 were obtained in experiments that used pure deionized water in the clay suspension, so the clay cluster was in the largest state throughout the duration of the tests (Figure 3.2).

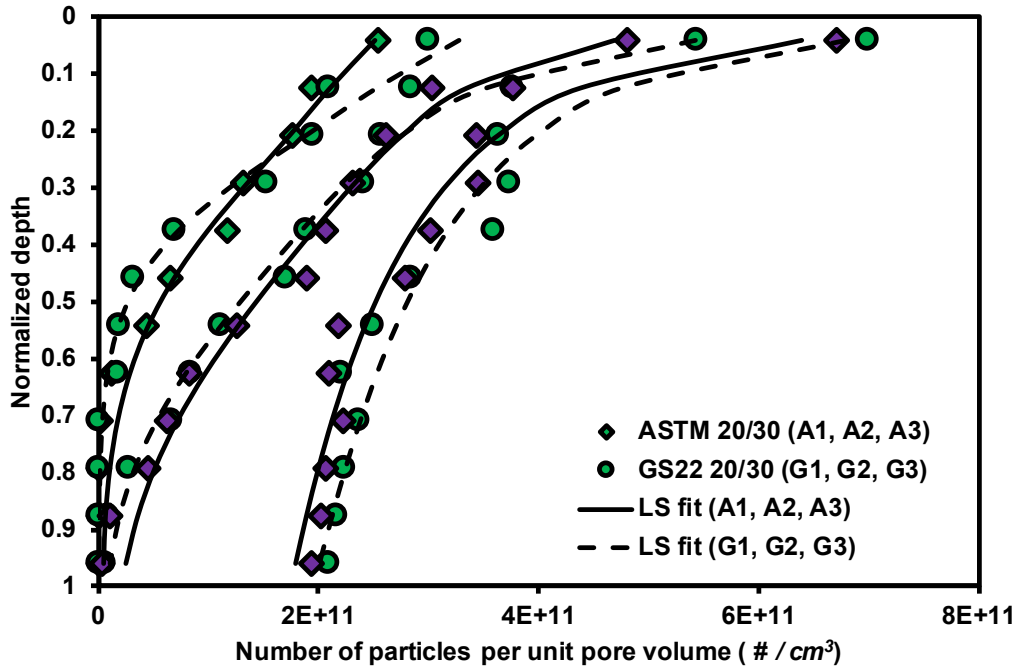


Figure 3.5. Experimental (open markers) and curve fitted clay RP (solid and dotted lines) with depth according to the type of sand and the concentration of clay suspension: The biggest value for number of particles at the same depth represent the experiments A3 and G3 whereas the smallest number of particles represent the experiments A1 and G1. From the left hand side, LS fit curves represent A1, A2 and A3 for solid lines and G1, G2 and G3 for dotted lines.

The impact of ionic strength on the RP of the clay was quantified as a function of influent kaolinite concentration (Figure 3.6 and Figure 3.7). At a relatively low concentration of clay suspension ($1 \text{ g} / \text{L}$), the RPs showed similar trends, nearly independent of the ionic strength of the pore fluid due to the relatively short run pore volumes (Figure 3.2). Notably, when the concentration of the clay suspension was increased to $5 \text{ g} / \text{L}$ (Figure 3.7), no straining occurred at relatively high ionic concentration (0.1 M CaCl_2) and the clay particles were retained almost only by attachment (no clay strained at the surface), and the number of retained clay particles was constant with depth.

Consequently, if the size of clay cluster is identical at 1 g / L and 5 g / L, the shape of the retained clay profile in the experiment with low influent particle concentration (Figure 3.6) resulted from the relatively low clay concentration (1 g / L), and was not a result of particle straining. As the number of pore volumes of flow increased, the shape of the RP at low concentration and high ionic strength would approach that of the higher concentration influent until the amount of attached clay particles reach to S_{max} .

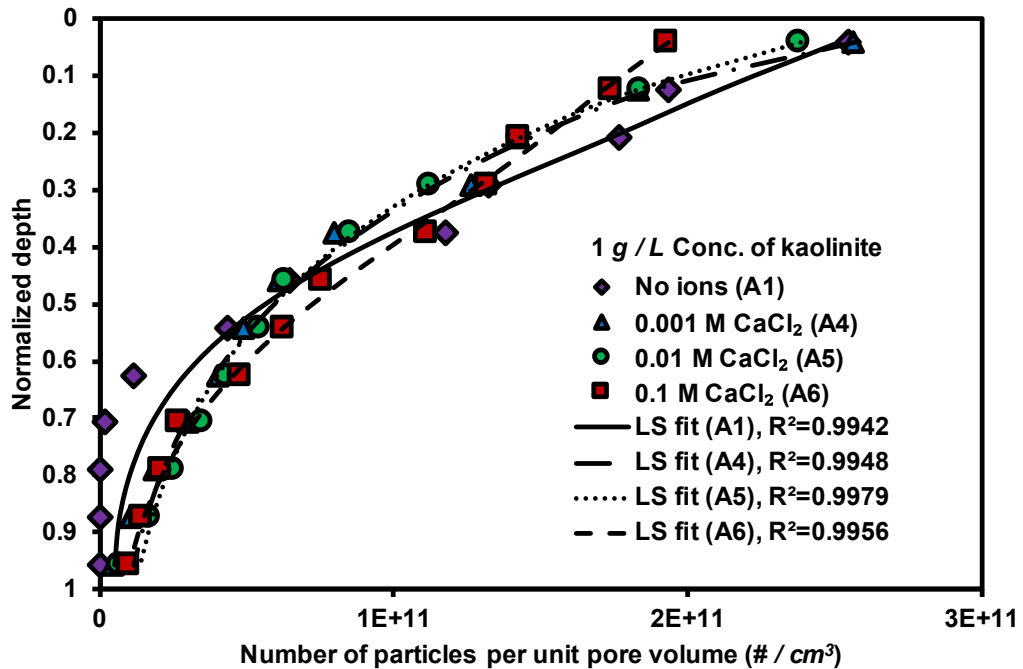


Figure 3.6. Experimental (open markers) and curve fitted clay RP (solid and dotted lines) with depth according to the solution chemistry at the relatively low concentration (1 g / L) of clay suspension.

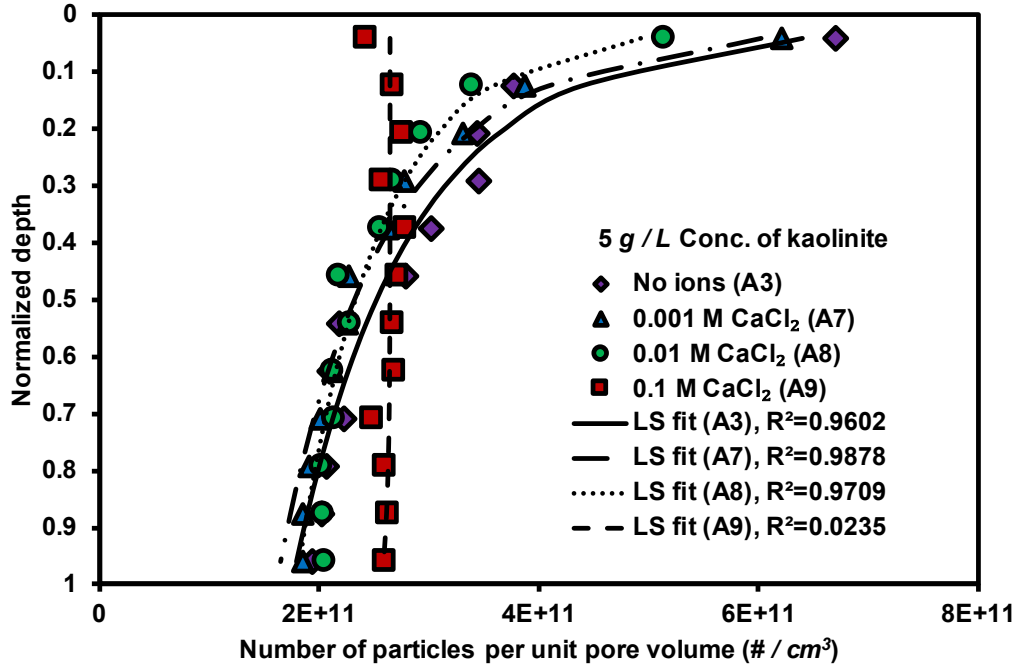


Figure 3.7. Experimental (open markers) and curve fitted clay RP (solid and dotted lines) with depth according to the solution chemistry at the relatively high concentration (5 g / L) of clay suspension.

3.4.3 Optimization of first order attachment coefficients (k_{att} , k_{det} and k_{str})

The first order attachment coefficients were optimized for the clay RPs at ten pore volumes of flow under two scenarios: k_{att} and k_{det} optimized with k_{str} held constant and k_{att} , k_{det} , and k_{str} optimized simultaneously (Table 3-3). In all cases, the R^2 values (used to optimize) were higher in the second scenario (optimized k_{att} , k_{det} , and k_{str}) than the first scenario because k_{str} was fixed. Nevertheless, the R^2 values evaluated in the first scenario were higher than 0.9, with the exception of the case of extremely high straining (B1) and essentially no straining (A9). Consequently, Equation (3-7) may be valid for evaluating k_{str} in most cases, with the exception of low d_s / d_c ratio (B1) or high-influent clay concentrations in high-ionic-strength pore fluids (A9).

Table 3-3. Evaluated First-Order Coefficient (k_{att} , k_{det} and k_{str}) as a Result of the Optimization Analyses in the Least Square Sense in Two Scenarios

Optimized k_{att} and k_{det} with fixed k_{str} (Equation (3-7))					Optimized k_{att} , k_{det} and k_{str}				
Exp. name	$k_{att} \times 10^2$ (/s)	$k_{det} \times 10^2$ (/s)	$k_{str} \times 10^2$ (/s)	R^2	Exp. name	$k_{att} \times 10^2$ (/s)	$k_{det} \times 10^2$ (/s)	$k_{str} \times 10^2$ (/s)	R^2
A1	32.43	1.28	2.38	0.993	A1	41.49	1.71	2.84	0.994
A2	6.90	0.29	2.38	0.972	A2	34.27	2.07	4.12	0.991
A3	17.34	3.26	2.38	0.951	A3	25.38	5.25	2.68	0.960
G1	26.44	0.77	2.38	0.988	G1	33.21	1.01	2.82	0.988
G2	2.45	5.3×10^{-2}	2.38	0.956	G2	25.45	1.59	4.55	0.981
G3	2.25	3.78	2.38	0.929	G3	25.76	4.09	2.22	0.933
B1	3.88	1.02×10^{-10}	6.38	0.855	B1	3.71×10^{-8}	99.02	22.2	0.991
A4	4.48	0.15	2.38	0.995	A4	5.14	0.21	2.86	0.995
A5	2.96	5.1×10^{-2}	1.34	0.998	A5	2.87	4.4×10^{-2}	1.24	0.998
A6	6.50	0.20	0.68	0.996	A6	6.88	0.22	0.85	0.996
A7	17.17	4.05	2.38	0.982	A7	58.45	15.19	2.62	0.988
A8	1.50	0.24	1.34	0.918	A8	17.88	3.84	1.83	0.971
A9	19.29	2.34	0.67	- 12.37	A9	7.28	0.69	1.29×10^{-9}	0.024
A10	0.45	3.3×10^{-2}	1.34	0.976	A10	1.21	0.32	1.79	0.986

Note: for the first scenario (optimized k_{att} and k_{det} with fixed k_{str}), k_{str} in each experiment case is calculated by Equation (3-7) with fixed $\beta = 0.43$ by adopting d_{50} of each sand (Table 3-1) as d_s and d_{50} of the kaolinite cluster in each solution (Figure 3.2) as d_c .

Additionally, optimized k_{att} and k_{str} were determined under constant k_{det} for all experimental data except experiment B1 under the assumption that detachment was proportional to the applied flow rate (Table 3-4). These results demonstrated that the detachment of clay colloids for the experimental conditions in this work were a primary function of the flow rate. In spite of varying pore water velocity in different types of sand due to the different porosity at the same level of relative density, the flow rates did not vary

significantly; consequently, additional work will be required to establish the relation between k_{det} and flow rate (or fluid drag force).

Table 3-4. Optimized k_{att} and k_{str} with Fixed k_{det} in the Least Squares Analysis

Exp. name	$k_{att} \times 10^2$ (/ s)	$k_{det} \times 10^2$ (/ s)	$k_{str} \times 10^2$ (/ s)	R^2
A1	41.49	1.71	2.84	0.994
A2	28.53	1.71	4.08	0.991
A3	8.28	1.71	2.68	0.960
G1	39.11	1.71	4.80	0.965
G2	27.38	1.71	4.56	0.981
G3	10.78	1.71	2.21	0.932
B1	1.31×10^{-6}	0.86	22.20	0.991
A4	27.32	1.71	4.92	0.986
A5	25.55	1.71	4.73	0.982
A6	33.99	1.71	2.62	0.973
A7	6.58	1.71	2.62	0.988
A8	7.97	1.71	1.83	0.971
A9	17.95	1.71	2.19×10^{-7}	9.64×10^{-4}
A10	5.85	1.71	1.88	0.984

Note: k_{det} is assumed identical with the optimized k_{det} for the experiment A1 in the second scenario (Table 3-3) for $q = 0.073$ cm / s (Table 3-1). For the experiment B1, k_{det} is taken half of the rest of the cases since flow rate in the experiment B1 is half assuming that k_{det} is linearly proportional to the flow rate.

3.4.4 K_s reduction curve according to the depth

The reduction in the saturated hydraulic conductivity due to colloidal attachment was determined by applying Equation (3-15) to the entire column length and also applying it to three sections of column depth (top 7.6 cm, second 7.6 cm, and last 15.2 cm). Data are shown for experiment A9, which was representative of the data set (Figure 3.8). For the theoretical calculation, $\alpha^* = 0.9$ cm (Arya and Dierolf 1992) was applied and the pore-size distribution of each sand was calculated based on the particle size distribution (Arya et al. 1999a) to substitute the pore radius (R_i) in Equation (3-11), with half the diameter of the

kaolinite cluster taken as the particle radius (r_j). The theoretical reduction in saturated hydraulic conductivity with time (i.e., pore volume) was determined using the amount of deposited kaolinite obtained from the optimized k_{att} , k_{det} and k_{str} Table 3-5.

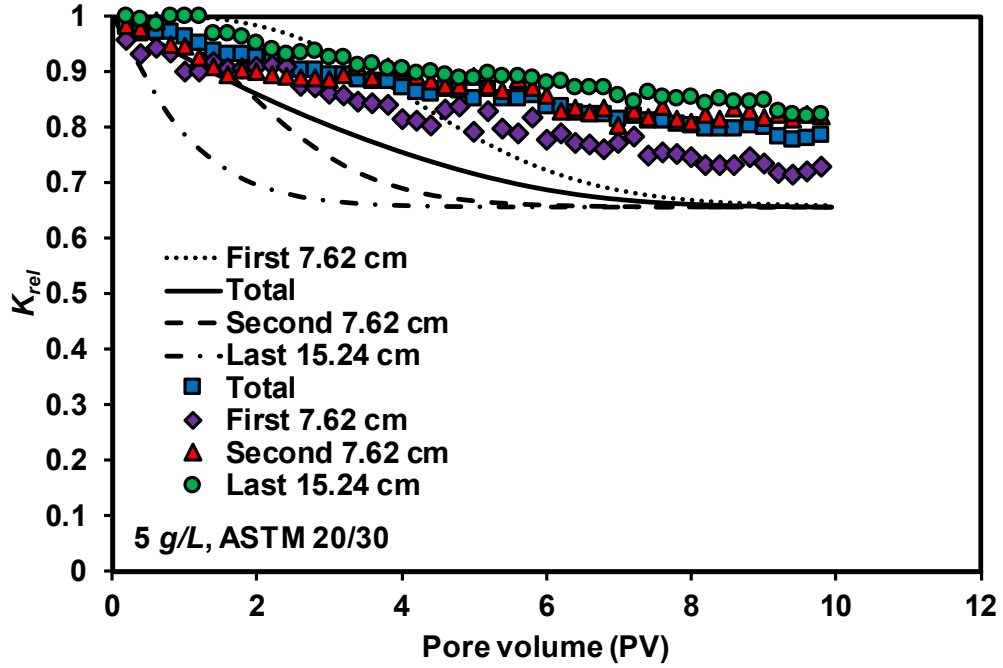


Figure 3.8. The reduction of K_{rel} with PV for the experiment A1

Table 3-5. The Experimental and Theoretical K_{rel} after 10 PV

Exp. name	Experimental K_{rel}				Theoretical K_{rel} (Equation (3-15))			
	First 7.6 cm	Second 7.6 cm	Last 15.2 cm	Total	First 7.6 cm	Second 7.6 cm	Last 15.2 cm	Total
A1	0.733	0.892	0.971	0.858	0.663	0.815	0.968	0.833
A2	0.586	0.718	0.751	0.677	0.538	0.694	0.882	0.718
A3	0.577	0.702	0.719	0.658	0.479	0.615	0.695	0.607
G1	0.714	0.952	0.975	0.859	0.642	0.831	0.986	0.835
G2	0.584	0.805	0.834	0.720	0.538	0.705	0.884	0.722
G3	0.560	0.619	0.868	0.685	0.477	0.606	0.682	0.599
B1	0.076	0.980	0.988	0.188	0.214	0.748	0.955	0.493
A4	0.737	0.899	0.968	0.860	0.683	0.831	0.945	0.836
A5	0.725	0.866	0.975	0.851	0.701	0.837	0.941	0.843
A6	0.739	0.852	0.981	0.858	0.722	0.814	0.944	0.845
A7	0.656	0.920	0.994	0.840	0.498	0.637	0.716	0.628
A8	0.692	0.800	0.814	0.764	0.548	0.655	0.713	0.650
A9	0.788	0.814	0.795	0.796	0.656	0.656	0.658	0.657
A10	0.730	0.819	0.822	0.786	0.562	0.673	0.741	0.671

The calculated theoretical relative hydraulic conductivity was lower than the experimentally measured values K_{rel} in all cases, in part due to the assumptions that the shape of particles (the kaolinite cluster in this calculation) and pores were spherical and cylindrical, respectively. Theoretical calculation of K_{rel} values presented in Table 3-5 were qualitatively consistent with the experimental K_{rel} , meaning that Equation (3-15) can be utilized to estimate the reduction of K_s if the amount of deposited kaolinite at any time is properly evaluated by the optimized first order coefficients in Equation (3-5).

It is important to note that in almost all experiments with $d_c/d_s = 0.01 \sim 0.025$ the saturated hydraulic conductivity was reduced approximately 15 % to 35 % within the first ten pore volumes of flow. Straining was significant in the reduction of conductivity as the most significant reductions occurred in the first 7.6 cm of flow, with the only exception being the experiment with high clay and high ionic concentration. Notably, in experiment

B1, the overall reduction in saturated hydraulic conductivity was greater than 80% due to heavy straining at the surface, with greater than a 90% reduction in the first 7.6 cm of flow. For experiment A9, which demonstrated constant removal as a function of depth, the reduction in saturated hydraulic conductivity was also constant. Little straining will occur with the diameter of the cluster (d_c) equals to d_{50} of the individual kaolinite particle (when perfectly dispersed) and $d_c / d_s = 6.25 \times 10^{-4}$. The threshold boundary for particle retention at the sand surface caused by arching occurs at ratios smaller than $d_c / d_s = 0.156$ (Santamarina et al. 2001). Consequently, prediction of the reduction in saturated hydraulic conductivity is dependent on straining, which is a function of solution chemistry, as well as d_c / d_s ratio.

According to the DLVO theory, colloids preferably attach on the sand surfaces as ionic strength increases owing to the deeper secondary minimum energy and stronger van der Waals attraction. It has been demonstrated that colloid breakthrough has a higher concentration as ionic strength is decreased (Compère et al. 2001; Saiers and Hornberger 1999; Tufenkji and Elimelech 2005), and in some cases, straining becomes more significant at the higher ionic strength for latex colloid deposition in a sand medium because of the deeper secondary minimum energy (Bradford et al. 2007; Li et al. 2004). Much of the work on colloid straining is conducted under conditions of highly unfavorable deposition (solution pH > 10) with manufactured latex colloids, which results in perfectly negatively charged colloids and that are perfectly dispersed. However, it is important to note that the pH has a fundamental influence on the arrangement of the clay particles, which can vary from edge-to-face and face-to-face associations due to pH dependent surface charge. At pH \sim 5.6, the kaolinite particles aggregated in edge-to-face association

(Palomino and Santamarina 2005), and forming different sizes of clay cluster in different levels of ionic strength (Figure 3.2). Consequently, straining was more significant at the lower ionic strength due to the larger diameters of the clay clusters that formed in a solution with $\text{pH} \sim 5.6$ and at higher ionic strength. This is in contrary to the trend found in the above literatures which implies the aggregation behavior of colloids should be taken into account for clay colloids retention. If the same sets of experiments were performed at a solution pH higher than edge isoelectric point (IEP) of kaolinite ($\text{pH} > 7$), the kaolinite RP with depth and the breakthrough curves would be more similar to the profiles under unfavorable condition as previously reported in the literatures.

3.5 Summary

The work performed in this study examined the deposition behavior of clay particles in three different sand filter mediums, under conditions of constant flow rate and pH . The variation of the clay RPs and saturated hydraulic conductivity was determined as a function of solution chemistry, median sand-grain size, shape of sand particles, and concentration of clay suspensions, with the following conclusions.

1. The behavior of the clay-particle association according to the solution chemistry impacted the size of the clay cluster, which resulted in variation of the amount of clay colloids that were strained at the sand-filter surface.
2. When adopting the clay cluster diameter as the particle diameter, the single-collector efficiency was dominated by interception and gravity, rather than diffusion. This was due to the relatively large diameter of the clay cluster compared to the diameter of a single perfectly dispersed kaolinite particle.

3. The trend of clay RPs as a function of concentration of clay suspension demonstrated that the blocking phenomenon was more descriptive than ripening phenomenon for sand-clay interaction at neutral pH.
4. The straining decreased as the ionic concentration of clay suspension increased, which was more evident at the relatively high clay concentration. This can be attributed to the smaller diameter of the clay clusters at relatively high ionic concentration. The reduced straining allowed more clay colloids to penetrate deeper into the sand medium.
5. An angular sand filter medium may pose an advantage of retaining clay colloids compared to a rounded sand filter medium with a similar reduction of saturated hydraulic conductivity.
6. The size ratio (d_c / d_s) between the colloids and the filter medium was dominant because straining is significant when the median grain size of the filter sand is small. This resulted in significantly decreased saturated hydraulic conductivity of the sand medium (more than 80 % after 10 pore volumes of flow).

CHAPTER 4 IMPACT OF SOLUTION CHEMISTRY ON THE DEPOSITION AND BREAKTHROUGH BEHAVIORS OF KAOLINITE IN A SILICA SAND

4.1 Introduction

The work performed in this chapter quantified the reduction of the hydraulic conductivity (K_s) of a sand filter medium as a function of ionic strength (IS) and pH. Laboratory-scale soil column tests were performed to obtain breakthrough curves (BTC) and deposition profiles in eight different solution chemistries, with two flow rates and identical initial inlet concentrations of clay particle suspensions. Experimental results were analyzed in terms of two main mechanisms, attachment and straining, for the association and deposition of clay particles in the sand filter.

Chapter 3 presented the deposition behavior of kaolinite in three sand media with varying inlet concentration and IS under the identical flow rate for 10 PVs, while this chapter presents not only the deposition behavior of kaolinite, but also the breakthrough behavior of kaolinite for 30 PVs under varied IS, pH and flow rate. The inlet concentration in all experiments was remained constant and a column was redesigned to run soil-column experiments for 30 PV.

4.2 Experimental program

4.2.1 Materials

ASTM 20/30 sand and Georgia kaolinite were selected for the sand medium and clay particle, respectively. The sand was cleaned to remove the impurities through immersion in deionized water (Barnstead E-pure), followed by treatment in the ultrasonic

bath for two hours before rinsing several times with deionized water. Specific gravities of the sand (2.65) and kaolinite (2.55) were measured according to ASTM D854, and median grain sizes were measured according to ASTM D422, with the resulting D_{50} for sand = 720 μm and D_{50} for kaolinite = 0.45 μm (Table 3-1). NaCl was used to control the IS of the pore fluid (0.001, 0.01 and 0.1 M), and HCl (1 M) and KOH (1 M) were used to control the equilibrium pH (~ 3 , ~ 6 and ~ 9). All chemicals were used as received (Fisher Scientific) and high quality deionized water ($\sim 18 \text{ M}\Omega\cdot\text{cm}$) was used in all experiments.

4.2.2 Experimental methods

Column tests were performed using an acrylic cylinder (5.08 cm (2 in.) diameter by 15.24 cm (6 in.) height) for the sand column experiment. Perforated aluminum discs and # 200 plastic mesh were installed at the top and the bottom of the column, respectively, for the purpose of distributing the inlet flow at the top of the column and to retain the sand filter media at the base of the column. In addition, a pulse dampener was installed between the column inlet and the pump to minimize pulsations generated by the pump. A schematic drawing of experimental setup is illustrated in Figure 4.1. Sand was placed in the cell at relative density = 70 % (initial porosity = 0.365, based on maximum and minimum void ratio presented in Table 3-1) using the wet pluviation method in order to obtain saturated initial conditions. The flow rate for all experiments was set to $15 \text{ cm}^3\text{min}^{-1}$ and $45 \text{ cm}^3\text{min}^{-1}$ (corresponding to a pore water velocity of 0.74 cm min^{-1} and 2.22 cm min^{-1} respectively) (peristaltic pump (Cole-Parmer)) and the inlet concentration of the kaolinite suspension (C_0) was fixed at 1 g L^{-1} in all experiments. The quantity of HCl and KOH to alter the pH of 1 g L^{-1} kaolinite suspension was predetermined experimentally by titration to achieve the desired pH at equilibrium for the kaolinite suspension. Before the injection into the

column experiment, the kaolinite suspension was suspended in the background solution at the chosen ionic strength and pH solution, followed by preparation in an ultrasonic bath for 2 hour, with stirring to disperse the kaolinite particles. Suspensions were then gently stirred using a magnetic stirrer for an additional hour to allow kaolinite particles to associate and develop clusters as a function of pore fluid conditions.

A background solution at the given ionic strength and pH, but without kaolinite particles, was injected for five pore volumes (PVs) of flow to flush the column and to equilibrate the system. After five pore volumes of flow, the injection of the kaolinite suspension was initiated and continued for 20 PVs, followed by 10 PVs of flow of deionized water. The concentration of kaolinite particles in the outflow was determined by measuring turbidity (turbidimeter, Orbeco-Hellige Inc.) in every 0.4 PV of effluent collected by the fractional collector. After termination of the experiment, the kaolinite particles deposited in the sand medium was determined by carefully sampling every 1.27 cm (0.5 in.) of column depth. The column sections were vigorously stirred for ten minutes with a known amount of water to evaluate the deposition profile of kaolinite from measured turbidity. Concentration of kaolinite and turbidity showed a good positive linear relation which was evaluated prior to the column experiment (data not shown here). The pressure difference across the column was obtained from pressure transducers installed at the top and the bottom of the column (Figure 4.1) and the K_s was calculated using Darcy's equation.

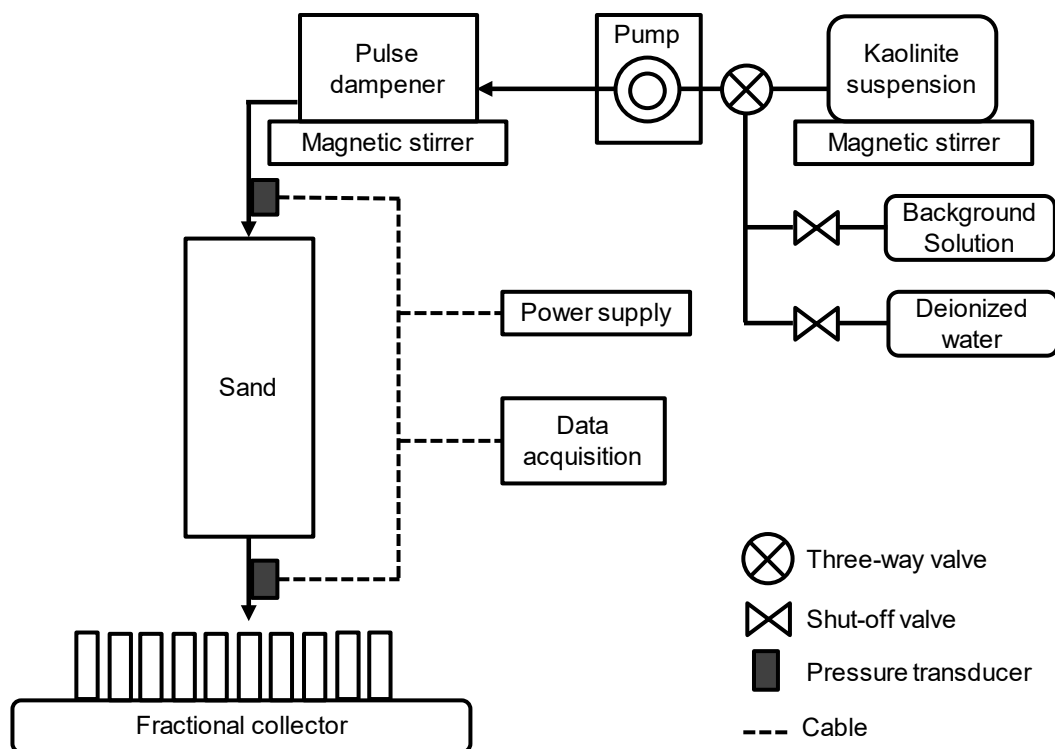


Figure 4.1. Schematic of experimental setup.

4.3 Results and discussion

4.3.1 Low flow rate

The breakthrough curves for the kaolinite effluent concentration, the pressure difference between the inlet and outlet during the injection, and the kaolinite deposition profile in the sand medium under the low flow rate were determined as a function of solution chemistry (Figure 4.2 - Figure 4.4). Most of the kaolinite (> 99 %) was deposited in the sand (Table 4-1), with the exception of the experiment conducted at pH ~ 6 and IS ~ 0.1 M, and the experiment conducted at pH ~ 9 and IS ~ 0.001M. As a result of the decreased deposition, low values of normalized pressure difference (dP / dP_0) were observed for those two cases after twenty pore volumes of flow ($dP / dP_0 = 2.17$ for IS ~

0.1 M and pH \sim 9 and $dP / dP_0 = 2.15$ for pH \sim 9, IS \sim 0.001 M, Figure 4.3). Note that normalized K_s is not presented here because the K_s is the reciprocal of pressure difference in Darcy's equation under the constant flow rate. Therefore, the relatively large amount of kaolinite observed in the effluent for the two experiments resulted in a lower reduction of K_s compared to other cases.

In contrast, the values of dP / dP_0 after 20 PV decreased as ionic strength increased: IS \sim 0.001 $>$ 0 $>$ 0.01 $>$ 0.1 at pH \sim 6, followed by pH \sim 3 $>$ 6 $>$ 9 at IS \sim 0.001 M, and pH \sim 3 $>$ 9 $>$ 6 at IS \sim 0.1 M (Figure 4.3). This result suggests that the reduction of K_s due to the deposition of kaolinite was more significant under acidic conditions than neutral or basic pH, regardless of IS. In addition, the trend of pressure difference was consistent with the trend of the amount of deposited kaolinite in the first top layer of the sand medium (Figure 4.4, with the exception of IS \sim 0.001 $<$ 0 at pH \sim 6). The more exponential deposition profile resulted in a more significant reduction of K_s .

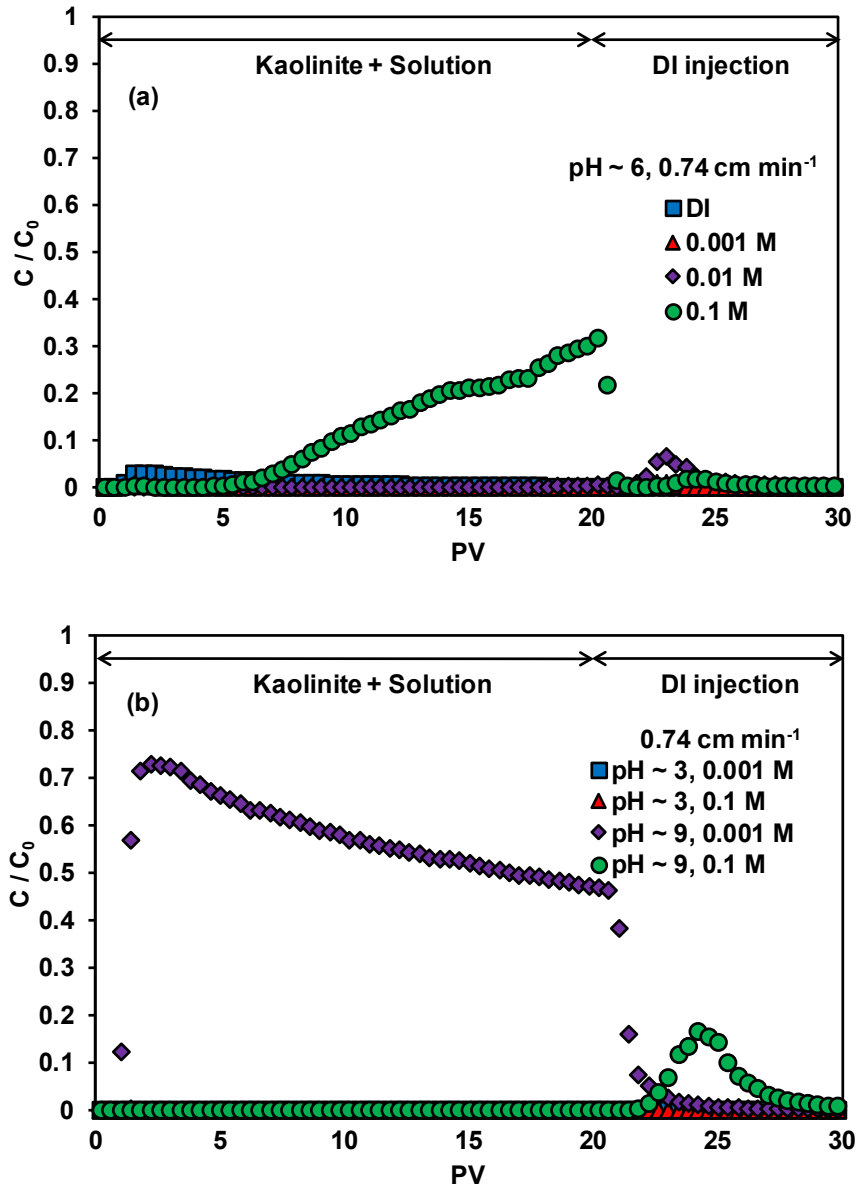


Figure 4.2. Breakthrough curves of kaolinite under low flow rate: (a) pH ~ 6 under different IS and (b) pH ~ 3 and 9 with IS = 0.001 and 0.1 M. C/C_0 on y axis represents the normalized concentration of kaolinite colloids at effluent.

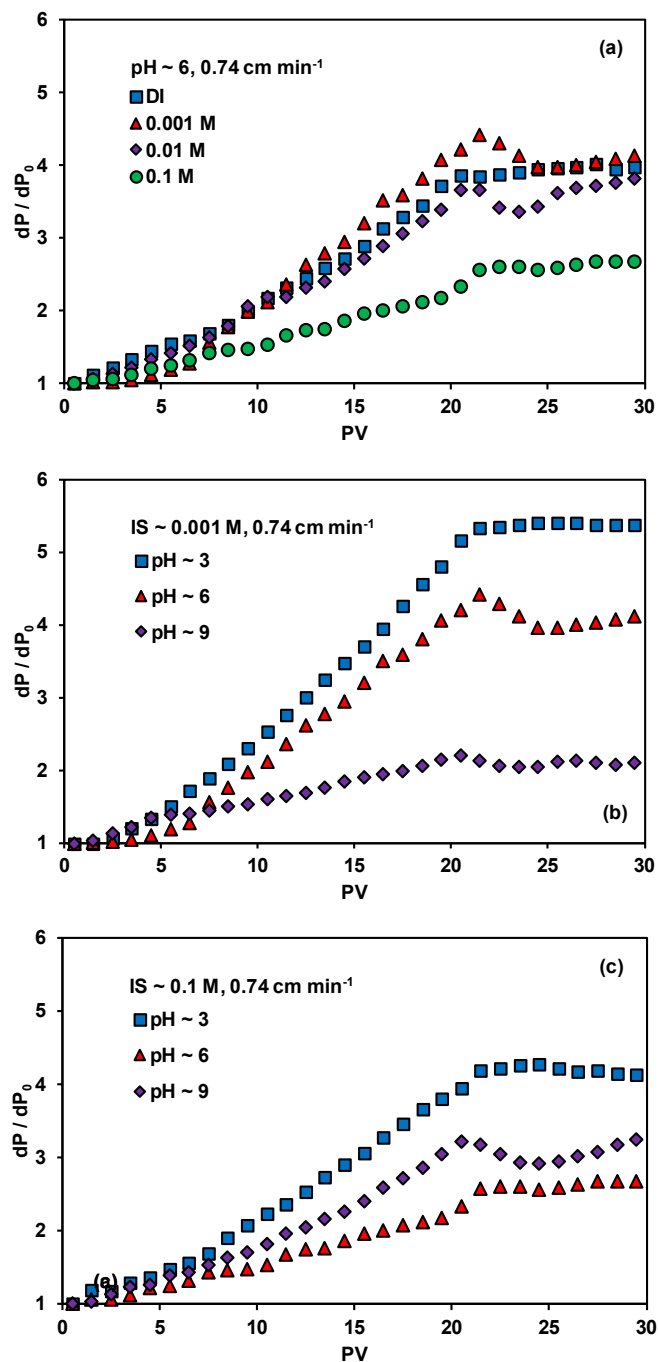


Figure 4.3. Normalized pressure difference (dP / dP_0) during the injection under low flow rate: (a) as function of ionic strength at $\text{pH} \sim 6$, (b) as function of pH at $\text{IS} \sim 0.001 \text{ M}$ and (c) as function of pH at $\text{IS} \sim 0.1 \text{ M}$.

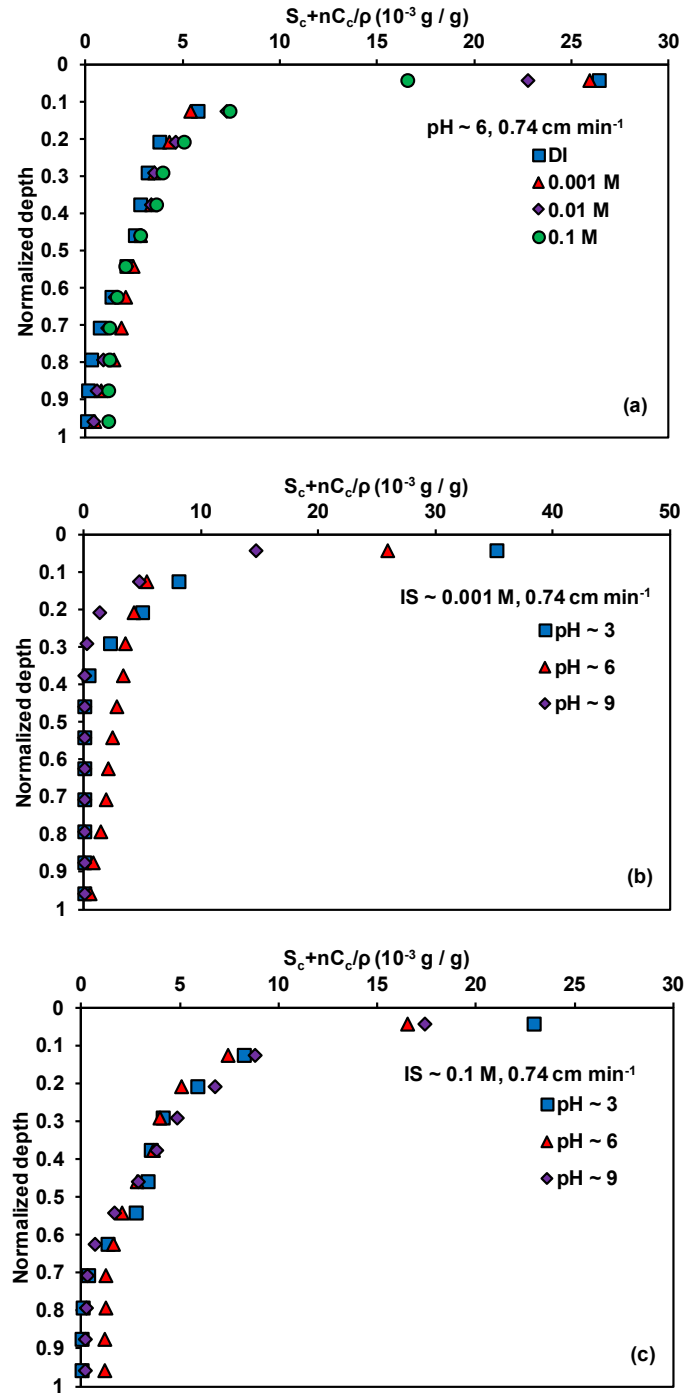


Figure 4.4. Kaolinite deposition profile after the injection under low flow rate: (a) as function of ionic strength at $\text{pH} \sim 6$, (b) as function of pH at $\text{IS} \sim 0.001 \text{ M}$ and (c) as function of pH at $\text{IS} \sim 0.1 \text{ M}$.

Straining and attachment mechanisms can be taken into account to fundamentally explain the differences in the breakthrough curves and deposition profiles as a function of the solution chemistry. Straining is defined as particle immobilization due to narrow pore size of the sand medium (Auset and Keller 2006; Xu et al. 2006). Therefore, the size ratio between the kaolinite and sand particles is the most important factor affecting the mass of strained kaolinite particles because larger grain sizes of sand generally lead to larger pore openings and throats (Arya et al. 1999b). In contrast, attachment of particles can be explained by the net attractive interaction energy between the particle and the sand grain. The theory, originally proposed by Derjaguin, Landau, Verwey and Overbeek (DLVO theory), has been used to account for the attachment mechanism of particles (Torkzaban et al. 2007), with van der Waals attraction and double layer repulsion representing the two key interaction energies that can affect particle attachment. If the sizes of the kaolinite clusters formed as a function of solution chemistry are relatively large, most of them are more likely to be deposited at the filter surface by straining, which results in a more exponential deposition profile. In contrast, attachment mechanisms may be dominant when the sizes of kaolinite cluster are relatively small, which allows kaolinite aggregates to penetrate more deeply into the filter. This deep penetration of kaolinite results in a less exponential deposition profile.

Based on the shape of the deposition profile (exponential) and the absence of kaolinite particles within the deep sand medium at low ionic strength, straining was likely the dominant removal mechanism for kaolinite deposition at $\text{pH} \sim 3$ and $\text{pH} \sim 9$ (Figure 3b). In contrast, the less exponential deposition profile and deposited kaolinite particles measured at all depths demonstrated that attachment of kaolinite occurred in experiments

performed at pH ~ 6. According to the kaolinite fabric map proposed by Palomino and Santamarina (2005), kaolinite particles at pH ~ 3 will form clusters with face to face aggregation while kaolinite particles will disperse at pH ~ 9. Additionally, the surface charge of the sand and kaolinite particles tend to be same sign due to the protonation / deprotonation of surface hydroxyl groups on the silica faces of kaolinite particles. This leads to low attachment efficiency and high repulsive energy between sand and kaolinite at pH ~ 3 and 9. In addition, a lower mass of kaolinite was deposited at pH ~ 9 when compared to pH ~ 3 (56 % of kaolinite was observed in effluent at pH ~ 9 compared to pH ~ 3 (Table 4-1) due to the highly dispersed kaolinite particles). In contrast, pH ~ 6 is located between the edge and face isoelectric points, meaning that negative and positive sites coexist on the kaolinite particles, which will likely lead to more significant attachment of kaolinite at pH ~ 6 than at other pH levels. From the observed deposition profiles, roughly 28 % of total injected kaolinite was recovered at pH ~ 6 at the normalized depth (depth divided by total depth of the column) of sand medium larger than 0.3 while only 1.4 and 0.5 % were recovered at pH ~ 3 and 9 respectively. At the high ionic strength, the significance of pH as a factor in the form of the deposition profile and pressure difference decreased due to prevalent Na⁺ ions that can potentially compensate for the impact of pH.

At pH ~ 6, the quantity of strained kaolinite increased as ionic strength decreased (Figure 4a). Based on DLVO Theory, kaolinite particles (or clusters) may more preferably attach to the sand grain as ionic strength increased due to a decrease in double layer repulsion. However, the lower amount of deposited kaolinite was observed at ionic strength ~ 0.1 M, and 12 % of kaolinite mass was recovered in the effluent. This may be mainly attributed to the smaller size of kaolinite clusters under high IS at pH ~ 6. The adsorption

of Na^+ to the kaolinite particles may also decrease the available negative sites available to associate with positive sites of another kaolinite particle. This leads to the smaller size of kaolinite clusters and less exponential deposition profiles under higher ionic strength, which resulted in the lowest pressure difference at ionic strength ~ 0.1 M.

Overall, the most significant decrease in K_s was $K_s / K_{s0} = 0.2$ (at pH ~ 3 , IS ~ 0.001 M) while the least decrease was $K_s / K_{s0} = 0.46$ (at pH ~ 9 , IS ~ 0.001 M), when measured after twenty pore volumes of kaolinite suspension flow. Consequently, it can be concluded that the solution chemistry of the kaolinite suspension was a crucial factor for the reduction of K_s under identical kaolinite concentration and flow rate. From the observed breakthrough curves and deposition profiles, this may be attributed to the different size of kaolinite clusters because of different association behavior between kaolinite particles and different interaction energy (attraction or repulsion) between kaolinite cluster (or particle) and sand grains according to the solution chemistry. As was anticipated, the straining of kaolinite more substantially affected the reduction of K_s in a sand medium than the attachment of kaolinite.

4.3.2 High flow rate

The breakthrough curves for the kaolinite effluent concentration, the pressure difference between the inlet and outlet during the injection, and the kaolinite deposition profiles as a function of solution chemistry under high flow rate are presented in Figure 4.5, Figure 4.6, and Figure 4.7 respectively. In addition, recovery fractions of deposited kaolinite, transported kaolinite, and detached kaolinite are summarized in Table 4-1.

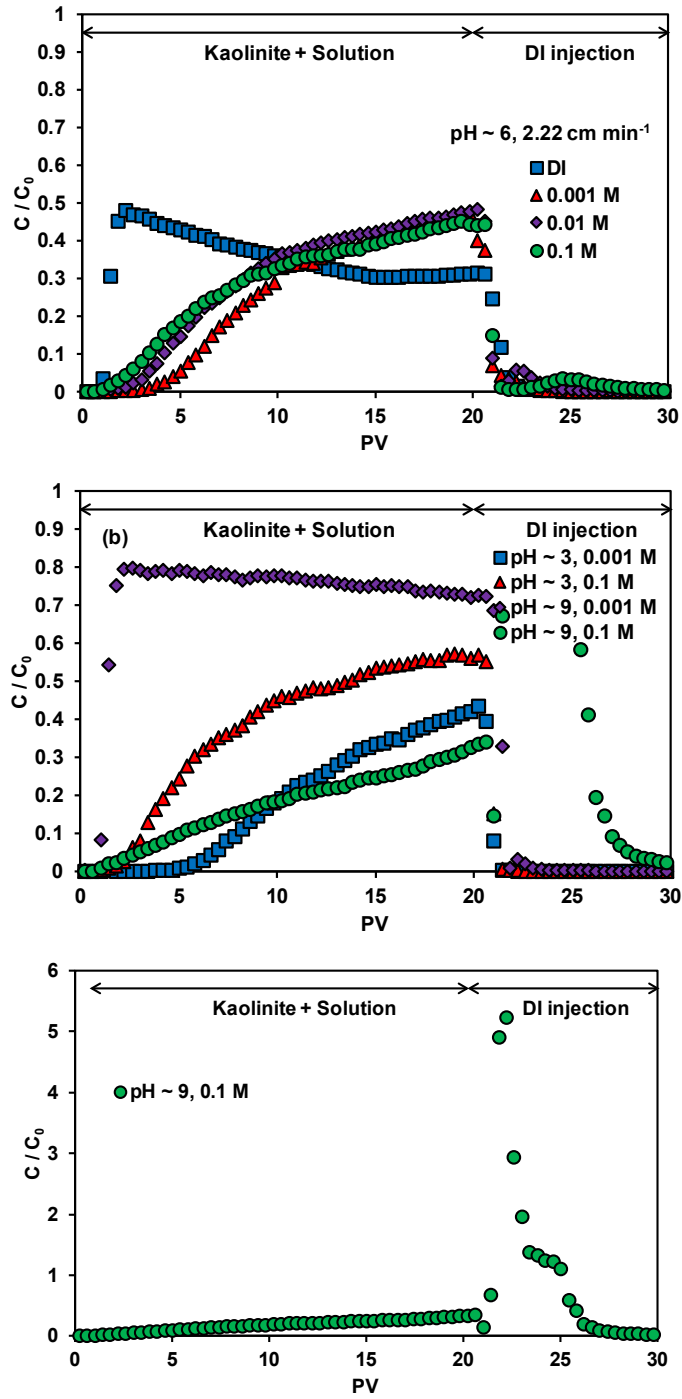


Figure 4.5. Breakthrough curves of kaolinite under high flow rate: (a) pH ~ 6 under different IS and (b) pH ~ 3 and 9 with IS = 0.001 and 0.1 M (c) pH ~ 9 and IS = 0.001 M in a larger C/C_0 scale.

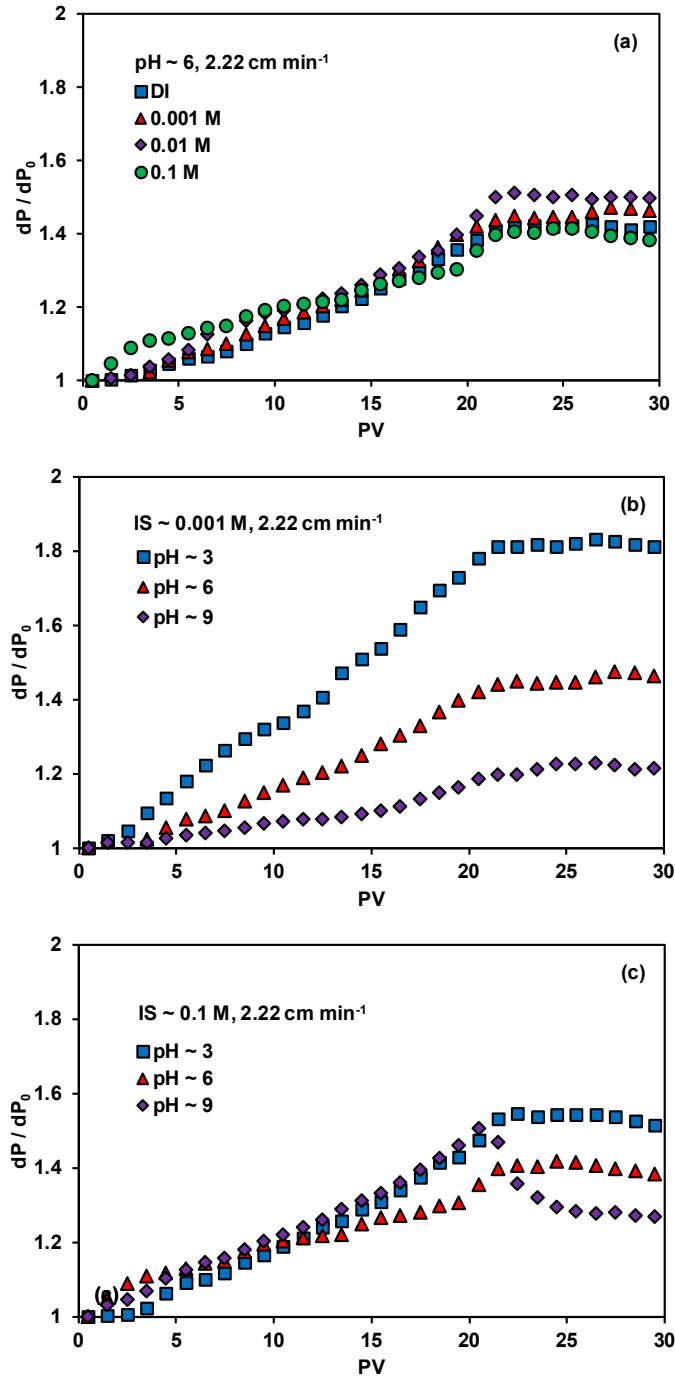


Figure 4.6. Normalized pressure difference (dP / dP_0) during the injection under high flow rate: (a) as function of ionic strength at $\text{pH} \sim 6$ (b) as function of pH at $\text{IS} \sim 0.001 \text{ M}$ and (c) as function of pH at $\text{IS} \sim 0.1 \text{ M}$.

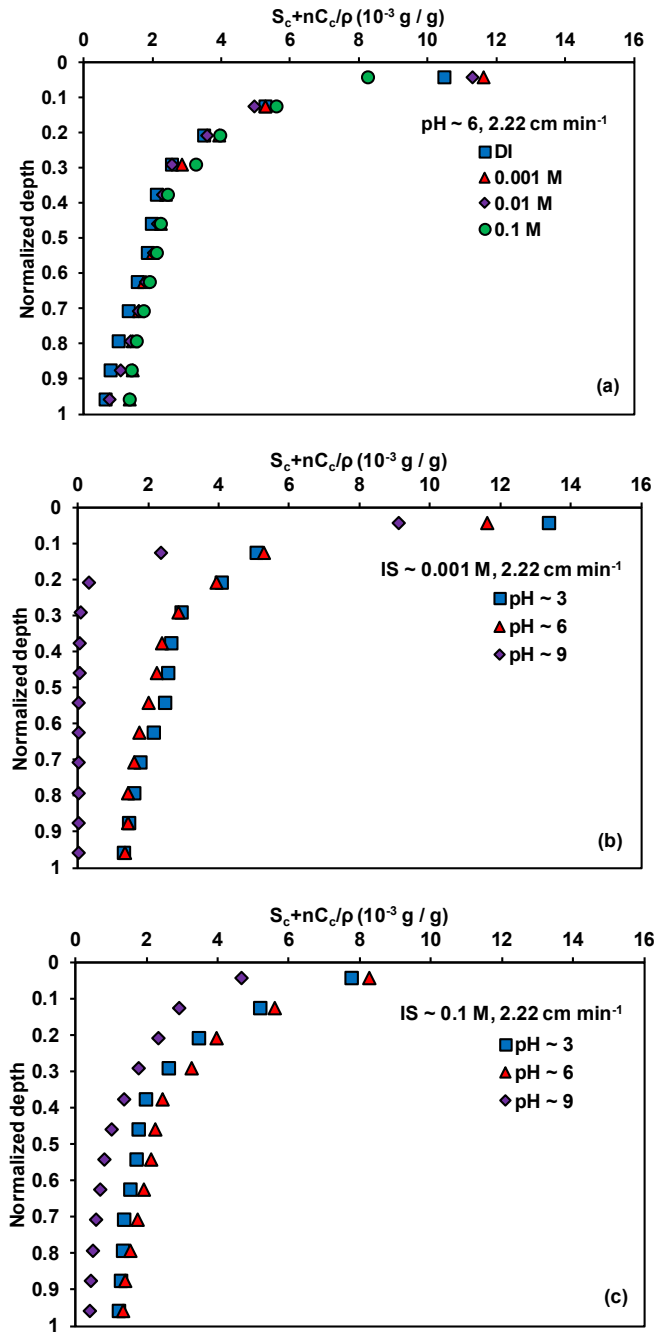


Figure 4.7. Kaolinite deposition profile after the injection under high flow rate: (a) as a function of ionic strength at pH ~ 6 (b) as a function of pH at IS ~ 0.001 M and (c) as a function of pH at IS ~ 0.1 M.

Table 4-1. Recovered Fraction of Attached Kaolinite in a Sand Medium (M_s), Observed Kaolinite at Effluent during 20 PVs Injection (M_e), Detached Kaolinite during 10 PVs of DI Water Injection (M_d), and Kaolinite Mass Balance (MB)

Experimental Condition			Recovered Fraction (%)			MB (%)
pH	IS (M)	v_s (cm / s)	M_s	M_e	M_d	
~ 6	~ 0		99.05	0.95	0.02	95.90
~ 6	0.001		99.91	0.09	0.09	104.82
~ 6	0.01		99.88	0.12	0.74	99.12
~ 6	0.1	0.74	87.63	12.37	0.34	96.82
~ 3	0.001	(low)	99.90	0.10	0.03	98.70
~ 3	0.1		99.93	0.07	0.03	101.63
~ 9	0.001		43.51	56.49	0.95	99.07
~ 9	0.1		99.96	0.04	2.41	94.63
~ 6	~ 0		64.41	35.59	1.05	90.99
~ 6	0.001		73.30	26.70	0.56	92.65
~ 6	0.01		69.06	30.94	0.96	96.11
~ 6	0.1	2.22	69.83	30.17	1.20	96.06
~ 3	0.001	(high)	79.96	20.04	0.20	94.00
~ 3	0.1		60.39	39.61	0.37	91.34
~ 9	0.001		24.84	75.16	6.34	109.58
~ 9	0.1		81.26	18.74	58.50	92.84

Note: M_e and M_d were evaluated by area under experimental breakthrough curves presented in Figure 4.2 and Figure 4.5.

In general, high flow rate causes a large fluid drag force applied to kaolinite colloids, which leads to a large amount of transported kaolinite, low amount of deposited kaolinite and low increase in normalized pressure difference as shown in Figure 4.5, Figure 4.6, Figure 4.7, and Table 4-1. Specifically, as seen in Figure 4.5(a), a significant amount of kaolinite was observed at effluent under high flow rate regardless of IS at pH ~ 6. In contrast to breakthrough behaviors observed under the low flow rate (almost no kaolinite was observed at IS = 0.001 and 0.01 M, Figure 4.2(a)), similar breakthrough behaviors were observed throughout the injection in $0.001 \text{ M} < \text{IS} < 0.1 \text{ M}$. These behaviors imply that the relatively high flow rate rather than IS governs the breakthrough curves of kaolinite at pH ~ 6. Conversely, the evolutions of breakthrough curves are analogous in the two flow

rates; in case of using DI water as a background solution, the peak value of C/C_0 was observed in the beginning of breakthrough and decreases over time while C/C_0 gradually increases throughout the injection of kaolinite in all IS range. These two evolutions can be explained by two potential reasons: ripening and blocking phenomena for the attachment of kaolinite or pore plugging due to the straining. As mentioned in the section 3.4.2, the ripening phenomenon explains the increase in the attachment rate as increase in retained kaolinite, whereas the blocking phenomenon describes the decrease in the attachment rate as increase in retained kaolinite (section 3.2.2). Therefore, decrease in C/C_0 throughout the injection (DI water) implies that the ripening is dominant, and increase in C/C_0 over time (0.001 – 0.1 M solution) indicates that the blocking is dominant for the attachment of kaolinite. The assumption of pore plugging due to straining may not be able to explain the two types of evolutions of breakthrough curves. As presented in Figure 4.7(a), larger retained kaolinite in the first layer at IS ~ 0.01 M and IS ~ 0.001 M than that in the first layer at DI water indicates that evolutions of breakthrough curves at IS ~ 0.01 and 0.001 M is not acceptable if the plugging assumption is valid. More hypoexponential deposition profiles at IS ~ 0.01 and 0.001 M imply the larger number of plugged pores, which lead to increase in deposition rate and a decrease in C/C_0 over time if the evolutions of breakthrough curves are because of pore plugging.

As presented in Table 4-1, the detached kaolinite fraction (M_d) shows larger value in all solution chemistries under high flow rate. These larger M_d values are qualitatively consistent with the hydrodynamic shear presented in Bergendahl and Grasso (2000a): high flow rate causes high hydrodynamic shear, leading to the larger amount of detached colloids (kaolinite in this work). In thermodynamic standpoint, change in background

solution to DI water for the injection of last 10 PVs alters the interaction energy between sand and kaolinite. The classical DLVO theory (combination of van der Waals attraction and double layer repulsion, Figure 2.1) cannot explain the effect of pH, but M_d values presented in Table 4-1 indicate that altering pH ~ 9 to pH ~ 6 (pH of DI water) is more critical in the detachment of kaolinite than varying pH ~ 3 to pH ~ 6 irrespective of ionic strength (IS is changed from 0.1 M or 0.001 M to ~ 0 at pH ~ 3 and 9). Therefore, relatively large fraction of attached kaolinite colloids on sand grains are detached by the induced repulsion energy between sand and kaolinite because of the injection of DI water. In other words, the amount of induced repulsion energy may be large enough overcoming the net attraction energy at pH ~ 9 , while it may be less than the net attraction energy at pH ~ 3 for the attached kaolinite. Notably, more than half of attached kaolinite colloids were detached at pH ~ 9 and IS ~ 0.1 , and extremely high C / C_0 values were observed during the injection of DI water (Figure 4.5(c)). The significant amount of detached kaolinite implies that the background solution with high pH and IS may have the low net attraction energy, which leads to the susceptibility of attached kaolinite colloids to the alternation of solution chemistry.

One another possible hypothesis is that kaolinite colloids are deposited only by the straining mechanism as pH ~ 3 due to the identical surface charge of sand and kaolinite, which leads to almost no detachment of kaolinite under the identical flow rate regardless of alternation of solution chemistry. The straining mechanism is only a function of size, and the alternation of interaction energy between sand and kaolinite merely applies to the attached kaolinite.

Apparently, high flow rate induces the low amount of deposited kaolinite, leading to the less reduction of K_s . Under the high flow rate, dP / dP_0 in Figure 4.6 shows less than 2 during 20 PVs, which is equivalent to the normalized $K_s > 0.5$ in all solution chemistries. In addition, IS and pH is not significant variables for the reduction of K_s when $pH \sim 6$ and $IS \sim 0.1$ respectively under the high flow rate (Figure 4.6(a) and Figure 4.6(c)). The values of dP / dP_0 are in order of $pH \sim 3 > 6 > 9$ at $IS \sim 0.001$ M, which is consistent with the order under low flow rate. However, the variation of dP / dP_0 among three pH values is significantly reduced under high flow rate. Therefore, the high flow rate reduces the effect of solution chemistry on the reduction of K_s . The hydrodynamic forces applied to kaolinite is a more critical factor for the reduction of K_s in high flow regime.

4.4 Summary

In this chapter, reduction of hydraulic conductivity in a sand medium during the injection of kaolinite suspensions was experimentally quantified as a function of different solution chemistries and the flow rate. Based on the observed deposition profiles and breakthrough curves of kaolinite and pressure increase during the injection of kaolinite, the following conclusion can be drawn:

1. Relatively large amounts of kaolinite were observed in effluent when $pH \sim 6$, $IS \sim 0.1$ M and $pH \sim 9$, $IS \sim 0.001$ M under low flow rate, which resulted in relatively lower decrease in hydraulic conductivity when compared to other cases where most of the kaolinite deposited in the sand medium. In contrast, under high flow rate (Darcy's velocity = 2.22 cm min^{-1}), a significant amount

of kaolinite was observed at effluent in all solution chemistries due to the large hydrodynamic force.

2. Under low flow rate, the reduction of hydraulic conductivity was greatest at pH ~ 3 (pH $\sim 3 > 6 > 9$ under low ionic strength) while it exhibited different order at high ionic strength: pH $\sim 3 > 9 > 6$. Nevertheless, this suggested that the reduction of k was more significant at acidic conditions regardless of ionic strength, which may be attributed to the large kaolinite clusters that formed by face to face association of kaolinite particles.
3. Detachment of kaolinite was not significant under low flow rate, while relatively large amount of detached kaolinite was observed under high flow rate followed by the injection of DI water. This implies that the detachment of kaolinite occurs when the combination of induced repulsive interaction energy (thermodynamics) and hydrodynamic force exceed the net attraction energy between sand and kaolinite.
4. Notably, more than half of attached kaolinite colloids were detached at pH ~ 9 and IS ~ 0.1 , and extremely high C / C_0 values were observed during the injection of DI water (Figure 4.5(c)). The significant amount of detached kaolinite implies that the background solution with high pH and IS may have the low net attraction energy, which leads to the susceptibility of attached kaolinite colloids to the alternation of solution chemistry.
5. At pH ~ 6 and low flow rate, kaolinite was observed in the effluent at ionic strength ~ 0.1 M and a more exponential deposition profile was observed as ionic strength decreased, in spite of higher attractive interaction energy at high

ionic strength as predicted by DLVO theory. Thus, the size of kaolinite clusters can explain the straining mechanism as well as the attachment mechanism and their impact on the deposition behavior of kaolinite particles.

6. From the observed deposition profiles and pressure difference, it can be concluded that the solution chemistry was one of the crucial factors that can impact to the reduction of hydraulic conductivity, as observed in the shape of the resulting retention profiles. However, under high flow rate, the effect of solution chemistry on the reduction of hydraulic conductivity is reduced.

CHAPTER 5 A STOCHASTIC APPROACH OF CLAY COLLOID TRANSPORT IN A SAND MEDIUM

5.1 Introduction

Many mathematical continuum-scale models, based on the assumptions of the deep-bed filtration model (Rajagopalan and Tien 1976), have been developed to describe colloid transport in porous media using sand as the model filter medium. More recent models incorporate additional constraints, including first-order attachment and detachment coefficients in the advection-dispersion equation (Corapcioglu and Choi 1996; Harvey and Garabedian 1991; Ryan and Gschwend 1994), straining and size exclusion in addition to attachment and detachment (Bradford et al. 2002, 2003, 2004; Ginn 2002; Ryan and Elimelech 1996), a two-site kinetics approach (Compère et al. 2001; Hendry et al. 1997; Yan 1996), a dual-porosity approach (Corapcioglu and Wang 1999), and colloid filtration theory to evaluate attachment efficiency (Ryan and Elimelech 1996; Tufenkji and Elimelech 2004, 2005). These models have made significant contributions to explaining the observed retention profiles of colloid transport in laboratory scale experiments. They are dependent on the experimental conditions, which include the type of colloids, solution chemistry, and flow rate used in the experiment, and typically exhibit an exponential profile. Depending on the shape of the retention profiles and the breakthrough curves, the optimal model can be chosen from among those conditions.

Additionally, stochastic models can be a useful method to describe colloidal transport in order to account for inherent uncertainties of transport due to the complexity of the subsurface environment. Tufenkji et al. (2003) proposed a model to investigate the effect of chemical heterogeneity of microbial colloids on their transport by taking the

attachment coefficient (k_{att}) as a stochastic parameter at given predetermined distributions. Bradford and Toride (2007) developed a model to account for the hyper-exponential retention profiles of latex colloids by taking k_{att} as a stochastic parameter. Bekhit and Hassan (2005) developed a model based on Monte Carlo simulation to investigate the effect of spatial heterogeneity of hydraulic conductivity, distribution coefficient, and k_{att} on contaminant transport under the presence of colloids. In addition, a number of stochastic models have been introduced to mathematically describe random physical properties of porous media and colloids including pore size distribution, pore length, and flow characteristics (Bedrikovetsky 2008; Berkowitz et al. 2006; Boano et al. 2007; Cortis 2007; Cortis et al. 2004). These well-established models interpreted colloid transport in a stochastic manner, rather than in a deterministic approach.

The relative size of colloidal particles versus the sand particles is one of the key factors impacting retention profiles and breakthrough curves because different size ratios cause variations of geometry and interaction energy between the two materials (Bradford et al. 2011). Experimental results have revealed that a larger size ratio leads to a larger amount of retained colloids, due to straining and higher attractive energy between the colloid and the sand. However, most of these experimental studies used a monodispersed latex colloid and a median grain size (d_{50}) to represent colloids and porous media in the subsurface. In addition, they used d_{50} as a representative grain size of sand for the calculation of interaction energy or optimization analysis to back-calculate relevant coefficients embedded in governing equations (Bradford et al. 2002, 2003; Elimelech and O'Melia 1990; Wan and Wilson 1994; Xu et al. 2006; Xu and Saiers 2009). Using monodispersed colloids in a colloid transport experiment and d_{50} of sand in optimization

analysis is appropriate to represent the semi-monodispersed colloid (e.g., pathogenic bacteria), but may not be valid for the transport of polydispersed colloids such as clay, which is more likely to be present in nature with highly variable sizes. The coefficient of uniformity (C_u) for the sand particles and clay colloids can frequently be as high as ten in natural systems (Mitchell and Soga 2005), which implies that the largest particle can be more than ten times larger than the smallest particle. Therefore, the polydispersed characteristics of the two materials must be reflected in the prediction of clay colloid transport in a sand medium in order to correctly model retention and transport.

Additionally, clay colloids aggregate into four different types of fabric formations as a function of solution chemistry (e.g., pH and ionic strength): edge-to-face, edge-to-edge, face-to-face association and combined face-to-face in edge-to-face association (Palomino and Santamarina 2005). Significant aggregation of clay colloids takes place under high ionic strength, mainly because of the predominant van der Waals attraction caused by the resulting thin double layer of clay colloids. High attraction energy between clay colloids leads to larger clay clusters (or flocs, which are the assembly of clay colloids caused by any type of physico-chemical association), while clay colloids are perfectly dispersed under some chemical conditions (e.g., high pH and low IS). Therefore, determining the precise size of a clay cluster is challenging, particularly under the condition of geochemical perturbations, which leads to complexity in predicting colloidal transport through the subsurface.

To date, no stochastic model is available for modeling the effect of size variability of the soil media on the transport of clay colloids. From a mathematical standpoint, the

first-order coefficients in the governing equation that are used to account for attachment and straining mechanisms increase nonlinearly with an increase in the sizes of the clay or a decrease in the sizes of the sand. As a result, taking the polydispersed characteristics of sand and clay by using multiple sizes in the calculation may yield different retention profiles and breakthrough curves when compared to those evaluated using median sizes of the filter medium.

The main objective of this study was to investigate the inherent uncertainty of clay colloid retention profiles in a sand filter medium with variability in the size of both the sand and the clay particles. Sizes of clay and sand were determined using Metropolis-Hastings sampling and Latin Hypercube sampling at given distributions. Experimental grain size distributions of clay and sand were fitted to the best lognormal distribution (least square fit), and the sampled clay and sand were then used in the numerical calculation. The calculation was first performed based on the experimentally obtained grain size distribution and experimental conditions, and the sensitivity analysis was then performed. The analysis demonstrated the impact of a well-distributed clay or sand particle size on the retention profile, and on the uncertainty of the retention profile, under different particle sizes. Standard deviation and mean were used to represent grain size distributions of the sand and clay.

5.2 Mathematical models

5.2.1 Colloids transport in saturated porous media

The governing equations for advection-dispersion including attachment, detachment, and straining mechanisms for colloidal transport in saturated porous media are expressed as (full expression of Equation (3-5))

$$\frac{\partial(nC)}{\partial t} = -U \frac{\partial C}{\partial z} + \frac{\partial}{\partial z} \left(nD \frac{\partial C}{\partial z} \right) - nk_{att}\psi_{att}C + \rho_b k_{det} S_{att} - nk_{str}\psi_{str}C, \quad (5-1)$$

$$\rho_b \frac{\partial S}{\partial t} = nk_{att}\psi_{att}C - \rho_b k_{det} S_{att} + nk_{str}\psi_{str}C, \quad (5-2)$$

where n (-) is porosity, C (ML^{-3}) is the colloid concentration in aqueous phase, t (T) is time, U (LT^{-1}) is the Darcy velocity, z (L) is the depth, D (L^2T) is the dispersion coefficient, k_{att} (T^{-1}), k_{det} (T^{-1}) and k_{str} (T^{-1}) are the attachment, detachment and straining coefficient respectively, ψ_{att} (-) and ψ_{str} (-) are the attachment and the straining function respectively, ρ_b (ML^{-3}) is the bulk density, and S_{att} (MM^{-1}) is the solid phase concentration of attached colloids. Note that n is set equal to the volumetric water content (θ_w) in this work, assuming that all colloids in the aqueous phase are accessible to the water in the medium. Available sites for attachment on surface of the sand may decrease over time as attached colloids block the part of the sand, while the most of the colloids straining take place at the surface layer of medium mainly due to the pore size restriction. To account for these characteristics of two mechanisms into Equation (5-1), ψ_{att} (Adamczyk et al. 1994; Camesano et al. 1999; Johnson and Elimelech 1995) and ψ_{str} (Bradford et al. 2003) may be respectively written as Equation (3-8) and Equation (3-6). In geometrical standpoint, S_{max} may be expressed as Equation (3-9) assuming that shapes of sand and clay colloid (or cluster) are spheres. The

empirical relation proposed by Bradford et al. (2003) between k_{str} (unit in sec^{-1}) and the size ratio (r_c/r_s , r_c (L) is the radius of colloid and r_s (L) is the radius of sand grain) (Equation (3-7)) was used in this chapter.

5.2.2 DLVO and k_{att} calculation

k_{att} presented in Equation (5-1) can be obtained by calculating the Derjaguin-Landau-Verwey-Overbeek (DLVO) interaction energy combined with colloid filtration theory (Bradford et al. 2011). Note that non-DLVO forces such as Born repulsion or hydration forces were not considered in this calculation. Under the condition of $r_s \gg r_c$, total interaction energy (G) between the clay colloids and sand can be expressed as (Israelachvili 2011):

$$G = G_{DL} + G_{VDW} = (r_c Z \exp(-\kappa H)) + (-A_{swc} r_c / 6H), \quad (5-3)$$

where G_{DL} (ML^2T^{-2}) and G_{VDW} (ML^2T^{-2}) are interaction energies attribute to double layer repulsion and Van der Waals attraction respectively, Z (ML^2T^{-3}) is an interaction constant as a function of surface potential of sand and clay, κ (L^{-1}) is a reverse of Debye length as a function of ionic concentration and valence, H (L) is the separation distance, and A_{swc} (ML^2T^{-2}) is the Hamaker constant in sand-water-clay system calculated by the refractive indices and dielectric constants of those three materials. In colloidal filtration theory, k_{att} is estimated as (Yao et al. 1971)

$$k_{att} = \frac{3(1-\theta_w)}{2d_{s50}} \alpha \eta_0 v_s, \quad (5-4)$$

where α (-) is the attachment efficiency, η_0 (-) is the single-collector collision efficiency obtained by a sum of collision efficiencies of colloids associated with diffusion, interception, and gravitational effects (Rajagopalan and Tien 1976; Tufenkji and Elimelech 2004), and v_s (LT^{-1}) is the average seepage velocity. The value of η_0 in this study was obtained by the correlation equation proposed by Tufenkji and Elimelech (2004).

Most of the colloidal attachment takes place at the separation distance corresponding to the secondary minimum because of dominant repulsive double layer interaction at a close separation distance, which generally prevents colloids from overcoming this energy barrier. Therefore, α can be estimated with the assumption that the velocity distribution of colloids follows the Maxwell distribution in the secondary minimum. However, even though it is very rare, colloids can attach to the primary minimum when the secondary minimum energy is relatively low, and the energy barrier is sufficiently low for colloids to overcome it. To account for the attachment at both primary and the secondary minimum, the following was used (Shen et al. 2007).

$$\alpha = \alpha_{pri} + \alpha_{sec} = 1 - \int_{\sqrt{\Phi_{sec}}}^{\sqrt{\Delta\Phi}} \frac{4}{\pi^{0.5}} x^2 \exp(-x^2) dx, \quad (5-5)$$

where α_{pri} (-) and α_{sec} (-) are the attachment efficiency attribute to the primary minimum and the secondary minimum respectively, $\Delta\Phi$ (-) is a sum of Φ_{max} and Φ_{sec} (Φ_{max} is maximum interaction energy at the energy barrier and Φ_{sec} is interaction energy at the secondary minimum, Φ_{max} and Φ_{sec} are interaction energies normalized by kT , where k ($ML^2T^{-2}K^{-1}$) denotes the Boltzmann constant, and T (K) denotes the absolute temperature), and x^2 (-) is the dimensionless kinetic energy of colloids. Employing Equation (5-4) and (5-5) provides an analytical calculation of k_{att} in Equation (5-1).

5.2.3 Sampling procedure from GSD of sand and clay

Two sampling techniques were utilized to sample clay colloids and sand at given lognormal distributions: the Metropolis-Hastings algorithm, (Metropolis et al. 1953), which is one of the popular algorithms for implementing Markov chain Monte Carlo analysis, and the Latin Hypercube Sampling (LHCS) method originally proposed by McKay et al. (1979). For the sampling, a fit of the lognormal cumulative distribution function (CDF) to the experimental grain size distribution curves using least squares yielded target lognormal distributions. Experimental grain size distributions were evaluated by the hydrometer test (ASTM D422) for clay colloids (Georgia kaolinite), and by sieve analysis (ASTM C136) for sand (ASTM 20/30 sand).

A key mathematical expression of the Metropolis-Hastings algorithm is given as:

$$u < \Gamma(x_s, x^*) = \min\left\{1, \frac{p(x^*)}{p(x_s)}\right\}, \quad (5-6)$$

where s is an integer between 1 and $N-1$, u is a random number generated from 0 to 1, $p(x)$ is the probability at target CDF corresponding to the value x , x_s is the value of s^{th} sampling, x^* is the random number generated based on the proposal function (q) at given x_s ($q(x^* | x_s)$ is a normal distribution centered at x_s). If the condition in Equation (5-6) is satisfied, x_{s+1} is equal to x^* , otherwise, $x_{s+1} = x_s$ with the continuous iteration of the algorithm until s reaches to the given sampling size (N). Note that the condition in Equation (5-6) assumes a symmetric random walk (i.e., $q(x_s | x^*) = q(x^* | x_s)$). On the other hand, the LHCS method is a technique fundamentally different from the common Monte Carlo method because it provides a constraint for evaluating evenly distributed samples at the target CDF even

under relatively small N. The mathematical formulation of constraint in the LHCS method is given as

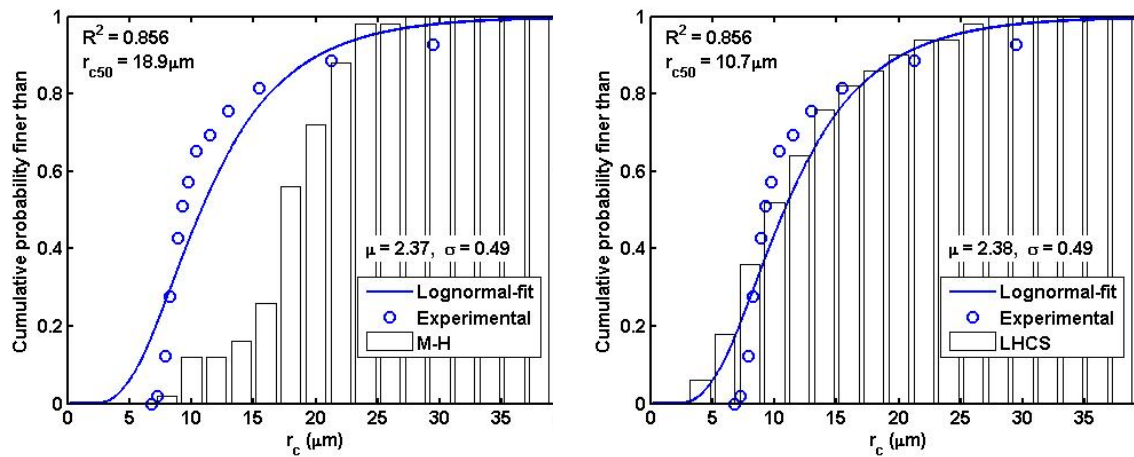
$$P_m = \left(\frac{1}{N}\right)u_m + \left(\frac{m-1}{N}\right), \quad (5-7)$$

where m is an integer between 1 and N, u_m is the random number generated from 0 to 1 in each m, P_m is the random probability value at target CDF for the m^{th} interval located between $1/N$ and $(m-1)/N$. Generated random P_m values in Equation (5-7), which ensure evenly distributed sampling values in target CDF, were used to evaluate samples from the inverse CDF (F^{-1}):

$$x_m = F^{-1}(P_m). \quad (5-8)$$

As presented in Equation (5-6), (5-7), and (5-8), Metropolis-Hastings algorithm allows replacement during sampling, while LHCS method is sampling without replacement. In other words, Metropolis-Hastings algorithm potentially generates identical values successively if selected x^* fails to satisfy the condition in Equation (5-6), while each sampled value is different in LHCS method and well distributed throughout the target CDF regardless of N. Therefore, the LHCS method is a more efficient method to describe grain size distributions than Metropolis-Hastings sampling, particularly under low N (Figure 5.1). Nevertheless, Metropolis-Hastings sampling was used in this work to account for the inherent uncertainty of sizes of clay colloids during transport. Sizes of clay colloids may not follow the grain size distribution under alteration of chemical conditions or unexpected high hydrodynamic forces, which impacts the size of the clay cluster. The randomness of Metropolis-Hastings sampling at given CDF provides an implementation of the transport

simulation using random sizes of clay colloids or clay clusters in a reasonable range (Figure 5.1). Sampling in this work was performed within the 95% confidence interval of corresponding normal PDF for the target lognormal PDF in order to avoid physically unacceptable size ratios between sand and clay (i.e., $r_c/r_s > 1$ can occur for sampling without the confidence interval).



(a) Metropolis-Hastings algorithm

(b) LHCS method

Figure 5.1. Sampling under $N = 50$ using the Metropolis-Hastings algorithm and the LHCS method at the target lognormal CDF from the clay colloids grain size distribution, where μ and σ are mean and standard deviation of lognormally fitted target CDF, r_{c50} is the median value of sampled r_c , and R^2 is the coefficient of determination between the CDF and the experimental grain size distribution. The experimental grain size distribution was obtained by hydrometer test using Georgia kaolinite with ionic strength = 3×10^{-3} M (CaCl_2). Unexpectedly high r_{c50} was observed in this sampling for Metropolis-Hastings algorithm due to the relatively small N , while r_{c50} evaluated by LHCS method was almost identical to the r_{c50} in the lognormal CDF and well distributed to the target CDF, even under small N .

5.2.4 Numerical procedure

The governing equations presented in Equation (5-1) and (5-2) produce a nonlinear algebraic equation in the numerical scheme because C in Equation (5-1) and S in Equation (5-2) are dependent each other in each time step. Therefore, the Picard iteration (Celia et al. 1990; Huang et al. 1998) in each time step, which provided iterations until 0.1 % of accuracy for C in all discretized depths, was used to solve Equation (5-1) numerically. The number of iterations generally increased with an increase in k_{att} or k_{str} , which is attributed to increasing in nonlinearity caused by the large increment of S . The backward Euler scheme was used in the numerical calculation for the time marching equation with forward in time and centered in space at given initial and boundary conditions.

If the presented blocking theory is valid in colloidal attachment (i.e., the attachment between colloids in aqueous phase and attached colloids on the sand is neglected primarily due to identical surface charge characteristics of the colloid and the sand), then r_c and r_s sampled by Metropolis-Hastings algorithm or LHCS method at given N_{rc} and N_{rs} (N_{rc} and N_{rs} here indicate the sampling size for r_c and r_s respectively) may be applied independently to calculate $C_{ij}(z,t)$, where i and j indicate i^{th} sampled r_c and j^{th} sampled r_s respectively. To account for the independent calculation for any sampled r_c or r_s , a uniform distribution for the probability of r_c or r_s was used. This uniform distribution is valid because the target CDF is from mass-based grain size distribution. Hence, total inlet mass-based concentration of colloids at any given time ($C_0(t)$) can be decomposed to the inlet boundary concentration of colloids for i^{th} r_c and j^{th} r_s ($C_{0ij}(t)$):

$$C_{0ij}(t) = C_0(t)p(r_c)p(r_s) = C_0(t) \frac{1}{N_{rc}} \frac{1}{N_{rs}}. \quad (5-9)$$

Using a backward Euler method, Equation (5-1) can be rewritten as:

$$n^{q+1} \frac{C_{ij}^{q+1} - C_{ij}^q}{\Delta t} = -U \frac{\partial C_{ij}^{q+1}}{\partial z} + \frac{\partial}{\partial z} \left(n^{q+1} D_{ij} \frac{\partial C_{ij}^{q+1}}{\partial z} \right) - n^{q+1} (k_{att})_{ij} \psi_{att}^{q+1} C_{ij}^{q+1} + \rho_b (k_{det})_{ij} (S_{att})_{ij}^{q+1} - n^{q+1} (k_{str})_{ij} (\psi_{str})_j C_{ij}^{q+1}. \quad (5-10)$$

Note that the U and the ρ_b are independent to the sampled r_c or r_s because all simulations were under constant flow rate and the identical sand medium. k_{att} and k_{str} both can be expressed as a function of r_c and r_s (Equation (3-7) and (5-4), η_0 in Equation (5-4) was determined from r_c and r_s , which led to k_{att} values as a function of r_c and r_s : see details in Tufenkji and Elimelech (2004) for the η_0 calculation), and ψ_{str} is expressed here as a function of sampled diameter of sand d_s ($d_s = 2 \times r_s$) to replace d_{s50} in Equation (3-6). In addition, the dispersion coefficient D, which is obtained from the empirical equations proposed by Delgado (2007), is expressed as a function of r_c and r_s . The equations presented in Delgado (2007) provide the value of empirical longitudinal dispersivity according to normalized numbers such as the Peclet number and Reynolds number (details in Delgado (2007)).

The ψ_{att} and n in Equation (5-10) was globally updated every time step without reflecting the number of sampled r_c and r_s (note that ψ_{att} and n is expressed as ψ_{att}^{q+1} and n^{q+1} in Equation (5-10) respectively without i and j). Numerically, S_{att} may severely be overestimated if ψ_{att} is updated independently for every r_c and r_s based on $(S_{att})_{ij}$, because ψ_{att} still remains roughly 1 until the end of time even under large S_{att} (inlet boundary concentration of colloids $C_{0ij}(t)$ decreases as N_{rc} or N_{rs} increases as presented in Equation

(5-9)). This large ψ_{att} value under large S_{att} is not valid in order to take the blocking effect into account as presented in Equation (3-8). Therefore, for physically realistic colloid transport in the separate calculations, ψ_{att} should globally be updated, which can be obtained by the summation of $(S_{att})_{ij}$ in each time step. In addition, porosity n should also be updated globally for the calculation in next time step:

$$n(z,t) = \frac{n_0 G_c - G_s (1 - n_0) \sum_i \sum_j ((S_{str}(z,t))_{ij} + (S_{att}(z,t))_{ij})}{G_c} \quad (5-11)$$

where G_c (-) and G_s (-) are the specific gravity values of clay and sand respectively, and n_0 (-) is the initial porosity of sand medium. Note that r_{c50} and r_{s50} were adopted for S_{max} calculation in Equation (3-9) herein to be consistent with taking ψ_{att} as a global function.

η_0 in Equation (5-4) is defined as the ratio between the rate of colloid successful collision with a single grain and the rate of approach advective colloid flux to the projected area of the grain (Yao et al. 1971; Rajagopalan and Tian 1976). Therefore, it is physically unrealistic that the single collector collision is larger than 1 (the rate of colloids collision should be equal or smaller than the rate of colloid flux). However, η_0 is occasionally larger than 1 based on the calculation of relatively high r_c / r_s ratio. Hence, any η_0 larger than 1 caused by the high size ratio was set equal to 1. In addition, $(k_{det})_{ij}$ was assumed to $0.05 \times (k_{att})_{ij}$ for all simulations implemented in this work. Example figures for $(k_{att})_{ij}$ and $(k_{str})_{ij}$ are illustrated in Figure 5.2.

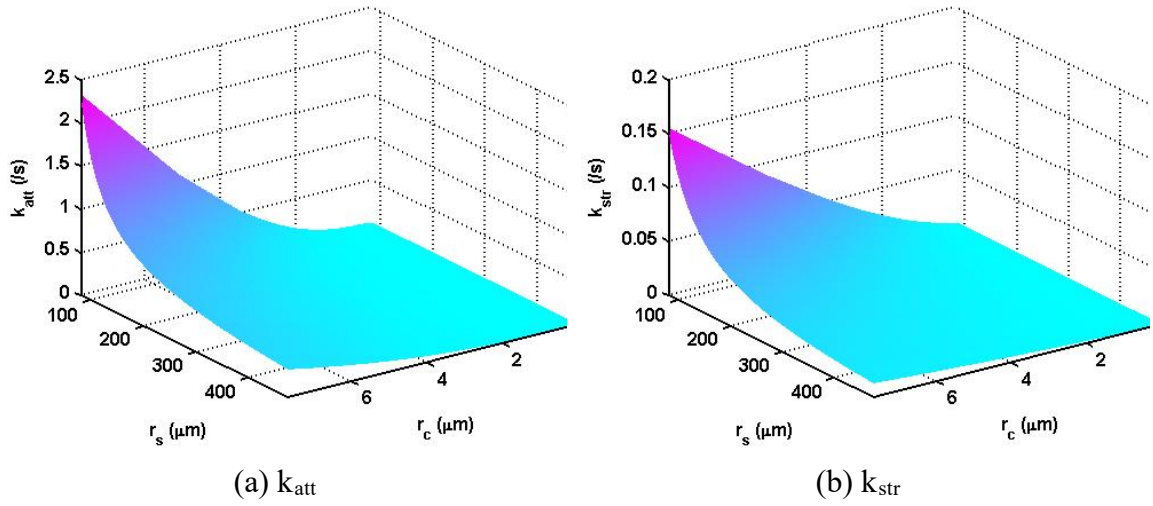


Figure 5.2. Example calculation of k_{att} and k_{str} as a function of r_c and r_s when $N_{rc} = N_{rs} = 1000$. Both k_{att} and k_{str} nonlinearly increase as r_c / r_s ratio decreases. The target lognormal PDFs used in the calculation were $\mu_s = 5.17$, $\sigma_s = 0.34$, $\mu_c = -0.93$, and $\sigma_c = 1.52$ (μ and σ indicate mean and standard deviation of normal PDF corresponding to the target lognormal PDF, subscript $s = \text{sand}$, $c = \text{clay}$), $r_{c50} \approx 0.47 \mu\text{m}$, and $r_{s50} \approx 181.27 \mu\text{m}$. The Metropolis-Hastings algorithm was used for sampling here.

5.3 Results and discussion

5.3.1 Simulated RP with experimental result

To demonstrate the validity of the outlined model quantitatively, the simulated retention profile was plotted with the experimental retention profile obtained through soil column experiments, using Georgia kaolinite as the clay colloidal medium, and ASTM 20/30 as the sand medium. The procedure of experiment was as follows: 10 pore volumes (PV) of kaolinite suspension at a concentration of $1 \times 10^{-3} \text{ g} / \text{cm}^3$ was injected into the sand column, (30.48 cm in length). A constant Darcy velocity of $U = 7.3 \times 10^{-2} \text{ cm} / \text{s}$ was applied at the top of the column and was controlled by a peristaltic pump, and the suspension was stirred continuously by a magnetic stirrer during the injection to prevent

the kaolinite colloids from settling. After the injection, the amount of retained kaolinite colloids was evaluated from the retained mass of kaolinite in every 2.54 cm depth of sand. In the column test, CaCl_2 was used as the background electrolyte with $\text{IS} = 3 \times 10^{-3} \text{ M}$.

To sample r_c and r_s consistently with the experimental conditions, target CDFs for sand and clay were obtained based on the results of sieve analysis for the ASTM 20/30 sand and the hydrometer test for kaolinite. To account for the size variation of clay clusters under different IS, the grain size distribution of kaolinite with $\text{IS} = 3 \times 10^{-3} \text{ M}$ was selected. Note that selecting the grain size distribution for perfectly dispersed kaolinite colloids may not represent the experimental condition because of their aggregating characteristics (Figure 5.3a). In contrast, the grain size distribution of ASTM 20/30 exhibited a highly uniform size of sand, and r_s was fixed to the median size of the experimental grain size distribution for the sand in the simulations presented in Figure 5.3 (i.e., $N_{rs} = 1$).

Prediction of the retention profile using the sampled r_c from the grain size distribution with $\text{IS} = 3 \times 10^{-3} \text{ M}$ (colloids were in the flocculated state) was comparable to the experimentally observed retention profile (Figure 5.3). However, the sampled r_c from the grain size distribution measured with the dispersant (colloids were dispersed as individual particles) underestimated the amount of retained clay colloids within the column. The discrepancy between these two simulated retention profiles is attributed to an increase in the k_{att} and k_{str} values as the size ratio increased (Figure 5.2); that is, the larger values of k_{att} and k_{str} for the flocculated conditions led to increased colloid retention, which more accurately reflected experimental conditions. These results demonstrate that the solution chemistry and aggregating behavior of clay colloids must be included to properly predict

retention profiles of clay within sand filtration media. Note that dispersed conditions for kaolinite are encountered under conditions of conditions of pH $\sim > 7.2$ (Palomino and Santamarina 2005). These results also indicate that predicting the retention profile of clay colloids is challenging, particularly under heterogeneous solution chemistry or changing geochemical conditions (e.g., de-icing salt runoff in winter conditions) due to significant changes in the size of clay clusters that form during transport. To investigate the uncertainty of the retention profiles, further simulations were performed using the grain size distribution with dispersant up to 10 PV under $C_0 = 1 \text{ g / L}$.

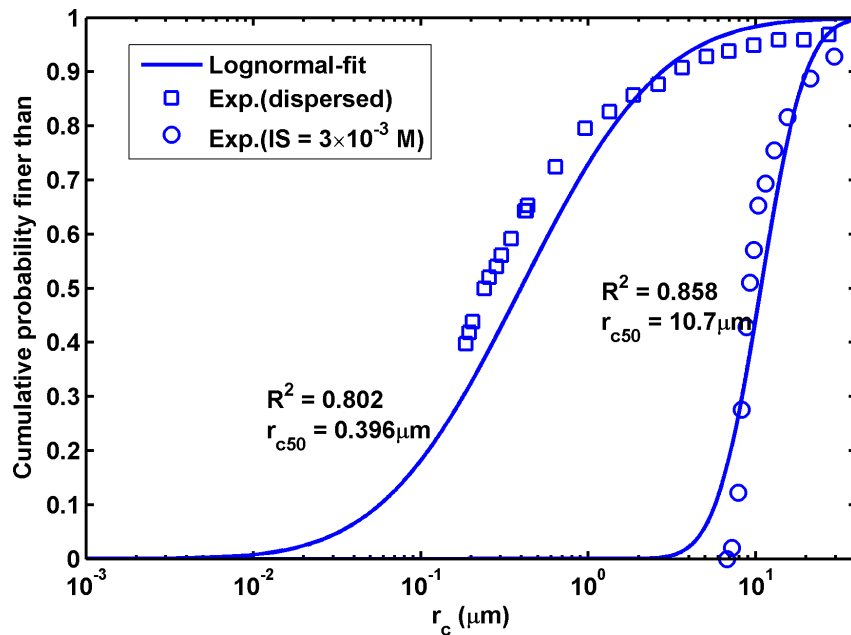


Figure 5.3. Experimental GSDs and corresponding target CDFs.

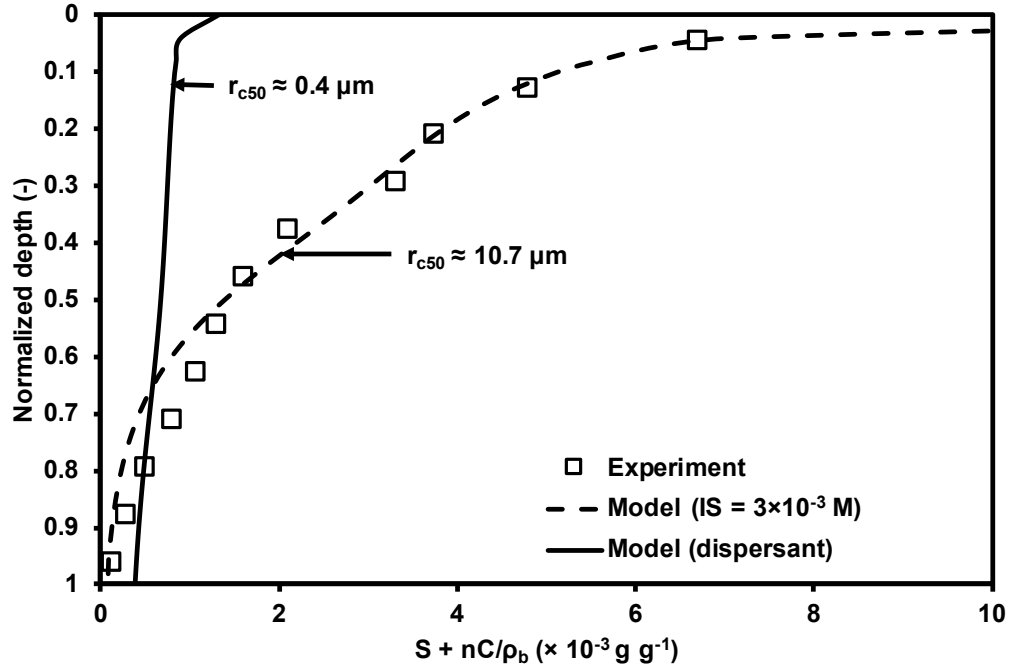


Figure 5.4. Observed and simulated RPs until 10 PV for dispersed kaolinite colloids and kaolinite cluster. Note that observed RP for the dispersed system is not available, Metropolis-Hastings algorithm used here with $N_{rc} = 10^4$ and $N_{rs} = 1$, and $r_{s50} = 360 \mu\text{m}$, $U = 7.3 \times 10^{-2} \text{ cm / s}$, $n_0 = 0.365$.

5.3.2 Uncertainty of RP using Metropolis-Hastings algorithm

The uncertainty of the retention profile caused by random sizes of clay colloidal flocs was investigated, where r_c was sampled by the Metropolis-Hastings algorithm at the given target CDF. To consider the randomness of sampled r_c in the simulation, N_{rc} was fixed to 100 in order to use the random nature of the Metropolis-Hastings algorithm (Figure 5.1). The low number for N_{rc} here was because the larger number of N_{rc} ($> 10^4$) led to a complete representation of the target CDF by sampled r_c and the Metropolis-Hastings sampling and the LHCS method showed an analogous result for large N_{rc} . In Metropolis-Hastings sampling, a starting point of sampling was fixed to

μ_c for avoiding the burn-in period and having equal probabilities of jumping in $r_c < \exp(\mu_c)$ and $r_c > \exp(\mu_c)$ in the first iteration of the sampling. One hundred sets of simulations were performed with $N_{rc} = 100$, which satisfied the average of $C_0 \sim 1 \text{ g / cm}^3$ and showed the median value of r_{c50} equal to target CDF (Figure 5.5).

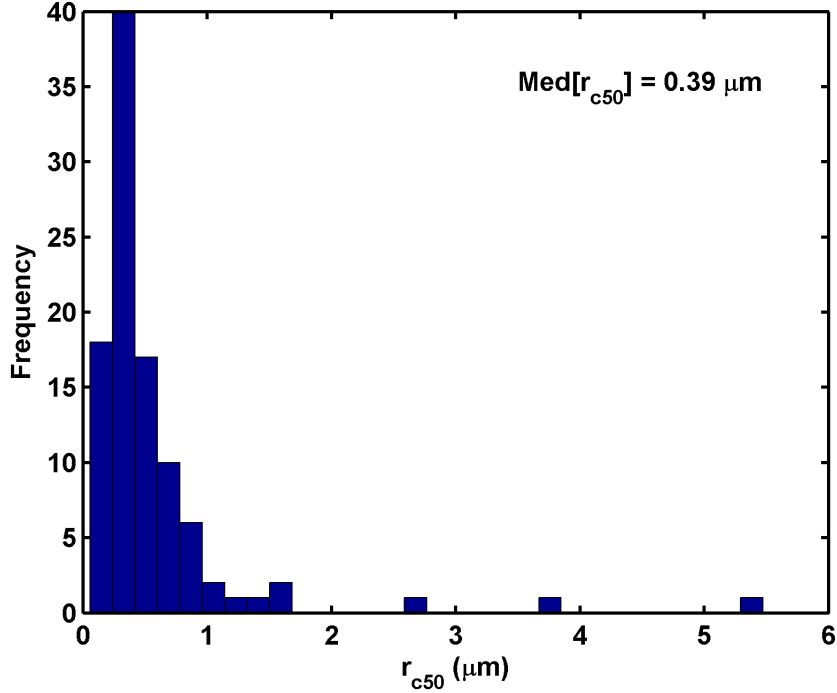


Figure 5.5. The histogram of r_{c50} in 100 sets of random sampling using the Metropolis-Hastings algorithm when $N_{rc} = 100$. The median value of r_{c50} ($\text{Med}[r_{c50}]$) is almost equal to the median value of the target CDF ($\approx 0.4 \mu\text{m}$, Figure 5.3), which indicates that the combination of 100 set of sampling is well distributed to the target CDF without biased toward the one direction.

Figure 5.5 represents the frequency of r_{c50} in each set of sampling with $N_{rc} = 100$ using Metropolis-Hastings algorithm. r_{c50} in seventy-five sets was less than $0.6 \mu\text{m}$, while r_{c50} in twenty-five sets were larger than $0.6 \mu\text{m}$. In the extreme case, r_{c50} used in one

particular simulation ranged between 5 μm and 6 μm and r_{c50} values in three sets were larger than 2 μm . Consequently, sampled r_c with large r_{c50} results in large retention profiles (Figure 5.6). The large r_{c50} values in the simulation for colloid transport reflected the uncertainty of r_c in the retention behavior. The maximum retention profile in Figure 5.6 (when 5 $\mu\text{m} < r_{c50} < 6 \mu\text{m}$, Figure 5.5) might significantly overestimate the retention profile at a given CDF, but 99 % of the whisker lines in each depth indicated that large uncertainty still existed behind the retention of clay colloids.

The box plot in each discretized space (Figure 5.6) is at least qualitatively consistent with the histogram in Figure 5.5. They are similarly shaped, with lognormal distribution, because the mean value of the histogram in Figure 5.5 is bigger than $\text{Med}[r_{c50}]$ and the mean values of the retention profile are bigger than the median values of the retention profile in all discretized depths (median values of box plots are also not located in the center). This implies that the randomness of the retention profile in each depth may qualitatively follow the grain size distribution of clay colloids (Figure 5.4), and the large C_u of the clay colloids leads to large uncertainty in the retention profile.

From a mathematical standpoint, α increases almost linearly with an increase in r_c because of the perfect linear relation between α and Φ_{sec} in the DLVO calculation (Equation (2-1)), while η_0 decreases until $r_c \approx 0.3 \mu\text{m}$ and exponentially increases after r_c is bigger than 0.3 μm (Figure 5.7). This initial decreasing of η_0 is caused by the large collision efficiency induced by diffusion, with relatively small r_c and η_0 profile (Figure 5.7), and is qualitatively consistent with the literature (Auset and Keller 2006; Tufenkji and Elimelech 2004). The decrease of η_0 and increase in α in $r_c < 0.3 \mu\text{m}$ led to a slow increase

in k_{att} , whereas k_{str} was not impacted by α or η_0 and gradually increased with increasing r_c / r_s ratio (Equation (3-7)). Therefore, the retention profiles evaluated by sampled r_c less than $0.3 \mu\text{m}$ resulted in extremely small retention profiles (Figure 5.5). If sampled r_c values were larger than $0.3 \mu\text{m}$, the effect of a slow increase in k_{att} would vanish under this particular condition.

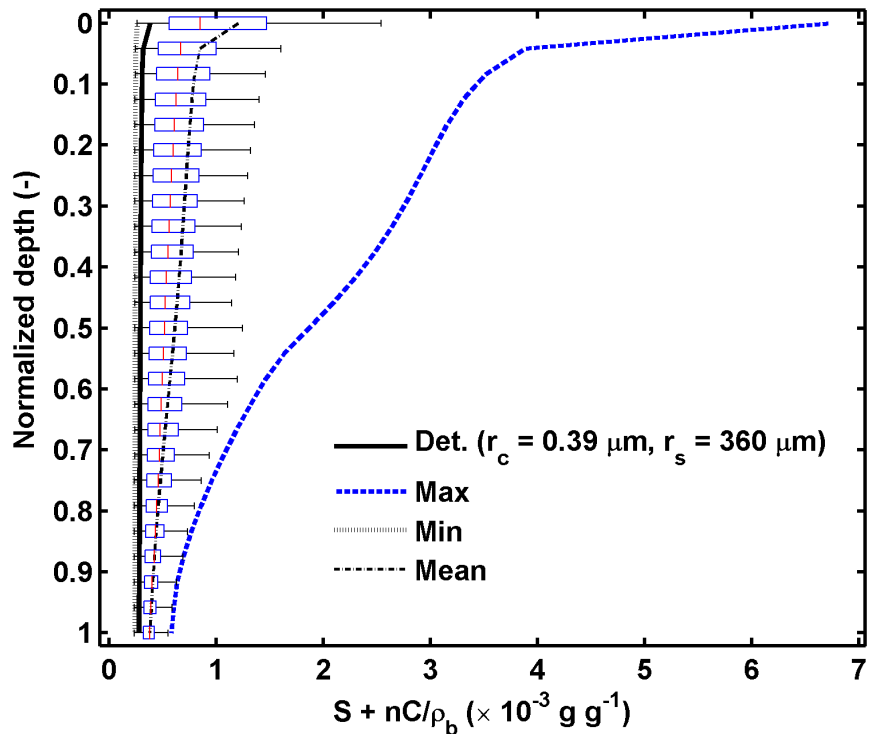


Figure 5.6. Maximum, minimum, and mean of simulated retention profile along with the box plot and retention profile from deterministic r_c and r_s (i.e. $N_{rc} = N_{rs} = 1$) with respect to 100 sets of sampled r_c (Figure 5.5). The edges of the boxes correspond to 25% and 75% coverage, and the central line in the boxes represents the median value of retained colloids

in each discretized spatial point. The whisker line of each box plot indicates 99 % coverage for a distribution in each depth.

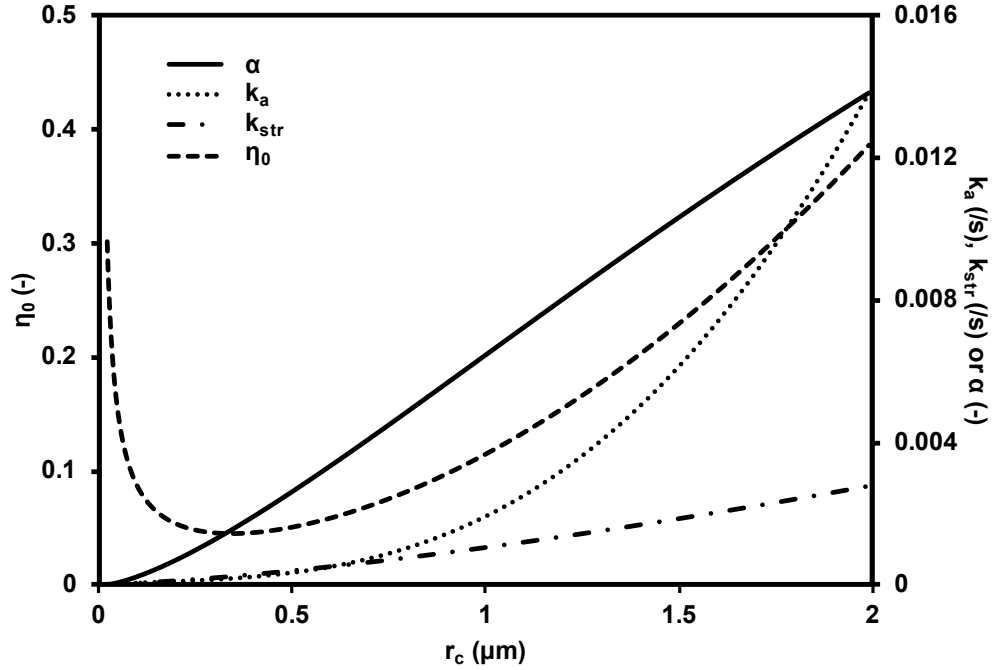


Figure 5.7. Variation of k_{att} (Equation (5-4)), k_{str} (Equation (3-7)), α (Equation (5-5)) and η_0 according to r_c . All other parameters (e.g. r_s , v_s , A_{swc}) in the calculation remain constant except the parameters change as a function of r_c (e.g. D_∞ , G_{DL} , G_{VDW} , where D_∞ (L^2T^{-1}) is the bulk diffusion coefficient).

In addition, the retention profile evaluated by the deterministic approach (i.e., $N_{rc} = N_{rs} = 1$, Figure 5.6) was much lower than the mean or median retention profile. $Med[r_{c50}]$ in Figure 5.5 was used in the deterministic calculation, indicating that the deterministic approach significantly underestimated the retention profile. The median retention profile (Figure 5.6) was more likely to appear for the polydispersed-clay colloids. The variation

of the deterministic retention profile and the median retention profile was less significant as C_u of the clay colloids decreased (discussed in the sensitivity analysis, next section).

5.3.3 Sensitivity analysis

As mentioned earlier, the C_u of a soil can range from 1 (uniformly graded particle size) to higher than 10 (well-graded particle size). Setting $\sigma_c \approx 1.52$ ($\mu_c \approx -0.93$) for the target CDF (Figure 5.6) corresponds to $C_u \approx 10$, which represents a well-graded soil. Therefore, in order to investigate the effect of grain size distribution shape on retention profile under constant μ_c (i.e., constant r_{c50}), a sensitivity analysis was performed with σ_c (or σ_s) = 1.5, 1.4, 1.2, 1.0, 0.5 and 0.1, which correspond to $C_u = 10, 8.57, 6.3, 4.64, 2.15$ and 1.16 (almost perfectly uniform). The LHCS method was utilized as the sampling technique for all simulations in the sensitivity analysis in order to represent grain size distributions effectively for sand and clay under the relatively small sampling size (see Figure 5.1).

Figure 5.8 and Figure 5.9 illustrate the simulated retention profiles and breakthrough curves according to the σ_c under identical r_{c50} and r_{s50} ($\sigma_s = 0$). The LHCS method provided $r_{c50} = \exp(\mu_c)$, regardless of the sampling size, which was in contrast to the randomness of sampling in the Metropolis-Hastings algorithm (Figure 5.5). Therefore, the LHCS method ensured the reproducibility of the retention profiles and the breakthrough curves under a particular σ_c . Retention profiles and breakthrough curves approached the deterministic values as σ_c decreased. In other words, the deterministic retention profile was more underestimated and the deterministic breakthrough curve was more overestimated as

the grain size distribution of the clay colloids was better distributed. The inconsistency of retention profiles and breakthrough curves according to σ_c revealed that the grain size distribution of clay colloids should be considered as an important factor for the transport/retention behavior of clay colloids in porous media. For example, the overestimation of the breakthrough curve by the deterministic approach (Figure 5.9) may result in the overestimated transport of contaminants that are favorably adsorbed by clay colloids. Likewise, the underestimation of the retention profile by the deterministic approach led to the underestimation of the reduction of hydraulic conductivity in the sand medium.

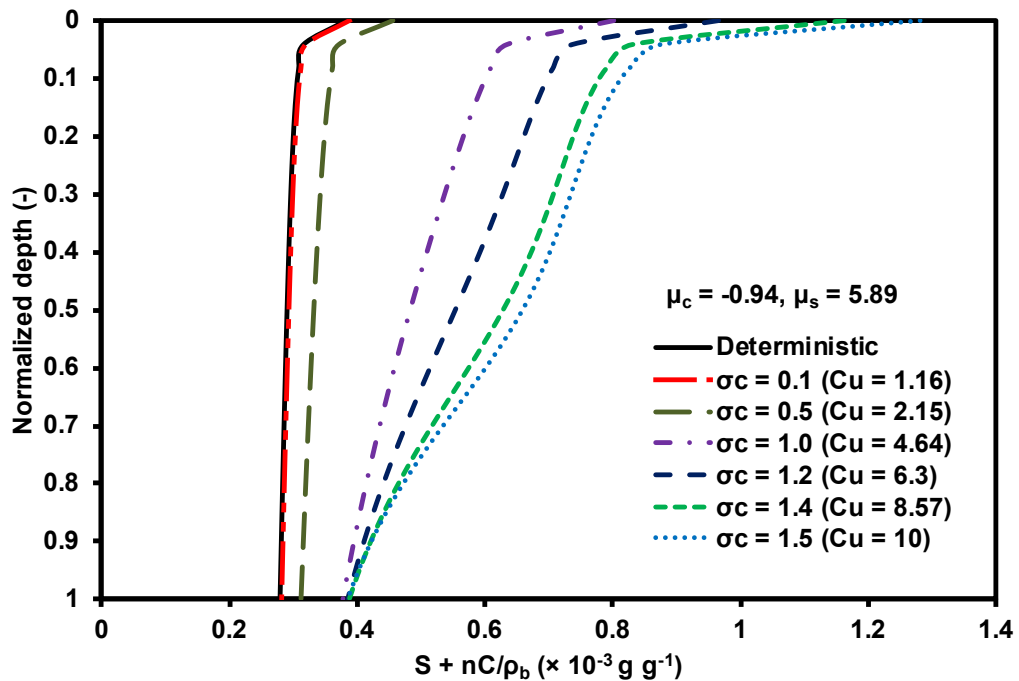


Figure 5.8. Simulated retention profiles according to the different σ_c (or C_u) under constant μ_c and μ_s (i.e. r_{c50} and r_{s50}). LHCS method was used here with $N_{rc} = 1000$ and $N_{rs} = 1$ (again, $r_s = 360 \mu\text{m}$).

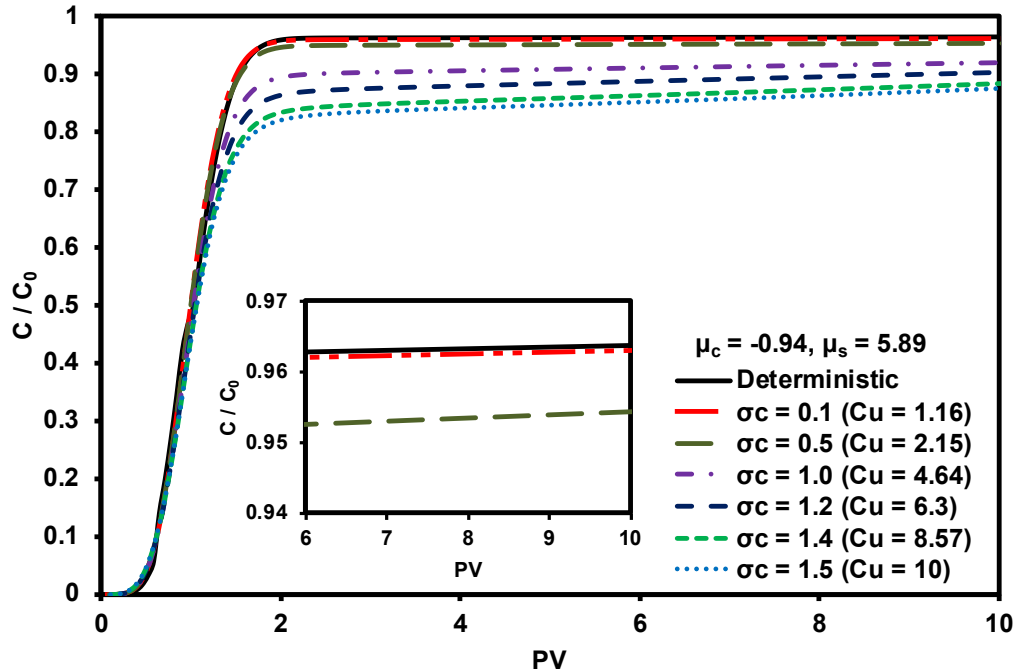


Figure 5.9. Simulated breakthrough curves according to the different σ_c (or C_u) under constant μ_c and μ_s .

The variation of the retention profiles or breakthrough curves between the deterministic and the stochastic approaches might be altered according to the r_{c50} / r_{s50} ratio and the polydispersity of colloids and sand. The retention profiles and the breakthrough curves presented in Figure 4 and Figure 5 were performed under $r_{c50} / r_{s50} \sim 0.001$ and $N_{rs} = 1$, which cannot represent various r_{c50} / r_{s50} ratios and the polydispersity of sand; consequently, the retention profiles were evaluated under three sampling conditions: 1) N_{rc}

= 1 and $N_{rs} = 10^3$, 2) $N_{rc} = 10^3$ and $N_{rs} = 1$, and 3) $N_{rc} = 10^2$ and $N_{rs} = 10^2$. In order to investigate the variation of the amount of retained colloids, the total amount of retained colloids in all discretized depths (S_{sum}) in six r_{c50} / r_{s50} ratios were normalized by S_{sum} in the corresponding ratio in the deterministic approach (Figure 6). The LHCS method was employed here with $u_m = 0.5$ in Equation (11) for the reproducibility of results, and both σ_c and σ_s were equal to 1 in all simulations.

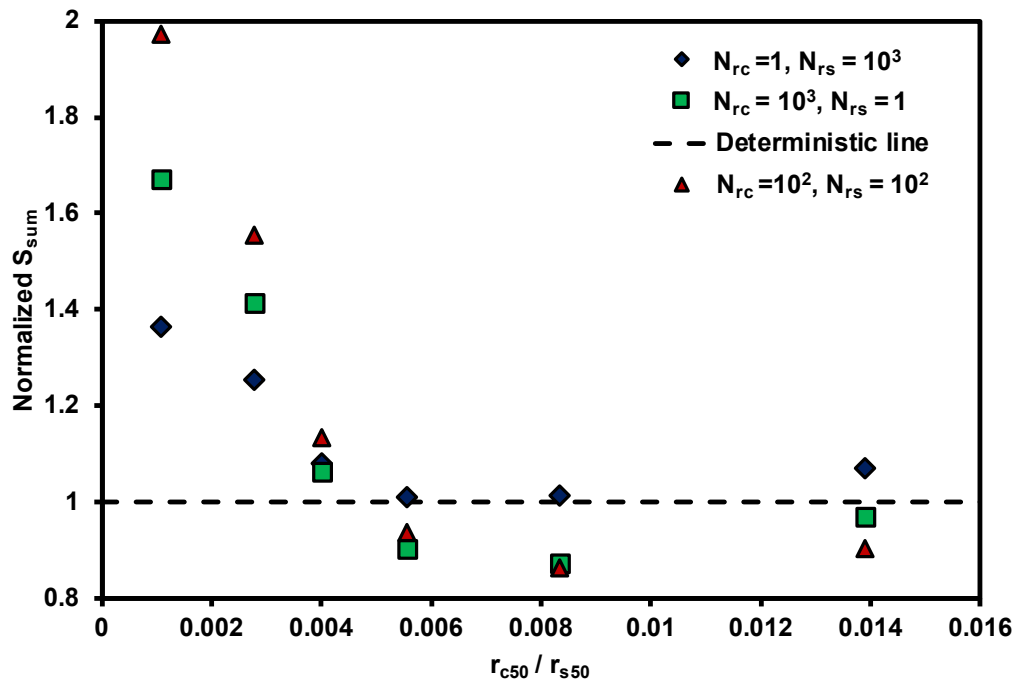


Figure 5.10. Normalized S_{sum} according to r_{c50} / r_{s50} ratios under three different simulated conditions.

The trend of normalized S_{sum} according to the r_{c50} / r_{s50} ratio in the three sampling conditions was comparable. In addition, values of normalized S_{sum} were larger than 1 in the three sampling conditions for all r_{c50} / r_{s50} ratios except $r_{c50} / r_{s50} > 5.6 \times 10^{-3}$ in $N_{rc} =$

10^3 , $N_{rs} = 1$ and $N_{rc} = 10^2$, $N_{rs} = 10^2$. Most of the colloids retained at high r_{c50} / r_{s50} ratio in both deterministic and stochastic approach, leading to less difference under relatively high r_{c50} / r_{s50} ratio. Therefore, the deterministic approach significantly underestimated the amount of retained colloids, particularly under low r_{c50} / r_{s50} ratio (Figure 5.10). Moreover, the result demonstrated that the underestimation of normalized S_{sum} in the deterministic approach was most significant when $N_{rc} = N_{rs} = 100$. This indicated that the polydispersed characteristics of clay and sand should be reflected in the analysis instead of reflecting the that of only one material. Note that the values of normalized S_{sum} in Figure 5.10 for $N_{rc} = 10^2$ and $N_{rs} = 10^2$ were underestimated for $r_{c50} / r_{s50} \geq 0.0056$ because of the applied restriction in the simulation: any sampled r_s smaller than 10 times of maximum sampled r_c was set equal to 10 times of maximum sampled r_c .

The limitation of the model used in this work was the failure to calculate k_{det} in Equation (3-5) analytically and the assumption of $k_{det} = 0.05k_{att}$ in all simulations. Calculation of torque for the detachment mechanism was performed based on the model proposed by Bergendahl and Grasso (2000), assuming that the hydrodynamic drag force was the primary detachment mechanism that caused the rolling of colloids on the sand surface (Bergendahl and Grasso 1998; Tsai et al. 1991). However, the calculation result revealed that the applied torque (T_{app}) was always bigger than the resistance torque (T_{res}) by several orders of magnitude (in all range of r_c/r_s and $U = 7.3 \times 10^{-2}$ cm / s), which was consistent with the result presented in Bradford et al. (2007). Even if $T_{res} > T_{app}$ for some sampled r_c , no method was available for converting the result of torque calculation into k_{det} in Equation (3-5). In addition, the shape of clay colloids or clusters and sand were not spherical as assumed in this work and the numerical calculation implemented in this work

may not be valid if clay colloids interact with each other during transport/retention. To account for the above limitations, additional work may be required.

5.4 Summary

This study explored the inherent uncertainty in clay colloid transport/retention in a sand medium by developing the stochastic model. Two sampling techniques used to reflect the polydispersed characteristics of the colloids and the sands provided a possible range of retention profile and reflection of grain size distributions. Comparison between the resulting retention profiles that were evaluated by the deterministic and stochastic sizes for sand and clay revealed that the retention profile with single median sizes of sand and clay was significantly underestimated as grain size distribution of sand and clay were more widely distributed. This effect was more noticeable under relatively small r_{c50} / r_{s50} ratio, which represented a well-dispersed clay colloidal system (i.e., less aggregation of clay colloids). In addition, the high uncertainty of the retention profile under random sampling of r_c at given target CDF implied a wide range of retention profiles may potentially be a result if the aggregated sizes of clay colloids were not accessible. Therefore, the stochastic approach used in this work can be beneficial to account more realistically for the transport of polydispersed colloids such as clay.

**CHAPTER 6 ESTIMATION OF MACROSCALE PARAMETERS FOR
COLLOID TRANSPORT IN POROUS MEDIA USING PORE NETWORK
MODELING**

6.1 Introduction

The modeling of colloidal transport at the continuum scale is a useful in contaminant transport simulations. It is common to upscale laboratory measured values for colloidal transport in saturated porous media with first order coefficients introduced to the advection-dispersion equation in order to describe the mass transfer of colloids during the transport. Different studies have used two, three, or five rate coefficients to predict transport: for example, two rate coefficients were used to account for the attachment and detachment of colloids (Bradford et al. 2002; Harvey and Garabedian 1991), three rate coefficients were used to explain reversible and irreversible retention of colloids (Compère et al. 2001) or straining of colloids in addition to attachment and detachment (Bradford et al. 2003), and five rate coefficients were used to explain colloid retention in kinetic and equilibrium sites with inactivation (Schijven and Hassanizadeh 2000). These modified advection-dispersion type equations well explained and fitted the data obtained in the laboratory for any type of colloids. In addition, filtration theory has been widely used to explain colloid transport at the microscale level (Rajagopalan and Tien 1976; Tufenkji and Elimelech 2004; Yao et al. 1971). An evaluated single-collector efficiency in filtration theory is generally used to estimate the attachment rate coefficient (Bradford et al. 2003, 2011; Harvey and Garabedian 1991; Ryan and Elimelech 1996) or the filter coefficient in deep-bed filtration (Rege and Fogler 1988; Zamani and Maini 2009). These estimations

allow upscaling of the simulation of colloid transport from microscale to macroscale level by incorporating governing microscale parameters for colloid filtration.

Using continuum models and filtration theory is beneficial for predicting colloid transport because of their applicability for many different types of colloids and their ability to reflect physical interactions associated with colloid filtration (e.g., hydrodynamic force and van der Waals interactions). In addition, continuum models allow long-term large-scale numerical simulation of the colloid transport. However, experimental results are needed to back-calculate rate coefficients or attachment efficiency in these models in order to express the colloidal transport in different conditions (e.g., solution chemistry, flow rate, size ratio, etc.). Moreover, laboratory scale experiments have been mostly used in back-calculation, which may not represent large-scale porous media well due to their inherent heterogeneous properties. Those back-calculated coefficients may not be expressed as a function of pore size distribution of porous media or particle size distribution of the colloids, which limits their applicability. Therefore, investigating a relation between the soil properties and the rate coefficients embedded in the advection-dispersion equation is needed to more accurately predict the transport of colloids at large-scale.

Pore network models have been used extensively to reflect the heterogeneity of porous media in a simulation. Pore network models are computationally less expensive than other pore-scale simulations such as lattice Boltzmann method and smoothed particle hydrodynamics (Raouf et al. 2013; Xiong et al. 2016), and they improve on the disadvantages of a macroscopic volume-averaged continuum model that originates from the absence of including the impact of microscopic features of porous media (Gostick et al.

2007). The ability to reflect microscopic features of porous media and properties of colloids are perhaps the main advantages of using pore network models for simulating colloid transport in porous media. In addition, pore network models allow tracking of individual colloids during transport, although it is computationally expensive, and it is capable of determining the representative volume of porous media for colloidal transport in a particular pore size distribution.

In this work, a three-dimensional cubic pore network model was constructed for simulating the colloid transport. By utilizing the pore network model, this work investigates the expression of first order coefficients in the continuum model as a function of pore size distribution of a sand medium and particle size distribution of colloids. To describe the two distributions in the network simulation, mean and standard deviation of proper lognormal distributions were used. In addition, the impact of mean and standard deviation of distributions on retention profiles and the reduction of hydraulic conductivity were examined. The size distributions of colloids in predicted retention profiles and breakthrough curves were further discussed to understand the process of colloidal transport at the pore-scale.

6.2 Model formulation

6.2.1 Network construction

The network model used in this work was constructed by using open-source project code OpenPNM, which is written in Python. OpenPNM was developed to simulate multiphase flow in porous media (Aghighi et al. 2016; Gostick et al. 2016; Tranter et al. 2016). A 3-dimensional simple cubic network was constructed to represent the sand

medium., and a cubic network was used for the efficiency of computational work and the effective description of transport process in the cubic network, which can be obtained by applying proper coordination number (Imdakh and Sahimi 1991; Rege and Fogler 1988). The applied coordination number (CN) in the model for describing the sand packing ranged from 5.4 - 5.5 in all simulations by randomly eliminating throats from the regular 3-dimensional cubic network (CN = 6 in the regular cubic network) (Valvatne et al. 2005). A distance between centers of pores in the network was set equal to the median grain size of sand (d_{50}), which is equivalent to the throat length of the pore network for uniform sand based on the geometry of the discrete element model as described in Zhang et al. (2013). The shapes of the pores and throats were assumed to be spheres and cylinders, respectively, and the diameters of the pores were initially determined at a given distribution and then evaluated lengths of throats subsequently as:

$$L_{ij} = D_{ij} - (d_{p(i)} + d_{p(j)}) / 2 \quad (6-1)$$

where L_{ij} (L) is the length of the throat between pore i and j, D_{ij} (L) is the Euclidean distance between centers of pore i and j, and d_p (L) is the diameter of the pore.

6.2.2 Calculation of fluid flow

Because all colloidal transport simulations in this work were performed in the saturated condition, single-phase flow was taken into account for the flow calculation in the network model. The Hagen-Poiseuille equation was used for calculating single-phase flow in a cylindrical tube (Dai and Seol 2014), where the hydraulic conductances of throats and half of pores are expressed as:

$$g_t = \frac{\pi d_t^4}{128 L \mu} \quad (6-2)$$

$$g_p = \frac{\pi d_p^4}{128 r_p \mu} = \frac{\pi d_p^3}{64 \mu} \quad (6-3)$$

where g_t ($M^{-1} L^4 T$) and g_p ($M^{-1} L^4 T$) are hydraulic conductances of throats and the half of pores respectively, d_t (L) is the diameter of throats, μ is the viscosity of fluid ($M L^{-1} T^{-1}$), and r_p (L) is the radius of pores. Using Equation (6-2) and (6-3), the hydraulic conductance of fluid between pore i and j (g_{ij}) can be obtained by the harmonic mean of three hydraulic conductances:

$$g_{ij} = \left(\frac{1}{g_{p(i)}} + \frac{1}{g_t} + \frac{1}{g_{p(j)}} \right)^{-1} \quad (6-4)$$

The flow rate between pore i and j (Q_{ij}) is obtained successively according to:

$$Q_{ij} = g_{ij} (P_i - P_j) \quad (6-5)$$

where P ($M L T^{-2}$) is the pressure at pores. Pressure values of each pore at given boundary conditions can be determined by solving a system of linear equations based on the mass conservation of fluid at all pores except the boundary pores. To simulate fluid flow from top to bottom, Dirichlet-type boundary conditions (specified pressure values) were applied at the top and bottom pores for the calibration of hydraulic conductivity (shown later) before injecting colloids into the network. During colloid injection, Neumann type boundary conditions (specified flow rate) were applied at bottom pores to evaluate the reduction of hydraulic conductivity (k) due to colloid retention under the constant flow rate. Colloid retention decreases d_t in Equation (6-2), and the hydraulic conductivity of the

network in each time step was evaluated using Darcy's equation from the total pressure drop of the model.

6.2.3 Sampling of colloids

Colloids were injected at top pores with a constant mass-based concentration in all simulations. Therefore, the proper number of colloids at the top pores, equivalent to the inlet concentration, was determined by the unit conversion using the volume and the density of colloids (shape of colloids was assumed spherical). The total number of colloids (N_c) to be sampled was obtained by:

$$N_c = \frac{V_{top} C_0}{4/3\pi\rho_s \exp(3\mu_c + 4.5\sigma_c)} \quad (6-6)$$

where V_{top} (L^3) is the total volume of top pores, C_0 ($M L^{-3}$) is the inlet concentration, ρ_s ($M L^{-3}$) is the density of the colloid, and μ_c and σ_c are respectively the mean and the standard deviation of lognormal distribution for the radius of colloids (r_c). Note that $\exp(3\mu_c + 4.5\sigma_c)$ in Equation (6-6) indicates the expected value of r_c^3 in lognormal distribution (the 3rd raw moment). After determining N_c , to sample colloids without replacement at the given distribution, Latin hypercube sampling was exploited. By using this sampling, the sampled r_c more accurately reflected the given distribution regardless of N_c . The cumulative probability of the m^{th} interval (P_m) by Latin hypercube sampling is given as:

$$P_m = \left(\frac{1}{N_c}\right)u_m + \left(\frac{m-1}{N_c}\right) \quad (6-7)$$

where m is an integer between 1 and N_c , and u_m is the m^{th} random number generated from 0 to 1. Using Equation (6-7), m sampled r_c corresponding to p_m values can be obtained by

inverting the cumulative distribution function. Note that u_m is fixed at 0.5 in all simulations to assure reproducibility of sampling and to eliminate randomness of sampling for the validity of N_c in Equation (6-6) ($\exp(3\mu_c + 4.5\sigma_c) \sim$ expected value of sampled r_c^3). A periodic boundary condition was applied at the top pores for the injection of colloids, and colloids were tracked individually during their transport in the network.

6.2.4 Colloids transport/retention in the network

The simultaneous transport of generated colloids between pores was obtained based on the corresponding mass transfer between pores in each time step. The amount of transferred mass from pore i to adjacent pores was calculated by flow rates of corresponding throats:

$$M_{ij} = C_i Q_{ij} \Delta t \left(\frac{L_{ij}}{L_{ref}} \right) \quad (6-8)$$

where M_{ij} (M) was transferred mass of colloids from pore i to pore j , C_i ($M L^{-3}$) was the concentration of colloids at pore i , Δt (T) was time for the one time step, and L_{ref} (L) was the reference length. Here, L_{ref} was employed to eliminate the error associated with mass transfer at pore-scale (M_{ij} is independent of L_{ij} at given Δt with an absence of (L_{ij} / L_{ref}) in Equation (6-8)). Note that Equation (6-8) is valid for pores adjacent to pore i only when $P_i > P_j$ (pore j can be multiple). By applying M_{ij} , the number of colloids moving from pore i to pore j in each time step was determined through unit conversion. Because of Q_{ij} in Equation (6-8), the concept used here for the colloids movement was analogous to the flow-biased probability concept presented in Yuan et al. (2012), which described the walking direction of particles based on the magnitude of flow rates at the neighboring throats. Colloids are regarded as retained at the throats if a random number between 0 and 1 for

each colloid was less than the capture probability (p_{cap}) which is expressed as (Hajra et al. 2002; Reddi et al. 2005):

$$P_{cap} = 4 \left[\left(\frac{\theta r_c}{r_t} \right)^2 - \left(\frac{\theta r_c}{r_t} \right)^3 \right] + \left(\frac{\theta r_c}{r_t} \right)^4 \quad (6-9)$$

where θ (-) is the lumped parameter which represents interparticle forces between colloids and sand grains, and r_t (L) the throat radius. To take the effect of water velocity at throats (v) into account, the lumped parameter, θ was expressed as:

$$\theta = \theta_0 \exp(-v/v_c) \quad (6-10)$$

where θ_0 (-) is a constant dependent on ionic strength or pH, and v_c (L T⁻¹) was the critical velocity to account for the velocity dependence of available deposition sites on a grain. Analytically, v_c is given by (Mackie et al. 1987):

$$v_c = \frac{A}{61.218\pi\mu h_0^2} \quad (6-11)$$

where A (M L² T⁻²) is the Hamaker constant, and h_0 (L) is the minimum separation distance. Because the network model was calibrated by experimental kaolinite retention profiles (as shown later), the Hamaker constant in silica sand-water-kaolinite system was used in all simulations, which was calculated by refractive indexes and dielectric constants of those materials (see detail, Israelachvili 2011). In addition, the interaction energy between sand and kaolinite was evaluated based on Derjaguin-Landau-Verwey-Overbeek (DLVO) theory. The result of the calculation (data not shown here) revealed that high energy barrier between sand and kaolinite colloids hinder the attachment of colloids at the primary minimum, which leads to the primary attachment at a secondary minimum (Bradford et al.

2011; Kuznar and Elimelech 2007; Litton and Olson 1996). Therefore, h_0 was set equal to the separation distance corresponding to the secondary minimum. As a result, v_c remained constant throughout the simulation at given conditions.

The retention of colloids caused a decrease in radius of throats and increase in pressure drop of the network. The pressure drop of the throat (ΔP_p) due to the retention of r_c was determined as (Happel and Howard 2012):

$$\Delta P_p = \frac{12\mu r_c U}{r_t^2} \left(1 - \left(1 - \frac{r_c}{r_t} \right)^2 \right)^2 K_1 \quad (6-12)$$

$$K_1 = \frac{1 - (2/3)(r_c/r_t)^2 - 0.202(r_c/r_t)^5}{1 - 2.105(r_c/r_t) + 2.086(r_c/r_t)^3 - 1.707(r_c/r_t)^5 + 0.726(r_c/r_t)^6} \quad (6-13)$$

where U ($L T^{-1}$) is the centerline velocity of throats ($= 2v$ for laminar pipe flow), and K_1 is the pore wall correction factor. The total pressure drop (ΔP_{total}) of the throat can be obtained by $\Delta P_{total} = \Delta P_{throat} + \Sigma \Delta P_p$. The new effective radius (r_{new}) for the calculation in next time step after N retained colloids is given by (Reddi et al. 2005):

$$\frac{1}{r_{new}^4} = \frac{1}{r_t^4} + \frac{0.75}{r_t^4} \sum_{i=1}^N \frac{r_c}{L} \left(1 - \left(1 - \frac{r_c}{r_t} \right)^2 \right)^2 K_1 \quad (6-14)$$

Note that the retention of colloids only takes place at throats, indicating that radius of pores are not affected by the retention and remain constant.

θ generally decreased as the amount of retained colloids increased under constant flow rate because of increase in v (r_t decreases as colloids retained). A flow chart of key features used for predicting colloid transport/retention is illustrated in Figure 6.1.

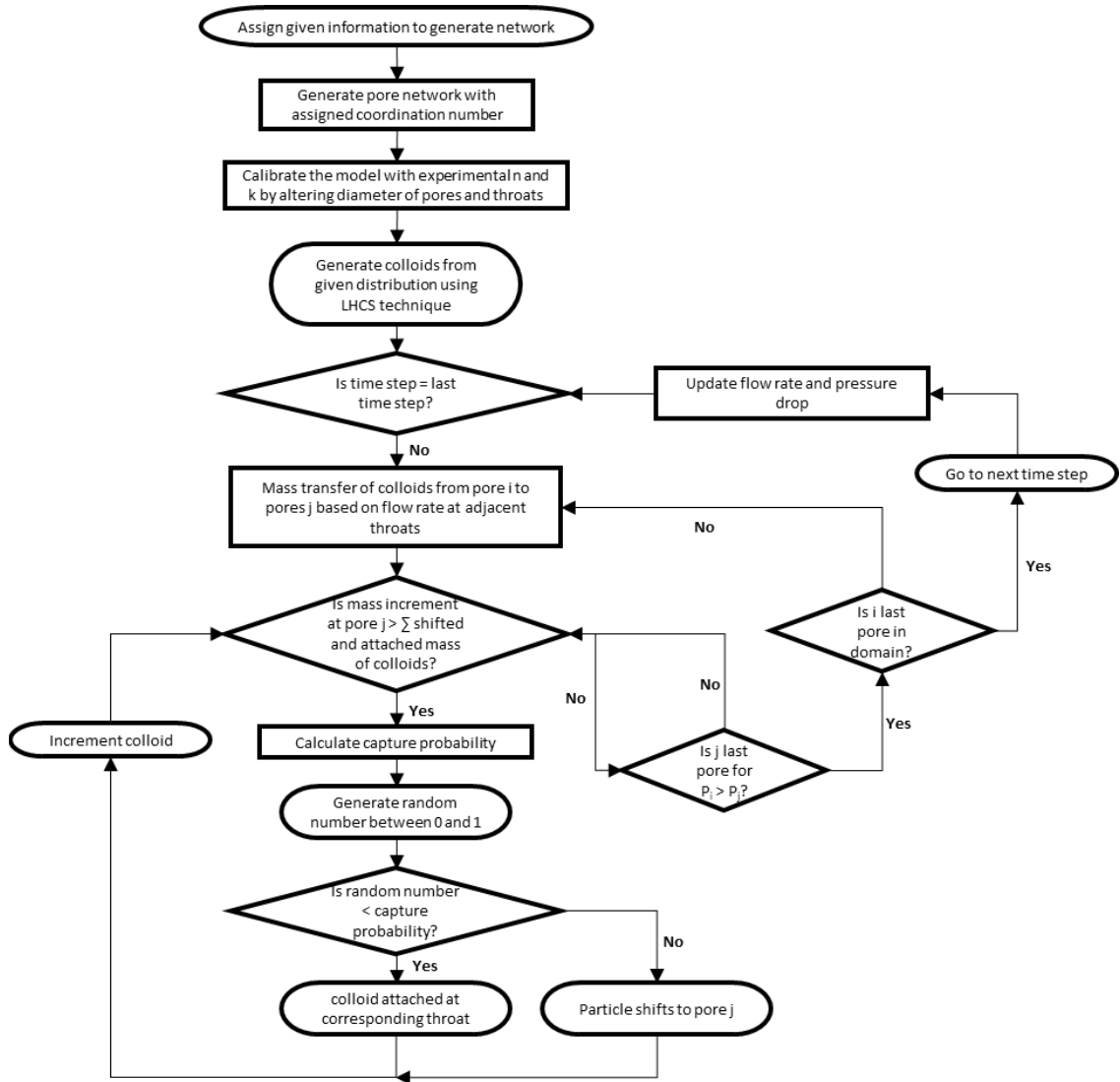


Figure 6.1. Flow chart describing key features of the model.

6.2.5 Continuum equation of colloids transport

The continuous macroscale model used in this work for describing colloid transport was an advection-dispersion equation with two first order coefficients to account for the attachment and the detachment of colloids:

$$\frac{\partial(nC)}{\partial t} = -\nabla \cdot J_T - nk_{att}\psi_{att}C + \rho_b k_{det}S_{att} \quad (6-15)$$

where n (-) is the porosity of the sand medium, C ($M L^{-3}$) is the colloid concentration in aqueous phase, t (T) is time, J_T ($M L^{-3} T^{-1}$) is the total colloid flux (sum of advective and dispersive fluxes), k_{att} (T^{-1}) and k_{det} (T^{-1}) are first order coefficients to account for attachment and detachment respectively, ψ_{att} is the dimensionless function for the attachment, ρ_b ($M L^{-3}$) is the bulk density of sand, and S_{att} ($M M^{-1}$) is the solid phase concentration of attached colloids.

The optimization analysis performed in this work yielded optimized first order coefficients at a given retention profile (RP) in the least square sense. Therefore, it may not be appropriate to find the trend for the colloid retention from optimized coefficients by including k_{str} to account for straining in Equation (3-5). The straining mechanism, which is defined as colloid immobilization due to the narrow throat size (Auset and Keller 2006; Bradford et al. 2007), is incorporated into k_{att} in Equation (3-5) in order to represent the retention of colloids by a single coefficient, k_{att} . Using a single coefficient for retention can effectively provide a relation between the coefficient and input parameters of the network model (colloid size distribution, pore and throat size distribution).

6.2.6 The size of the network and calibration of hydraulic conductivity (k)

Overestimation of the flow rate can be caused by the boundary effect of the network; consequently, to determine the minimum numbers of pores in the x and y axes (flow direction in z axis) to avoid overestimation, the hydraulic conductivity of the network under a various number of pores in the x and y axes (N_x and N_y) were evaluated. In addition, the effect of N_z (the number of pores in z axis) on the hydraulic conductivity was also investigated. The aspect ratio (AR, the ratio between the diameter of pores and the diameter of throats) was set to 2, the hydraulic gradient was 0.7, and CN was approximately 5.4 in this simulation. As seen in Figure 6.2, the hydraulic conductivity values were significantly impacted by N_x and N_y when $N_x = N_y < 10$, while the effect of N_z was negligible. By using the average value of hydraulic conductivity between $N_x=N_y=10$ and $N_x=N_y=40$ in the error calculation, $N_x=N_y=14$ was selected as a minimum network size to avoid boundary effects (mean absolute error $< 3\%$ for $N_x=N_y=14$). Therefore, $N_x=N_y=14$, and $N_z=40$ was selected as a size of the network in all simulations ($N_z = 40$ was selected to investigate the RP with depth, Figure 6.2).

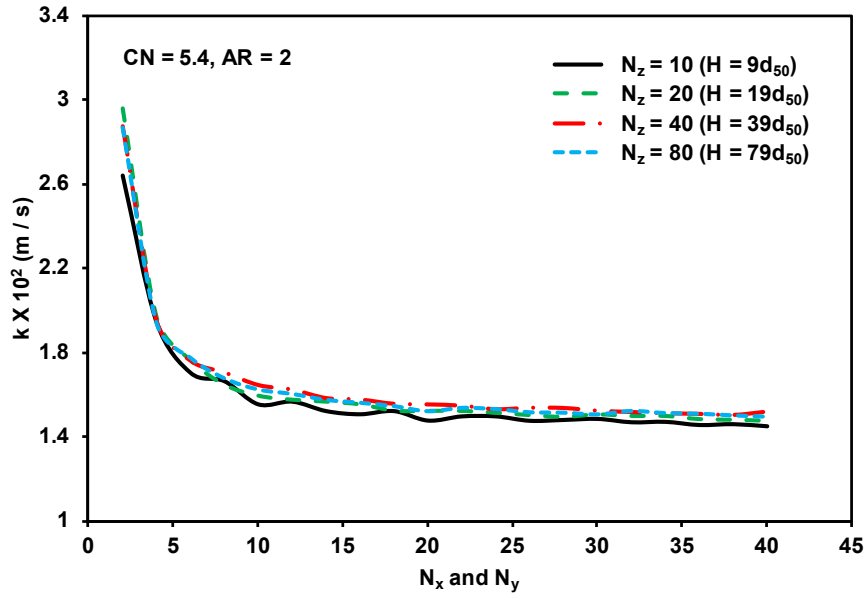


Figure 6.2. The effect of numbers of pores in x, y, and z axes (N_x , N_y , and N_z) on the hydraulic conductivity (k) of the network. Note that $N_x = N_y$ in this calculation.

In all simulations, the hydraulic conductivity of the network (k_{pnm}) was calibrated by increasing the aspect ratio until k_{pnm} reached the experimental k (k_{exp}) (Figure 6.4). The initial aspect ratio was set to 2 and the convergence criterion was set to 1 % of absolute error between k_{pnm} and k_{exp} . Because the throats were randomly eliminated until CN reached to ~ 5.4 , the calibration was performed in every simulation. Thus, Figure 6.4 presents a one representative calibration procedure. The value for hydraulic conductivity $k_{exp} = 0.283 \text{ cm} / \text{s}$ (Fleshman 2012) was used to represent densely packed ASTM 20/30 sand, which was used in all simulations.

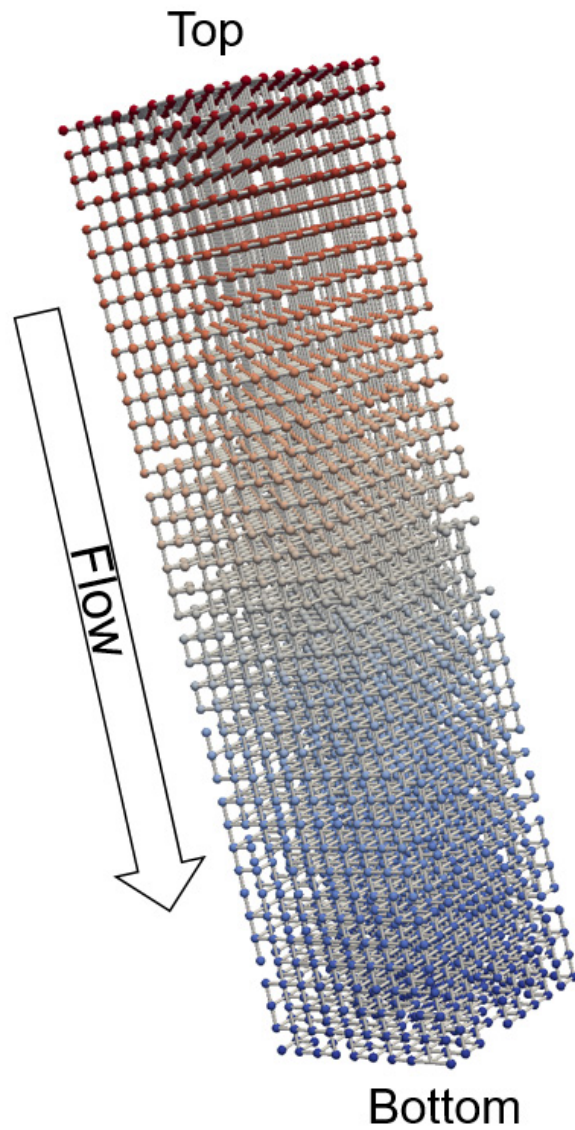


Figure 6.3. An example visualization of the regular cubic pore network used in this simulation. Colloid suspension was injected at the top of the network and part of throats were eliminated randomly until $CN \sim 5.4$. The color of pores indicates pressure values at pores from high (colored in red) to low (colored in blue).

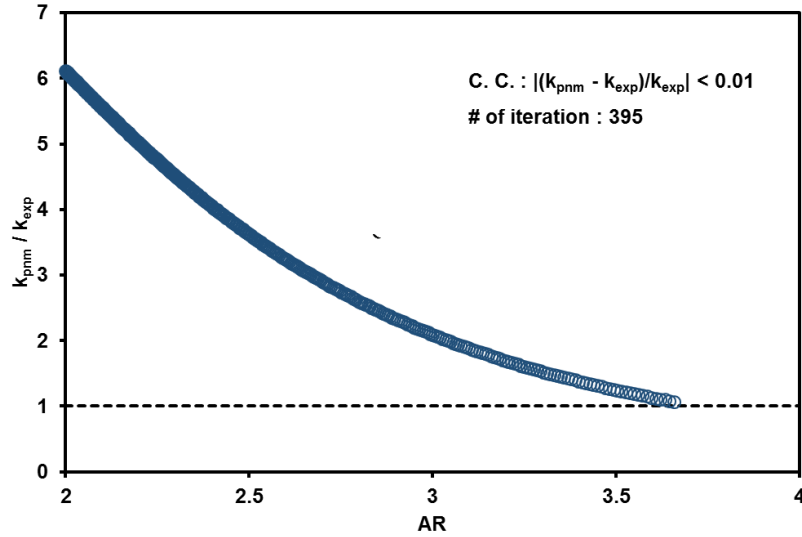


Figure 6.4. Calibration of the hydraulic conductivity of the network (k_{pnm}) to experimentally measured hydraulic conductivity (k_{exp}).

6.3 Results and discussion

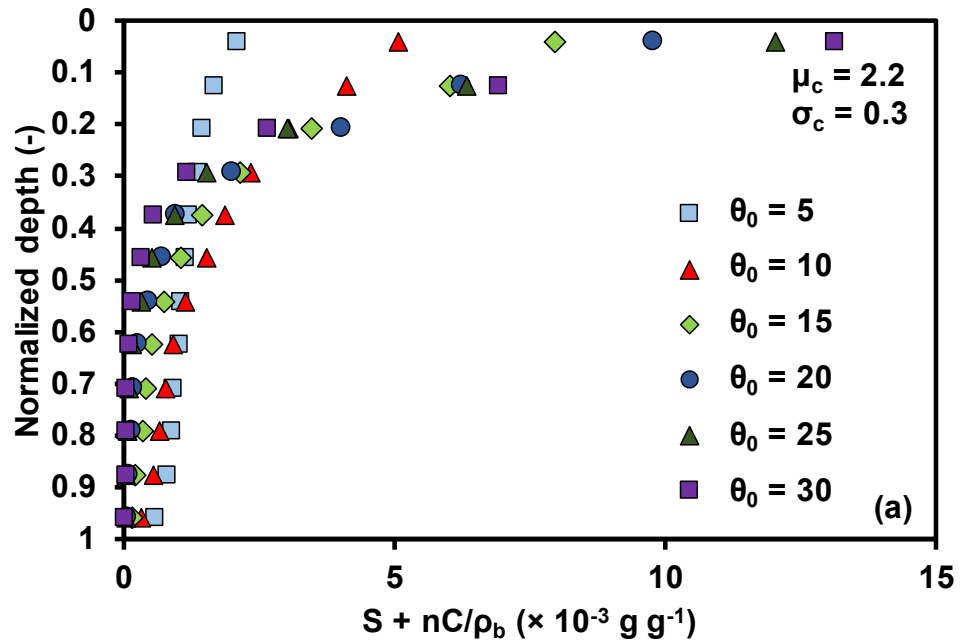
Simulations were performed under the following variables: three μ_c , four σ_c (Equation (6-6)), and six θ_0 (Equation (6-10)): $\mu_c = 1.3, 1.8, \text{ and } 2.2$, $\sigma_c = 0.01, 0.1, 0.2, \text{ and } 0.3$, and $\theta_0 = 2, 4, 6, 8, 10, \text{ and } 12$. The three μ_c values used in the simulation corresponded to the experimental median sizes of kaolinite colloids presented in Figure 3.2. Retention profiles, breakthrough curves, the reduction of hydraulic conductivity, and size distribution of colloids in the retention profiles and the breakthrough curves were evaluated for 72 cases. The mass-based concentration C_0 in Equation (6-6) was fixed at 1 g/L in all simulations.

6.3.1 *Effect of parameter θ_0 and particle size distribution of clay colloid (μ_c and σ_c)*

The retention profiles, breakthrough curves, and the reduction of hydraulic conductivity under varied θ_0 at given particle size distribution of colloid ($\mu_c = 2.2$ and $\sigma_c = 0.3$) are shown in Figure 6.5. An increase in θ_0 increased the amount of retained colloids and led to a more exponential retention profile due to an increase in the capture probability, as presented in Equation (6-9). The increase in capture probability resulted in a larger portion of colloids captured (or retained) at throats located at the inflow and allowed fewer colloids to penetrate deeper through a sand medium. This behavior reflected the retention profile at $\theta_0 = 30$ and a smaller amount of retained colloids at relatively deep positions (normalized depth > 0.5) was observed under $\theta_0 = 12$ than was observed under $\theta_0 = 6$. A larger amount of retained colloids in larger θ_0 led to lower C/C_0 in the breakthrough curve and lower K/K_0 during 10 pore volumes of flow (Figure 6.5(b) and Figure 6.5(c)). Almost no breakthrough was observed under $\theta_0 = 8, 10, \text{ and } 12$ (Figure 6.5(b)), and the reduction of hydraulic conductivity was more significant as θ_0 increased because of a more exponential retention profile at large θ_0 . Note that the results presented in this chapter are with an assumption of critical velocity (v_c in Equation (6-10)) equal to 0.18 cm/s (separation distance is assumed 5.2×10^{-7} cm, corresponding to the distance of kaolinite-water-sand system in 0.1 M monovalent salt solution). The θ_0 value for identical results might be significantly different depending on v_c , type of colloids, porous material, and solution chemistry used in the v_c calculation.

θ_0 physically represents the interaction energy between colloids and the sand grain: larger θ_0 values represent higher attractive energy (i.e., more favorable attachment). In addition, because θ_0 is an only one parameter representing all deposition mechanisms

(attachment and straining), large θ_0 also indicates a high chance for colloids to be retained by straining. Therefore, the results presented in Figure 6.5 are expected at given μ_c and σ_c . For clay colloid transport/retention in a sand medium, based on the experimental results presented in Chapter 3 and Chapter 4, large θ_0 values represent the solution chemistry of low pH and low ionic strength while low θ_0 values represent the condition of high pH and low ionic strength. Additional work may be needed to investigate the relation between θ_0 and solution chemistry for a particular colloid-porous media system.



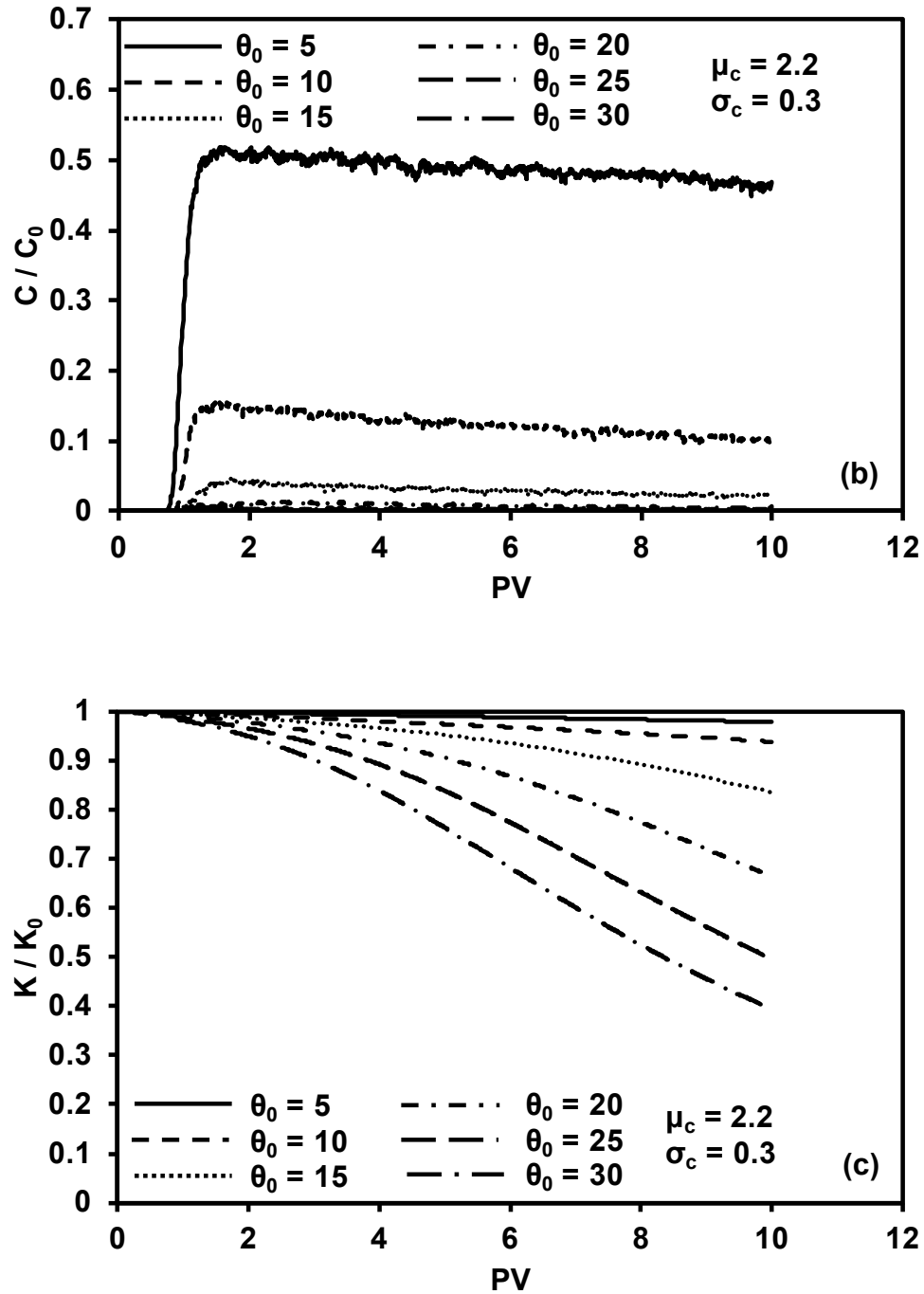


Figure 6.5. (a) Retention profiles after the injection, (b) breakthrough curves, and (c) the reduction of hydraulic conductivity during the injection under varied θ_0 at $\mu_c = 2.2$ and σ_c

= 0.01. $S+nC/\rho_b$ presented in (a) represents retained colloids in the solid phase (S) and aqueous phase (nC/ρ_b).

The bed efficiencies of colloids (β) and the final values of normalized hydraulic conductivity after injecting 10 pore volumes of flow of colloidal suspension under four σ_c was quantified (Figure 6.6). As θ_0 increased, β values asymptotically increased and K/K_0 at 10 pore volumes of flow asymptotically decreased. This implies that selecting θ_0 for modeling colloid transport under the condition of unfavorable retention (low β) is challenging due to the high sensitivity of β against θ_0 . At a given μ_c of colloids and θ_0 , as σ_c increased, β increased and K/K_0 at 10 pore volumes decreased. This trend of β was qualitatively consistent with the trend presented in Figure 5.8: larger σ_c at given μ_c resulted in a larger amount of retained colloids. In addition, representative retention profiles, breakthrough curves, and the reduction curves of K/K_0 (Figure 6.7) indicated that the higher β under larger σ_c was mainly attributed to the surface retention of colloids (larger amount of retained colloids at larger σ_c was significant at normalized depth < 0.3). The large σ_c of particle size distributions of colloids led to high chance for relatively large size colloids to be sampled, which have a high probability of capture in porous media. To take larger β under larger σ_c into account, the results presented in Figure 6.6 and Figure 6.7 imply that the mean size of particle size distribution of colloids can be used to model colloids transport/retention in porous media, as opposed to the median size of the particle size distribution (at given μ_c , expected value of particle size distribution is $\exp(\mu_c + \sigma_c^2/2)$, which increases as σ_c increases). Note that β values presented here are a mass-based bed efficiency, not related to the number of retained colloids.

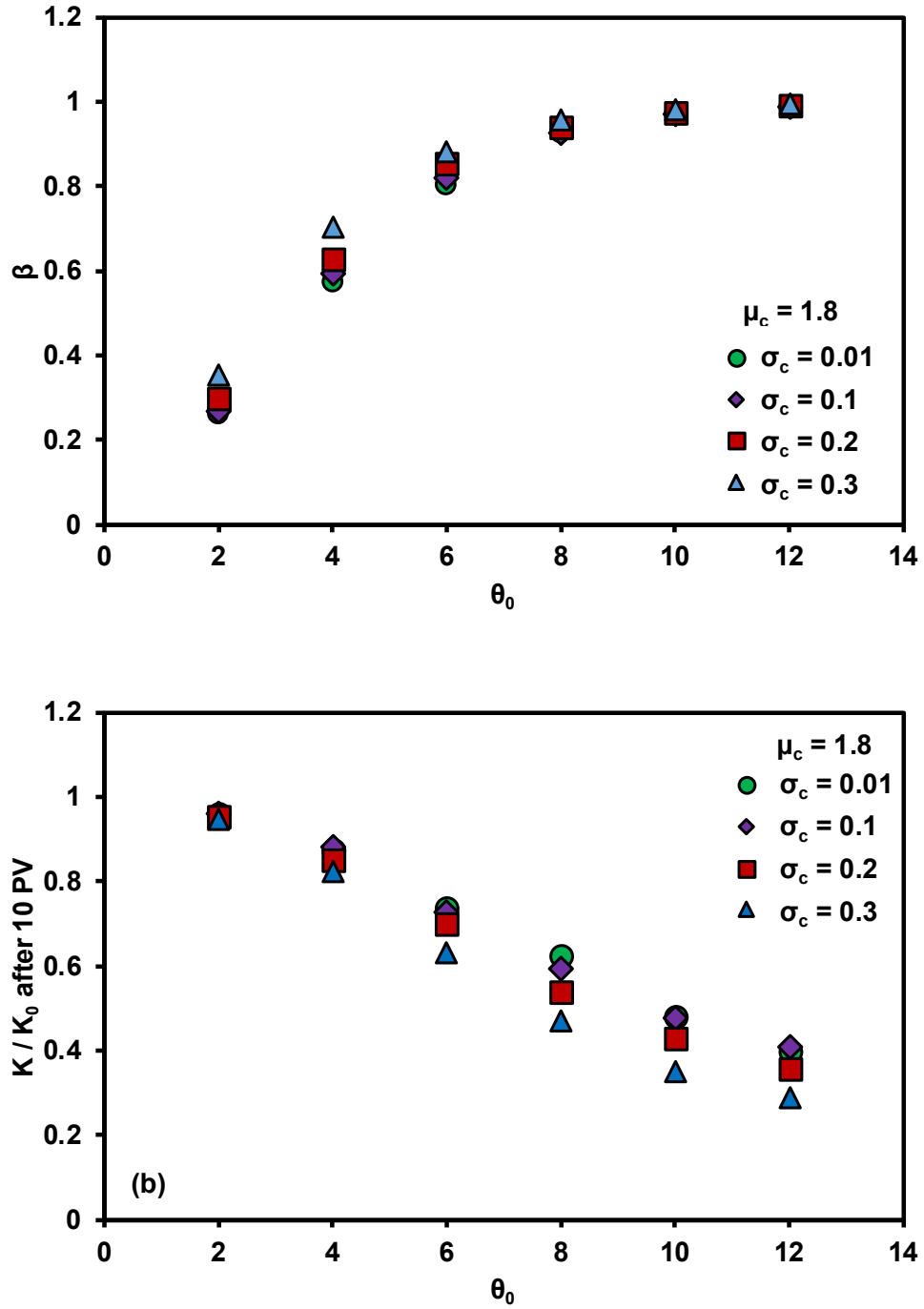
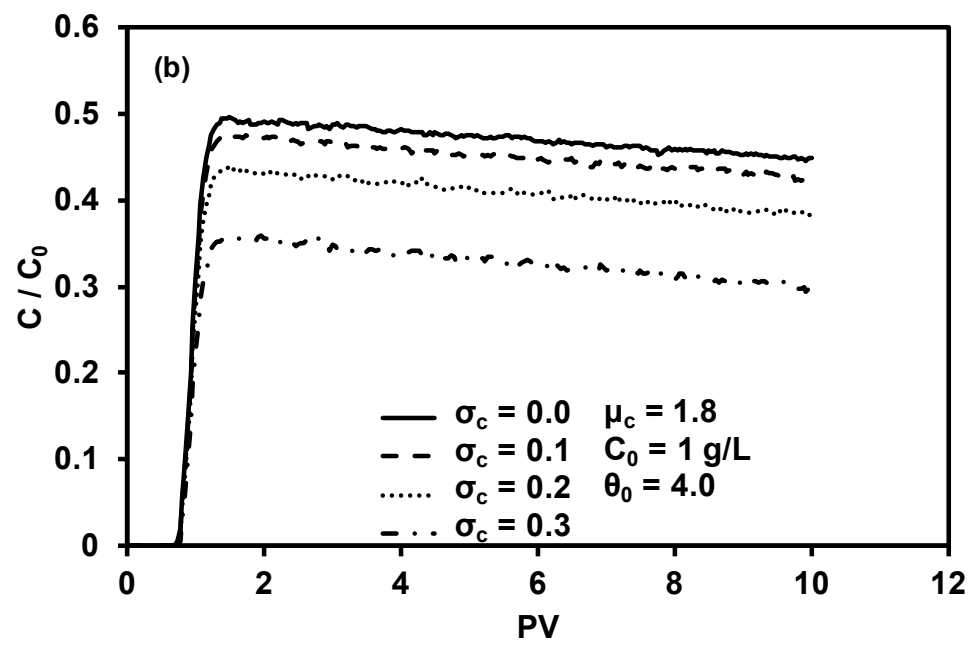
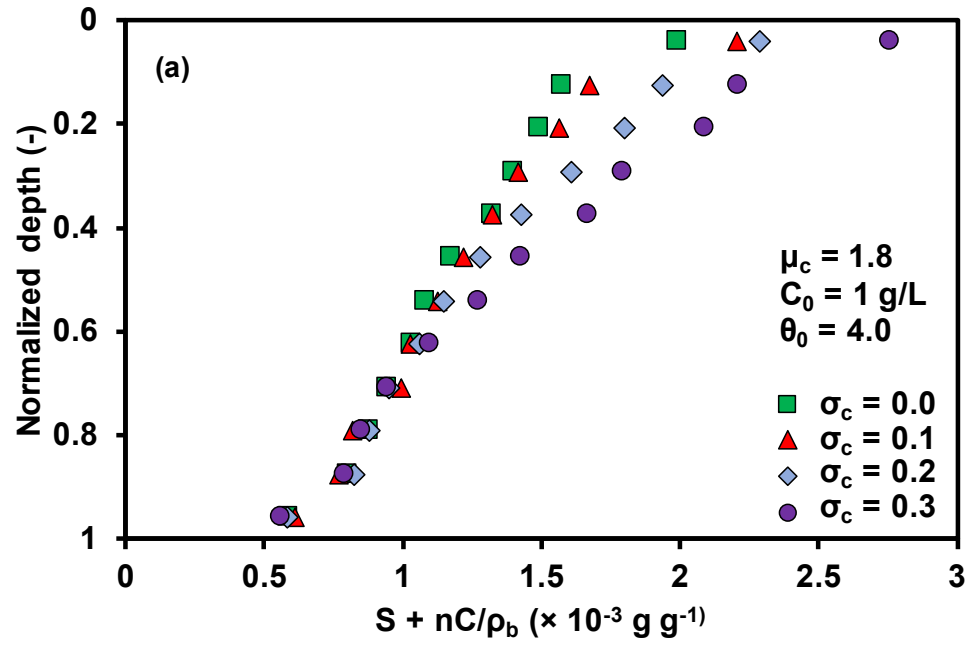


Figure 6.6. (a) Bed efficiency of colloids (β , Equation (7-13)), and (b) the final value of hydraulic conductivity after 10 PV of injection as a function of θ_0 .



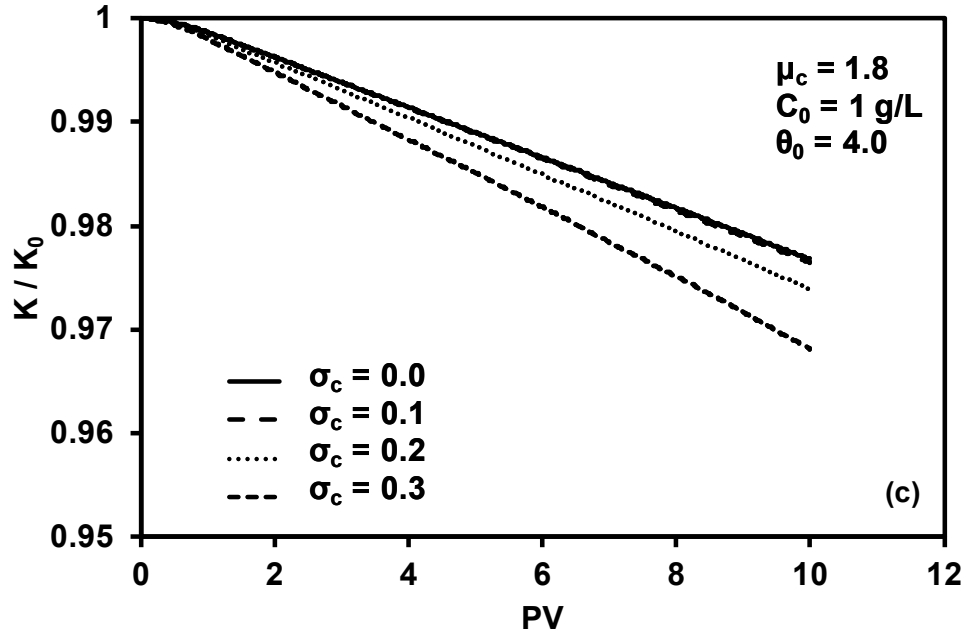
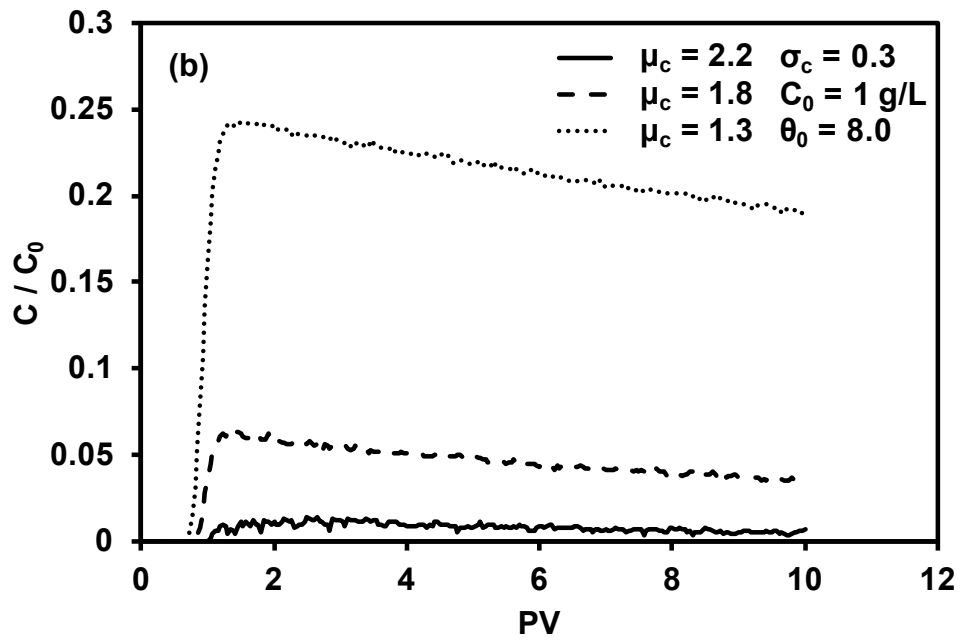
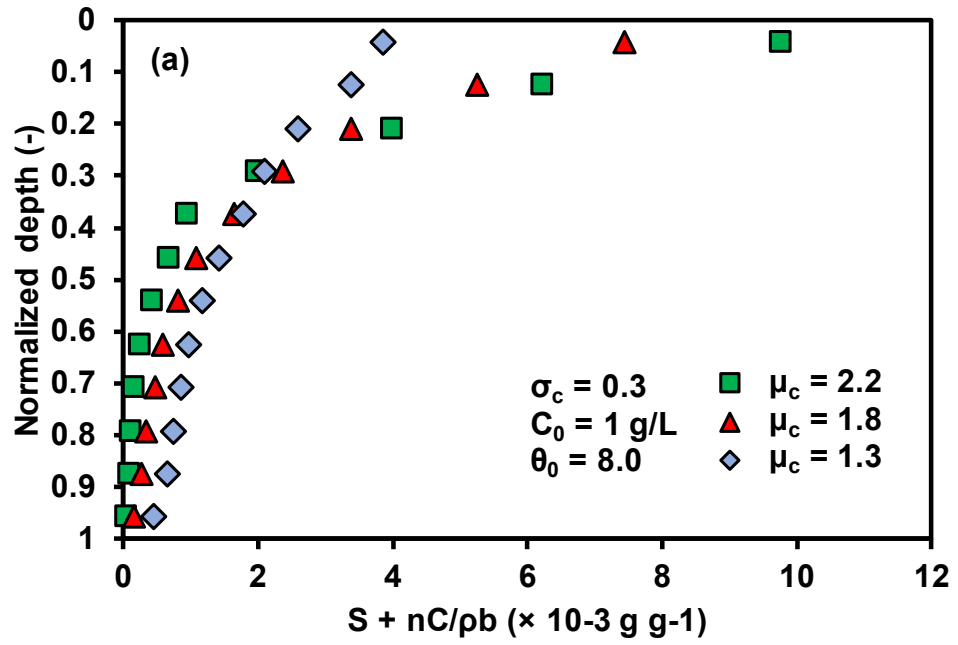


Figure 6.7. (a) Retention profiles after the injection, (b) breakthrough curves, and (c) the reduction of hydraulic conductivity during the injection under varied σ_c at $\mu_c = 1.8$ and $\theta_0 = 4$.

As expected, the retention profiles, breakthrough curves, and the reduction of K/K_0 were significantly impacted by μ_c : larger μ_c led to higher capture probabilities (Equation (6-9)), which caused a more exponential retention profile, lower C/C_0 , and more reduction of K/K_0 (Figure 6.8). Only the case of $\theta_0 = 8$ and $\sigma_c = 0.3$ are shown in Figure 6.8, but the trends of retention profile, breakthrough curve, and K/K_0 according to μ_c were consistent at given σ_c and θ_0 . From the exponential shape of the profile at $\mu_c = 2.2$ (Figure 6.8(a)), the straining mechanism played a more critical role in the retention of colloids as μ_c increased.



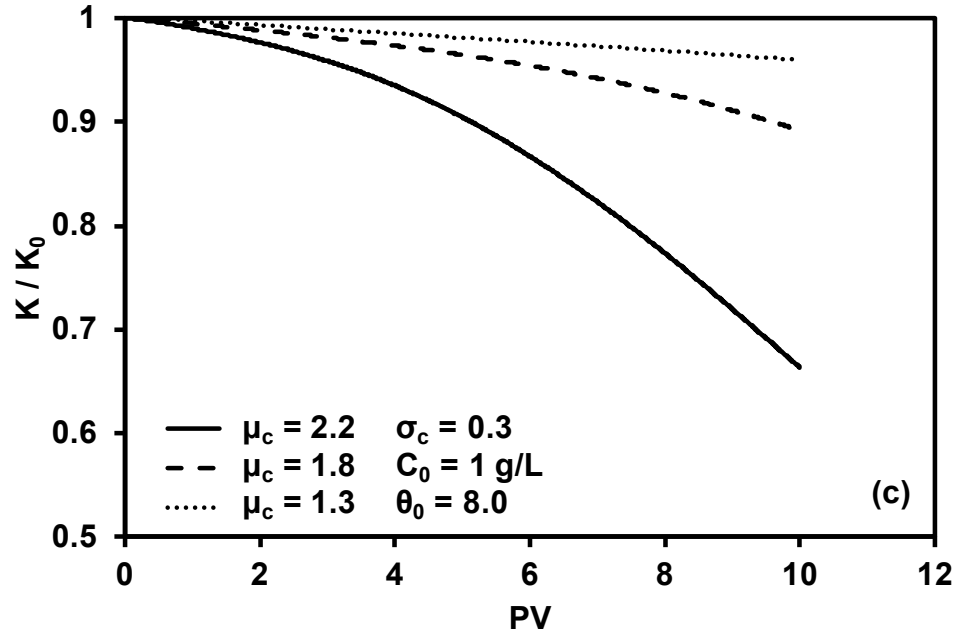


Figure 6.8. (a) Retention profiles after the injection, (b) breakthrough curves, and (c) the reduction of hydraulic conductivity during the injection at $\mu_c = 2.2, 1.8$ and 1.3 ($\theta_0 = 8$ and $\sigma_c = 0.3$).

6.3.2 Size distributions of colloids in retention profiles and breakthrough curves

The size distributions of retained colloids and effluent colloids were illustrated in box plots (Figure 6.9 and Figure 6.10). As seen in Figure 6.9, retained colloids showed even larger median sizes in all depths than the median size of particle size distribution of the colloids ($6 \mu\text{m}$ for $\mu_c = 1.8$) at low θ_0 while crossover points between median sizes of retained colloids and particle size distribution were observed at relatively high θ_0 . This trend of retained colloid size under varied θ_0 was comparable in all μ_c (data not shown) and implied that the most of the large colloids were retained near the injection point (inflow), which led to small colloids being retained in the bottom part of the network. In

contrast, low θ_0 resulted in the retention of colloids larger than median size of particle size distribution because of low capture probability. As a result, median sizes of effluent colloids at $\theta_0 = 2$ was roughly identical with the median size of colloids in all pore volumes, while median sizes of effluent colloids were lower than the median size of colloid at other θ_0 values. The difference between the median sizes of effluent colloids and the median sizes of colloid was more significant as θ_0 increased (Figure 6.10).

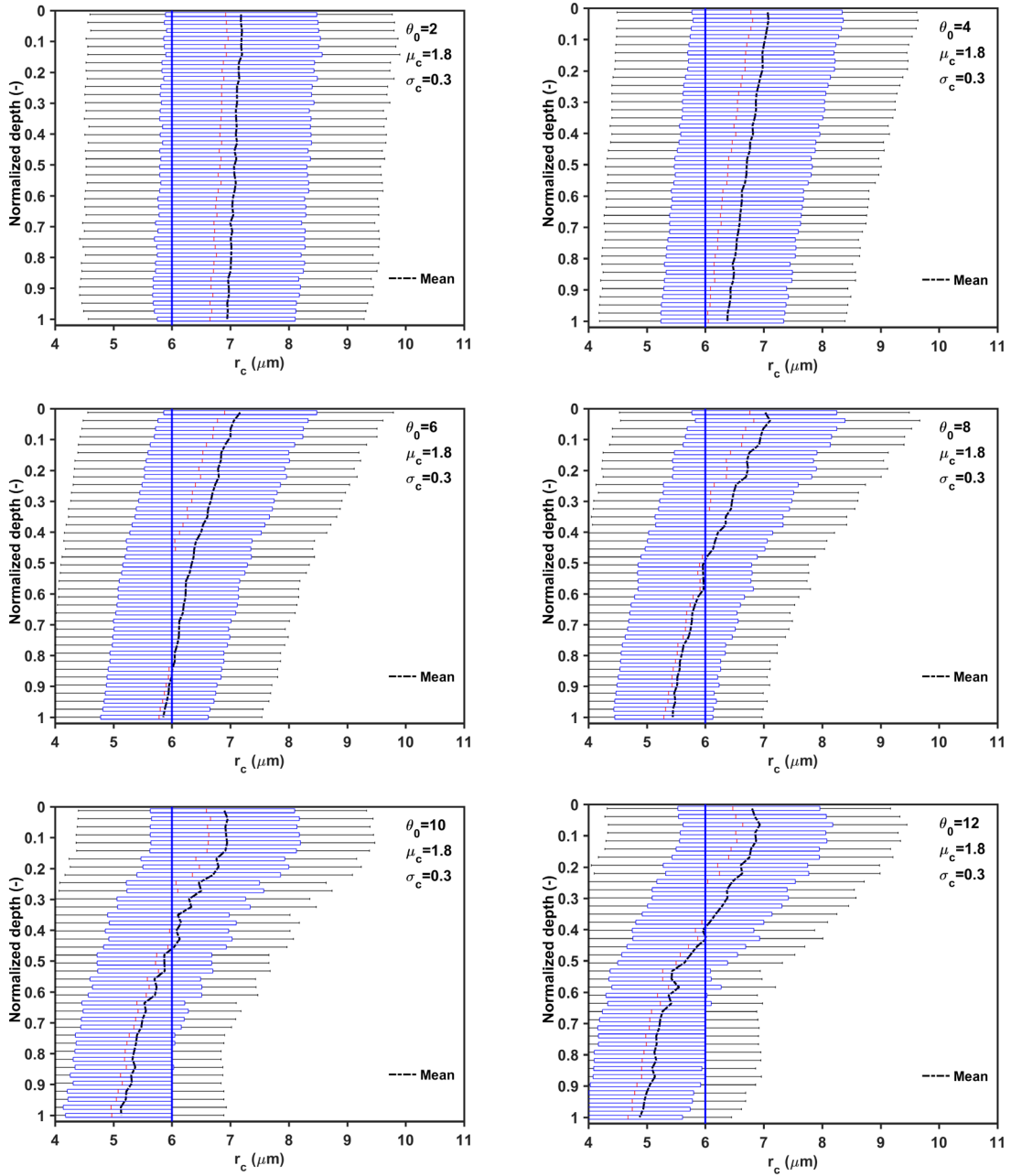


Figure 6.9. Size distributions of retained colloids under varied θ_0 at $\mu_c = 1.8$ and $\sigma_c = 0.3$. The edges of the boxes correspond to 25 and 75 % coverages, and the red lines in the boxes represent the median value of sizes of retained colloids. The whisker line of each box plot indicates 99 % coverage for a distribution in each depth.

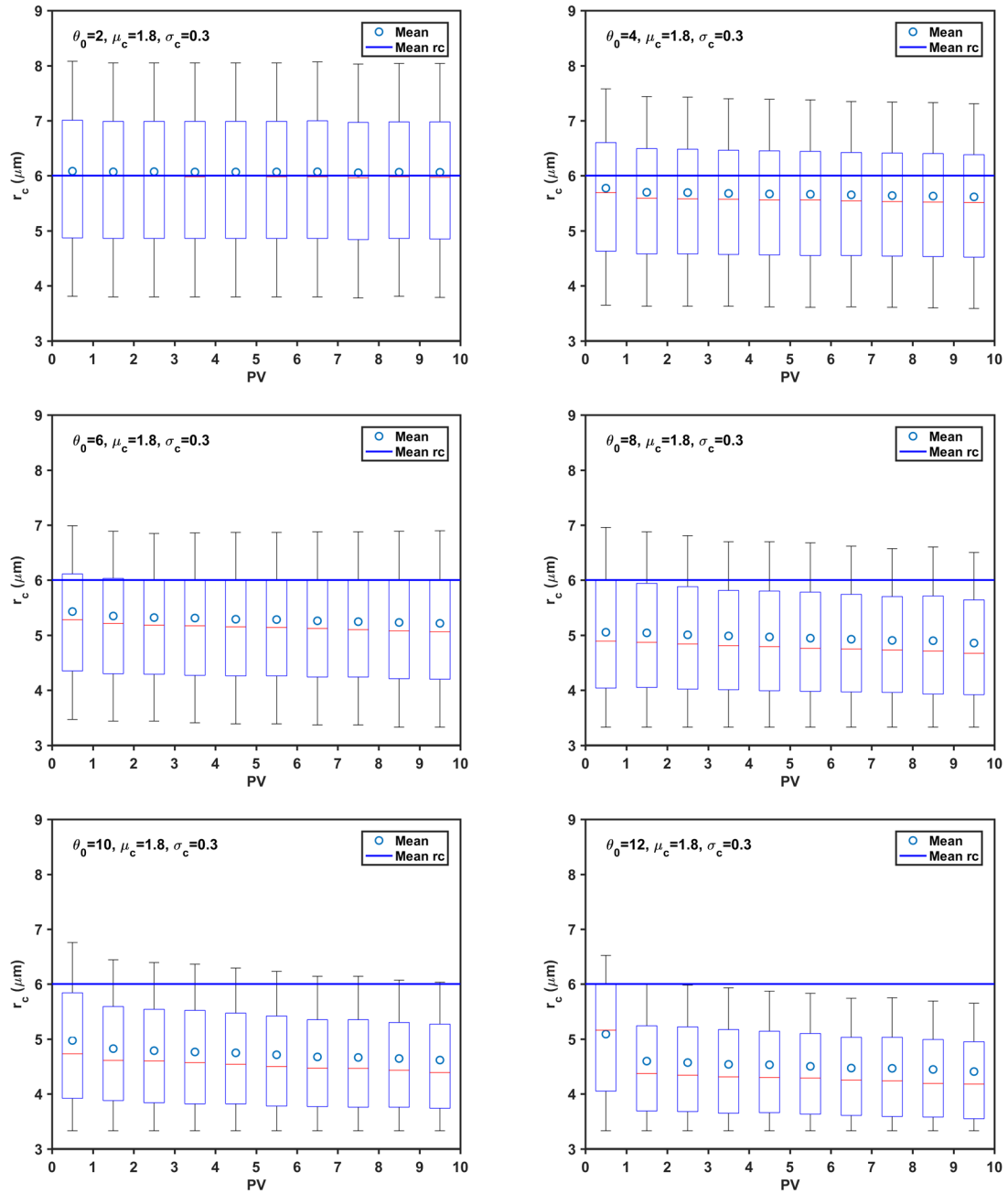


Figure 6.10. Size distributions of colloids in effluent under varied θ_0 at $\mu_c = 1.8$ and $\sigma_c = 0.3$.

6.3.3 *Optimized first-order coefficients in the continuum equation*

Table 6-1 presents optimized k_{att} (Equation (6-15)), obtained from best least squares fit to the retention profiles in all conditions. The value of k_{det} was fixed to 1×10^{-4} /s, assuming that the detachment coefficient of colloids was proportional to the flow rate (the flow rate was constant in all simulation in this chapter) and capable of quantitative comparison of k_{att} between each condition. It is apparent that k_{att} increased as θ_0 increased because of the increase in capture probability. In addition, under constant θ_0 , k_{att} increased as μ_c and σ_c increased (Figure 6.11). By performing the optimization analysis presented here, θ_0 can be estimated by the pore network model by using observed data for relatively short-term and small-scales. Then in the long-term and large-scale simulations, it can be converted into k_{att} in the continuum equation under different flow conditions, sizes of colloid and sand, and solution chemistry of colloid suspension (used for calculating v_c in (6-11)) (capture probability is a function of θ (Equation (6-9)), which is dependent on above factors).

Table 6-1. Optimized k_{att} in All Conditions (Equation (6-15))

μ_c	σ_c	θ_0	$k_{att} \times 10^2$ (/ s)	R^2	μ_c	σ_c	θ_0	$k_{att} \times 10^2$ (/ s)	R^2	μ_c	σ_c	θ_0	$k_{att} \times 10^2$ (/ s)	R^2
		2	1.54	0.86			2	0.68	0.74			2	0.24	0.67
		4	6.05	0.95			4	2.64	0.89			4	1.04	0.83
	0.01	6	12.92	0.98		0.01	6	5.88	0.96		0.01	6	2.29	0.87
		8	18.07	0.98			8	10.73	0.98			8	4.14	0.95
		10	22.58	0.99			10	14.81	0.97			10	6.98	0.93
		12	24.56	0.98			12	22.69	0.98			12	10.03	0.95
		2	1.57	0.92			2	0.72	0.80			2	0.26	0.54
		4	6.47	0.95			4	2.98	0.87			4	1.14	0.81
	0.1	6	14.21	0.98		0.1	6	6.67	0.95		0.1	6	2.45	0.92
		8	18.57	0.97			8	11.43	0.97			8	4.60	0.92
		10	22.04	0.98			10	14.91	0.98			10	7.85	0.91
		12	26.06	0.99			12	22.34	0.98			12	9.52	0.97
2.2		2	1.94	0.89	1.8		2	0.86	0.73	1.3		2	0.31	0.63
		4	7.10	0.96			4	3.34	0.93			4	1.31	0.80
	0.2	6	14.72	0.98		0.2	6	8.13	0.96		0.2	6	3.05	0.88
		8	18.77	0.98			8	13.01	0.97			8	5.49	0.93
		10	25.48	0.98			10	16.89	0.99			10	8.78	0.94
		12	30.54	0.99			12	23.30	0.99			12	12.90	0.96
		2	2.54	0.82			2	1.17	0.82			2	0.42	0.57
		4	9.72	0.96			4	4.31	0.93			4	1.68	0.88
	0.3	6	18.82	0.97		0.3	6	9.43	0.96		0.3	6	3.75	0.88
		8	25.31	0.99			8	17.12	0.97			8	7.38	0.92
		10	34.37	0.98			10	20.92	0.98			10	10.67	0.95
		12	41.38	0.98			12	27.74	0.98			12	14.78	0.95

Note: $k_{det} = 1 \times 10^{-4}$ /s.

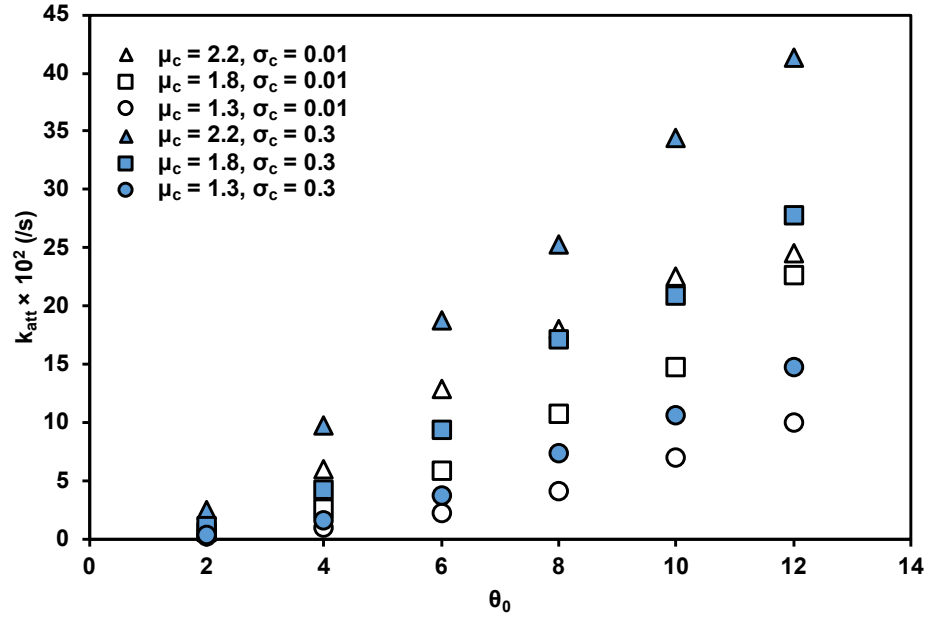


Figure 6.11. Optimized k_{att} under varied θ_0 at $\mu_c = 2.2, 1.8, 1.3$ and $\sigma_c = 0.01, 0.3$.

6.4 Summary

In this chapter, a pore network model for polydispersed colloid transport in porous media was presented. Optimized first-order rate coefficients were determined, which accounted for attachment and straining under varied standard deviation and mean of particle size distribution. Based on the observed retention profiles, breakthrough curves, and the reduction of hydraulic conductivity from the pore network simulation, the following conclusion can be drawn:

1. Increases in θ_0 , μ_c , and σ_c caused increases in capture probability of colloids, leading to a larger mass of retained colloid, lower breakthrough concentration, and more significant reduction of hydraulic conductivity.

2. Size distributions of colloid in retention profiles and breakthrough curves indicated that large sizes of colloids were retained near the injection point, which led to median sizes of effluent colloids that were smaller than the median size of colloid. More exponential retention profiles under larger σ_c attributed to the more preferential retention of larger colloids near the injection point.
3. Pore network modeling can be used to reflect the geometry of pores, particle size distribution of the colloids, and solution chemistry in the estimation of the first-order coefficients in the continuum equation for long-term and large-scale simulation.

CHAPTER 7 THE ROLE OF IMMOBILE KAOLINITE COLLOIDS IN THE METAL TRANSPORT: A LABORATORY STUDY

7.1 Introduction

Contaminants originating from human activities can be introduced into the subsurface through a variety of different sources ranging from stormwater events, leakage from waste disposal facilities, mining activities, to various other industrial activities. Those contaminants can subsequently transport to groundwater where they can pose a threat to public health. Consequently, significant research effort has focused on developing methods to adequately predict and assess contaminant transport in subsurface environments with the goal of protecting human health and ecosystems (Gao et al. 2013).

Notably, in the past few decades, many laboratory and field studies have determined that the presence and transport of colloidal particles in the subsurface can facilitate or enhance contaminant transport because colloids can facilitate contaminant transport. Colloidal particles are particles suspended in a liquid due to electrical forces, typically ranging in size from 1 nm to $\sim 10 \mu\text{m}$. This is due to the surface charge characteristics of colloidal particles, which can bind and transport charged contaminants (Corapcioglu and Jiang 1993; Grolimund et al. 1996; Ibaraki and Sudicky 1995; Penrose et al. 1990; Ryan and Elimelech 1996). For instance, transport of contaminants such as heavy metals or radionuclides can be facilitated by the presence of charged inorganic colloids including clay and oxide particles (Ho and Miller, N. H 1986; Kretzschmar et al. 1999; Torok et al. 1990); however, it is important to note that colloids do not always pass through porous media easily and they may be retained, which they can accumulate in pore space (i.e., clogging) due to pore size restriction, van der Waals attraction or electrostatic

attraction (Bradford et al. 2005; Torkzaban et al. 2008; Xu et al. 2006). Occasionally, colloids are generated within the subsurface geology due to geochemical alternation and breakdown of parent geologic material, and they remain stationary even under the groundwater flow condition of high hydrodynamic force. In these conditions when colloids are relatively immobile, it is predictable that contaminant transport is likely to be retarded, rather than facilitated, if the contaminant is favorably adsorbed by the colloid surface. For these reasons, Sen et al. (2002) termed the facilitation or retardation of contaminants in the presence of colloids as colloid associated contaminant transport.

Due to the ability of colloids to transport contaminants over long distances, many studies have focused on colloid facilitated contaminant transport. Penrose et al. (1990) observed that plutonium (Pu) traveled through an alluvial deposit with colloidal particles 1200 times faster than predicted by modeling, and Puls and Powell (1992) demonstrated arsenic (As^{2+}) transported 21 times faster in the presence of colloidal particles than it did in the absence of colloids. Both studies concluded that these consequences could be attributed to the presence of mobile colloids, which were acting as contaminant carriers. In addition, many laboratory studies have demonstrated that predicting the distance of contaminant transport without taking mobile colloids into account could result in an inaccurate estimate (Denaix et al. 2001; Grolimund et al. 1996; Jensen et al. 1999; Roy and Dzombak 1997; Zhuang et al. 2003).

In most cases, colloids are highly mobile in the subsurface due to their relatively small size range (McCarthy and Zachara 1989; Sen and Khilar 2006; Wan and Wilson 1994). In particular, they typically carry a negative surface charge and large double layer

at neutral to high pH and low ionic strength. These geochemical conditions result in colloids that are dispersed and extremely mobile (Bradford et al. 2011; Bunn et al. 2002; Kuznar and Elimelech 2007). However, some geochemical conditions result in colloids that settle under gravitational forces and may not be mobile in subsurface due to relatively small pore spaces/ throats, the presence of cementing/flocculating agents that aggregate clay-sized materials, and attractive electrostatic forces acting between colloids and large grains (McCarthy and Zachara 1989).

Colloidal particles consist of a variety of different substances, including mineral and organic phases; however, aluminosilicate clay minerals represent one of the most prevalent types of colloids found in groundwater. The mobility of these colloids is a function of the prevailing geochemical conditions, and they may be mobilized in the short term due to the alternation of the hydrogeological condition and aqueous chemistry, or they can be stationary in a nearly immobile state in the short to long terms. Most importantly, the immobility of clay colloids can significantly retard the transport of contaminants that are favorably adsorbed by the clay surface, which can have a measureable impact on the modeling of contaminant transport.

The objective of the work performed in this experimental study is to investigate contaminant transport in a sand medium in the presence of immobile kaolinite clay colloids. Lead (Pb(II)) was selected as the model contaminant to represent heavy metal species that are not easily degradable biologically and originate from human activities (e.g., industry emission, wastewater irrigation, solid waste disposal, mine tailings) (Khan et al. 2008; Wuana and Okieimen 2011; Zhang et al. 2010). The variation of the clay colloidal fraction

in the sand medium was selected as the primary variable to observe the degree of Pb(II) transport retardation as a function of mass of immobile clay colloids. Additionally, the solution chemistry (pH and ionic strength) and flow rate were varied in order to investigate the impact of surface charge of the clay colloidal particles and kinetic rate of adsorption of Pb(II) on the breakthrough curve. Finally, optimization analysis was performed on the measured breakthrough curves to evaluate first-order coefficients embedded in the advection-dispersion type governing equation to determine adsorption and desorption rates of Pb(II) onto clay colloids.

7.2 Theoretical framework

7.2.1 Colloid associated contaminant transport in porous media

A wide variety of colloid associated contaminant transport mass balance models have been developed over the past few decades (Corapcioglu and Jiang 1993; Mills et al. 1991; Saiers and Hornberger 1996; Sen et al. 2002, 2004). These models are based on the advection dispersion equation, but have different mathematical expressions as a function of the model assumptions in relation to soil grain-colloid-contaminant interaction. The model proposed in Šimůnek et al. (2006) was adopted in this work for the optimization analysis because this model is based on two assumptions to independently present equations for water flow (i.e., Richards equation), colloids, and contaminant. First, the presence of colloids in the soil matrix does not impact the transport properties of soil, and second, the sorption of a contaminant to a colloid does not impact the colloid transport. The mass balance equation for the total contaminant is given by (Šimůnek et al. 2006)

$$\begin{aligned} & \frac{\partial \theta C}{\partial t} + \rho \frac{\partial S_e}{\partial t} + \rho \frac{\partial S_k}{\partial t} + \frac{\partial \theta_w C_c S_{mc}}{\partial t} + \rho \frac{\partial S_c S_{ic}}{\partial t} + \frac{\partial A_{aw} \Gamma_c S_{ac}}{\partial t} \\ & = \frac{\partial}{\partial x} \left(\theta D \frac{\partial C}{\partial x} \right) - \frac{\partial q C}{\partial x} + \frac{\partial}{\partial x} \left(\theta_w S_{mc} D_c \frac{\partial C_c}{\partial x} \right) - \frac{\partial q_c C_c S_{mc}}{\partial x} + R \end{aligned} \quad (7-1)$$

where C is the dissolved contaminant concentration in aqueous phase (g / cm³), ρ is the bulk density of soil medium (g / cm³), θ and θ_w are volumetric water content and volumetric water content accessible to colloids respectively (cm³ / cm³), S_e and S_k are concentrations of contaminant sorbed instantaneously and kinetically to the solid phase respectively (g / g), C_c is the concentration of mobile colloid (g / cm³), S_c is colloids in solid phase (g / g), S_{mc}, S_{ic} and S_{ac} are amounts of contaminant sorbed by mobile colloids, immobile colloids, and air-water interface respectively (g / g), D and D_c are dispersion coefficients for contaminant and colloids respectively (cm² / s), q and q_c are water fluxes for contaminant and colloids respectively (cm / s), A_{aw} is the area of air-water interface per unit volume (cm² / cm³) and R is the reaction term accounting for various chemical and biological reactions (g / (cm³·s)). If the soil medium is saturated and only immobile colloids present in the soil medium, Equation (7-1) can be reduced to:

$$\frac{\partial \theta C}{\partial t} + \rho \frac{\partial S_e}{\partial t} + \rho \frac{\partial S_k}{\partial t} + \rho \frac{\partial S_c S_{ic}}{\partial t} = \frac{\partial}{\partial x} \left(\theta D \frac{\partial C}{\partial x} \right) - \frac{\partial q C}{\partial x} + R_{ic}, \quad (7-2)$$

where R_{ic} is the reaction term associated with immobile colloid (g / (cm³·s)) given by

$$R_{ic} = -k_c \rho S_c S_{ic}, \quad (7-3)$$

where k_c is the first-order rate constant (/ s) for the contaminant in the colloid phase.

Equation 2 describes the experimental conditions tested in this work (i.e., S_{mc}, A_{aw}, and Γ_c

= 0 in Equation (7-1)). Each term except the first term at the left-hand side of Equation (7-2) can respectively be expressed as (van Genuchten and Wagenet 1989):

$$\rho \frac{\partial S_e}{\partial t} = \rho f K_d q_{\max} \frac{\partial C}{\partial t}, \quad (7-4)$$

$$\rho \frac{\partial S_k}{\partial t} = \rho \omega \left[(1-f) \frac{q_{\max} K_d C}{1 + K_d C} - S_k \right], \quad (7-5)$$

$$\rho \frac{\partial S_c S_{ic}}{\partial t} = \theta k_a C - \rho k_d S_c S_{ic}, \quad (7-6)$$

where f is the fraction of instantaneously sorbed contaminant in two-site sorption model (see detail in van Genuchten and Wagenet (1989)), K_d is the distribution coefficient of dissolved contaminant to the solid phase (cm^3 / g), q_{\max} is the maximum amount of contaminant sorbed to solid phase (g / g), ω is the first-order rate constant ($/ \text{s}$), k_a and k_d are adsorption rate and desorption rate of contaminant for immobile colloids ($/ \text{s}$), respectively. Note that the Langmuir isotherm embedded in Equation (7-5) is to limit the maximum amount of sorbed contaminant on the solid phase.

7.2.2 Determination of dispersion coefficient

Dispersion in porous media can be expressed as a sum of effective molecular diffusion and mechanical dispersion. When water flows in one predominant direction, dispersivity in the transverse direction can typically be neglected, and the dispersion coefficient D in Equation (7-2) can be expressed as:

$$D = \tau D_m + \alpha_L v_s, \quad (7-7)$$

where τ , = tortuosity factor ($= n^{m-1}$, derived from Archie's equation (Boudreau 1996; Sahimi 1993), n = porosity, and $m = 1.3$ for unconsolidated sand (Archie 1942)), D_m = molecular diffusion coefficient ($= kT/(6\pi\mu r_m)$, described by the Stokes-Einstein equation), k = Boltzmann constant ($= 1.38 \times 10^{-23}$ J/K), T = absolute temperature (K), μ = dynamic viscosity of water ($N \cdot s/cm^2$), and r_m = atomic radius (cm), α_L = longitudinal dispersivity (cm), and v_s = seepage velocity (cm/s). Longitudinal dispersivity α_L is important in contaminant transport under intermediate or high fluid velocity. The empirical relationship presented in Delgado (2007) was used to obtain α_L as a function of the effective diffusion coefficient (D_m'), the effective Peclet number (Pe'), and the Schmidt number (Sc), where dispersion regimes were divided by the Peclet number (Pe) and the Reynolds number (Re). Because $Pe < 100$ and $Re < 10$ in all experiments performed in this work, the first three regimes among five were used (details in Delgado (2007)):

When $Pe < 0.1$ (diffusion regime),

$$\alpha_L = 0. \quad (7-8)$$

When $0.1 < Pe < 4$ (predominant diffusion regime),

$$\alpha_L = \left(\left(\frac{Pe'}{0.8/Pe' + 0.4} - 1 \right) D_m' - D_m' \right) / v_s. \quad (7-9)$$

When $Pe > 4$ and $Re < 10$ (predominant mechanical dispersion regime),

$$\alpha_L = \left(\left(\frac{Pe'}{(18Pe'^{-1.2} + 2.35Pe'^{-0.38})^{0.5}} \right) D_m' - D_m' \right) / v_s. \quad (7-10)$$

Equations (7-8), (7-9), and (7-10) determine α_L in each experimental condition.

7.2.3 *Optimization analysis for first-order coefficients*

Most simply, linear equilibrium sorption isotherms are applied to describe the mass transfer of contaminants to the colloidal or the solid phase during aqueous transport; however, many contaminants exhibit nonlinear sorption. Additionally, sorption of contaminants to the solid phase may be rate limited, and not in a state of equilibrium. One method of quantifying this complex phenomenon is by adding first-order coefficients to the advection-dispersion equation in order to represent the reactions between two phases (e.g., the reaction between colloids/solids, dissolved contaminants/solids, or dissolved contaminants/mobile and immobile colloids).

The work in this study was performed to quantitatively represent the reaction between dissolved contaminants and immobile colloids. An optimization analysis was performed to evaluate the three unknown first-order reaction coefficients (k_a and k_d in Equation (7-6) and k_c in Equation (7-3)). An initial guess of unknown coefficients with upper and lower bounds was used to initiate the optimization analysis, followed by iterative solving of the governing equation. Optimized coefficients were determined by varying coefficients in the least square sense with experimental data. The trust region algorithm was used for the optimization analysis with two stop criteria: the tolerance of coefficients less than $10^{-6} / s$ (i.e., the difference between the coefficient in the previous iteration and that in the current iteration), or the tolerance of a contaminant concentration less than $10^{-6} \text{ mg} / \text{cm}^3$ (i.e., the difference between the calculated contaminant concentration using optimized coefficients in a current iteration and an experimentally determined contaminant concentration).

7.3 Experimental investigation

7.3.1 Materials

Georgia kaolinite (Wilkinson Kaolin Associate) and ASTM-graded sand (U.S. Silica) were selected as the clay colloids and sand medium, and characterization data were measured for both soils (Table 7-1). The liquid limit (LL) was measured by the fall cone method (British Standard 1377) and the specific surface (S_s) was measured by the methylene blue method (Santamarina et al. 2002). The hydrometer test and the sieve analysis in ASTM D422 were performed to measure median particle sizes (d_{50}) of the kaolinite and the sand. The maximum and minimum void ratios (e_{\max} and e_{\min} , respectively) of the sand were measured according to ASTM D4253 and ASTM D4254, respectively, and the specific gravity (G_s) of both materials was measured according to ASTM D854. The zeta potential of the kaolinite particles was measured at varied pH using a zeta potential analyzer (Zetaplus, Brookhaven Instruments Corporation). All chemicals in the experiments ($\text{Pb}(\text{NO}_3)_2$, NaOH, HNO_3 , and CaCl_2 , Sigma Aldrich Corporation and Fisher Scientific) were used as received, and deionized water (Barnstead E-pure) was used in all experiments.

Table 7-1. Summary of Kaolinite and Sand Properties

Properties	G_s	e_{\max}	e_{\min}	d_{50} (cm)	LL (%)	S_s (m^2 / g)
ASTM-graded sand	2.65	0.762	0.514	0.036	-	-
Georgia Kaolinite	2.52	-	-	4.5×10^{-5}	72	52

To ensure the immobility of kaolinite colloids in the sand medium during the column experiment, the retention profile of kaolinite colloids was first obtained after the injection of 10 pore volumes (PV) of 1 g / L kaolinite suspension through the ASTM-graded sand (Figure 7.1). The hyperexponential retention profile in Figure 7.1 indicated that pore sizes of ASTM-graded sand were not sufficiently large for kaolinite colloids to penetrate deeply into the sand column. A surface filter cake was formed at the inlet of the sand medium, and the kaolinite colloids were trapped after initial placement in the small pore spaces within the sand. No kaolinite colloids were observed in the effluent after 10 pore volumes of flow, and kaolinite mass recovery after soil column extraction was approximately 100%.

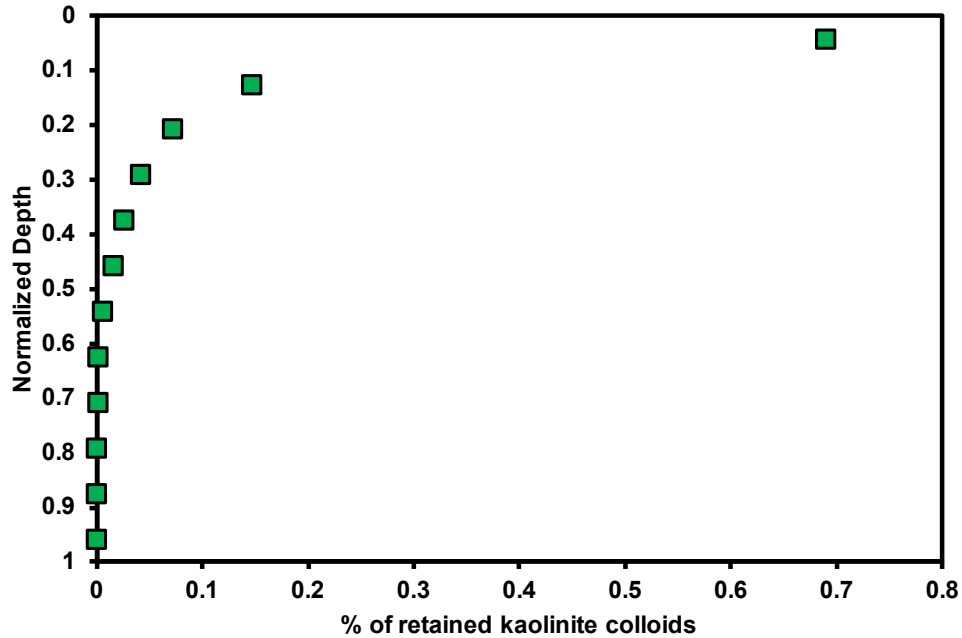


Figure 7.1. The retention profile of kaolinite colloids after injecting the kaolinite suspension into the ASTM-graded sand in deionized water: the diameter and the height of the column were 7.62 cm (3 inches) and 30.48 cm (12 inches), respectively, water flux was 0.0365 cm/s, and the sand was initially packed to $D_r = 70\%$ (D_r is relative density, $D_r = (e_{\max} - e) / (e_{\max} - e_{\min})$).

7.3.2 *Sample preparation and soil-column experiment*

The soil columns were prepared for experimentation as follows: to remove any impurities from the sand, deionized water was used to rinse the sand three to four times, after which the sand was submerged it in an ultrasonic bath for 1 hour, followed by drying in an oven at a temperature of 105 ± 5 °C. Then the given mass of kaolinite was mechanically mixed for 1 hour with a given mass of sand, chosen to form a sample with a corresponding $D_r = 70\%$ (i.e., $n = 0.37$). The sand-kaolinite sample was placed into the test column using wet pluviation (column dimensions = 5.08 cm in diameter and 4.61 cm in height). A perforated round metal plate was placed at the top and bottom of the column to

ensure even distribution of flow, and a # 200 plastic mesh (75 μm opening size) was placed at each end of the column to retain the sand grains. After the sand was placed, the column was submerged and assembled inside a water bath with the background solution to obtain saturation. The background solution (without Pb(II)) was injected through the column at a flowrate roughly 1.5 times higher than test velocity in order to dislodge loosely bound colloidal particles, until the sample reached the equilibrium. A turbidimeter (Orbeco-Hellige Inc., TB200) and a conductivity meter (Accumet Excel XL20) were utilized to monitor for the presence of kaolinite colloids and the stabilization of solution chemistry in effluent. A strong positive correlation between the concentration of kaolinite colloids and turbidity (data not shown) indicated that turbidity reliably estimated the concentration of kaolinite colloids in the effluent. To ensure the system reached to the equilibrium, turbidity and electrical conductivity for 15 pore volumes of flow were measured (Figure 7.2). The initial injection of the background solution led to a small amount of kaolinite colloids mobilization from the sand medium; however, the measured turbidities demonstrated that the concentration of mobilized kaolinite colloids was not significant ($< 0.5\%$ of initial kaolinite colloids in the column). After the turbidity and the electrical conductivity of effluent stabilized to background values (dotted line on Figure 7.2), Pb(II) was injected along with the background solution.

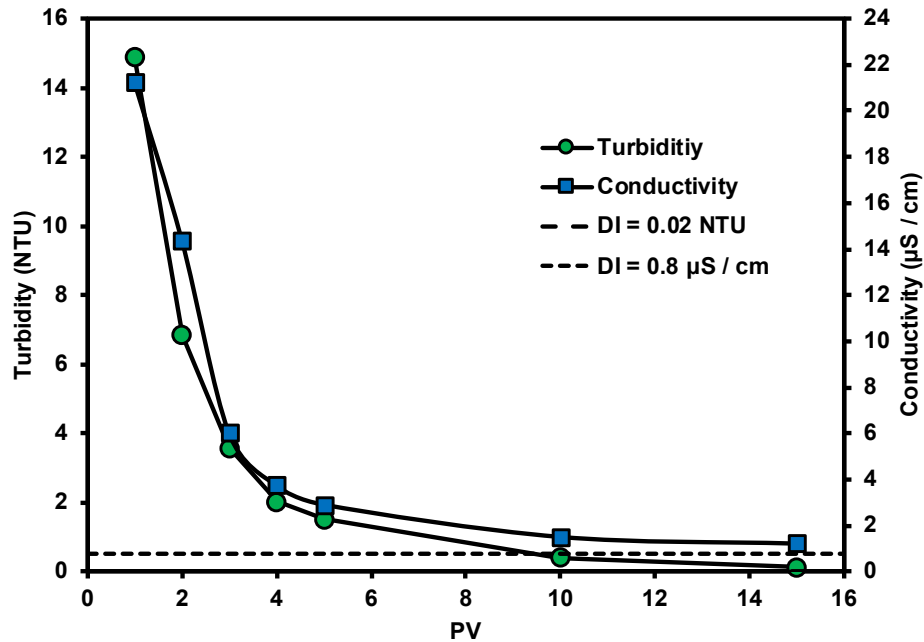


Figure 7.2. Turbidity and electrical conductivity measured during injection of first 15 PVs. Kaolinite concentration = 3%, and background solution was deionized water.

Concentrations of Pb(II) in the effluent were measured using a fraction collector to sample flow at the outlet of the column in each pore volume. In all experiments, a rate-adjustable peristaltic pump (Fisher Scientific) was used to inject the lead solution. Experiments were performed at two constant flow rates, three pH levels, and four levels of ionic strength to investigate the impact of the reaction rate, the surface charge of kaolinite colloids, and the presence of other ions on the Pb(II) breakthrough curve. The Pb(II) concentration in the influent was 5.0 ± 0.1 mg/L for 13 experiments, and 1.0 mg/L for two experiments. The influent was flowed through the column for 100 pore volumes, and the concentration of the effluent was measured by inductively-coupled plasma optical emission spectrometry (ICP-OES, PerkinElmer Optima 8000) at the outlet every 5 pore volumes of flow (Table 7-2).

Table 7-2. Experimental Conditions for Lead Sorption Column Tests

Variables	Kaolinite content by mass (KC)			Chemical used
	1%	3%	5%	
C_0 (mg/L)	1, 5	1, 5	5	$Pb(NO_3)_2$
pH	4, 5.6, 9	4, 5.6, 9	4, 5.6, 9	70% HNO_3 , 1N NaOH
IS (M)	-	0.001, 0.005, 0.01	-	$CaCl_2$
v_s (cm / s)	0.0136 (low), 0.0452 (high)	0.0141 (low), 0.0469 (high)	0.0146 (low), 0.0488 (high)	-

Note :IS = ionic strength, C_0 = inlet Pb(II) concentration. Note that porosity variations in the column setup resulted in slight variations in v_s .

7.3.3 Equilibrium and kinetic adsorption test

Equilibrium and kinetic adsorption tests were conducted for the sand and kaolinite to determine the maximum adsorption capacities (q_{max}) and the first-order rate constant (ω) (Equation (7-5) and Equation (7-14)). For both the equilibrium and kinetic tests, 3 g of solids were mixed with 30 ml solutions in a series of 50 ml tubes, and the tubes were rotated at 30 rpm for 24 hours for the equilibrium test, and for intervals of 5, 10, 15, 20, 30, 60, 120, 240, 360, and 1440 minutes for the kinetic test. After the tubes were removed from the shaker, they were centrifuged at 3000 rpm and the supernatant was filtered through a 0.45 μm filter prior to ICP-OES analysis. Sorption results were fitted to a linearized Langmuir isotherm expressed as (Langmuir 1918):

$$\frac{C_e}{q_e} = \frac{C_e}{q_{max}} + \frac{1}{K_d q_{max}}, \quad (7-11)$$

where C_e is the equilibrium concentration of Pb(II) and q_e is the amount of Pb(II) adsorbed per unit mass of the sand or the kaolinite at equilibrium (mg/g). The first-order kinetic equation was expressed as (Ghorai and Pant 2005):

$$\log(q_e - q) = \log(q_e) - \frac{\omega t}{2.303}, \quad (7-12)$$

where q (mg / g) was the amount of Pb(II) adsorbed per unit mass of sand or kaolinite at time t (sec).

7.4 Test results and discussion

7.4.1 Adsorption equilibrium and kinetic adsorption test

Uptake of lead by kaolinite was well modeled with the Langmuir isotherm; however, as was anticipated, Pb(II) adsorption by sand was essentially negligible (Figure 7.3) (Table 7-3). The specific surface (S_s) of kaolinite was roughly 1200 times larger than that of the sand (based on d_{50} and G_s , Table 7-1); therefore, it was assumed that Pb(II) adsorption during transport took place at adsorption sites on the immobile kaolinite colloids. Equilibrium sorption occurred in less than 10 min (Figure 7.4), and the determined values of q_{\max} , K_d , and ω (Table 7-3) were used in the optimization analysis.

Table 7-3. Equilibrium and Kinetic Parameters Measured for Tested Soils

Material	Equilibrium (curve fit by Langmuir model)			Kinetic (Equation (7-12))
	q_{\max} (mg / g)	K_d (L / mg)	R^2	ω (/ s)
Sand	1.081×10^{-3}	2.202×10^{-3}	0.045	1.859×10^{-3}
Kaolinite	2.854	6.102×10^{-3}	0.986	4.258×10^{-3}

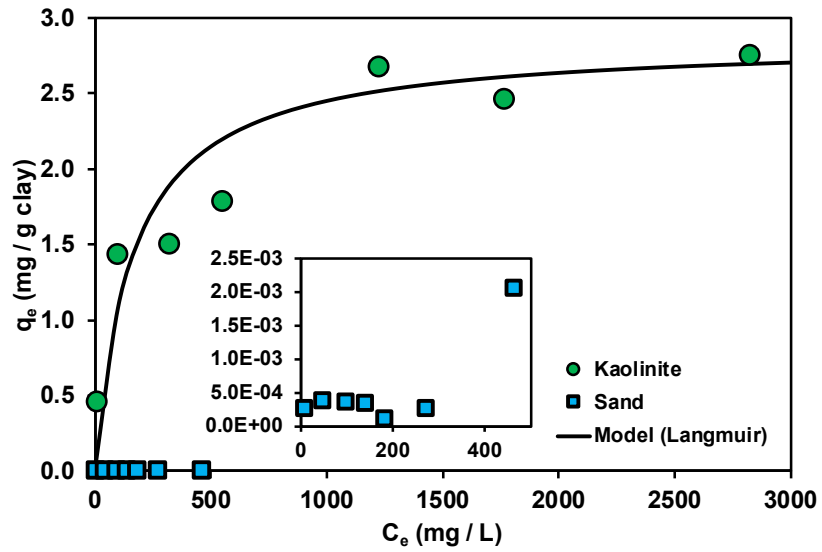


Figure 7.3. The result of the Pb(II) equilibrium adsorption test for the kaolinite and the sand.

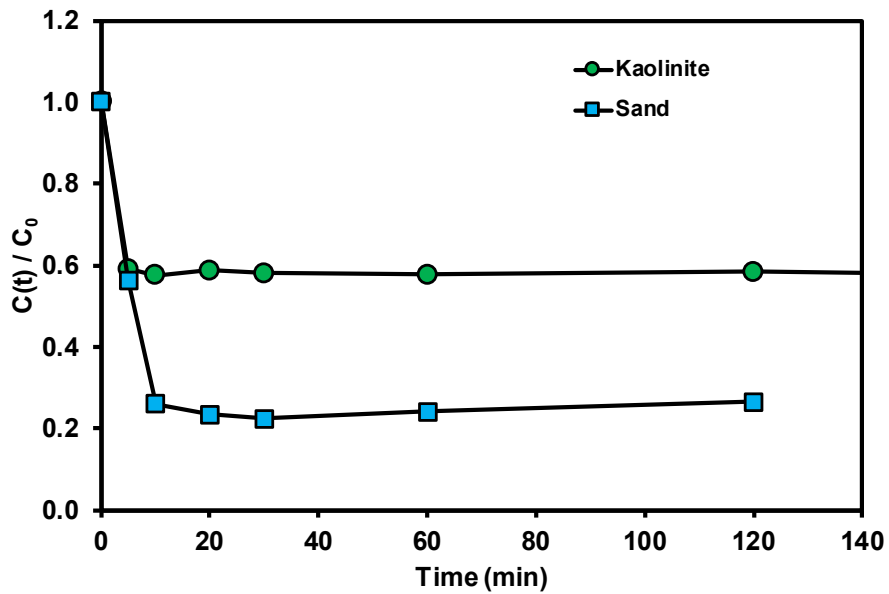


Figure 7.4. The result of the Pb(II) kinetic adsorption test for the kaolinite and the sand: the $C(t)$ represents the Pb(II) concentration of supernatant at time t .

7.4.2 *Soil-column experiment*

7.4.2.1 **Impact of inlet Pb(II) concentration (C_i)**

At low concentrations of colloids and lead (kaolinite = 1 % and $C_i = 1$ mg/L), almost no Pb(II) breakthrough was observed, indicating there were enough available sorption sites on the kaolinite to retard transport of the metal. In contrast, increasing Pb(II) concentration to 5 mg/L led to rapid breakthrough with $C / C_i > 0.9$ after 20 pore volumes (Figure 7.5). For KC = 3%, no Pb(II) was observed in effluent until 100 pore volumes for $C_i = 1$ mg/L, while the breakthrough of Pb(II) was initiated at roughly 30 pore volumes for $C_i = 5$ mg/L. The plateau concentration between 0.6 and 0.7 for KC = 3% and $C_i = 5$ mg/L indicated that Pb(II) adsorption still occurred after 100 PVs of flow. In deionized water at pH ~ 5.6, Pb^{2+} was the dominant dissolved species and the kaolinite was still predominantly negatively charged, causing most Pb(II) adsorption occurred through electrostatic attraction (Figure 7.5).

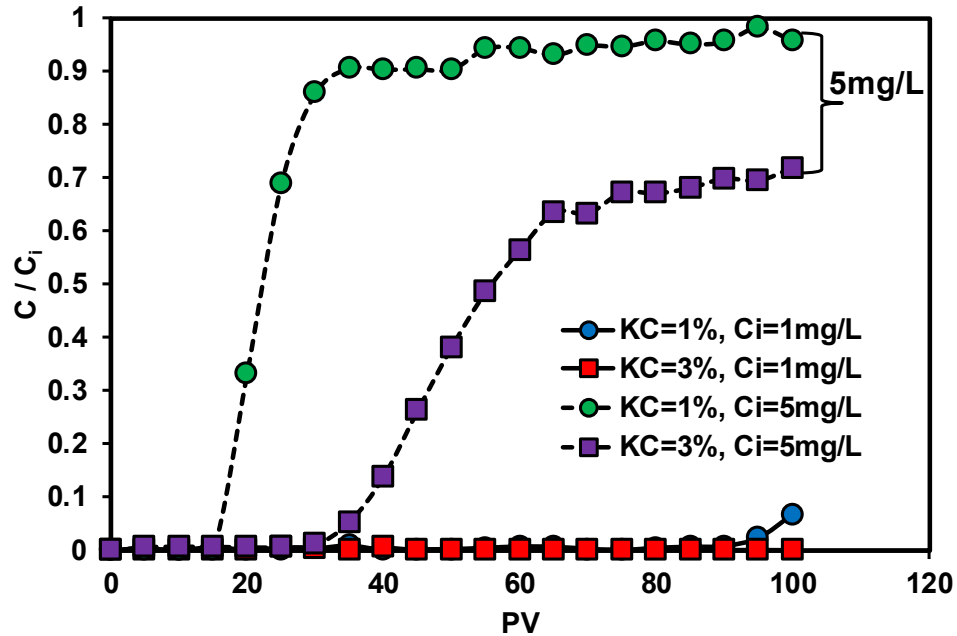


Figure 7.5. Pb(II) breakthrough curves under two KC and two C_i with deionized water.

7.4.2.2 Impact of flow rate (Q) and kaolinite content (KC)

An increase in the concentration of kaolinite colloids led to slower breakthrough and lower peak concentrations in the breakthrough curve (Figure 7.6) and an increase in the concentration of kaolinite colloids increased retardation of Pb(II), which demonstrates that the colloids were immobile within the sand bed. If kaolinite colloids were highly mobile and released from the bed (Roy and Dzombak 1997; Ryan and Elimelech 1996; Sainers and Hornberger 1996; Yin et al. 2010), transport would be facilitated because lead favorably sorbs to colloids (Riotte et al. 2003; Sheppard et al. 1980; Torok et al. 1990). Additionally, the flow rate (Darcy velocity), which ranged between 0.3 ~ 1 cm / min (typical of groundwater velocity (Camesano and Logan 1998)), was not significant in Pb(II) transport, with breakthrough times that were similar in all kaolinite concentration levels,

regardless of flow rate. The similar shapes of the breakthrough curves indicated rapid sorption of Pb(II) (Figure 7.4), which resulted in the similar masses of sorbed Pb(II) despite differences in flow rate. In addition, very high flow rates can shear and detach immobile colloids from the sand bed by large hydrodynamic force (Bradford et al. 2007; Kretzschmar et al. 1999; McDowell-Boyer 1992); however, that was not observed at the levels tested in this work.

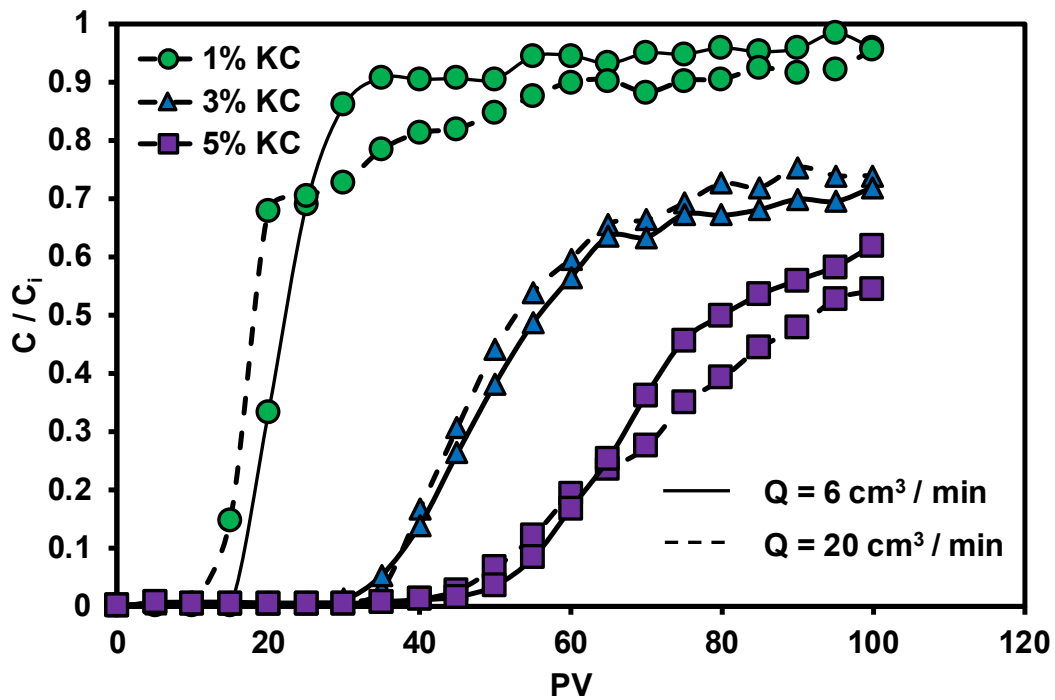


Figure 7.6. Pb(II) breakthrough curves under two flow rates and three KC: $Q = 6$ and $20 \text{ cm}^3 / \text{min}$ are corresponding to low and high v_s for each KC in Table 7-1, elapsed time for $Q = 6$ and $20 \text{ cm}^3 / \text{min}$ were roughly 9.5 hrs and 2.8 hrs, and $C_i \approx 5 \text{ mg/L}$ and deionized water was used for all cases.

Quantitative comparison of the Pb(II) breakthrough curve in each experimental condition was achieved by determining the calculated bed efficiency (β) and Pb(II) saturation.

$$\beta = 1 - \left(\sum_{j=1}^{PV_f/\lambda} (\lambda \cdot ((C/C_i)_j + (C/C_i)_{j+1}) / 2) \right) / PV_f, \quad (7-13)$$

where PV_f is the elapsed pore volume for the experiment ($PV_f = 100$ in this study), λ is the pore volume interval of experimental measurement ($\lambda = 5$ in this work), and j is an order of measured normalized concentration starting from 0 pore volumes ($j = 21$ corresponds to the normalized concentration at 100 pore volumes in this work). Then, Pb(II) saturation of the bed can be expressed as:

$$Pb(II) \text{ saturation} = (C_i \cdot V_{PV} \cdot \beta \cdot PV_f) / \left(\sum_{k=1}^N (q_{\max})_k \cdot W_k \right), \quad (7-14)$$

where V_{PV} is the volume of 1 pore volume calculated by the corresponding porosity of the bed, N is the total number of materials in the bed ($N = 2$ in this study), $(q_{\max})_k$ and W_k are the experimentally determined maximum adsorption capacity of Pb(II) (mg / g) (Table 7-3) and the weight of k th material in the bed (g), respectively.

β values for the breakthrough curves demonstrated that more Pb(II) was removed by the bed as the kaolinite content increased (Figure 7.7), and, Pb(II) saturation decreased as the kaolinite content increased, implying that many available adsorption sites were still available in the sand-kaolinite bed at kaolinite concentration = 5 % after 100 pore volumes of flow for the Pb(II) solution. This means that roughly 50 % of the sorption sites remained unbound when the kaolinite concentration was 5 %. Lead saturation was approximately 1 for kaolinite content equal to 1 %, meaning that the adsorption of Pb(II) in the bed would

not occur at any significant level after 100 pore volumes of flow due to the low maximum adsorption capacity. High Pb(II) saturation led to $C / C_i \sim 1$ in the breakthrough curve after 100 pore volumes, which would remain true unless solution chemistry was changed. β and Pb(II) saturation also showed the insignificance of flow rate in Pb(II) transport (Figure 7.7), which was consistent with the breakthrough curves exhibited in Figure 7.6. Overall, the kaolinite content retained in the sand medium was more crucial than flow rate in Pb(II) transport, particularly for kaolinite colloids that were immobile.

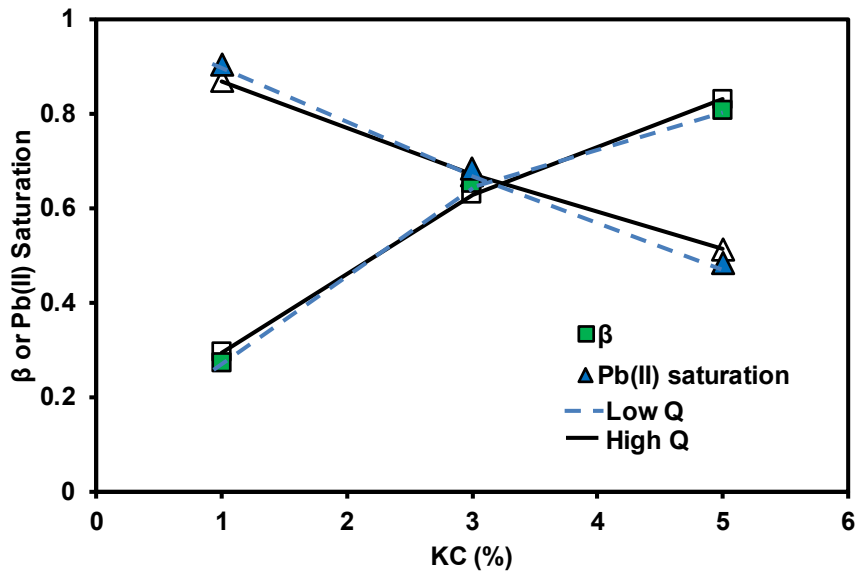


Figure 7.7. Calculated β and Pb(II) saturation of the bed from Equation (7-13) and (7-14), respectively according to kaolinite concentration and flow rate.

7.4.2.3 Impact of pH

Kaolinite has a 1:1 clay structure with one alumina octahedral sheet (i.e., gibbsite) and one silica tetrahedral sheet (i.e., silica sheet) held together through hydrogen bonding. The permanent negative charges of kaolinite colloids are attributed to isomorphous substitution in the mineral structure and uncompensated charge at the edge of the colloids (Mitchell and Soga 2005). Because the hydroxyl groups ($\equiv\text{SOH}$) located on the surface and edge of the kaolinite particles are amphoteric, the surface charges are highly sensitive to pH. At high pH, H^+ ions release into solution from surface hydroxyl groups ($\equiv\text{SOH} \rightarrow \equiv\text{SO}^- + \text{H}^+$), a process that is known as deprotonation of surface groups. Negatively charged $\equiv\text{SO}^-$ sites result in an increase in the adsorption of metal species, forming metallic surface complexes such as $\equiv\text{SOMe}^+$ or $\equiv\text{SOMeOH}$. In contrast at low pH, the surface hydroxyl groups sorb a proton to become $\equiv\text{SOH}_2^+$ through protonation ($\equiv\text{SOH} + \text{H}^+ \rightarrow \equiv\text{SOH}_2^+$), which leads to a decrease in adsorption of metal species (Gu and Evans 2008). This trend is reflected to the experimental Pb(II) breakthrough curves measured in this work (Figure 7.8).

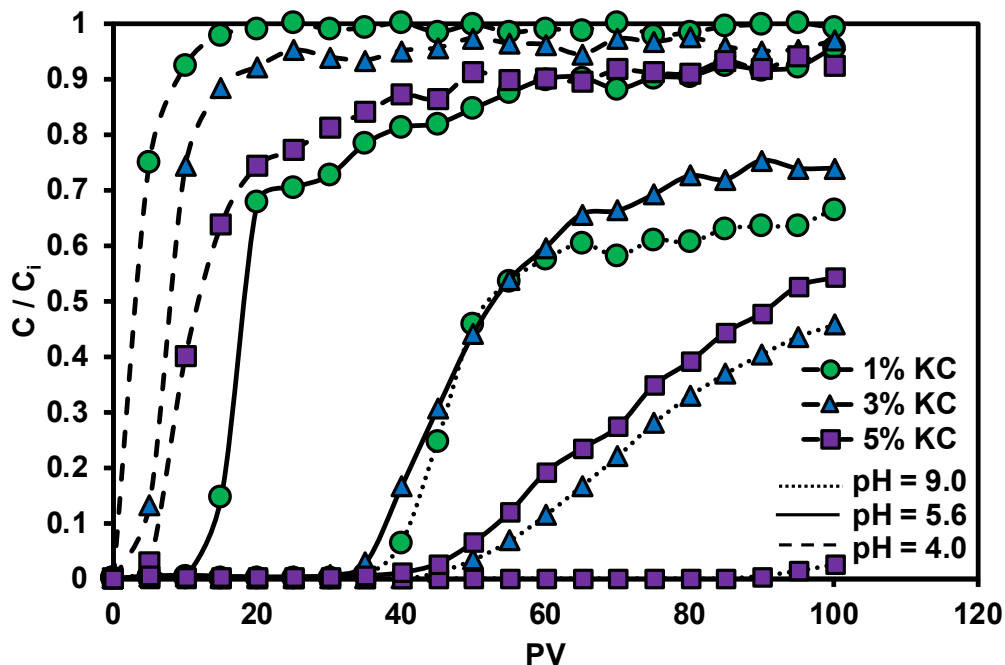


Figure 7.8. Pb(II) breakthrough curves according to pH at three different values of kaolinite concentration: $Q = 20 \text{ cm}^3 / \text{min}$, $C_i \approx 5 \text{ mg/L}$ and $IS \approx 0$ for all experiments.

Pb(II) breakthrough curves were significantly impacted by the variation of pH due to the change in surface charge: protonation at low pH (pH = 4.0) and deprotonation at high pH (pH = 9.0). Extremely early breakthrough was observed in the experiments conducted for a kaolinite content equal to 1 % at pH = 4.0, while almost no breakthrough was observed in experiments conducted at a kaolinite concentration of 5 % at pH = 9.0. Notably delayed Pb(II) breakthrough was observed at pH = 5.6 and kaolinite concentration equal to 1 % when compared to all kaolinite concentrations at pH = 4.0. This implies that a change in the pH of the solution more significantly impacted the Pb(II) transport than kaolinite concentration when concentration were approximately = 1 ~ 5 %. In addition, higher pH increased the impact of kaolinite concentration on the Pb(II) breakthrough curve due to

deprotonation of the kaolinite surface groups. The trend of breakthrough curves presented in Figure 7.8 is consistent with batch adsorption tests of heavy metals as a function of pH (Abollino et al. 2003; Benjamin and Leckie 1981; Farrah and Pickering 1979; Harter 1983). Except in the presence of ligands in solution, heavy metal species are generally more preferably adsorbed by the clays at high pH, as observed in the breakthrough curves in Figure 7.8.

Earlier elution of Pb(II) was observed in breakthrough curves measured at low pH (Figure 7.8), which was consistent with the measured values of zeta potential of kaolinite (Figure 7.9). While the zeta potential is not equal to the surface potential, it is a good estimator for the surface charge characteristics of the clay mineral. As seen in Figure 7.9, the pH at the point of zero charge of kaolinite was approximately 2.5, with a range of the measured zeta potential from 3 mV at low pH to -42 mV at high pH. These ranges are consistent to literature values of zeta potential for other natural kaolinites (Smith and Narimatsu 1993; Vane and Zang 1997; Williams and Williams 1978). All experiments were conducted above the point of zero charge, which resulted in negative values of zeta potential in all three experimental conditions (pH = 4, 5.6 and 9), with the zeta potential becoming more negative as pH increased. Consequently, the transport of Pb(II) was retarded at high pH due to the favorable adsorption of Pb species by immobile kaolinite colloids.

The Pb(II) saturation is indicative of the percentage of occupied sorption sites on the colloidal surfaces. At pH = 9 and kaolinite concentration equal to 1 % (Figure 7.10), beta is larger than one because the baseline calculation was based on q_{\max} of the sand and

the kaolinite in deionized water at pH \sim 5.6, which indicated that the adsorption capacity of the bed substantially increased as pH increased. Pb(II) saturation was 2.2 at pH = 9 and kaolinite concentration equal to 1 % after 100 pore volumes of flow. Interestingly, the shape of the breakthrough curve under these conditions (Figure 7.8) implies that Pb(II) adsorption would continue to occur after 100 pore volumes of flow. In contrast, Pb(II) saturation at pH = 4 and kaolinite concentration equal to 1 % was less than 0.5, but the breakthrough concentration maxed out at $C / C_i \sim 1$, which is indicative of the lower adsorption capacity of the bed at low pH. In addition, based on evaluated β values, the amount of adsorbed Pb(II) during transport in the bed was not significantly increased as the kaolinite concentration increased at pH = 4, which showed that the kaolinite concentration was not a critical factor in the transport of lead at low values of pH.

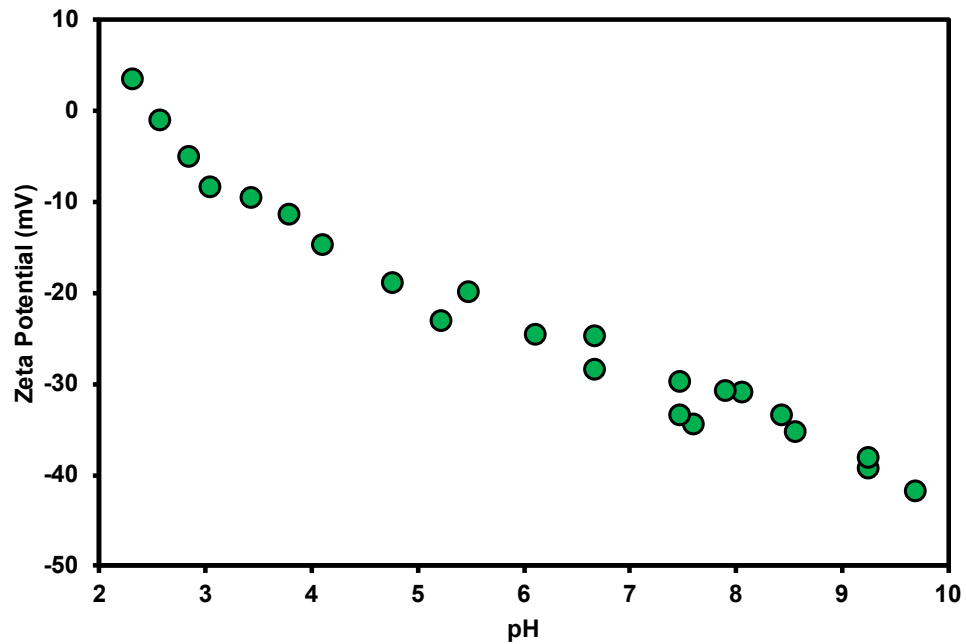


Figure 7.9. Zeta potential of kaolinite as a function of pH: Samples were prepared by mixing 500 mg/L of the kaolinite in deionized water for 30 min, and controlling pH with HNO_3 and NaOH .

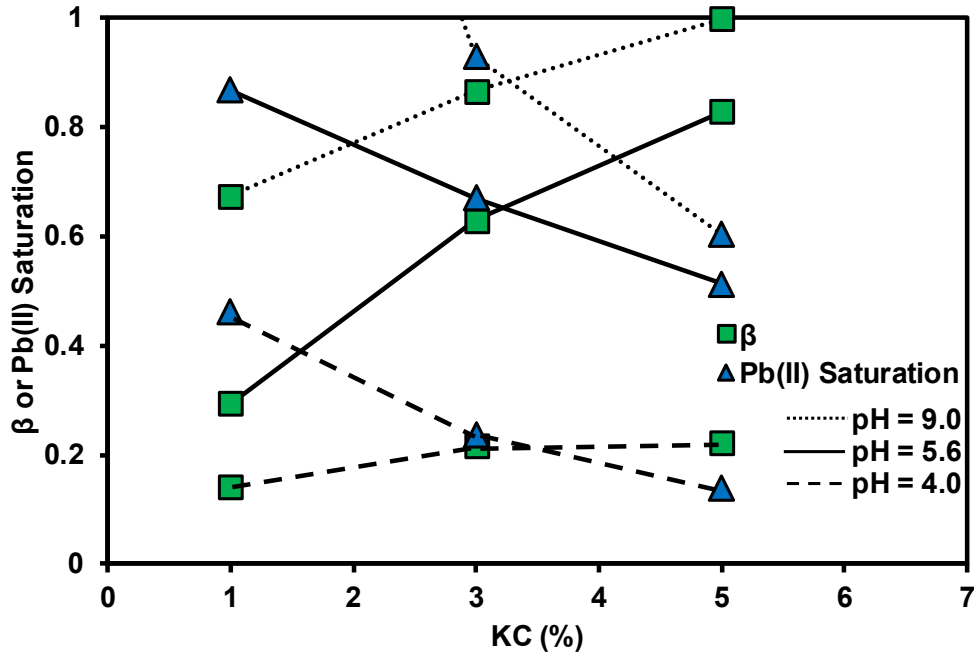


Figure 7.10. Calculated β and Pb(II) saturation of the bed from Equation (7-13) and (7-14) respectively according to kaolinite concentration and pH: Pb(II) saturation = 2.2 at kaolinite concentration = 1% and pH = 9 (data not shown).

7.4.2.4 Impact of Ionic strength (IS)

The impact of ionic strength on the deposition of negatively charged colloids on the sand medium has been well established in the literature, with generally more favorable attachment of colloids with an increase in ionic strength (Bradford et al. 2007; Compère et al. 2001; Ryan and Gschwend 1994), as is predicted by DLVO theory. This behavior facilitates contaminant transport at relatively low ionic strength due to the high repulsive force between colloids and sand grains at low ionic strength, which results in mobile colloids with sorbed contaminants (Saiers and Hornberger 1996; Um and Papelis 2002). However, for immobile colloids permanently retained in the sand bed (independent of ionic strength), retardation of Pb(II) transport increased as ionic strength decreased (Figure

7.11). This resulted from competitive adsorption between Pb(II) and Ca²⁺ on the immobile kaolinite colloids. Increased sorption of Ca²⁺ ions on kaolinite resulted in less availability of adsorption sites for Pb(II), leading to earlier Pb(II) breakthrough (Figure 7.11), lower β , and lower Pb(II) saturation (Figure 7.12).

In the case of competitive sorption for different cations with identical valence in solution, the cation with smallest hydrated radius has stronger affinity for the surface. The hydrated radii of Pb²⁺ ions and Ca²⁺ ions are 401 pm and 430 pm, respectively (Chen et al. 2010; Tan 2010), which indicates that Pb²⁺ ions preferentially adsorb to kaolinite when compared to Ca²⁺. Therefore, Pb(II) breakthrough curves should be similar, regardless of the presence of Ca²⁺ ions, particularly between ionic strength = 0 and 0.001 M. At values of ionic strength = 0 and 0.001 M with C_i = 5 mg/L and P_{CO2} (assumed = 10^{-3.5} atm), lead will be in the form of Pb²⁺ and should preferentially sorb to kaolinite; however, earlier breakthrough of Pb(II) was observed at ionic strength = 0.001 M. This may be attributable to similar hydrated radius of the two cations and high Ca²⁺ concentration in solution ([Pb(II)] = 2.41 × 10⁻⁵ M and [Ca²⁺] = 3.33 × 10⁻⁴ M). In addition, a slight increase of ionic strength from 0 to 0.001 M resulted in more facilitated Pb(II) transport than did an increase in ionic strength from 0.001 to 0.05 M (Figure 7.11 and Figure 7.12). Note that β and Pb(II) saturation decreased considerably between ionic strength changes from 0 to 0.001 M.

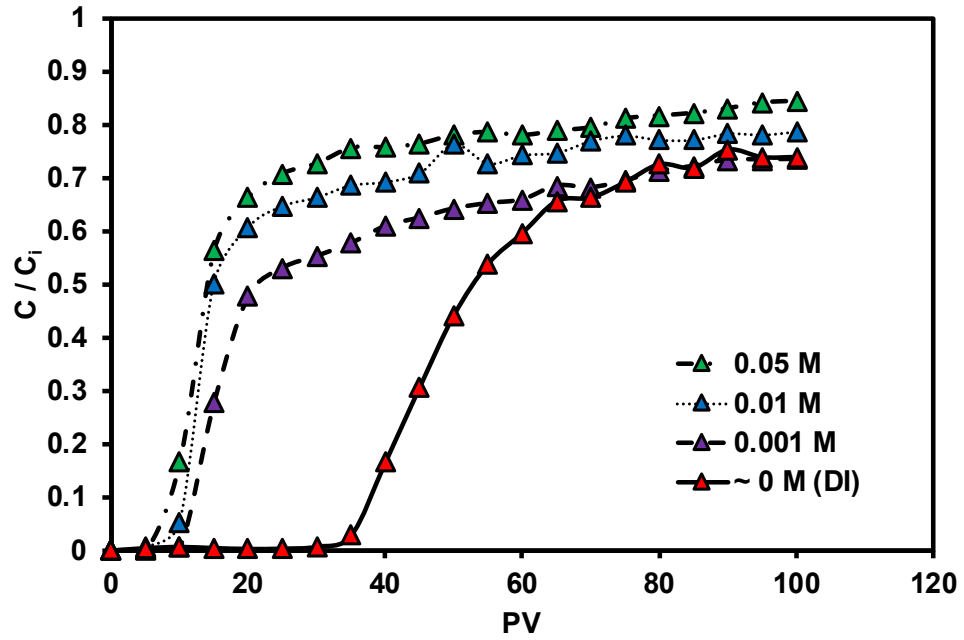


Figure 7.11. Pb(II) breakthrough curves according to four different level of IS: $Q = 20 \text{ cm}^3 / \text{min}$, $C_i \approx 5 \text{ mg/L}$, $\text{pH} \approx 5.6$ and $\text{KC} = 3 \%$ for all experiments.

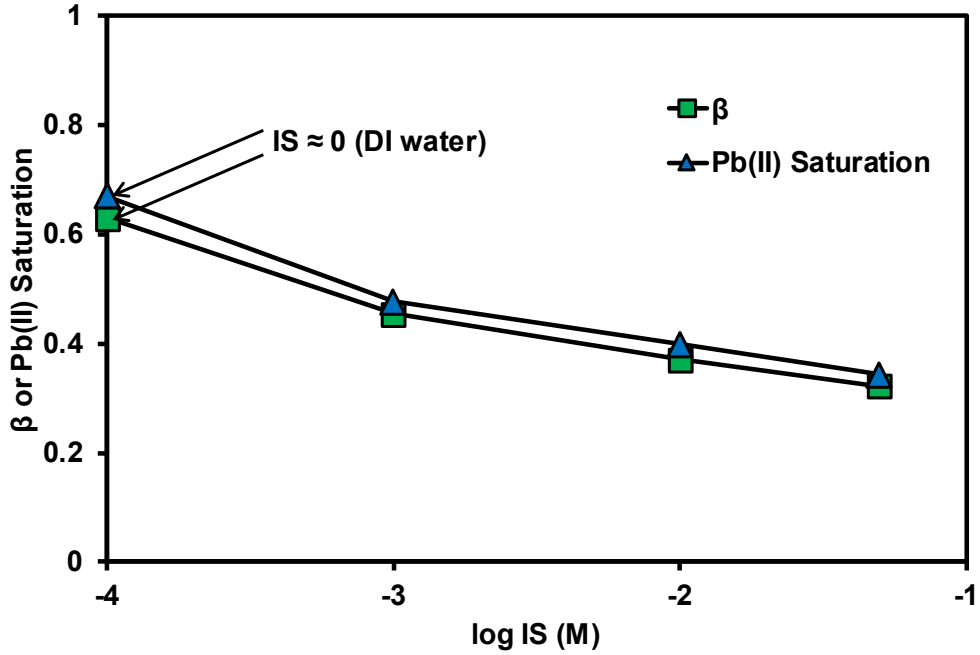


Figure 7.12. Calculated β and Pb(II) saturation of the bed from Equation (7-13) and (7-14) respectively according to IS.

7.4.3 Optimization analysis

The result of optimization analysis for the first-order coefficients (k_a and k_d in Equation (7-6) and k_c in Equation (7-3)) is presented in Table 7-5, with the parameters used in the analysis summarized in Table 7-4. Experimental breakthrough curves with early breakthrough and high plateau were well described by two first-order coefficients in Equation (7-6), while breakthrough curves with late breakthrough and low plateau were not well described by optimized k_a and k_d . In particular, R^2 values less than 0.8 for $IS > 0.001$ M (Table 7-5) implied that two first-order coefficients may not be sufficient to explain those breakthrough curves. By introducing an additional reaction term (presented in Equation (7-3)), three optimized coefficients (k_a , k_d and k_c) more accurately described the experimental breakthrough curves obtained ($R^2 > 0.95$ in all cases, Table 7-5). The bilinear shape of the breakthrough curve (rapid increase after breakthrough and slow

increase after additional pore volumes of flow) can be modeled using these three coefficients (Figure 7.11).

Because the algorithm used in the optimization analysis automatically gives optimized coefficients after satisfying the stop criteria, quantitative comparison of breakthrough curve in each condition is not feasible in second scenario since both of k_a and k_c are coefficients associated with the adsorption of Pb(II). They counterbalance each other with different magnitude. Nevertheless, by restricting the range of coefficient, k_a / k_d ratio in first scenario allows to compare each breakthrough curve, even though same k_a / k_d not necessarily gives the identical result. k_a / k_d ratio is not sensitive to the flow rate, but it increases as IS decreases and KC increases. This is consistent with the experimental results presented in Figure 7.6, Figure 7.8 and Figure 7.11. Notably, increase in k_a / k_d ratio along with KC increases implies that increase in immobile kaolinite not only increases the amount of adsorbed Pb(II), but also increases adsorption rate if desorption rate is constant. The optimization analysis of experimental Pb(II) breakthrough curves presented here might be the one advantageous way to model contaminant transport in large scale based on the results obtained in laboratory scale.

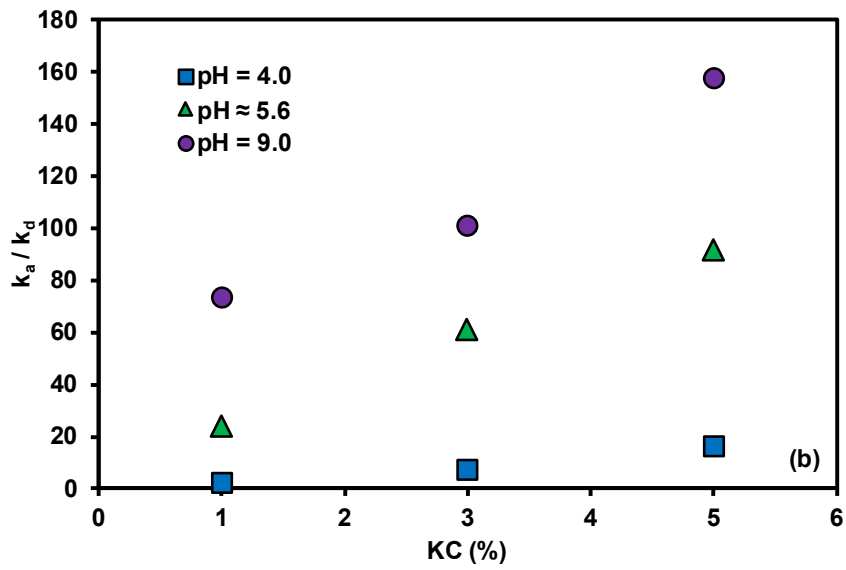
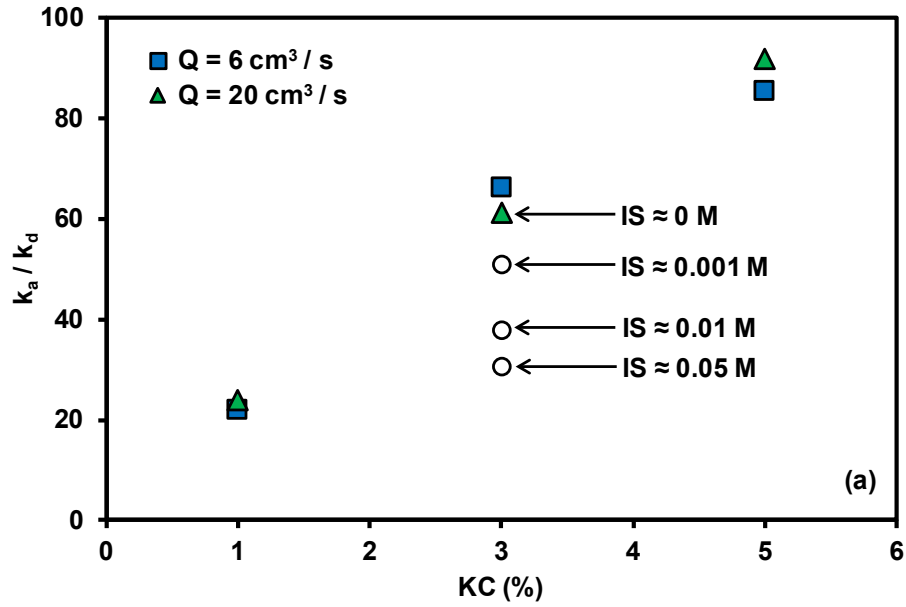


Figure 7.13. k_a / k_d ratio based on the optimization analysis according to KC : (a) flow rate and IS, (b) pH.

Table 7-4. Transport Parameters used in Optimization Analysis

Parameter	Q = 20 cm ³ / s			Q = 6 cm ³ / s		
	KC = 1 %	KC = 3 %	KC = 5 %	KC = 1 %	KC = 3 %	KC = 5 %
θ (-)	0.363	0.350	0.337	0.363	0.350	0.337
Sc (-)	0.01	0.03	0.05	0.01	0.03	0.05
f (-)	0.01					
$\alpha \times 10^{-2}$ (cm)	8.77	8.78	8.79	8.27	8.30	8.33
ρ (g / cm ³)	1.67					
q_{\max} (g / g)	1.081×10^{-6}					
K_d (cm ³ / g)	2.202×10^3					
ω (/ s)	1.859×10^{-3}					
Pe' (-)	92.72	97.26	102.19	27.81	29.18	30.66
τ (-)	0.74	0.73	0.72	0.74	0.73	0.72
$D_m' \times 10^{-5}$ (cm ² / s)	1.76	1.74	1.72	1.76	1.74	1.72
$D \times 10^{-3}$ (cm ² / s)	3.99	4.14	4.30	1.14	1.19	1.23

Note: $f = 0.01$ assuming that most of the Pb(II) adsorption onto the sand takes place kinetically (Equation (7-4) and (7-5)), q_{\max} , K_d and ω are adopted from the kinetic adsorption test (Table 7-3).

Table 7-5. Results of Optimization Analysis in Two Scenarios for Each Condition

Experimental condition				First scenario (k_a and k_d)			Second scenario (k_a , k_d and k_c)			
KC (%)	Q (cm ³ /s)	pH	IS	$k_a \times 10^{-2}$ (/s)	$k_d \times 10^{-4}$ (/s)	R ²	$k_a \times 10^{-2}$ (/s)	$k_d \times 10^{-4}$ (/s)	$k_c \times 10^{-5}$ (/s)	R ²
1	6	≈ 5.6	≈ 0	28.6	131	0.975	667.3	3146	0.87	0.996
3	6	≈ 5.6	≈ 0	2.96	4.46	0.939	56.06	114	2.27	0.999
5	6	≈ 5.6	≈ 0	8.1	9.48	0.972	1727	2542	2.25	0.999
1	20	≈ 5.6	≈ 0	5.02	21	0.88	836.5	4843	8.06	0.96
3	20	≈ 5.6	≈ 0	11.2	18.3	0.94	362.3	754	6.79	0.997
5	20	≈ 5.6	≈ 0	19.3	21.1	0.989	60.3	82	7.22	0.998
1	20	4	≈ 0	0.92	35.1	0.958	1.01	39	2.36	0.968
3	20	4	≈ 0	12.4	169	0.933	17.1	245	7.05	0.991
5	20	4	≈ 0	2.67	15.7	0.86	6.29	52	9.35	0.971
1	20	9	≈ 0	8.08	11.6	0.879	999.9	2100	9.28	0.987
3	20	9	≈ 0	0.202	20.3	0.983	146.2	195	9.61	0.999
5	20	9	≈ 0	577.2	366	0.965	582.5	370	5.89×10^{-7}	0.965
3	20	≈ 5.6	0.001	1.94	3.81	0.781	10.01	52	20.2	0.954
3	20	≈ 5.6	0.01	1.62	4.27	0.689	49.4	365	22.8	0.958
3	20	≈ 5.6	0.05	1.57	5.15	0.701	18.5	144	18.7	0.973

7.5 Summary

This experimental study investigated the transport behavior of Pb(II) in the presence of immobile kaolinite colloids in a sand medium. The transport was measured as a function of ionic strength, pH, and immobile kaolinite concentration. Based on the measured breakthrough curves and the results of an optimization analysis, the following conclusions can be drawn:

1. Based on the results of batch adsorption tests, Pb(II) adsorption capacity of the sand-kaolinite bed depended on the immobile kaolinite concentration, even at

concentrations = 1 %. The amount of immobile kaolinite colloids determined the Pb(II) transport behavior within the bed.

2. Earlier Pb(II) breakthrough resulted when the inlet Pb(II) concentration was high due to the relatively limited amount of available adsorption surface sites on the immobile kaolinite colloids.
3. Flow rate was not a significant factor for the Pb(II) transport when the kaolinite concentration ranged from 1 % to 5 %, based on these experimental results. In contrast, a decrease in pH and increase in ionic strength facilitated Pb(II) transport due to the protonation of surface hydroxyl groups on kaolinite colloids and competitive adsorption between other cations and Pb(II).
4. Bed efficiency and Pb(II) saturation evaluated from the experimental breakthrough curves revealed that an increase in kaolinite concentration significantly impacted the breakthrough curve at high pH, while the kaolinite concentration was not a critical factor at low pH.
5. Optimized k_a and k_d allowed quantitative representation of experimental Pb(II) breakthrough curves; however, introducing an additional reaction coefficient k_c resulted in more accurate modeling of the curves.

CHAPTER 8 AN EXPERIMENTAL STUDY OF COTRANSPORT OF HEAVY METALS WITH KAOLINITE COLLOIDS

8.1 Introduction

Contamination of groundwater caused by human activities, such as uncontrolled waste disposal, septic system, landfills, and agricultural runoff, is of considerable concern due to its threat to public health. Among various possible contaminants present in groundwater, heavy metals are one of the most problematic contaminants because they are toxic to humans and challenging to treat because unlike organic contaminants, they cannot be degraded through biodegradation (Fu and Wang 2011; Khan et al. 2008; Wuana and Okieimen 2011). Heavy metals frequently remain in the soil matrix for extended periods of time, in either precipitated forms or adsorbed onto organic/inorganic matter, but can be remobilized by the geochemical alterations in the pore fluid (e.g., changing pH) (Yin and Allen 1999). Therefore, an extensive amount of research has focused on the remediation of heavy metals by means of chemical, biochemical, and physicochemical technologies (Hashim et al. 2011); for instance, permeable reactive barriers, adsorption, and electrokinetic treatment are three typical technologies for physicochemical treatment of heavy metals (Brunori et al. 2005; Lee and Kim 2010; Mulligan and Yong 1999). While many of the mechanisms that influence the transport of heavy metals in the subsurface are understood, fundamental questions remain regarding transport of metals that are sorbed to colloidal particles that transport with the groundwater. To select a proper treatment technology that ensures efficiency in physicochemical treatment, fundamental understanding of these mechanisms controlling heavy metal transport and migration in soil is needed.

To explain contaminant transport in saturated porous media, a two-phase model has been conventionally applied to describe the partitioning of contaminant between the immobile solid phase and the mobile aqueous phase (van Genuchten and Wierenga 1976). However, a three phase model is now generally accepted when there are mobile or immobile colloids present in the medium (Corapcioglu and Kim 1995; Šimůnek et al. 2006; Um and Papelis 2002). A colloid is typically defined as a relatively small particle, less than 10 μm (McCarthy and Zachara 1989), which is suspended due to electrical forces and can either travel through pore space with sorbed contaminants or attach to the fixed bed. Colloidal transport or retention may not be crucial in contaminant transport if the reaction between the colloid and the contaminant is negligible, but the transport of sorbed contaminants can be facilitated, or retarded, depending on the behavior of colloid transport or retention (Sen and Khilar 2006). For example, previous experimental studies reported that the transport of radionuclides (e.g. ^{137}Cs and ^{239}Pu) can be enhanced or facilitated by the mobile clay or oxide colloidal particles and can transport much faster than advective-dispersive flux (Kretzschmar et al. 1999; Penrose et al. 1990; Torok et al. 1990). In these cases, predicting the contaminant transport without taking colloids into account can significantly underestimate the travel distance of the contaminant. To properly understand this phenomenon, transport of colloids and contaminant and their reaction mechanisms in the colloid-contaminant-solid system should be taken into account simultaneously (Flury and Qiu 2008).

Colloidal particles are made up of a variety of different materials including organic matter, metal oxides, bacteria, and a variety of other nano-sized minerals (Bradford et al. 2015); however, clay colloids are one of the predominant types encountered in the

subsurface environment. Quantifying the transport of clay colloids is more challenging than other types of colloids due to two properties of clay minerals: aggregation behavior that is dependent on the solution chemistry of the pore fluid (Palomino and Santamarina 2005) and highly variable sizes, up to a coefficient of uniformity of 10 (Mitchell and Soga 2005). Most importantly, clay colloids have a strong tendency to act as adsorbents for heavy metals and radionuclides (Bhattacharyya and Gupta 2008; Li and Li 2000; Norrfors et al. 2016; Rabung et al. 2015; Sari et al. 2007; Syed 1999; Veli and Alyüz 2007). This implies that highly mobile clay colloids in porous media may act as carriers and facilitate the transport of contaminants that are favorably adsorbed to the clay colloids or conversely, immobile clay colloids may retard the transport of heavy metals through sorption.

Experimental research into the transport of heavy metals in the presence of colloids has demonstrated often contradictory results in the transport of metals. Sen et al. (2002) demonstrated that Ni(II) transport was delayed in a kaolinite-sand bed as the fraction of kaolinite increased. In contrast, Yin et al. (2010) and Sun et al. (2010) showed that the transport of Pb(II) was facilitated by mobile clay colloids at the field and laboratory scales. These results indicate that the presence of clay colloids do impact the transport behavior of heavy metals, but questions remain regarding the mechanisms. Batch kinetic studies (Al-Degs et al. 2003; Sari et al. 2007; Tang et al. 2009) demonstrated that flow rate may be one of the dominant factors for the transport of heavy metals because higher flow rate/lower residence time of heavy metals resulted in breakthrough before reaching sorption equilibrium. In addition, a change in flow rate also changes the retention profile of clay colloids due to different levels of hydrodynamic forces applies to the colloids (Compère et al. 2001; Molnar et al. 2015; Pazmino et al. 2014; Ryan and Gschwend 1994; Tufenkji and

Elimelech 2004). These two essential pieces of knowledge must be taken into account simultaneously to properly investigate clay colloid associated heavy metal transport under the different levels of flow rate.

The objective of the work performed in this chapter was to experimentally investigate the impact of flow rate on the behavior of heavy metal transport in multiple or single metal systems as a function of clay colloid concentration. Single or multiple heavy metals were injected into the sand column, with varying clay colloidal concentration at two different flow rates. Breakthrough curves for each heavy metal and retention profiles of the clay colloids were measured, and the bed efficiency and saturation for each metal were determined based on the batch adsorption test results. In addition, an optimization analysis was performed in order to quantitatively account for the reaction between immobile clay colloids (i.e., retained clay) and metal by evaluating optimized first order coefficients.

8.2 Materials and methods

8.2.1 Materials

ASTM 20/30 sand (median grain size = 720 μm from sieve analysis) and Georgia kaolinite were selected as the sand medium and clay colloidal minerals. The specific gravity of sand and kaolinite were 2.65 and 2.52, respectively (ASTM D584), and median size and specific surface of kaolinite were 0.45 μm and 52 m^2 / g obtained by hydrometer test (ASTM D422) and methylene blue method (Santamarina et al. 2002) (Table 3-1). Deionized water ($> 18 \text{ M}\Omega \cdot \text{cm}$, Barnstead E-pure) was used for all experiments. The sand was washed with deionized water several times and submerged in an ultrasonic bath for 2 hours to eliminate any impurities on the sand surface prior to use. All metal solutions were

prepared by diluting 3000 mg L⁻¹ of stock solution. Metal solutions including Cu(II), Pb(II), and Zn(II) were prepared by dissolving Cu(NO₃)₂, Pb(NO₃)₂, and Zn(NO₃)₂ to prepare a stock solution. CaCl₂ was added to control the ionic strength of the solution and all chemicals (Cu(NO₃)₂, Pb(NO₃)₂, Zn(NO₃)₂, CaCl₂, and NaBr) were obtained from Sigma Aldrich Corporation and Fisher Scientific and were used as received.

8.2.2 Column experiments and experimental conditions

Column tests (5.08 cm diameter by 15.24 cm height) were performed with the sand as the bulk soil media. Perforated aluminum discs and #200 plastic mesh (opening size of 75 μm) were installed at the top and bottom of the column to distribute inlet flow and prevent the loss of sand at the outflow. The metal solutions, mixed with kaolinite colloids, were injected to the top of the column for 10 pore volumes of flow using a peristaltic pump (Cole-Parmer). The effluent was collected in a fraction collector (ISCO) at the outlet of the column. A pulse dampener was installed between the pump and the column inlet to minimize the pulsating flow generated by the peristaltic pump. Metal concentration of samples collected in the fraction collector were measured using inductively coupled plasma – optical emission spectrometry (ICP-OES, PerkinElmer) and the concentration of kaolinite colloids (C_c) was determined by measuring turbidity (Orbeco-Hellige Inc.), which showed a good positive linear relation with C_c (data not shown here). After measuring turbidity, all samples collected at the outlet were filtered using 0.45 μm microfilter to remove all kaolinite colloids before measuring the metal concentration.

Sand was packed in the column through wet pluviation to ensure saturation, and resulted in porosity = 0.365. The metal solution was mixed with the kaolinite suspension

and was placed in an ultrasonic bath for 1 hour to stabilize the kaolinite colloids. Next, the suspension was continuously stirred using a magnetic stirrer for an additional hour to reach equilibrium for heavy metal sorption onto kaolinite before injection. Competitive and single metal batch kinetic studies of the kaolinite used in this study revealed that 20 min was sufficient to reach equilibrium at an initial concentration (C_i) = 5 mg L⁻¹. Therefore, the injection of the suspension into column after 2 hours of contact time between the metals and the kaolinite was performed to ensure that there was no reaction between mobile kaolinite and heavy metal species during the injection, unless the solution chemistry (e.g. ionic strength or pH) was changed. The ionic strength (IS) was controlled at 3×10^{-3} M for all experiments using CaCl₂ and two Darcy velocities of 3.7×10^{-2} and 1.23×10^{-2} cm s⁻¹ were tested. C_i was set to 5 mg L⁻¹ for both types of experiments (cotransport of three metals (Cu, Pb, and Zn) and transport of single metals) and the proper amount of kaolinite corresponding to 100, 500 and 1000 mg L⁻¹ were added to the solution. 500 and 1000 mg L⁻¹ kaolinite concentration were selected to identify the effect of kaolinite concentration under this short-term experiment, even though it is higher than the clay concentration normally encountered in the natural subsurface (Saiers and Hornberger 1996; Wikiniyadhane et al. 2015). After 10 PV of injection of a metal-kaolinite suspension, retention profile of kaolinite were obtained by sampling sand every 1.27 cm (0.5 in) depth. The samples were vigorously stirring for 10 minutes with amount of water, and the turbidity of the suspension was determined. Prior to introducing metal-kaolinite suspension, approximately 5 pore volumes of background solution (IS = 3×10^{-3} M of CaCl₂ with deionized water) was injected to remove any unbound particles that may have originated

in the silica sand and also to preequilibrate the sand with the background solution. In addition, the sand was replaced between each column test.

8.2.3 Batch adsorption equilibrium and kinetic test for single and multi-metal

Batch adsorption tests were performed for the single and multi-metal systems to evaluate metal saturation of the column experiments. Equilibrium batch tests were used to obtain maximum adsorption capacity (q_{\max}) and kinetic batch tests were used to determine the elapsed time to reach equilibrium. Tests were performed by adding 30 ml of metal solution to 500 mg of kaolinite in 50 ml test tubes. The tubes were shaken by the rotating shaker at approximately 30 rpm for 24 hours with $C_i = 5 \sim 1000 \text{ mg L}^{-1}$ for the equilibrium test. Tubes were sampled at the following intervals: 5, 10, 15, 20, 30, 40, 60, 120, 240, and 1440 minutes. After the targeted elapsed time, the suspension was centrifuged at 3000 rpm, filtered using a $0.45 \text{ }\mu\text{m}$ microfilter, and the supernatant metal concentration was determined. In the competitive sorption tests, metal ratios of 1:1:1 initial concentration for Cu, Pb and Zn were used and the ionic strength was fixed to $3 \times 10^{-3} \text{ M}$ in all tests. The maximum sorption capacity (q_{\max}) of each equilibrium test was evaluated using the Langmuir isotherm model (Equation (7-11)) (Ghorai and Pant 2005; Langmuir 1918).

8.3 Mathematical model

8.3.1 Kaolinite colloid transport

Kaolinite colloid transport was described using the advection-dispersion equation combined with first order rate terms for attachment, detachment, and straining (Equation (3-5)). In addition, to account for the blocking of colloids on the sand surface because

available sites for attachment of colloids decrease over time and also for the characteristic of straining with respect to space, Equation (3-8) and Equation (3-6) were used for ψ_{att} and ψ_{str} (Adamczyk et al. 1994; Bradford et al. 2003; Johnson and Elimelech 1995).

8.3.2 Cotransport of kaolinite colloid and heavy metal

Colloid associated heavy metal transport can be explained by considering the adsorbed metal on the solid (sand) phase, on the mobile colloids (kaolinite), and on the immobile colloids (kaolinite) during transport. In addition, the two site model can be taken into account to simulate the reaction between sand and metal (van Genuchten and Wagenet 1989). Consequently, the mass balance equation of metals in saturated porous media can be expressed as (Šimůnek et al. 2006):

$$\begin{aligned} & \frac{\partial \theta C}{\partial t} + \rho \frac{\partial S_e}{\partial t} + \rho \frac{\partial S_k}{\partial t} + \frac{\partial \theta C_c S_{mc}}{\partial t} + \rho \frac{\partial S_c S_{ic}}{\partial t} \\ & = \frac{\partial}{\partial x} \left(\theta D \frac{\partial C}{\partial x} \right) - \frac{\partial q C}{\partial x} + \frac{\partial}{\partial x} \left(\theta S_{mc} D_c \frac{\partial C_c}{\partial x} \right) - \frac{\partial q C_c S_{mc}}{\partial x} \end{aligned} \quad (8-1)$$

where C (M L^{-3}) is the dissolved metal concentration, S_e (M M^{-1}) and S_k (M M^{-1}) are metal mass adsorbed to the sand instantaneously and kinetically, respectively, S_{mc} (M M^{-1}) and S_{ic} (M M^{-1}) are metal mass adsorbed to the mobile and the immobile kaolinite colloid, respectively, and D ($\text{L}^2 \text{T}^{-1}$) is the dispersion coefficient for metal. By applying the Langmuir isotherm to the sand-metal reaction each time derivative term presented in Equation (8-1) can be expressed as:

$$\frac{\partial S_e}{\partial t} = f K_d q_{\text{max}} \frac{\partial C}{\partial t} \quad (8-2)$$

$$\frac{\partial S_k}{\partial t} = \omega \left[(1-f) \frac{q_{\max} K_d C}{1 + K_d C} - S_k \right] \quad (8-3)$$

$$\begin{aligned} \frac{\partial \theta C_c S_{mc}}{\partial t} = \frac{\partial}{\partial x} \left(\theta S_{mc} D_c \frac{\partial C_c}{\partial x} \right) - \frac{\partial q C_c S_{mc}}{\partial x} + \theta \psi_m k_{amc} C - \theta k_{dmc} C_c S_{mc} \\ - \theta (\psi_{att} k_{att} + \psi_{str} k_{str}) C_c S_{mc} + \rho k_{det} S_c S_{ic} \end{aligned} \quad (8-4)$$

$$\rho \frac{\partial S_c S_{ic}}{\partial t} = \theta \psi_i k_{aic} C - \rho k_{dic} S_c S_{ic} + \theta (\psi_{att} k_{att} + \psi_{str} k_{str}) C_c S_{mc} - \rho k_{det} S_c S_{ic} \quad (8-5)$$

where f (-) is the fraction of instantaneous sites of sand, ω (T^{-1}) is the first order rate constant, k_{amc} (T^{-1}) and k_{dmc} (T^{-1}) are the attachment and detachment coefficients associated with the metal-mobile kaolinite colloid, k_{aic} (T^{-1}) and k_{dic} (T^{-1}) are the attachment and detachment coefficients associated with metal-immobile kaolinite colloid, and ψ_m (-) and ψ_i (-) are dimensionless variables varied from 0 to 1 based on the reference number of mobile and immobile kaolinite colloids.

8.3.3 Optimization analysis

Optimization analysis was performed to evaluate k_{aic} , k_{dic} , and ω for each experimental breakthrough curve by solving the governing equation presented in the previous section (Equation (3-5), (8-1), (8-2), (8-3), (8-4), and (8-5)). An implicit finite difference method was used to solve the transport equations and the Picard iterative scheme was applied in each time step until the mass balance error (Equation (8-1)) was less than $|10^{-8}|$ % (Huang et al. 1998). First-type boundary conditions and a no flux boundary condition were applied to the inlet and outlet of the column, respectively. With the assumption that the transport of kaolinite colloids was not affected by the adsorption of metal, regardless of their mobility (mobile or immobile colloids) (Šimůnek et al. (2006)),

the equations for kaolinite colloid transport (Equation (3-5), (3-8), and (3-6)) were solved independently with the equations for colloid associated metal transport (Equation (8-1), (8-2), (8-3), (8-4) and (8-5)). Therefore, the optimized first order coefficients involved in colloid transport (k_{att} , k_{det} and k_{str}) were obtained based on the experimental retention profile. C_c and S_c ($= S_{att} + S_{str}$, where S_{str} ($M M^{-1}$) is the amount of strained kaolinite colloid) from optimized k_{att} , k_{det} and k_{str} in every time step throughout the discretized space were applied to solve the Equation (8-1), (8-4) and (8-5). S_{max} (Equation (3-6)) was set to 0.029 by assuming that shapes of the kaolinite colloid cluster and the silica sand were spherical (Equation (3-9) and (3-10)). In addition, parameters associated with the metal adsorption to sand (ω , f , q_{max} , K_d in Equation (8-2) and (8-3)) were evaluated by the optimization analysis from the experimental breakthrough curve in the absence of kaolinite colloids. Langmuir parameters (q_{max} and K_d) of the sand for each heavy metal can be obtained by batch adsorption equilibrium test, but the values for the optimized q_{max} and K_d of the sand from the column experiment were used here owing to the difficulty related to the extremely small amount of sorption (q_{max}) on pure silica sand.

Br^- (bromide) was used as a non-reactive tracer to determine D (Equation (8-1)) of the sand medium and the optimized D values were assumed to be same as the D value for the heavy metal species due to their similar molecular size relative to the sand grains, which assumes that the flow path of the metal species was similar to the Br^- ion (Pang and Šimůnek (2006)). A solution of approximately 2 mg / L of Br^- (dissolved NaBr) was injected into the column, and the breakthrough curve of Br^- was measured using UV-spectrophotometer (Shimadzu UV-1800) at a wavelength equal to 197 nm. The dispersion of kaolinite colloids (D_c in Equation (8-1)) could not be determined experimentally due to

the considerable amount of kaolinite colloid retention during flow through the column; therefore, D_c was estimated using the empirical equations presented in Delgado (2007) which detailed a method to evaluate D_c empirically in the different regimes (diffusion dominated or mechanical dispersion dominated). The flow regime is determined by Peclet number ($= v_s d_s / D_m$, where v_s ($L T^{-1}$), where v_s is pore water velocity equal to q / n , q is flow rate ($L^3 T^{-1}$), n is the porosity, and D_m ($L^2 T^{-1}$) is the molecular diffusion coefficient determined using Stock-Einstein equation) (see section 7.2.2).

Because the metal-kaolinite suspension was preequilibrated before the injection, the initial condition of S_{mc} (Equation (8-1) and (8-4)) in all discretized depths was set equal to q_e (Equation (7-11)), which satisfies the total metal concentration of 5 mg L^{-1} based on the Langmuir isotherm. In addition, k_{amc} and k_{dmc} were back-calculated based on the batch kinetic test using the analytical solution in order to reduce the optimized parameters (Schijven and Hassanizadeh 2000):

$$\frac{C}{C_0} = \frac{k_{dmc} + k_{amc} \exp[-(k_{amc} + k_{dmc})t]}{k_{amc} + k_{dmc}} \quad (8-6)$$

where C_0 ($M L^{-3}$) is the initial metal concentration used in the batch kinetic test. The kaolinite concentration (16.7 g / L) for the batch kinetic test was applied as the reference kaolinite concentration (C_r) for ψ_m ($\psi_m = C_c / C_r$), while ψ_i was assumed equal to one in all optimization analysis because no information on the reference kaolinite concentration was available for immobile kaolinite colloids.

While it is well known that the size exclusion effect causes inconsistency between porosity and the colloid accessible volumetric water content (Bradford et al. 2003; Flury

and Qiu 2008; Sirivithayapakorn and Keller 2003), this effect becomes negligible for sand with uniform pore size distribution. Because the sand used in these experiments exhibited a uniform grain size distribution, implying that the pore size distribution was similarly uniform (Arya et al. 1999b), the colloid accessible volumetric water content and the pore water velocity of colloids were assumed equal to those values for the metal transport.

Table 8-1. Optimized Coefficients Associated with Metal Adsorption/Desorption to the Mobile Kaolinite Colloids (Equation (8-6)) Based on Batch Kinetic Test (ionic strength = 0.003 M, $C_r = 16.7 \text{ g / L}$)

Type	Experimental condition		Optimized results			
	Metal	$C_0 \text{ (mg L}^{-1}\text{)}$	$k_{amc} \times 10^2 \text{ (min}^{-1}\text{)}$	$k_{dmc} \times 10^2 \text{ (min}^{-1}\text{)}$	R^2	$SSRs \times 10^3$
Competitive	Cu	5	3.48	20.11	0.94	1.29
	Pb	5	10.23	21.40	0.98	2.07
	Zn	5	3.28	21.36	0.98	0.32
Single	Cu	5	11.30	46.31	0.99	0.24
	Pb	5	20.72	33.98	0.99	0.48
	Zn	5	3.92	19.33	0.88	3.27

Note: SSRs denotes the sum of squared residuals

Table 8-2. Optimized Rates (k_{att} , k_{det} and k_{str} in Equation (3-5)) Associated with the Transport of Kaolinite Colloids from the Experimental Retention Profiles after 10 Pore Volumes of Injection (ionic strength = 0.003 M)

Experimental condition			Optimized results			
C_{c0} (mg L ⁻¹)	q (cm min ⁻¹)	k_{att} (min ⁻¹)	k_{det} (min ⁻¹)	k_{str} (min ⁻¹)	R^2	$SSRs \times 10^7$
100	2.22	3.89	0.60	5.35	0.98	4.22
500	2.22	4.15	0.57	4.07	0.98	3.50
1000	2.22	5.78	0.89	3.29	0.99	0.23
100	0.74	0.59	0.35	6.11	0.96	1.07
500	0.74	0.57	2.69	4.33	0.99	9.25
1000	0.74	0.34	25.77	3.61	0.99	18.01

Note: C_{c0} denotes the inlet concentration of kaolinite colloid

Table 8-3. Optimized Langmuir Parameters for Three Metals in the Absence of Kaolinite Colloids. Data from Experimental Breakthrough Curves of Competitive Heavy Metal Transport and Dispersion Coefficients (D and D_c) of Metal and Kaolinite Colloids (ionic strength = 0.003 M)

Experimental condition		Optimized results								β and φ (Equation (8-7) and (8-8))	
Metal	q (cm ³ min ⁻¹)	D (cm ² min ⁻¹)	D _c (cm ² min ⁻¹)	f	ω × 10 ² (min ⁻¹)	K _d (cm ³ mg ⁻¹)	q _{max} × 10 ² (mg g ⁻¹)	R ²	SSRs × 10 ³	β × 10 ²	φ × 10 ²
Cu				0.22	10.26	3.13	7.09	0.99	8.62	19.32	2.95
Pb	2.22	0.66	1.09	0.23	9.62	6.52	9.52	1.00	6.59	33.79	3.85
Zn				0.61	43.82	0.95	5.77	0.99	27.51	12.80	2.41
Cu				0.33	2.00	3.89	7.68	1.00	6.32	20.83	2.94
Pb	0.74	0.60	0.37	0.26	2.20	8.62	9.56	1.00	2.96	37.19	4.22
Zn				0.69	591.63	1.25	5.81	1.00	7.71	13.49	2.52

8.3.4 Bed efficiency and metal saturation

Optimization analysis presented in the previous section is an effective way to quantitatively characterize the experimental breakthrough curves; however, quantitative descriptions of the breakthrough curves can also be performed with bed efficiency (β) and metal saturation of the bed (φ) (Sen et al. 2002). β and φ can be mathematically expressed as:

$$\beta = 1 - \left(\sum_{j=1}^{PV_f/\lambda} (\lambda \cdot ((C/C_i)_j + (C/C_i)_{j+1}) / 2) / PV_f \right) \quad (8-7)$$

$$\phi_{metal} = (C_i \cdot V_{PV} \cdot \beta \cdot PV_f) / \left(\sum_{k=1}^N ((q_{max})_{metal})_k \cdot W_k \right) \quad (8-8)$$

where PV_f (-) is the final pore volume for the experiment ($PV_f = 10$ in this work), λ (-) is the pore volume interval of experimental breakthrough curve ($\lambda = 0.4$ in this work), j is the index of experimental data in order of increasing time in the breakthrough curve, V_{PV} (L^3) is the volume of 1 PV of the bed, N is the total number of adsorbent sites in the bed, k is the index of the adsorbent, W_k (M) is the weight of the k^{th} material in the bed after the injection. β provides the fraction of metal species adsorbed to the bed while ϕ provides the adsorption efficiency of the bed, including the retained kaolinite colloids into account.

8.4 Results and discussion

8.4.1 Results of batch kinetic and equilibrium tests

For competitive sorption isotherms, the sorption preference follows the sequence $Pb > Cu > Zn$ (Figure 8.1(a)), which is consistent with past experimental results (Echeverría et al. 1998; Helios Rybicka et al. 1995). However, $q_{max(Cu)}$ is only slightly lower when compared to $q_{max(Pb)}$ and much higher than $q_{max(Zn)}$ in the single-metal systems (Figure 8.1(b)). Overall, q_{max} of Cu and Pb exhibited substantially higher values in the single-metal system when compared to multi-metal systems, while $q_{max(Zn)}$ remained similar regardless of competitive sorption. In addition, longer elapsed timeframes were required to reach equilibrium in the multi-metal systems (roughly 20 ~ 30 min) than in single-metal systems (roughly 10 ~ 20 min) (Figure 8.2), and lower C / C_0 at equilibrium in the single-metal system for the three metals led to larger k_{amc} / k_{dmc} values (Table 8-1).

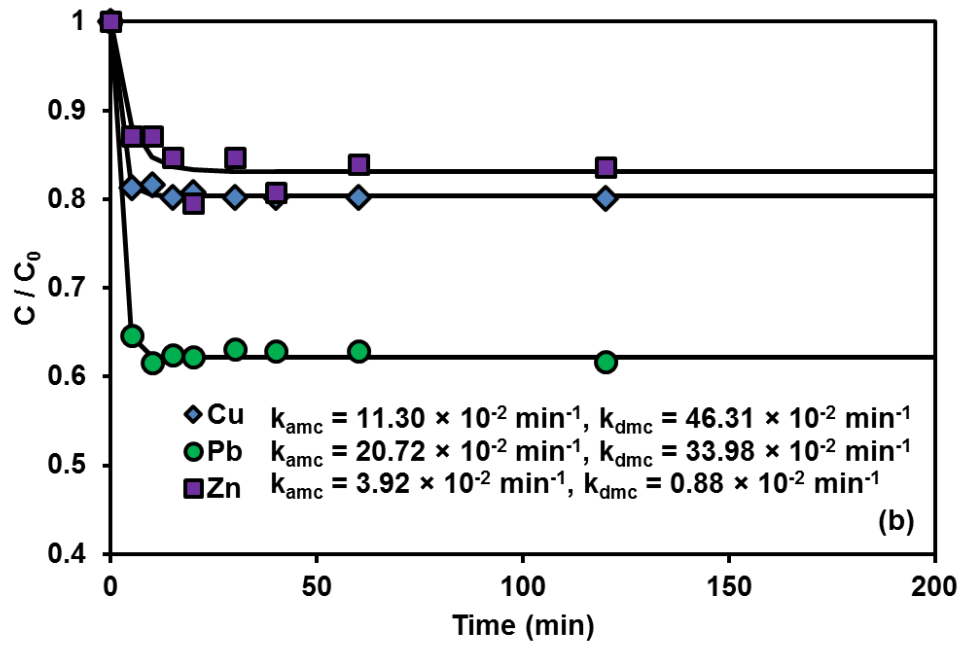
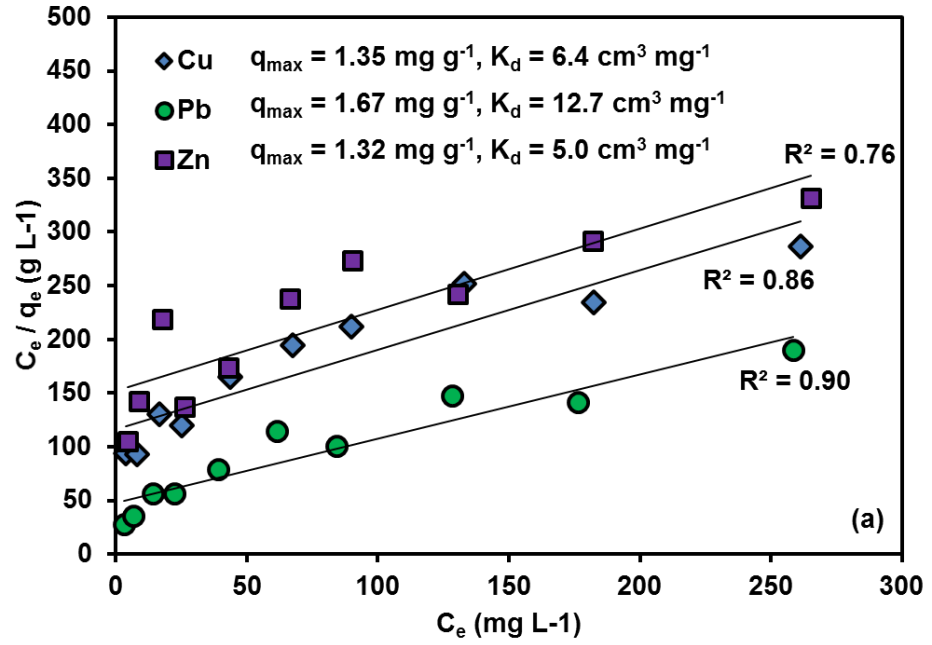


Figure 8.1. Batch equilibrium test results of kaolinite colloids in (a) multi-metal system and (b) single-metal system.

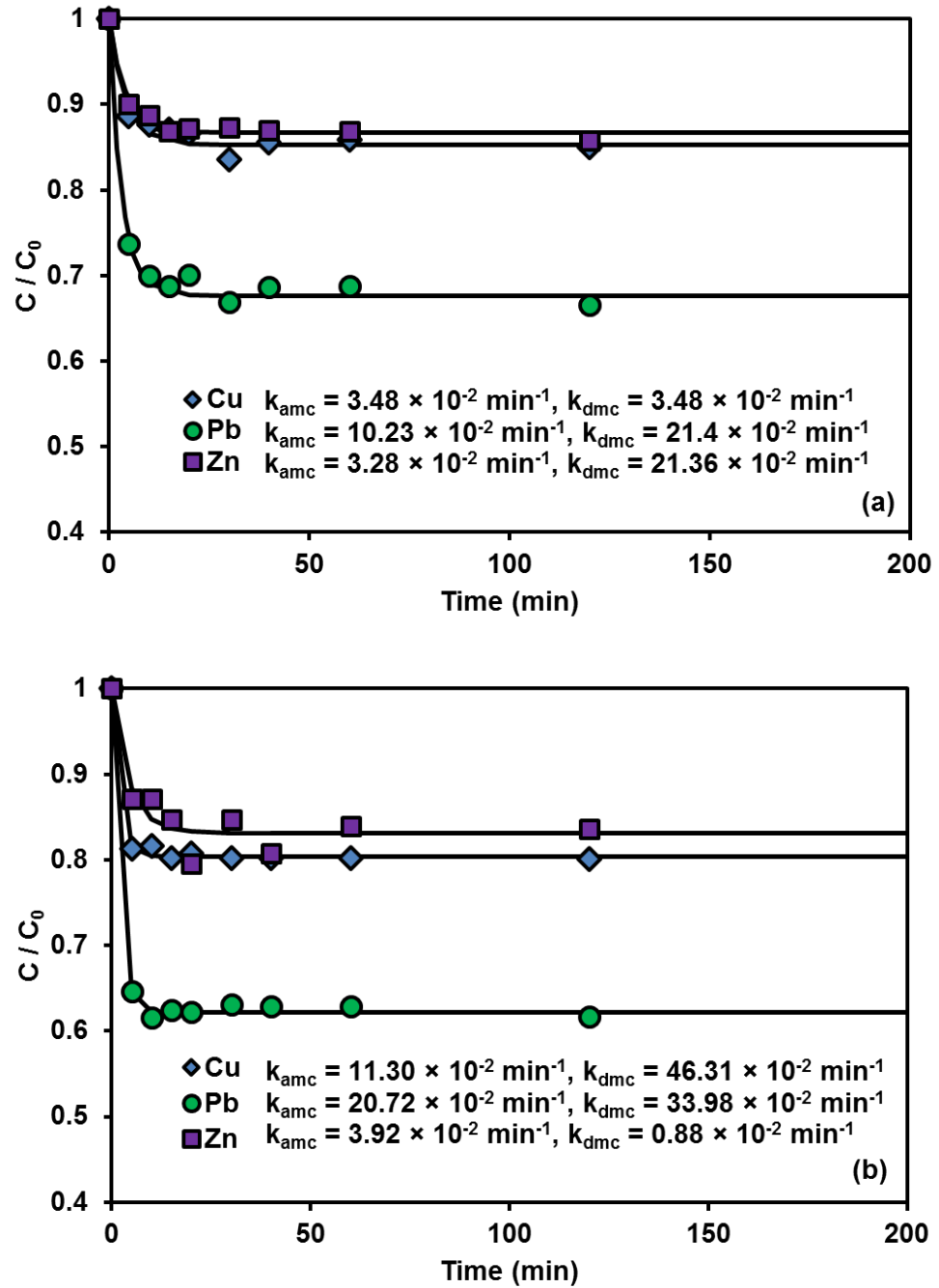


Figure 8.2. Batch kinetic test results of kaolinite colloids ($C_i = 5 \text{ mg L}^{-1}$) in (a) multi-metal system and (b) single-metal system. Data fitted to Equation (8-6) and the corresponding k_{amic} and k_{dmc} values are presented in Table 8-1. Data for 240 and 1440 min are not presented here.

8.4.2 Cotransport of heavy metals in silica sand

Because the column experiments performed in this work terminated after the injection of metals or metal-kaolinite solutions, tailing phenomena were not investigated here. Earlier breakthrough and a sharper rise was observed for Zn when compared to Pb and Cu, regardless of flow rate (Figure 8.3). Moreover, the plateau of breakthrough curve showed the sequence of $Pb > Cu > Zn$ which implies the predominant adsorption of Pb on the sand surface during transport may impede the adsorption of Cu and Zn and facilitate the transport of those two metals, which is reflected in the optimized Langmuir parameters (Table 8-3). The sharp rise of the Zn breakthrough curve resulted in high values determined for instantaneous equilibrium sorption sites (f) (consistent with $f_{Zn} > f_{Pb}$ presented in (Chotpantararat et al. 2012)) and lower values of distribution coefficient (K_d) for Zn than for Pb or Cu. In addition, the sequence of plateau concentrations resulted in q_{max} values as $Pb > Cu > Zn$ in both flow rate tests. Furthermore, slight increases in β and ϕ of the three metals under low flow rate (Table 8-3) indicated that the lower flow rate (increased residence time (t_r) of metal solution, $t_r \approx 150$ sec and 450 sec for $q = 2.22$ cm min^{-1} and 0.74 cm min^{-1}) in the bed resulted in a larger quantity of metals adsorbed to the sand (except the ϕ values of Cu, attributed to higher $q_{max(Cu)}$ under low flow rate). The high R^2 and low SSR values (Table 8-3) indicate that the two-site sorption with Langmuir isotherm (Equation (8-2) and (8-3)) well described the cotransport of Pb, Cu, and Zn in sand. This result was consistent with the result presented in Wikiniyadhane et al. (2015).

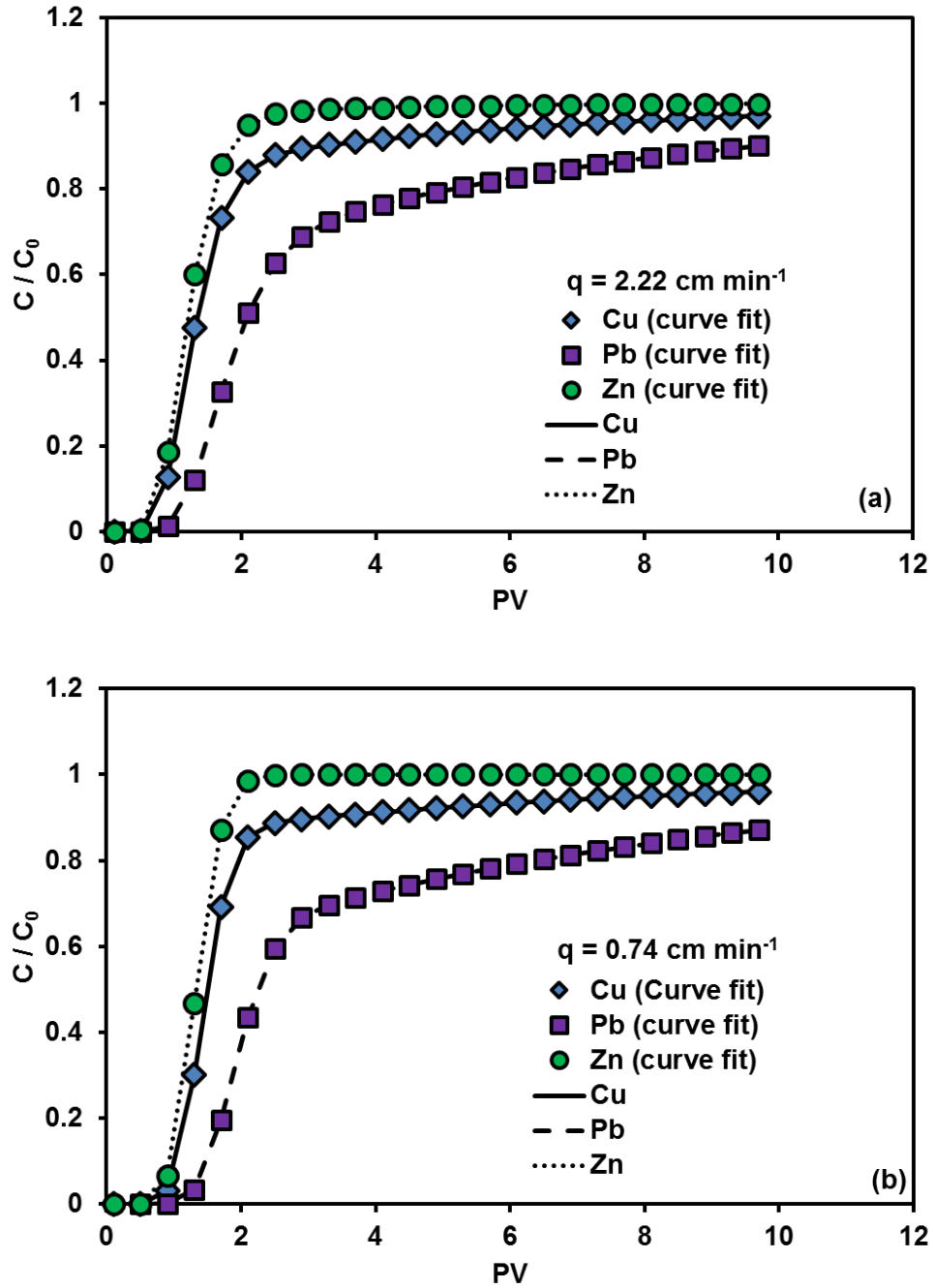


Figure 8.3. Observed and simulated breakthrough curves of three metals under the absence of kaolinite colloids: (a) $q = 2.22 \text{ cm/min}$; (b) $q = 0.74 \text{ cm/min}$.

8.4.3 Cotransport of heavy metals under presence of kaolinite colloids (multi-metal system)

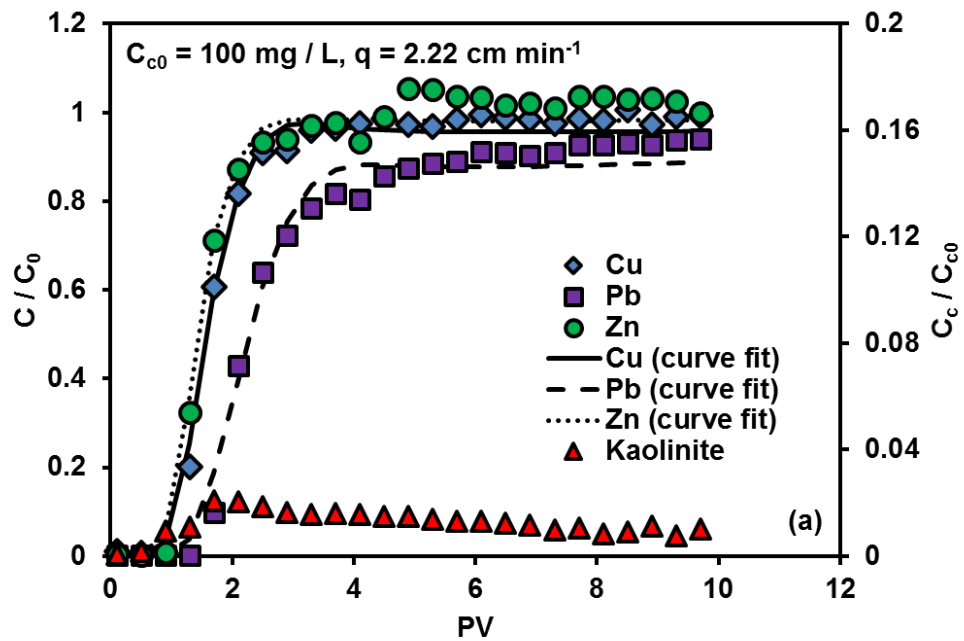
The adsorption preference for the breakthrough curves in the multi-metal system ($Pb > Cu > Zn$) in the presence of kaolinite colloids followed the same order as breakthrough curves without kaolinite (Figure 8.3 -Figure 8.5), which was anticipated based on the sequence of adsorption for those three metals to silica sand and kaolinite (Figure 8.3 and Figure 8.1(a)). In contrast, regardless of kaolinite concentration, more similar plateaus ($C / C_0 \approx 1$) and β values between Cu and Zn were observed under high flow rate (q) with kaolinite colloids when compared to without kaolinite colloids. This trend implies that the adsorption of Cu and Zn to the bed is hindered more substantially by the adsorption of Pb with kaolinite colloids under relatively high q . In addition, regardless of q , a decrease in β values for Pb, Cu, and Zn with kaolinite colloids implied that the presence of kaolinite may impede the adsorption of the three metals to the sand due to more favorable adsorption of the metals to the kaolinite. This is well reflected the optimization analysis where lower optimized ω appears with kaolinite colloids (Table 8-4) than without kaolinite colloids (Table 8-3). Because two unknown coefficients (k_{aic} and ω) were involved in the adsorption of the metal ion to the bed (two coefficients counterbalance each other), quantitative comparison of the optimized coefficients in each experiment was not possible (Table 8-4). However, high R^2 and low SSRs values indicated that the model used in this work (Equation (8-1)) simulated the experimental breakthrough curves well.

Based on the determined β values (Table 8-4), the transport of Pb and Cu were slightly facilitated under high flow rate and retarded under low flow rate as the kaolinite concentration increased (no trend of β was observed for Zn). This can be attributed to the

different transport/retention behavior of kaolinite colloids in the two different flow rates (Figure 8.6). Higher flow rate applied larger hydrodynamic forces to the attached/strained kaolinite colloids and possibly caused more colloidal rolling on the sand surface (i.e., detachment of colloids (Bergendahl and Grasso 2000b; Bradford et al. 2013; Tsai et al. 1991)). As a result, retained kaolinite colloids were better distributed throughout the column under the high flow rate conditions, and were observed at the outflow particularly at high kaolinite concentrations, $C_{c0} = 1000 \text{ mg L}^{-1}$ (Figure 8.4(c)). Therefore, an increase in C_{c0} under high flow rate may hinder the adsorption of metals to the sand throughout the column and facilitate the transport of metals. Also, even higher C_c / C_{c0} (Figure 8.4(c)) and deeper penetration of kaolinite (Figure 8.6(a)) at $C_{c0} = 1000 \text{ mg L}^{-1}$ compared to the other concentrations can be explained by the Langmuir dynamic applied to the mathematical model (Equation (3-8)).

In contrast, almost no kaolinite colloids were observed under low flow rate. Lower hydrodynamic torque resulted in severe straining and most of the kaolinite colloids were retained at the top of the sand column (Figure 8.6(b)). This resulted in the adsorption of heavy metal ions at the top of the column due to the concentrated adsorption sites provided by severe straining of kaolinite colloids, which retarded the transport of Pb and Cu with an increase in C_{c0} . Overall, no significant differences of breakthrough curves was observed as a function of kaolinite concentration (less variation of β and ϕ), which is primarily attributed to the short-term experimental time frame and the relatively low fraction of adsorbed metal ions on kaolinite colloids in the preequilibrated metal-kaolinite solution before the injection ($< 3\%$ estimated by the fitted Langmuir isotherm presented in Figure 8.1(a)). Nevertheless, the results presented in Figure 8.4, Figure 8.5 and Table 8-4 allow

the comparison of breakthrough curves between transport with kaolinite colloids and without kaolinite colloids, and quantified the behavior of cotransported of heavy metals with kaolinite colloids under the preequilibrated condition. The trend of breakthrough curves might have been different if the kaolinite colloids and the metal solution were introduced simultaneously due to the interaction between mobile kaolinite colloids and metal ions.



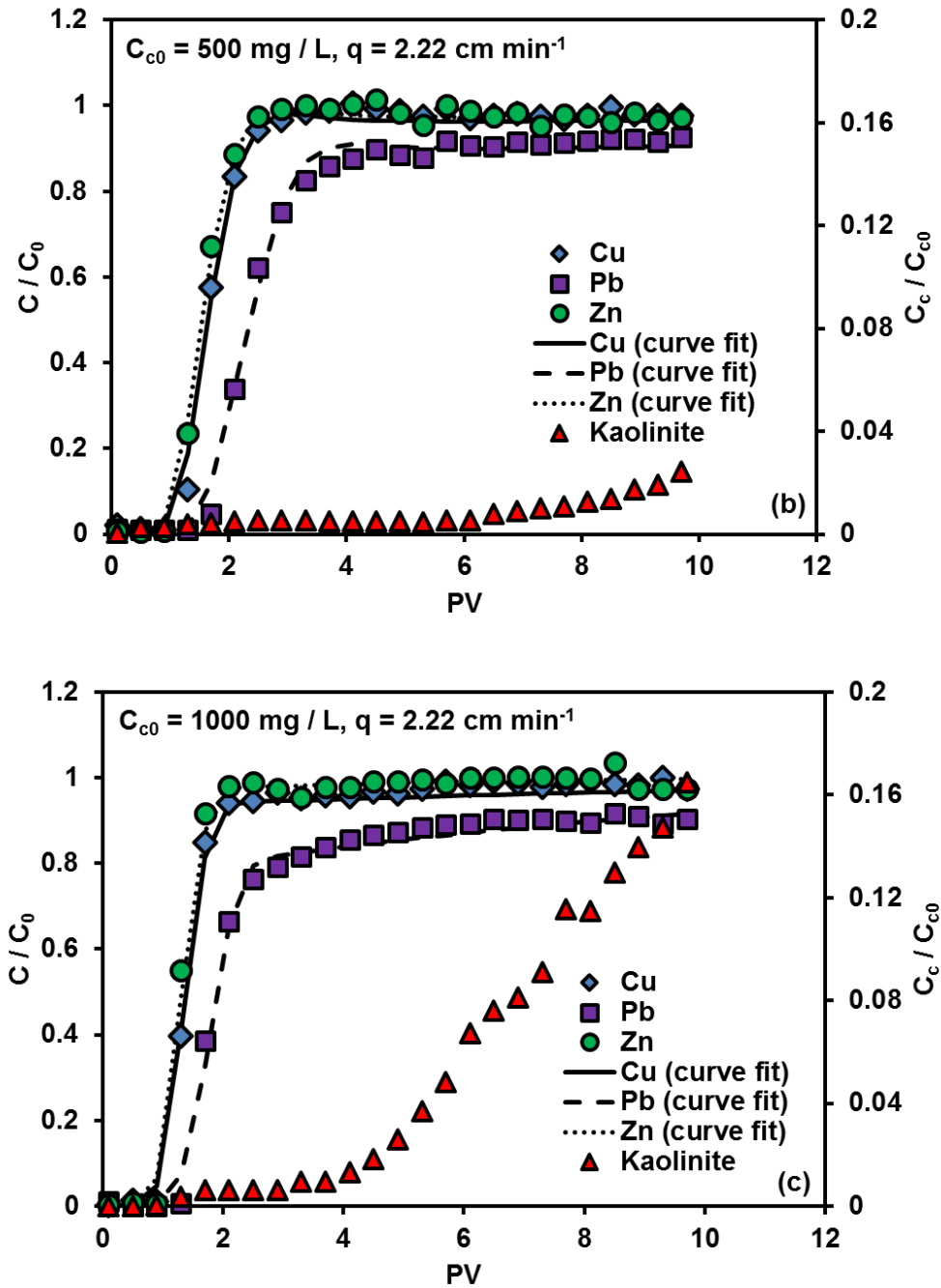
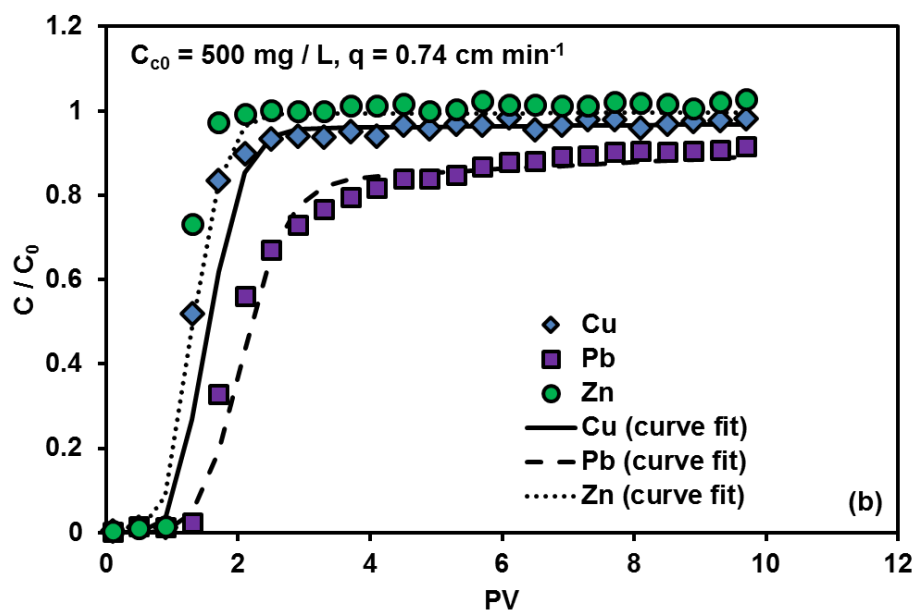
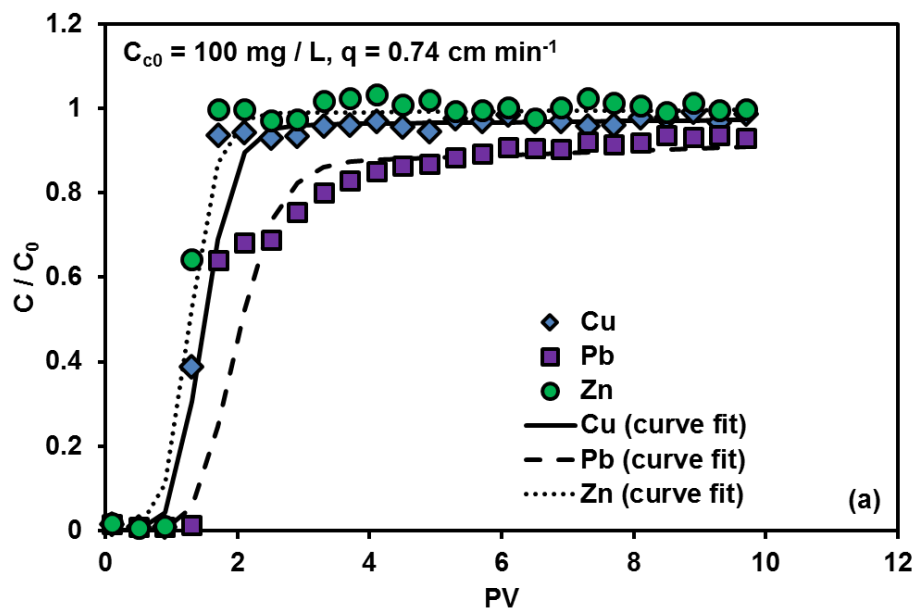


Figure 8.4. Observed and simulated breakthrough curve of heavy metals and kaolinite in the multi-metal system under the difference kaolinite concentration under high flow rate.



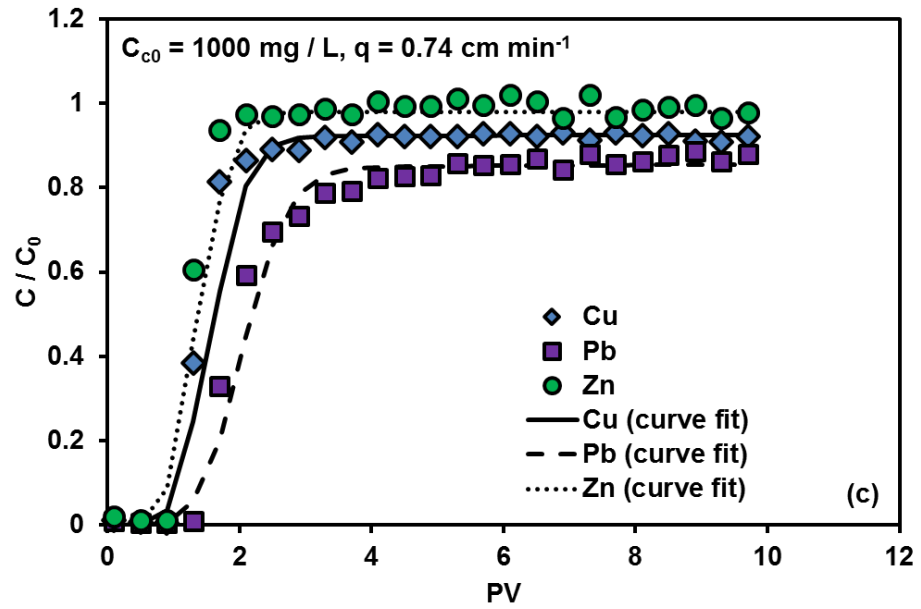


Figure 8.5. Observed and simulated breakthrough curve of heavy metals in the multi-metal system under the difference kaolinite concentration with low flow rate. No kaolinite was observed ($C_c / C_{c0} < 0.01$ for 10 pore volumes).

Table 8-4. β and ϕ of Experimental Breakthrough Curve and Optimized k_{aic} , k_{dic} , and ω in Multi-metal System

Experimental data			Optimized results						
C_{c0} (mg L^{-1})	q (cm min^{-1})	Metal	$\beta \times 10^2$	$\phi \times 10^2$	$k_{aic} \times 10^2$ (min^{-1})	k_{dic} (min^{-1})	$\omega \times 10^2$ (min^{-1})	R^2	SSRs $\times 10^2$
100	2.22	Cu	18.41	2.80	40.37	1.65	0.96	0.99	1.97
		Pb	30.94	3.51	49.79	1.21	2.16	0.99	4.26
		Zn	14.79	2.77	33.90	2.16	86.53	0.99	4.20
500	2.22	Cu	18.40	2.76	72.29	2.55	0.44	1.00	1.45
		Pb	30.48	3.40	111.89	2.08	1.23	0.99	1.62
		Zn	17.17	3.16	56.37	2.30	0.81	1.00	0.68
1000	2.22	Cu	16.07	2.37	41.99	10.06	3.55	1.00	1.05
		Pb	28.48	3.12	38.68	10.87	4.70	0.99	1.51
		Zn	14.01	2.53	50.36	8.00	12.97	0.99	1.33
100	0.74	Cu	16.48	2.32	2.59	63.16	0.65	0.97	7.45
		Pb	27.06	3.05	0.87	65.07	0.76	0.92	20.27
		Zn	12.09	2.24	14.17	50.15	1.85	0.98	4.77
500	0.74	Cu	16.76	2.32	23.35	41.02	0.62	0.95	11.42
		Pb	30.68	3.40	30.63	33.76	0.98	0.98	4.86
		Zn	11.14	2.03	16.43	48.21	0.59	0.96	9.45
1000	0.74	Cu	21.00	2.85	18.80	47.44	0.28	0.96	9.35
		Pb	31.87	3.46	35.43	49.29	0.35	0.98	5.39
		Zn	13.61	2.43	7.57	57.88	0.31	0.97	7.05

Note: preoptimized values of D , k_{amc} , k_{dmc} , k_{att} , k_{det} , k_{str} , f , K_d and q_{max} (Table 8-1, Table 8-2 and Table 8-3) were used for optimizing k_{aic} , k_{dic} , and ω .

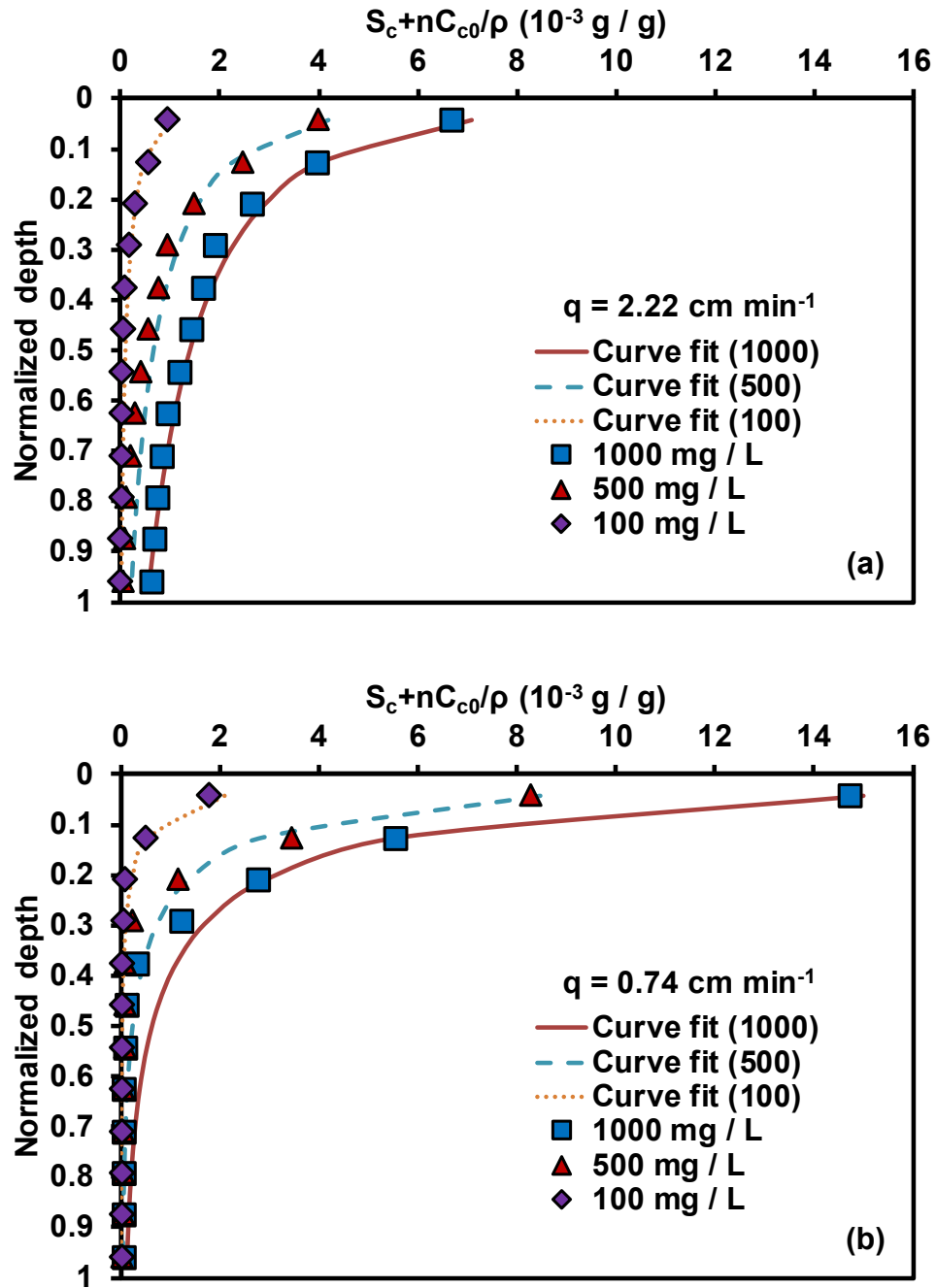
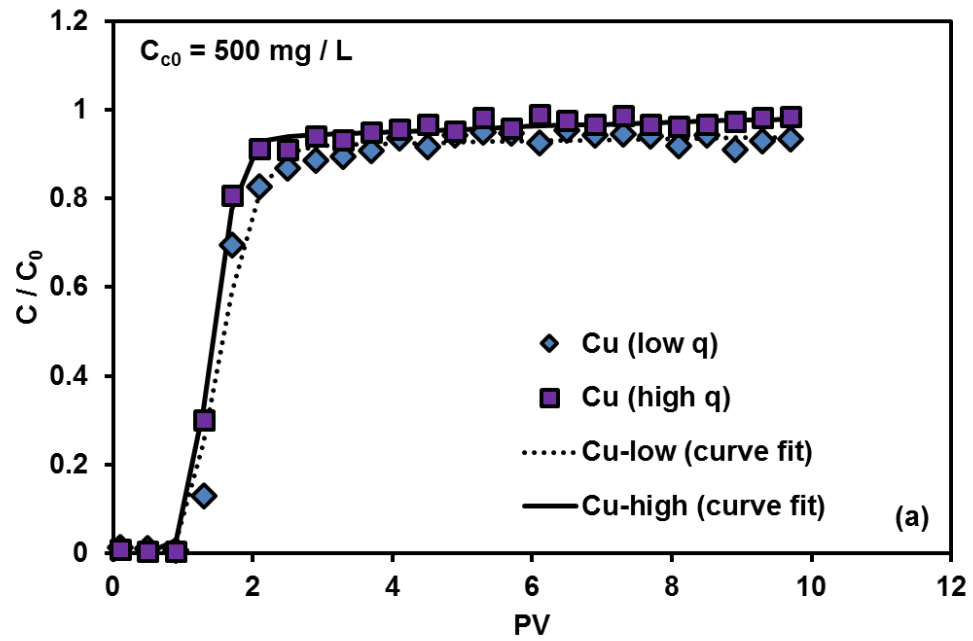


Figure 8.6. Observed and simulated retention profiles of kaolinite colloids under (a) high flow rate and (b) low flow rate in three different inlet concentrations. Optimized coefficients associated with retention profiles are presented in Table 8-2.

8.4.4 Cotransport of heavy metals under presence of kaolinite colloids (multi-metal system)

All transport experiments for the single-metal system with kaolinite colloids were performed with $C_{c0} = 500 \text{ mg / L}$ (Figure 8.7).



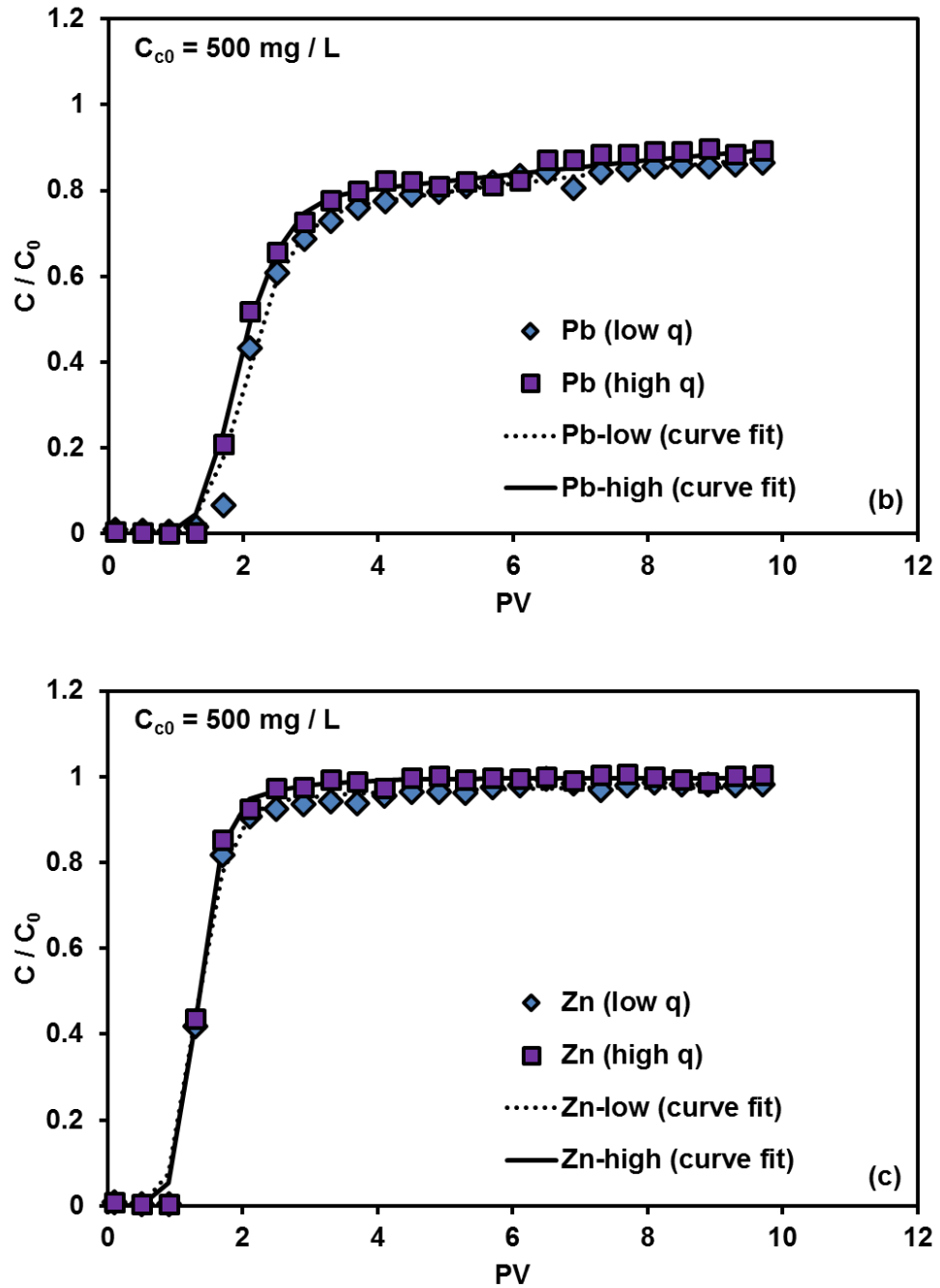


Figure 8.7. Observed and simulated breakthrough curve of heavy metal ions in the single-metal system under two different flow rates.

Table 8-5. β and ϕ of Experimental Breakthrough Curve and Optimized k_{aic} , k_{dic} and ω in Single-metal System

Experimental data					Optimized results				
C_{c0} (mg L^{-1})	q (cm min^{-1})	Metal	$\beta \times 10^2$	$\phi \times 10^2$	$k_{aic} \times 10^2$ (min^{-1})	k_{dic} (min^{-1})	$\omega \times 10^2$ (min^{-1})	R^2	SSRs $\times 10^2$
500	2.22	Cu	17.64	2.46	240.76	20.16	4.37	1.00	0.57
500	2.22	Pb	32.81	3.62	27.37	1.52	5.71	1.00	0.73
500	2.22	Zn	14.62	2.69	71.13	8.32	49.96	1.00	0.42
500	0.74	Cu	21.95	3.01	46.65	8.54	0.92	0.99	3.27
500	0.74	Pb	36.01	3.98	19.76	45.36	1.66	0.99	1.67
500	0.74	Zn	16.86	3.09	38.60	15.00	8.02	1.00	1.01

In the single-metal system, the slightly lower peak concentration of all metal ions was observed under low flow rate (Figure 8.7) and reflected β values (Table 8-5) with higher β in low flow rate. The difference of β values under different flow rate might have been more significant for long-term transport because of low ϕ values for all experiments. The data indicate that more than 95 % of adsorption sites were still available in the bed. This was mainly caused by the shorter residence time of the kaolinite-metal solution in the column under high flowrate, which allowed less sorption of metal ions to the sand or the kaolinite. The transport of each metal ion in the single-metal system was not significantly impacted by the number of metal ions under high flowrate, as seen by comparing β values in a single-metal system with those in the multi-metal system ($C_{c0} = 500 \text{ mg L}^{-1}$, $q = 2.22 \text{ cm min}^{-1}$ in Table 8-4). In contrast, larger β values were evaluated in the single-metal system under low flowrate, meaning that the transport of Cu, Pb or Zn was facilitated in the single-metal system. This resulted from competition for adsorption sites in the multi-metal system (Chotpantararat et al. 2011; Ding et al. 2014). The behavior of heavy metal

transport in the presence of kaolinite colloids in the single-metal tests was dependent on the flow rate, in contrast to the results from the multi-metal system. (Table 8-4), Experimental breakthrough curves in a single-metal ion system were also well described by the model with high R^2 values (Table 8-5). Moreover, the lower optimized ω values in the single-metal system than those values in Table 8-3 may suggest that less adsorption of metal to the sand occurred even under single-metal conditions due to the presence of kaolinite colloids (except ω for Zn in high q).

8.5 Summary

Transport of Cu, Pb, and Zn with and without kaolinite colloids at two different flowrates was investigated in the work performed in this chapter. In addition, a two-site Langmuir sorption model was used to describe the experimental breakthrough curves with the optimized first-order rate coefficient associated with the immobile kaolinite-metal ion and sand-metal ion interaction. The key findings from the experimental breakthrough curves and the optimization analysis include:

1. Based on the evaluated bed efficiency from the experimental breakthrough curves, the adsorption preference in competitive sorption tests followed the sequence $Pb > Cu > Zn$ with/without kaolinite colloids. Although the batch equilibrium test result of silica sand was not presented, the adsorption sequence during column transport tests followed the same sequence as in competitive batch equilibrium tests of kaolinite.
2. Increasing the concentration of kaolinite colloids facilitated the transport of Pb in the multi-metal conditions at high flow rate; however, transport of Cu and Zn was

not impacted significantly by the concentration of kaolinite colloids. Transport of Pb and Cu was retarded with increasing kaolinite colloid concentration at low flow rate. This may be attributed to the severe straining of kaolinite colloids under low flow rate, which resulted in more adsorption sites at the inlet of the sand column.

3. Based on the optimization analysis results and bed efficiency, the presence of kaolinite colloids in the sand medium may hinder the adsorption of Pb, Cu, and Zn and facilitate the transport of metal ions regardless of the flow rate.
4. Experimental breakthrough curves in single ion tests demonstrated that the behavior of heavy metal transport (facilitated or almost equal) with kaolinite colloids in single ion system and multi-ion tests was a function of the flow rate.
5. Applying preoptimized parameters associated with sand-heavy metal ion interaction and mobile kaolinite-heavy metal ion interaction, the colloid associated heavy metal transport model used in this work produced a good fit of the experimental breakthrough curves.

CHAPTER 9 CONCLUSION AND FUTURE WORK

The work performed in this dissertation explored the retention and transport behavior of colloidal clay particles transporting through saturated porous media. Experimental investigations and numerical modeling were performed to quantify colloidal impacts on hydraulic properties of the soil media, as well as impacts on the transport of single and competitive heavy metal ion solutions as they transported through laboratory soil columns. All experimental results were curve-fitted through numerical solutions to governing equations in order to obtain relevant first-order coefficients embedded in the governing equations. The major findings of the work performed are summarized as follows:

Experimental investigation of clay colloid retention/transport

- Solution chemistry (pH or ionic strength) controls the types of clay-particle associations (aggregation versus dispersion), the size of the clay cluster, and the interaction energy between sand grains and clay particles. Due to the association characteristics of clay particles (or colloids), the behavior of clay colloid retention/transport is critically impacted by solution chemistry.
- The trend of clay retention profiles and breakthrough curves demonstrated that blocking was more descriptive than ripening at neutral pH: blocking of clay colloids on the surface of sand grains by attachment resulted in inhibition of further colloidal attachment.
- In general, the mass of strained colloids decreased as the ionic strength of clay suspension increased, particularly under relatively high clay concentration. This

was primarily attributable to the smaller sizes of clay clusters at high ionic strength, which resulted in deeper penetration of clay colloids into the sand medium at a given flow rate.

- The size ratio between the colloids and the filter medium was critical in the retention of clay colloids because of significant straining at values of size ratio. This resulted in substantially decreased saturated hydraulic conductivity in the sand medium at low size ratio.
- At low flow rate, relatively large amounts of kaolinite were observed in the effluent for conditions of neutral pH/high ionic strength, and high pH/low ionic strength. In contrast, at high flow rates, a significant mass of kaolinite was observed in the effluent regardless of solution chemistry due to the large hydrodynamic forces applied to the attached colloidal particles. This implied that solution chemistry should only be considered a critical factor in clay colloidal transport at low flow rate.
- The reduction of hydraulic conductivity due to the retention of kaolinite colloids was greatest at pH ~ 3, independent of flow rate. However, at low flow rate, the reduction was more significant at pH ~ 6 than pH ~ 9 while reverse order was observed in high flow rate conditions.
- Previously attached kaolinite colloids could be detached through alteration of the prevailing geochemical conditions in the pore fluid. Detachment occurred when the induced repulsive interaction energy combined with prevailing hydrodynamic force exceed the net attraction energy between kaolinite and sand.

- The reduction of hydraulic conductivity due to colloidal retention was not only a function of the amount of retained kaolinite colloids but also depended on the dominant retention mechanism of kaolinite colloids (i.e., attachment or straining). The reduction of hydraulic conductivity was more significant when straining mechanism was dominant, which resulted in a more exponential retention profile of kaolinite colloids.

Modeling of clay colloid transport in a sand medium

- The uncertainty of retention profiles and breakthrough curves for clay colloids was examined by sampling multiple sizes of clay colloids at a given particle size distribution in order to reflect the polydispersed characteristics of clay colloids in the advection-dispersion type governing equation.
- The deterministic approach (i.e., use a median size of sand and clay in the modeling) significantly underestimated the amount of retained colloids, particularly at low size ratio. A stochastic representation of particle sizes was a better descriptor of transport for polydispersed colloids.
- The pore network model can be effectively used to reflect the geometry of pores, particles size distribution of colloids, and solution chemistry for colloid transport in porous media. In addition, by performing nonlinear least square fit of retention profiles, the model was used to estimate the first-order coefficients in the continuum equation for long-term and large-scale simulations.

Experimental investigation of clay colloid associated heavy metal ion transport

- In the presence of an immobile kaolinite colloidal phase in the sand medium, bed efficiency and Pb(II) saturation was evaluated from observed breakthrough curves of Pb(II). These revealed that an increase in kaolinite content significantly decreased the plateau concentration of Pb(II) at high pH, while kaolinite content was not critical in the plateau concentration of Pb(II) at low pH.
- Optimized first-order coefficients provided quantitative assessment of the adsorption/desorption behavior of Pb(II) from the immobile kaolinite phase, as observed from breakthrough curves.
- The flow rate was not always a critical factor for Pb(II) transport in a sand medium in the presence of immobile kaolinite colloids. However, more rapid Pb(II) transport was observed when there was a decrease in pH and an increase in ionic strength due to the protonation of surface hydroxyl groups on kaolinite.
- Based on the optimized first-order coefficients associated with adsorption/desorption between mobile kaolinite colloids and heavy metal ions and the calculated bed efficiency observed in breakthrough curves, the presence of kaolinite colloids in the sand medium can hinder the adsorption of Pb, Cu, and Zn and facilitate their transport through the column.
- Under relatively high flow rate, increases in the concentration of the kaolinite suspension at the injection point facilitated Pb transport without significantly impacting Cu and Zn transport. However, transport of Pb and Cu was retarded as kaolinite colloidal mass increased under low flow rate due to more significant

straining at low flow rate, which provided more adsorption sites near the injection point.

Future work

- All experimental and numerical modeling work presented in this dissertation was for saturated conditions. Additional work regarding clay colloid transport or clay colloid associated contaminant transport should be performed under unsaturated conditions, which would result in additional first-order coefficients in the continuum governing equation to account for attachment/adsorption takes place at the air-water interface.
- Kaolinite colloids and pure silica sand were used as clay colloids and sand medium in all laboratory experiments presented in this work. Therefore, using other clay minerals (e.g., illite or montmorillonite) with different surface charge characteristics, particularly as a function of pH, would be beneficial.
- The stochastic models presented in this work can be extended by taking factors such as uncertainty of interaction energy between colloids and grains and hydrodynamic forces into consideration.
- A regular cubic network with identical pore and throat sizes was used for the pore network model in this study. Because this is representative of semi-uniform sand, the sizes of pores and throats could be altered to account for the heterogeneity of pore sizes in other sand media.
- Constant flow rate was applied in the experiments in this work. However, at given conditions, much more clay colloids will be retained under conditions of constant

head. Because both flow conditions (constant flowrate / constant head) are ubiquitous in geotechnical and geoenvironmental applications, it would be beneficial to study clay colloid transport under conditions of constant head.

REFERENCES

- Abollino, O., Aceto, M., Malandrino, M., Sarzanini, C., and Mentasti, E. (2003). "Adsorption of heavy metals on Na-montmorillonite. Effect of pH and organic substances." *Water Research*, 37(7), 1619–1627.
- Adamczyk, Z., Siwek, B., Zembala, M., and Belouschek, P. (1994). "Kinetics of localized adsorption of colloid particles." *Advances in Colloid and Interface Science*, 48, 151–280.
- Aghighi, M., Hoeh, M. A., Lehnert, W., Merle, G., and Gostick, J. (2016). "Simulation of a Full Fuel Cell Membrane Electrode Assembly Using Pore Network Modeling." *Journal of The Electrochemical Society*, 163(5), F384–F392.
- Akan, A. O. (2002). "Sizing Stormwater Infiltration Structures." *Journal of Hydraulic Engineering*, 128(5), 534–537.
- Al-Degs, Y. S., Tutunji, M. F., and Baker, H. M. (2003). "Isothermal and kinetic adsorption behaviour of Pb²⁺ ions on natural silicate minerals." *Clay Minerals*, 38(4), 501–509.
- Amirtharajah, A., and Raveendran, P. (1993). "Detachment of colloids from sediments and sand grains." *Colloids and Surfaces A: Physicochemical and Engineering Aspects*, 73, 211–227.
- Archie, G. E. (1942). "The Electrical Resistivity Log as an Aid in Determining Some Reservoir Characteristics." *Transactions of the AIME*, 146(1), 54–62.
- Arya, L. M., and Dierolf, T. S. (1992). "Predicting soil moisture characteristics from particle-size distributions: An improved method to calculate pore radii from particle radii. In Indirect methods for estimating the hydraulic properties of unsaturated soils." *In Proceedings of the International Workshop on Indirect Methods for Estimating the Hydraulic Properties of Unsaturated Soils*, University of California. Riverside, CA, 115–124.
- Arya, L. M., Leij, F. J., van Genuchten, M. T., and Shouse, P. J. (1999a). "Scaling Parameter to Predict the Soil Water Characteristic from Particle-Size Distribution Data." *Soil Science Society of America Journal*, 63(3), 510.
- Arya, L. M., Leij, F. J., Shouse, P. J., and van Genuchten, M. T. (1999b). "Relationship between the Hydraulic Conductivity Function and the Particle-Size Distribution." *Soil Science Society of America Journal*, 63(5), 1063.
- Auset, M., and Keller, A. (2006). "Pore-scale visualization of colloid straining and filtration in saturated porous media using micromodels." *Water Resources Research*, 42(12).
- Bailey, S. E., Olin, T. J., Bricka, R. M., and Adrian, D. D. (1999). "A review of potentially low-cost sorbents for heavy metals." *Water Research*, 33(11), 2469–2479.

- Bedrikovetsky, P. (2008). "Upscaling of stochastic micro model for suspension transport in porous media." *Transport in Porous Media*, 75(3), 335–369.
- Bekhit, H. M., and Hassan, A. E. (2005). "Stochastic modeling of colloid-contaminant transport in physically and geochemically heterogeneous porous media." *Water Resources Research*, 41(2), 1–18.
- Benjamin, M. M., and Leckie, J. O. (1981). "Competitive adsorption of cd, cu, zn, and pb on amorphous iron oxyhydroxide." *Journal of Colloid and Interface Science*, 83(2), 410–419.
- Bergendahl, J., and Grasso, D. (1998). "Colloid generation during batch leaching tests: mechanics of disaggregation." *Colloids and Surfaces A: Physicochemical and Engineering Aspects*, 135(1–3), 193–205.
- Bergendahl, J., and Grasso, D. (1999). "Prediction of colloid detachment in a model porous media: Thermodynamics." *AIChE Journal*, 45(3), 475–484.
- Bergendahl, J., and Grasso, D. (2000a). "Prediction of colloid detachment in a model porous media: hydrodynamics." *Chemical Engineering Science*, 55(9), 1523–1532.
- Bergendahl, J., and Grasso, D. (2000b). "Prediction of colloid detachment in a model porous media: hydrodynamics." *Chemical Engineering Science*, 55(9), 1523–1532.
- Bergendahl, J., and Grasso, D. (2003). "Mechanistic Basis for Particle Detachment from Granular Media." *Environmental Science & Technology*, 37(10), 2317–2322.
- Berka, M., and Rice, J. A. (2005). "Relation between Aggregation Kinetics and the Structure of Kaolinite Aggregates." *Langmuir*, 21(4), 1223–1229.
- Berkowitz, B., Cortis, A., Dentz, M., and Scher, H. (2006). "Modeling non-Fickian transport in geological formations as a continuous time random walk." *Reviews of Geophysics*, 44(2).
- Bhattacharyya, K. G., and Gupta, S. Sen. (2008). "Adsorption of a few heavy metals on natural and modified kaolinite and montmorillonite: A review." *Advances in Colloid and Interface Science*, 140(2), 114–131.
- Boano, F., Packman, A. I., Cortis, A., Revelli, R., and Ridolfi, L. (2007). "A continuous time random walk approach to the stream transport of solutes." *Water Resources Research*, 43(10).
- Boudreau, B. P. (1996). "The diffusive tortuosity of fine-grained unlithified sediments." *Geochimica et Cosmochimica Acta*, 60(16), 3139–3142.
- Boulding, J. R., and Ginn, J. S. (2003). *Practical handbook of soil, vadose zone, and ground-water contamination: assessment, prevention, and remediation*. CRC Press.
- Bouwer, H. (1996). "Issues in artificial recharge." *Water Science and Technology*, 33(10–11), 381–390.
- Bradford, S. A., Bettahar, M., Simunek, J., and van Genuchten, M. T. (2004). "Straining

- and attachment of colloids in physically heterogeneous porous media.” *Vadose Zone Journal*, 3(2), 384–394.
- Bradford, S. A., Simunek, J., Bettahar, M., van Genuchten, M. T., and Yates, S. R. (2003). “Modeling Colloid Attachment, Straining, and Exclusion in Saturated Porous Media.” *Environmental Science & Technology*, 37(10), 2242–2250.
- Bradford, S. A., Simunek, J., Bettahar, M., van Genuchten, M. T., and Yates, S. R. (2006). “Significance of straining in colloid deposition: Evidence and implications.” *Water Resources Research*, 42(12).
- Bradford, S. A., Simunek, J., Bettahar, M., Tadassa, Y. F., van Genuchten, M. T., and Yates, S. R. (2005). “Straining of colloids at textural interfaces.” *Water Resources Research*, 41(10).
- Bradford, S. A., and Toride, N. (2007). “A Stochastic Model for Colloid Transport and Deposition.” *Journal of Environment Quality*, 36(5), 1346–1356.
- Bradford, S. A., Torkzaban, S., Leij, F., and Simunek, J. (2015). “Equilibrium and kinetic models for colloid release under transient solution chemistry conditions.” *Journal of Contaminant Hydrology*, Elsevier B.V., 181, 141–152.
- Bradford, S. A., Torkzaban, S., and Shapiro, A. (2013). “A Theoretical Analysis of Colloid Attachment and Straining in Chemically Heterogeneous Porous Media.” *Langmuir*, 29(23), 6944–6952.
- Bradford, S. A., Torkzaban, S., and Simunek, J. (2011). “Modeling colloid transport and retention in saturated porous media under unfavorable attachment conditions.” *Water Resources Research*, 47(10).
- Bradford, S. A., Torkzaban, S., and Walker, S. L. (2007). “Coupling of physical and chemical mechanisms of colloid straining in saturated porous media.” *Water Research*, 41(13), 3012–3024.
- Bradford, S. A., Yates, S. R., Bettahar, M., and Simunek, J. (2002). “Physical factors affecting the transport and fate of colloids in saturated porous media.” *Water Resources Research*, 38(12), 63-1-63–12.
- Brunori, C., Cremisini, C., Massanisso, P., Pinto, V., and Torricelli, L. (2005). “Reuse of a treated red mud bauxite waste: studies on environmental compatibility.” *Journal of Hazardous Materials*, 117(1), 55–63.
- Bunn, R. A., Magelky, R. D., Ryan, J. N., and Elimelech, M. (2002). “Mobilization of Natural Colloids from an Iron Oxide-Coated Sand Aquifer: Effect of pH and Ionic Strength.” *Environmental Science & Technology*, 36(3), 314–322.
- Camesano, T. A., and Logan, B. E. (1998). “Influence of Fluid Velocity and Cell Concentration on the Transport of Motile and Nonmotile Bacteria in Porous Media.” *Environmental Science & Technology*, 32(11), 1699–1708.
- Camesano, T. A., Unice, K. M., and Logan, B. E. (1999). “Blocking and ripening of

- colloids in porous media and their implications for bacterial transport.” *Colloids and Surfaces A: Physicochemical and Engineering Aspects*, 160(3), 291–307.
- Celia, M. A., Bouloutas, E. T., and Zarba, R. L. (1990). “A general mass-conservative numerical solution for the unsaturated flow equation.” *Water resources research*, 26(7), 1483–1496.
- Chen, G., and Flury, M. (2005). “Retention of mineral colloids in unsaturated porous media as related to their surface properties.” *Colloids and Surfaces A: Physicochemical and Engineering Aspects*, 256(2–3), 207–216.
- Chen, G., Flury, M., Harsh, J. B., and Lichtner, P. C. (2005). “Colloid-facilitated transport of cesium in variably saturated Hanford sediments.” *Environmental science & technology*, 39(10), 3435–3442.
- Chen, S. B., Ma, Y. B., Chen, L., and Xian, K. (2010). “Adsorption of aqueous Cd²⁺, Pb²⁺, Cu²⁺ ions by nano-hydroxyapatite: Single- and multi-metal competitive adsorption study.” *Geochemical Journal*, 44(3), 233–239.
- Chotpantarat, S., Ong, S. K., Sutthirat, C., and Osathaphan, K. (2011). “Competitive sorption and transport of Pb²⁺, Ni²⁺, Mn²⁺, and Zn²⁺ in lateritic soil columns.” *Journal of Hazardous Materials*, Elsevier B.V., 190(1–3), 391–396.
- Chotpantarat, S., Ong, S. K., Sutthirat, C., and Osathaphan, K. (2012). “Competitive modeling of sorption and transport of Pb²⁺, Ni²⁺, Mn²⁺ AND Zn²⁺ under binary and multi-metal systems in lateritic soil columns.” *Geoderma*, Elsevier B.V., 189–190, 278–287.
- Compère, F., Porel, G., and Delay, F. (2001). “Transport and retention of clay particles in saturated porous media. Influence of ionic strength and pore velocity.” *Journal of Contaminant Hydrology*, 49(1–2), 1–21.
- Corapcioglu, M. Y., and Choi, H. (1996). “Modeling Colloid Transport in Unsaturated Porous Media and Validation with Laboratory Column Data.” *Water Resources Research*, 32(12), 3437–3449.
- Corapcioglu, M. Y., and Jiang, S. (1993). “Colloid-facilitated groundwater contaminant transport.” *Water Resources Research*, 29(7), 2215–2226.
- Corapcioglu, M. Y., and Kim, S. H. (1995). “Modeling Facilitated Contaminant Transport By Mobile Bacteria.” *Water Resources Research*, 31(11), 2639–2647.
- Corapcioglu, M. Y., and Wang, S. (1999). “Dual-porosity groundwater contaminant transport in the presence of colloids.” *Water Resources Research*, 35(11), 3261–3273.
- Cortis, A. (2007). “Péclet-dependent memory kernels for transport in heterogeneous media.” *Physical Review E*, 76(3), 30102.
- Cortis, A., Chen, Y., Scher, H., and Berkowitz, B. (2004). “Quantitative characterization of pore-scale disorder effects on transport in ‘homogeneous’ granular media.”

- Physical Review E*, 70(4), 41108.
- Covelo, E. F., Vega, F. A., and Andrade, M. L. (2007). "Simultaneous sorption and desorption of Cd, Cr, Cu, Ni, Pb, and Zn in acid soils." *Journal of Hazardous Materials*, 147(3), 852–861.
- Crites, R. W. (1985). "Nitrogen Removal in Rapid Infiltration Systems." *Journal of Environmental Engineering*, 111(6), 865–873.
- Dai, S., and Seol, Y. (2014). "Water permeability in hydrate-bearing sediments, A pore scale study." *Geophysical Research Letters*, 41(May), 4176–4184.
- Delgado, J. M. P. Q. (2007). "Longitudinal and Transverse Dispersion in Porous Media." *Chemical Engineering Research and Design*, 85(9), 1245–1252.
- Denaix, L., Semlali, R. M., and Douay, F. (2001). "Dissolved and colloidal transport of Cd, Pb, and Zn in a silt loam soil affected by atmospheric industrial deposition." *Environmental pollution*, 114(1), 29–38.
- Derjaguin, B. V., and Landau, L. D. (1941). "Theory of the stability of strongly charged lyophobic sols and the adhesion of strongly charged particles in solutions of electrolytes." *Acta Physicochim. USSR*, 14, 633–662.
- Deshpande, P. A., and Shonnard, D. R. (1999). "Modeling the effects of systematic variation in ionic strength on the attachment kinetics of *Pseudomonas fluorescens* UPER-1 in saturated sand columns." *Water Resources Research*, 35(5), 1619–1627.
- Ding, Z., Hu, X., Morales, V. L., and Gao, B. (2014). "Filtration and transport of heavy metals in graphene oxide enabled sand columns." *CHEMICAL ENGINEERING JOURNAL*, Elsevier B.V., 257, 248–252.
- Dong, H., Onstott, T. C., Ko, C.-H., Hollingsworth, A. D., Brown, D. G., and Mailloux, B. J. (2002). "Theoretical prediction of collision efficiency between adhesion-deficient bacteria and sediment grain surface." *Colloids and Surfaces B: Biointerfaces*, Elsevier, 24(3), 229–245.
- Echeverría, J. C., Morera, M. T., Mazkiarán, C., and Garrido, J. J. (1998). "Competitive sorption of heavy metal by soils. Isotherms and fractional factorial experiments." *Environmental Pollution*, 101(2), 275–284.
- Elimelech, M., and O'Melia, C. R. (1990). "Kinetics of deposition of colloidal particles in porous media." *Environmental Science & Technology*, 24(10), 1528–1536.
- Farrah, H., and Pickering, W. F. (1979). "pH effects in the adsorption of heavy metal ions by clays." *Chemical Geology*, 25(4), 317–326.
- Fleshman, M. S. (2012). "Laboratory Modeling of Critical Hydraulic Conditions for the Initiation of Piping." *Utah State University, Logan*.
- Flury, M., and Qiu, H. (2008). "Modeling Colloid-Facilitated Contaminant Transport in the Vadose Zone." *Vadose Zone Journal*, 7(2), 682.

- Fu, F., and Wang, Q. (2011). "Removal of heavy metal ions from wastewaters : A review." *Journal of Environmental Management*, Elsevier Ltd, 92(3), 407–418.
- Gao, G., Fu, B., Zhan, H., and Ma, Y. (2013). "Contaminant transport in soil with depth-dependent reaction coefficients and time-dependent boundary conditions." *Water Research*, Elsevier Ltd, 47(7), 2507–2522.
- van Genuchten, M. T., and Wagenet, R. J. (1989). "Two-Site/Two-Region Models for Pesticide Transport and Degradation: Theoretical Development and Analytical Solutions." *Soil Science Society of America Journal*, 53(5), 1303.
- van Genuchten, M. T., and Wierenga, P. J. (1976). "Mass Transfer Studies in Sorbing Porous Media I. Analytical Solutions1." *Soil Science Society of America Journal*, 40(4), 473.
- Ghorai, S., and Pant, K. K. (2005). "Equilibrium, kinetics and breakthrough studies for adsorption of fluoride on activated alumina." *Separation and Purification Technology*, 42(3), 265–271.
- Ginn, T. R. (2002). "A travel time approach to exclusion on transport in porous media." *Water Resources Research*, 38(4), 12-1-12–11.
- Gostick, J., Aghighi, M., Hinebaugh, J., Tranter, T., Hoeh, M. A., Day, H., Spellacy, B., Sharqawy, M. H., Bazylak, A., Burns, A., Lehnert, W., and Putz, A. (2016). "OpenPNM: A Pore Network Modeling Package." *Computing in Science and Engineering*, 18(4), 60–74.
- Gostick, J. T., Ioannidis, M. A., Fowler, M. W., and Pritzker, M. D. (2007). "Pore network modeling of fibrous gas diffusion layers for polymer electrolyte membrane fuel cells." *Journal of Power Sources*, 173(1), 277–290.
- Grolimund, D., Borkovec, M., Barmettler, K., and Sticher, H. (1996). "Colloid-Facilitated Transport of Strongly Sorbing Contaminants in Natural Porous Media: A Laboratory Column Study." *Environmental Science & Technology*, 30(10), 3118–3123.
- Hahn, M. W., Abadzic, D., and O'Melia, C. R. (2004). "Aguasols: On the Role of Secondary Minima †." *Environmental Science & Technology*, 38(22), 5915–5924.
- Hajra, M. G., Reddi, L. N., Glasgow, L. A., Xiao, M., and Lee, I. M. (2002). "Effects of Ionic Strength on Fine Particle Clogging of Soil Filters." *Journal of Geotechnical and Geoenvironmental Engineering*, 128(8), 631–639.
- Happel, J. (1958). "Viscous flow in multiparticle systems: Slow motion of fluids relative to beds of spherical particles." *AIChE Journal*, 4(2), 197–201.
- Happel, J., and Howard, B. (2012). *Low Reynolds number hydrodynamics: with special applications to particulate media (Vol. 1)*. Springer Science & Business Media.
- Harter, R. D. (1983). "Effect of Soil pH on Adsorption of Lead, Copper, Zinc, and Nickel1." *Soil Science Society of America Journal*, 47(1), 47.

- Harvey, R. W., and Garabedian, S. P. (1991). "Use of colloid filtration theory in modeling movement of bacteria through a contaminated sandy aquifer." *Environmental Science & Technology*, 25(1), 178–185.
- Hashim, M. A., Mukhopadhyay, S., Narayan, J., and Sengupta, B. (2011). "Remediation technologies for heavy metal contaminated groundwater." *Journal of Environmental Management*, Elsevier Ltd, 92(10), 2355–2388.
- Heidmann, I., Christl, I., and Kretzschmar, R. (2005). "Aggregation Kinetics of Kaolinite–Fulvic Acid Colloids as Affected by the Sorption of Cu and Pb." *Environmental Science & Technology*, 39(3), 807–813.
- Helios Rybicka, E., Calmano, W., and Breeger, A. (1995). "Heavy metals sorption/desorption on competing clay minerals; an experimental study." *Applied Clay Science*, 9(5), 369–381.
- Hendry, M. J., Lawrence, J. R., and Maloszewski, P. (1997). "The Role of Sorption in the Transport of *Klebsiella oxytoca* Through Saturated Silica Sand." *Ground Water*, 35(4), 574–584.
- Ho, C. H., and Miller, N. H. (1986). "Adsorption of uranyl species from bicarbonate solution onto hematite particles." *Journal of Colloid and Interface Science*, 110(1), 165–171.
- Huang, K., Mohanty, B. P., Leij, F. J., and van Genuchten, M. T. (1998). "Solution of the nonlinear transport equation using modified Picard iteration." *Advances in Water Resources*, 21(3), 237–249.
- Ibaraki, M., and Sudicky, E. A. (1995). "Colloid-facilitated contaminant transport in discretely fractured porous media: 1. Numerical formulation and sensitivity analysis." *Water Resources Research*, 31(12), 2945–2960.
- Imdadm, A. O., and Sahimi, M. (1991). "Computer simulation of particle transport processes in flow through porous media." *Chemical Engineering Science*, 46(8), 1977–1993.
- Israelachvili, J. N. (2011). *Intermolecular and Surface Forces: revised third edition*. Academic press.
- Jensen, D. L., Ledin, A., and Christensen, T. H. (1999). "Speciation of heavy metals in landfill-leachate polluted groundwater." *Water Research*, 33(11), 2642–2650.
- Johnson, P. R., and Elimelech, M. (1995). "Dynamics of Colloid Deposition in Porous Media: Blocking Based on Random Sequential Adsorption." *Langmuir*, 11(3), 801–812.
- Johnson, W. P., Li, X., and Yal, G. (2007). "Colloid Retention in Porous Media: Mechanistic Confirmation of Wedging and Retention in Zones of Flow Stagnation." *Environmental Science & Technology*, 41(4), 1279–1287.
- Kaplan, D. I., Bertsch, P. M., and Adriano, D. C. (1993). "Soil-borne mobile colloids as

- influenced by water flow and organic carbon.” *Environ. Sci. and Technol.*, 27(6), 1192–1200.
- Khan, S., Cao, Q., Zheng, Y. M., Huang, Y. Z., and Zhu, Y. G. (2008). “Health risks of heavy metals in contaminated soils and food crops irrigated with wastewater in Beijing, China.” *Environmental Pollution*, 152(3), 686–692.
- Kraepiel, A. M. L., Keller, K., and Morel, F. M. M. (1999). “A Model for Metal Adsorption on Montmorillonite.” *Journal of Colloid and Interface Science*, 210(1), 43–54.
- Kraft, D. J., Ni, R., Smallenburg, F., Hermes, M., Yoon, K., Weitz, D. a., van Blaaderen, A., Groenewold, J., Dijkstra, M., and Kegel, W. K. (2012). “Surface roughness directed self-assembly of patchy particles into colloidal micelles.” *Proceedings of the National Academy of Sciences*, 109(27), 10787–10792.
- Kretzschmar, R., Borkovec, M., Grolimund, D., and Elimelech, M. (1999). “Mobile Subsurface Colloids and Their Role in Contaminant Transport.” 121–193.
- Kuznar, Z. A., and Elimelech, M. (2007). “Direct microscopic observation of particle deposition in porous media: Role of the secondary energy minimum.” *Colloids and Surfaces A: Physicochemical and Engineering Aspects*, 294(1–3), 156–162.
- Langmuir, I. (1918). “THE ADSORPTION OF GASES ON PLANE SURFACES OF GLASS, MICA AND PLATINUM.” *Journal of the American Chemical Society*, 40(9), 1361–1403.
- Lee, K.-Y., and Kim, K. (2010). “Heavy Metal Removal from Shooting Range Soil by Hybrid Electrokinetics with Bacteria and Enhancing Agents.” *Environmental Science & Technology*, 44(24), 9482–9487.
- Lenhart, J. J., and Saiers, J. E. (2002). “Transport of Silica Colloids through Unsaturated Porous Media: Experimental Results and Model Comparisons.” *Environmental Science & Technology*, 36(4), 769–777.
- Li, L. Y., and Li, R. S. (2000). “The role of clay minerals and the effect of H⁺ ions on removal of heavy metal (Pb²⁺) from contaminated soils.” *Canadian Geotechnical Journal*, 37(2), 296–307.
- Li, X., Scheibe, T. D., and Johnson, W. P. (2004). “Apparent Decreases in Colloid Deposition Rate Coefficients with Distance of Transport under Unfavorable Deposition Conditions: A General Phenomenon.” *Environmental Science & Technology*, 38(21), 5616–5625.
- Litton, G. M., and Olson, T. M. (1996). “Particle size effects on colloid deposition kinetics: evidence of secondary minimum deposition.” *Colloids and Surfaces A: Physicochemical and Engineering Aspects*, 107, 273–283.
- Mackie, R. I., Horne, R. M. W., and Jarvis, R. J. (1987). “Dynamic modeling of deep-bed filtration.” *AIChE Journal*, 33(11), 1761–1775.

- McCarthy, J. F., and Zachara, J. M. (1989). "Subsurface transport of contaminants." *Environmental Science & Technology*, 23(5), 496–502.
- McDowell-Boyer, L. M. (1992). "Chemical mobilization of micron-sized particles in saturated porous media under steady flow conditions." *Environmental Science & Technology*, 26(3), 586–593.
- McKay, M. D., Beckman, R. J., and Conover, W. J. (1979). "Comparison of Three Methods for Selecting Values of Input Variables in the Analysis of Output from a Computer Code." *Technometrics*, 21(2), 239–245.
- Metropolis, N., Rosenbluth, A. W., Rosenbluth, M. N., Teller, A. H., and Teller, E. (1953). "Equation of State Calculations by Fast Computing Machines." *The Journal of Chemical Physics*, 21(6), 1087.
- Mills, W. B., Liu, S., and Fong, F. K. (1991). "Literature Review and Model (COMET) for Colloid/Metals Transport in Porous Media." *Ground Water*, 29(2), 199–208.
- Mitchell, J. K., and Soga, K. (2005). *Fundamentals of soil behavior*. John Wiley and Sons, Inc., Hoboken, NJ.
- Mohanty, S. K., Saiers, J. E., and Ryan, J. N. (2015). "Colloid Mobilization in a Fractured Soil during Dry–Wet Cycles: Role of Drying Duration and Flow Path Permeability." *Environmental Science & Technology*, 49(15), 9100–9106.
- Molnar, I. L., Johnson, W. P., Gerhard, J. I., Willson, C. S., and O'Carroll, D. M. (2015). "Predicting colloid transport through saturated porous media: A critical review." *Water Resources Research*, 51(9), 6804–6845.
- Mulligan, C. N., and Yong, R. N. (1999). "Removal of Heavy Metals from Contaminated Soil and Sediments Using the Biosurfactant Surfactin." 8(2), 231–254.
- Nocito-Gobel, J., and Tobiasson, J. E. (1996). "Effects of ionic strength on colloid deposition and release." *Colloids and Surfaces A: Physicochemical and Engineering Aspects*, 107, 223–231.
- Norrfors, K. K., Marsac, R., Bouby, M., Heck, S., Wold, S., Lützenkirchen, J., and Schäfer, T. (2016). "Montmorillonite colloids: II. Colloidal size dependency on radionuclide adsorption." *Applied Clay Science*, Elsevier B.V., 123, 292–303.
- Olsen, H. W. (1960). "Hydraulic Flow Through Saturated Clays." *Clays and Clay Minerals*, 9(1), 131–161.
- Ouyang, Y., Shinde, D., Mansell, R. S., and Harris, W. (1996). "Colloid-enhanced transport of chemicals in subsurface environments: A review." *Critical Reviews in Environmental Science and Technology*, 26(2), 189–204.
- Palomino, A. M., and Santamarina, J. C. (2005). "Fabric map for kaolinite: effects of pH and ionic concentration on behavior." *clays and clay minerals*, 53(3), 211–223.
- Pang, L., and Šimůnek, J. (2006). "Evaluation of bacteria-facilitated cadmium transport

- in gravel columns using the HYDRUS colloid-facilitated solute transport model.” *Water Resources Research*, 42(12), n/a-n/a.
- Pazmino, E., Trauscht, J., and Johnson, W. P. (2014). “Release of Colloids from Primary Minimum Contact under Unfavorable Conditions by Perturbations in Ionic Strength and Flow Rate.” *Environmental Science & Technology*, 48(16), 9227–9235.
- Penrose, W. R., Polzer, W. L., Essington, E. H., Nelson, D. M., and Orlandini, K. A. (1990). “Mobility of plutonium and americium through a shallow aquifer in a semiarid region.” *Environmental Science & Technology*, 24(2), 228–234.
- Philip, J. R. (1957). “THE THEORY OF INFILTRATION.” *Soil Science*, 84(3), 257–264.
- Puls, R. W., and Powell, R. M. (1992). “Transport of inorganic colloids through natural aquifer material: implications for contaminant transport.” *Environmental Science & Technology*, 26(3), 614–621.
- Rabung, T., Lu, J., Schnurr, A., and Geckeis, H. (2015). “ScienceDirect Sorption of Cm (III) and Eu (III) onto clay minerals under saline conditions : Batch adsorption , laser-fluorescence spectroscopy and modeling.” 151, 192–202.
- Rajagopalan, R., and Tien, C. (1976). “Trajectory analysis of deep-bed filtration with the sphere-in-cell porous media model.” *AIChE Journal*, 22(3), 523–533.
- Raof, A., Nick, H. M., Hassanizadeh, S. M., and Spiers, C. J. (2013). “PoreFlow: A complex pore-network model for simulation of reactive transport in variably saturated porous media.” *Computers and Geosciences*, Elsevier, 61, 160–174.
- Reddi, L. N., Xiao, M., Hajra, M. G., and Lee, I. M. (2005). “Physical clogging of soil filters under constant flow rate versus constant head.” *Canadian Geotechnical Journal*, 42(3), 804–811.
- Rege, S. D., and Fogler, H. S. (1987). “Network model for straining dominated particle entrapment in porous media.” *Chemical Engineering Science*, 42(7), 1553–1564.
- Rege, S. D., and Fogler, H. S. (1988). “A network model for deep bed filtration of solid particles and emulsion drops.” *AIChE Journal*, 34(11), 1761–1772.
- Rice, R. C., and Rice, C. (1974). “Soil Clogging during Infiltration of Secondary Effluent.” 46(4), 708–716.
- Riotte, J., Chabaux, F., Benedetti, M., Dia, A., Gérard, M., Boulègue, J., and Etamé, J. (2003). “Uranium colloidal transport and origin of the 234U–238U fractionation in surface waters: new insights from Mount Cameroon.” *Chemical Geology*, 202(3–4), 365–381.
- Roy, S. B., and Dzombak, D. A. (1997). “Chemical Factors Influencing Colloid-Facilitated Transport of Contaminants in Porous Media.” *Environmental Science & Technology*, 31(3), 656–664.

- Roy, S. B., and Dzombak, D. A. (1998). "Sorption nonequilibrium effects on colloid-enhanced transport of hydrophobic organic compounds in porous media." *Journal of Contaminant Hydrology*, 30(1–2), 179–200.
- Ryan, J. N., and Elimelech, M. (1996). "Colloid mobilization and transport in groundwater." *Colloids and Surfaces A: Physicochemical and Engineering Aspects*, 107(95), 1–56.
- Ryan, J. N., and Gschwend, P. M. (1994). "Effects of Ionic Strength and Flow Rate on Colloid Release: Relating Kinetics to Intersurface Potential Energy." *Journal of Colloid and Interface Science*, 164(1), 21–34.
- Sahimi, M. (1993). "Flow phenomena in rocks: from continuum models to fractals, percolation, cellular automata, and simulated annealing." *Reviews of Modern Physics*, 65(4), 1393–1534.
- Saiers, J. E., and Hornberger, G. M. (1996). "The Role of Colloidal Kaolinite in the Transport of Cesium through Laboratory Sand Columns." *Water Resources Research*, 32(1), 33–41.
- Saiers, J. E., and Hornberger, G. M. (1999). "The influence of ionic strength on the facilitated transport of cesium by kaolinite colloids." *Water Resources Research*, 35(6), 1713–1727.
- Saiers, J. E., and Lenhart, J. J. (2003). "Colloid mobilization and transport within unsaturated porous media under transient-flow conditions." *Water Resources Research*, 39(1).
- Sang, W., Morales, V. L., Zhang, W., Stoof, C. R., Gao, B., Schatz, A. L., Zhang, Y., and Steenhuis, T. S. (2013). "Quantification of Colloid Retention and Release by Straining and Energy Minima in Variably Saturated Porous Media." *Environmental Science & Technology*, 47(15), 130724151622003.
- Santamarina, J. C., Klein, K. A., and Fam, M. A. (2001). *Soils and Waves: Particulate Materials Behavior, Characterization and Process Monitoring*. England: John Wiley and Sons Ltd.
- Santamarina, J. C., Klein, K. A., Wang, Y. H., and Prencke, E. (2002). "Specific surface: determination and relevance." *Canadian Geotechnical Journal*, 39(1), 233–241.
- Sari, A., Tuzen, M., Citak, D., and Soylak, M. (2007). "Equilibrium, kinetic and thermodynamic studies of adsorption of Pb(II) from aqueous solution onto Turkish kaolinite clay." *Journal of Hazardous Materials*, 149(2), 283–291.
- Schijven, J. F., and Hassanizadeh, S. M. (2000). "Removal of Viruses by Soil Passage: Overview of Modeling, Processes, and Parameters." *Critical Reviews in Environmental Science and Technology*, 30(1), 49–127.
- Scholes, L., Revitt, D. M., and Ellis, J. B. (2008). "A systematic approach for the comparative assessment of stormwater pollutant removal potentials." *Journal of Environmental Management*, 88(3), 467–478.

- Sen, T. K., Mahajan, S. P., and Khilar, K. C. (2002). "Colloid-Associated contaminant transport in porous media: 1. Experimental studies." *AIChE Journal*, 48(10), 2366–2374.
- Sen, T. K., Shanbhag, S., and Khilar, K. C. (2004). "Subsurface colloids in groundwater contamination: a mathematical model." *Colloids and Surfaces A: Physicochemical and Engineering Aspects*, 232(1), 29–38.
- Sen, T., and Khilar, K. C. (2006). "Review on subsurface colloids and colloid-associated contaminant transport in saturated porous media." *Advances in Colloid and Interface Science*, 119(2–3), 71–96.
- Shen, C., Lazouskaya, V., Zhang, H., Wang, F., Li, B., Jin, Y., and Huang, Y. (2012a). "Theoretical and experimental investigation of detachment of colloids from rough collector surfaces." *Colloids and Surfaces A: Physicochemical and Engineering Aspects*, Elsevier B.V., 410, 98–110.
- Shen, C., Li, B., Huang, Y., and Jin, Y. (2007). "Kinetics of coupled primary- and secondary-minimum deposition of colloids under unfavorable chemical conditions." *Environmental Science and Technology*, 41(20), 6976–6982.
- Shen, C., Wang, L.-P., Li, B., Huang, Y., and Jin, Y. (2012b). "Role of Surface Roughness in Chemical Detachment of Colloids Deposited at Primary Energy Minima." *Vadose Zone Journal*, 11(1).
- Sheppard, J. C., Campbell, M. J., Cheng, T., and Kittrick, J. A. (1980). "Retention of radionuclides by mobile humic compounds and soil particles." *Environmental Science & Technology*, 14(11), 1349–1353.
- Šimůnek, J., He, C., Pang, L., and Bradford, S. a. (2006). "Colloid-Facilitated Solute Transport in Variably Saturated Porous Media." *Vadose Zone Journal*, 5(3), 1035.
- Sirivithayapakorn, S., and Keller, A. (2003). "Transport of colloids in saturated porous media: A pore-scale observation of the size exclusion effect and colloid acceleration." *Water Resources Research*, 39(4).
- Siriwardene, N. R., Deletić, A., and Fletcher, T. D. (2007). "Clogging of stormwater gravel infiltration systems and filters: Insights from a laboratory study." *Water Research*, 41(7), 1433–1440.
- Smith, R. W., and Narimatsu, Y. (1993). "Electrokinetic behavior of kaolinite in surfactant solutions as measured by both the microelectrophoresis and streaming potential methods." *Minerals Engineering*, 6(7), 753–763.
- Sun, H., Gao, B., Tian, Y., Yin, X., Yu, C., Wang, Y., and Ma, L. Q. (2010). "Kaolinite and Lead in Saturated Porous Media : Facilitated and Impeded Transport." 136(November), 1305–1308.
- Syed, H. S. (1999). "Comparison studies adsorption of thorium and uranium on pure clay minerals and local Malaysian soil sediments Adsorption experiments." 241(1), 11–14.

- Tan, K. H. (2010). *Principles of soil chemistry*. CRC Press.
- Tang, Q., Tang, X., Li, Z., Chen, Y., Kou, N., and Sun, Z. (2009). “Adsorption and desorption behaviour of Pb(II) on a natural kaolin: equilibrium, kinetic and thermodynamic studies.” *Journal of Chemical Technology & Biotechnology*, 84(9), 1371–1380.
- Tang, X.-Y., and Weisbrod, N. (2009). “Colloid-facilitated transport of lead in natural discrete fractures.” *Environmental Pollution*, 157(8–9), 2266–2274.
- Torkzaban, S., and Bradford, S. A. (2016). “Critical role of surface roughness on colloid retention and release in porous media.” *Water Research*, Elsevier Ltd, 88, 274–284.
- Torkzaban, S., Bradford, S. A., van Genuchten, M. T., and Walker, S. L. (2008). “Colloid transport in unsaturated porous media: The role of water content and ionic strength on particle straining.” *Journal of Contaminant Hydrology*, 96(1–4), 113–127.
- Torkzaban, S., Bradford, S. A., and Walker, S. L. (2007). “Resolving the coupled effects of hydrodynamics and DLVO forces on colloid attachment in porous media.” *Langmuir*, 23(17), 9652–9660.
- Torok, J., Buckley, L. ., and Woods, B. . (1990). “The separation of radionuclide migration by solution and particle transport in soil.” *Journal of Contaminant Hydrology*, 6(2), 185–203.
- Tranter, T. G., Gostick, J. T., Burns, A. D., and Gale, W. F. (2016). “Pore Network Modeling of Compressed Fuel Cell Components with OpenPNM.” *Fuel Cells*, 16(4), 504–515.
- Tsai, C., Pui, D. Y. H., and Liu, B. Y. H. (1991). “Particle detachment from disk surfaces of computer disk drives.” *Journal of Aerosol Science*, 22(6), 737–746.
- Tufenkji, N., and Elimelech, M. (2004). “Correlation Equation for Predicting Single-Collector Efficiency in Physicochemical Filtration in Saturated Porous Media.” *Environmental Science & Technology*, 38(2), 529–536.
- Tufenkji, N., and Elimelech, M. (2005). “Breakdown of Colloid Filtration Theory: Role of the Secondary Energy Minimum and Surface Charge Heterogeneities.” *Langmuir*, 21(3), 841–852.
- Tufenkji, N., Redman, J. A., and Elimelech, M. (2003). “Interpreting Deposition Patterns of Microbial Particles in Laboratory-Scale Column Experiments.” *Environmental Science & Technology*, 37(3), 616–623.
- Um, W., and Papelis, C. (2002). “Geochemical effects on colloid-facilitated metal transport through zeolitized tuffs from the Nevada Test Site.” *Environmental Geology*, 43(1–2), 209–218.
- Urbonas, B., and Stahre, P. (1993). *Stormwater: best management practices and detention for water quality, drainage, and CSO management*.

- Valdes, J., and Santamarina, J. (2006). "Particle Clogging in Radial Flow: Microscale Mechanisms." *SPE Journal*, 11(2), 193–198.
- Valvatne, P. H., Piri, M., Lopez, X., and Blunt, M. J. (2005). "Predictive pore-scale modeling of single and multiphase flow." *Upscaling Multiphase Flow in Porous Media: From Pore to Core and Beyond*, 23–41.
- Vane, L. M., and Zang, G. M. (1997). "Effect of aqueous phase properties on clay particle zeta potential and electro-osmotic permeability: Implications for electrokinetic soil remediation processes." *Journal of Hazardous Materials*, 55(1–3), 1–22.
- Veli, S., and Alyüz, B. (2007). "Adsorption of copper and zinc from aqueous solutions by using natural clay." *Journal of Hazardous Materials*, 149(1), 226–233.
- Verwey, E. J. W., and Overbeek, J. T. G. (1948). *Theory of the Stability of Lyophobic Colloids*. Elsevier, Amsterdam.
- Vilks, P., and Baik, M. H. (2001). "Laboratory migration experiments with radionuclides and natural colloids in a granite fracture." *Journal of contaminant hydrology*, 47(2–4), 197–210.
- Wadell, H. (1932). "Volume, shape, and roundness of rock particles." *The journal of Geology*, 443–451.
- Wan, J., and Tokunaga, T. K. (1997). "Film Straining of Colloids in Unsaturated Porous Media: Conceptual Model and Experimental Testing." *Environmental Science & Technology*, 31(8), 2413–2420.
- Wan, J., and Wilson, J. L. (1994). "Colloid transport in unsaturated porous media." *Water Resources Research*, 30(4), 857–864.
- van de Weerd, H., Leijnse, A., and van Riemsdijk, W. H. (1998). "Transport of reactive colloids and contaminants in groundwater: effect of nonlinear kinetic interactions." *Journal of Contaminant Hydrology*, 32(3–4), 313–331.
- Wikiniyadhane, R., Chotpantarat, S., and Kee, S. (2015). "Effects of kaolinite colloids on Cd²⁺ transport through saturated sand under varying ionic strength conditions : Column experiments and modeling approaches." *Journal of Contaminant Hydrology*, Elsevier B.V., 182, 146–156.
- Williams, D. J. ., and Williams, K. . (1978). "Electrophoresis and zeta potential of kaolinite." *Journal of Colloid and Interface Science*, 65(1), 79–87.
- Wuana, R. A., and Okieimen, F. E. (2011). "Heavy Metals in Contaminated Soils: A Review of Sources, Chemistry, Risks and Best Available Strategies for Remediation." *ISRN Ecology*, 2011, 1–20.
- Xiong, Q., Baychev, T. G., and Jivkov, A. P. (2016). "Review of pore network modelling of porous media: Experimental characterisations, network constructions and applications to reactive transport." *Journal of Contaminant Hydrology*, The Authors, 192, 101–117.

- Xu, S., Gao, B., and Saiers, J. E. (2006). "Straining of colloidal particles in saturated porous media." *Water Resources Research*, 42(12).
- Xu, S., and Saiers, J. E. (2009). "Colloid straining within water-saturated porous media: Effects of colloid size nonuniformity." *Water Resources Research*, 45(5).
- Yan, Y. D. (1996). "Pulse-Injection Chromatographic Determination of the." 7463(11), 3383–3388.
- Yao, K., Habibian, M. T., and O'Melia, C. R. (1971). "Water and waste water filtration. Concepts and applications." *Environmental Science & Technology*, 5(11), 1105–1112.
- Yin, X., Gao, B., Ma, L. Q., Saha, U. K., Sun, H., and Wang, G. (2010). "Colloid-facilitated Pb transport in two shooting-range soils in Florida." *Journal of Hazardous Materials*, 177(1–3), 620–625.
- Yin, Y., and Allen, H. E. (1999). *In-situ Chemical Treatment, Technology Evaluation Report*. Ground-Water Remediation Technologies Analysis Center, Pittsburg, PA.
- Yuan, H., Shapiro, A., You, Z., and Badalyan, A. (2012). "Estimating filtration coefficients for straining from percolation and random walk theories." *Chemical Engineering Journal*, Elsevier B.V., 210, 63–73.
- Yukselen-Aksoy, Y., and Kaya, A. (2011). "A study of factors affecting on the zeta potential of kaolinite and quartz powder." *Environmental Earth Sciences*, 62(4), 697–705.
- Zamani, A., and Maini, B. (2009). "Flow of dispersed particles through porous media — Deep bed filtration." *Journal of Petroleum Science and Engineering*, Elsevier B.V., 69(1–2), 71–88.
- Zbik, M. S., Smart, R. S. C., and Morris, G. E. (2008). "Kaolinite flocculation structure." *Journal of Colloid and Interface Science*, Elsevier Inc., 328(1), 73–80.
- Zevi, Y., Dathe, A., McCarthy, J. F., Richards, B. K., and Steenhuis, T. S. (2005). "Distribution of Colloid Particles onto Interfaces in Partially Saturated Sand." *Environmental Science & Technology*, 39(18), 7055–7064.
- Zhang, F., Damjanac, B., and Huang, H. (2013). "Coupled discrete element modeling of fluid injection into dense granular media." *Journal of Geophysical ...*, 118(April), 2703–2722.
- Zhang, M.-K., Liu, Z.-Y., and Wang, H. (2010). "Use of Single Extraction Methods to Predict Bioavailability of Heavy Metals in Polluted Soils to Rice." *Communications in Soil Science and Plant Analysis*, 41(7), 820–831.
- Zhuang, J., Flury, M., and Jin, Y. (2003). "Colloid-Facilitated Cs Transport through Water-Saturated Hanford Sediment and Ottawa Sand." *Environmental Science & Technology*, 37(21), 4905–4911.

VITA

Jong Muk Won received his B.S. and M.S in Civil and Environmental Engineering from Korea University in 2011 and 2013 respectively. He pursued his graduate study in the United States and joined geoenvironmental engineering group in the School of Civil and Environmental Engineering supervised by Dr. Susan E. Burns at the Georgia Institute of Technology, Atlanta, Georgia. He is expected to graduate in December 2017.